# THE EFFECT OF FRACTURES ON FLUID FLOW IN GEOTHERMAL SYSTEMS, TAUPO VOLCANIC ZONE, NEW ZEALAND

---

*A thesis submitted in partial fulfilment*

*of the requirements for the degree of*

Doctor of Philosophy in Geology

in the University of Canterbury

by

**JONATHAN ROBERT JOSEPH DAVIDSON**

University of Canterbury

2014

---

*DEDICATED TO ALL SIZES OF 'POUPSE' IN MY LIFE*

# ABSTRACT

The goal of this thesis is to evaluate the effect of fractures on the bulk permeability of rocks. Several methods are used to address this problem: 1) surface radon gas measurements, 2) stress induced fracture permeability 3) fracture generation conditions. Each method was variably effective in providing answer to the initial question.

The radioactive radon isotopes ($^{220}$Rn and $^{222}$Rn) were measured in soil gas extracted from 1 m depth in two areas and the concentrations for both isotopes tended to be higher near mapped faults. Soil samples recovered from 1 m depth indicate that the isotopic anomalies are coincident with changes in soil colour and the emanation of $^{220}$Rn, but are unrelated to the $^{222}$Rn emanation. The lack of a relationship for the latter can be explained by small-scale (~1m) diffusion for >90% of the soil gas measurements. However, diffusion cannot explain all of the observed patterns in the data, and in some specific locations along the fault, $^{222}$Rn concentrations are more likely sensitive to advective flow of sub-surface gases, suggesting channelizing of flow along faults.

Stress is estimated using Leak-off Tests, estimating overburden weigth, and using drilling induced features observable in boreholes to model stress conditions. The results of the stress interpretation in the Rotokawa Geothermal Field show a relationship between the differential stress and alteration zones containing smectite, where the presence of smectite lowers the differential stress in the crust. This confirms a well-recorded relationship between the friction of rocks, and the strength of the crust. The magnitude of the principal stress axes, which are determined in this thesis, are used to

predict the fracture orientations prone to slip in the Rotokawa Reservoir. The precise range of fracture orientations prone to slip is critically dependent on the poorly constrained intermediate stress. However, analysis of stresses on fracture orientations observed in the Rotokawa Andesite, coupled with independent permeability estimates reveal a complex relationship between fracture slip, and permeability, suggesting that slip on fractures can have both a positive or negative effect on slip. This is will depend on the degree of alteration of the Rotokawa Andesite.

Failure in the Rotokawa Andesite is a result of: 1) the constant tectonic strain and 2) the increase in fluid pressure. Mathematical models used in this thesis show that if failure occurs through increase in fluid pressure, it is unlikely that the overpressures required to induce rock mass failure are solely generated by porosity/permeability reduction in the Rotokawa geothermal reservoir, requiring a constant external flux of fluids to induce the overpressures. Large-scale failure of the Rotokawa Andesite is modelled as a rock mass using the Hoek-Brown failure criterion, and indicates that the current dominant mode of failure is for the Rotokawa Andesite is shear failure at depth. However, small scale changes in stress, or an increase in rock mass strength will favour tensile failure. High fracture densities observed in three wells of the Rotokawa Andesite are oriented consistent with fractures formed in shear mode, consistent with ‘Healy’ faulting being the main mode of fracture formation in the Rotokawa Andesite.

# ACKNOWLEDGEMENTS

First of all- I'd like to thank Marie-Claude, as without you, my world would not be the same in any way. There is too much to say here, so I'll just say- you're the best.

I'd like to thank Darren Gravely, Uwe Ring, Andy Nicol and David McNamara, the supervisor dream team. D- thanks for giving me a chance with this project, and for trusting me to take it where I wanted! Uwe- thanks for the efficient support, and for taking me out in the field. Andy- thank you for your hard work, for your time and your understanding, you really made a big impact on the quality of this thesis. Dave- thanks for sharing your knowledge and the work you put in on the AFIT data!

A special thanks to all my family – it was great to have you all down here, and have your constant support, constant cribbage matches, and constant supply of gin tonics. Mom & Dad, I can't wait to be as good a role model as you guys were and still are. Patty-pooh, thanks for doing everything first and making it seem less scary. Including the PhD. Fred – thanks for looking out for me, and letting me vicariously live the dream by being a national team hockey player! I hope that little Felix follows in your footsteps.

I'd like to thank Jim Cole- it was always comforting to see the light spilling through your door at the end of the hallway, knowing that an enthusiastic and sympathetic person was near, ready to revise yet another draft. Sorry for the Jonathanisms.

To Ben- thanks for introducing me to UC, putting me in contact with Darren, and general muppetry.

Special thanks to Irene Wallis- a large part of this work would never have happened without your input, your work and technical knowledge. Thanks to the rest of the MRP team; Steve Sewell, Jonathon Clearwater, Jaime Quinao, Candice Bardsley, Jeremy O'Brien, Novi Ganefianto and Mike Barnes. Also thank you Tom Powell, for early discussions on project avenues, and for your great hospitality every time I stopped by in Rotorua.

Flo & Paul- for the never-ending support in every possible situation, for the great office atmosphere, endless coffees, for sharing these past three years and for leading the way! Flo- thanks for shedding the light on the amazing benefits of using the whiteboard. Paul, a special thank you for enjoying everything related to SpongeBob nearly as much as I do.

Cam & Tom- cheers for the help with the fieldwork! Cam thanks for helping me work out the kinks with the radon sampling, and Tom thanks for helping me develop a taste for vegemite and lion brown…

Thanks to…

- the UC postgrads, past and present: Felix, Eva, Paul A., Johnny, Theo, Latasha, James, Jacqui, Alison, Louise, Greg, Josh, Hamish, Sarah, Nick, Narges, Tom, Penelopi, Lauriane.

- The old geology crew- Bahama, Michelle, Carol, Michelle, Louis- I hope that we will keep crossing paths as frequently as possible. Thanks to Andrew and John for the recommendations.
- To the UC lecturers, for great discussions on a variety of topics: Brendan, Travis, Ben, Chris, Mark, Stephan,Marlene.
- DHB- for always being in the building. The truly loneliest moment was the day when I realised that not even he came into the department.
- Technical staff- you guys have always been happy to help me whenever I asked. In fact, maybe a bit too happy; Matt, Rob, Cathy, Sacha, Vanessa, Chris Grim, John S. & Janet- are you guys hiding something?
- To the lovely admin ladies that keep the department running smoothly- Pat & Janet
- Staff at GNS Wairakei for providing me with an office space and resources while I was doing field work
- Rick Sibson- for the nice few chats and for casually sending me the Healy paper, which completely changed my perspective on the problem.
- Patches, Gionta, Marky, Plek, PK, and the rest of the team... this is the year!

None of this would have been possible without the generous funding of Mighty River Power through the Source to Surface program, TechNZ, the Mason Trust, and CEDIES.

Special thanks to Jerry Fairley for great discussions of all sorts. You really help to shape the way I think about scientific problems, and how to tackle them.

# TABLE OF CONTENTS

# LIST OF FIGURES

**CHAPTER 1**

**CHAPTER 2**

## CHAPTER 3

**CHAPTER 4**

## CHAPTER 5

**APPENDICES**



# LIST OF TABLES

**CHAPTER 2**



**CHAPTER 4**

## CHAPTER 5



## APPENDICES

# CHAPTER 1:

## Introduction

# Introduction

The geological wonders of the Taupo Volcanic Zone (TVZ) in New Zealand have been of interest for centuries. The earliest human inhabitants were kept warm by its hot springs and the knife-sharp obsidian rocks from the area were widely coveted; TVZ obsidian is found at archaeological sites throughout New Zealand (Williams and Walton, 2003). After Europeans colonised New Zealand, tourists were attracted to the world famous Pink and White Terraces, sinter terraces on the edge of Lake Rotomahana, and balneological tours, where long-term sufferers from the old continent crossed oceans to enjoy the invigorating effect of the thermal waters, were recommended by physicians (Herbert, 1921).

Today, people benefit widely from the exceptional geothermal activity of the TVZ. A tourism industry is centered on geothermal areas such as the Wai-o-Tapu hot springs. The fluid circulating through geothermal systems has been tapped at various other locations, one of which, the Wairakei system, has been generating renewable electricity for over 50 years (Rosenberg et al., 2009). Needless to say, the economic and social impact of the TVZ is probably greater than any other geological feature in New Zealand. Therefore, carefully conducted research has the potential of creating a significant societal impact, as not only can research increase the knowledge of geothermal processes in the TVZ, but also has the ability to affect the general quality of life of the people who benefit from the TVZ's natural resources.

This thesis assesses the effect of fractures on the permeability and hydrology of geothermal systems in the TVZ. To address the primary goals of this thesis, data from two locations in the TVZ are used. First, Chapter 2 focuses on surface gas measurements in an area of active faulting, which includes the Paeroa Fault and the Ngakuru Graben 10 km south of Rotorua (Figure 1). The remainder of the thesis (Chapters 3-5) focuses on the Rotokawa Geothermal Field, located 10 km NE of Taupo (Figure 1). The data for these chapters are primarily from wells drilled for the exploration and development of the Rotokawa Geothermal Field (Figure 2). These wells provide a range of information from depths of up to 2500 m, including; fracture locations and orientations, location of high fluid flow zones, bulk permeability of aquifers, mechanical properties of rocks and various other datasets.

# 1 THE TAUPO VOLCANIC ZONE

## 1.1 Geological setting

Plate boundary processes dominate the New Zealand tectonic setting. At the southern end of the Tonga-Kermadec system, the oblique subduction of the Pacific plate under the North Island produces volcanism in the TVZ (Cole and Lewis, 1981). To the south of the TVZ, the plate boundary progresses from the subduction system to a strike-slip system in the South Island of New Zealand (Walcott, 1978, 1998). The TVZ can be subdivided into three segments, defined by the composition of the dominant type of volcanism (Wilson et al., 1995). The southern and northern segments are mainly andesitic, whereas the central segment, where the studies of this thesis were conducted, is dominated by rhyolitic volcanism. The central TVZ comprises an active rift, referred

to as the Taupo Rift or the Taupo Fault Belt (Figure 1), as well as exceptionally high rates of volcanism that has produced in excess of 15,000 km$^3$ of volcanic material over the past 2 Ma, mostly through caldera forming eruptions (Wilson et al., 1995).

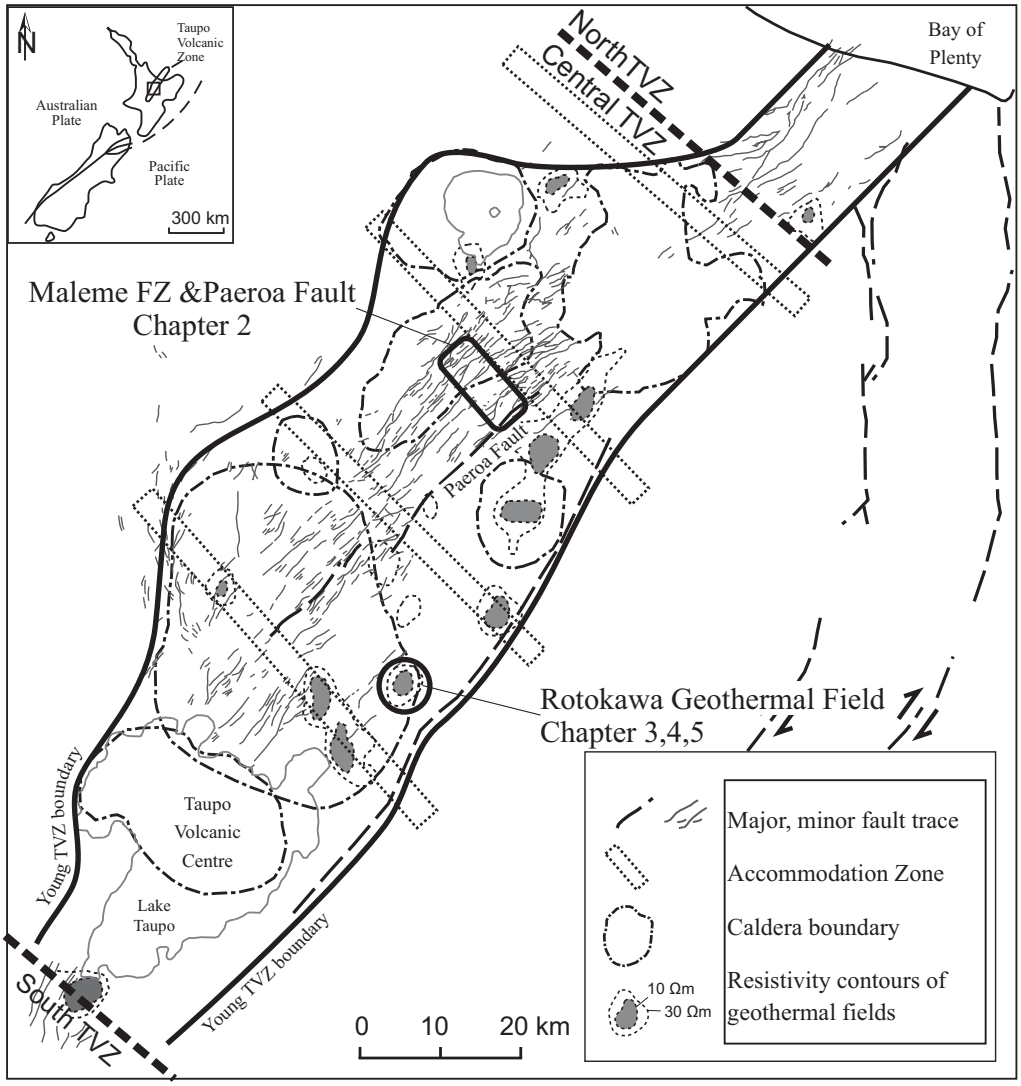


**Figure 1 Map of the central Taupo Volcanic zone (modified from Rowland and Sibson, 2004 and Bégué et al., 2014). The faults traces highlight the location of the Taupo rift. Note the absence of mapped fault traces at the surface along the southeastern edge of the central TVZ, where Quaternary faulting is known to have occurred at depth.**

The surface geology of the central TVZ is dominated by Quaternary volcanics in the form of rhyolitic explosive ignimbrites and effusive lava domes (Leonard et al., 2010). However at depth, a wider variety of volcanic and non-volcanic rocks have been encountered during drilling associated with geothermal development. These include

volcanics of various composition (such as the Rotokawa Andesite) and significant sedimentary units, such as lake deposits (Huka Falls formation , Manville and Wilson, 2003), and greywacke conglomerates (Waikora formation, Rae 2007). The Quaternary rocks are emplaced on top of Mesozoic greywacke basement that is geographically subdivided into the Torlesse Terrane on the east side of the TVZ, and the Waipapa Terrane on the west side of the TVZ. Both types of greywacke comprise poorly sorted sandstones that are variably interbedded with argillites (Leonard et al., 2010).

## 1.2 TVZ geothermal activity

The central TVZ hosts more than 20 geothermal fields (Bibby et al., 1995), six of which are currently being produced with an installed capacity of 829 MWe (NZGA). The geothermal systems associated with these fields transfer heat primarily through convection and, provide a total natural heat output of 4200±500 MW for the entire TVZ (Bibby et al., 1995). The hydrothermal fluids in these systems consist mostly of meteoric water (90±5%, Giggenbach, 1995), which when cold, makes its way to depth where it heats up and rises as buoyant plumes (Bibby et al., 1995; Bertrand et al., 2012). Dated hydrothermal deposit in active geothermal fields indicate that in cases they have occupied their present location for at least 200ka (Bibby et al., 1995).

Zones of intense clay alteration tend to form through the interaction of the hot rising hydrothermal fluids with the surrounding rocks (Browne, 1978). A combination of the clay alteration zones and conductive geothermal fluids have been detected using resistivity and magneto-telluric surveys, as they are less resistive than the surrounding rocks (Hatherton et al., 1966; Bibby et al., 1995; Bertrand et al., 2012). The clay caps

form the main hydrological feature of most TVZ geothermal systems, as they act as a barrier to vertical fluid flow (Winick et al., 2009; Boseley et al., 2010; O'Brien et al., 2011).

Some spatial relations have been drawn between the location of geothermal activity and mapped geologic structures at the surface. Specifically, geothermal systems are observed near mapped and inferred caldera boundaries (68%) and within the accommodation zones between rift segments (60%) (Rowland and Sibson, 2004). Geothermal activity in the TVZ is rarely observed along fault traces visible at the ground surface. The Paeroa Fault, which is studied in this thesis (see Chapter 2), is a notable exception having three geothermal systems at different locations along its length (Rowland and Sibson, 2004). Some developed fields are associated with faults at depth that were active in the Quaternary and have been subsequently buried by volcanic deposits, resulting in blind faults (Rae, 2007; Wallis et al., 2012). The focussed flow on deep structural controls are masked by distributed flow through permeable shallower rocks (Rowland and Sibson, 2004).

## 1.3 Rotokawa Geothermal Field

The Rotokawa Geothermal Field is a primary focus of this thesis (Figure 1). The resistivity anomaly associated with the field extends over an area of 17 to 28 $km^2$ (Rae, 2007), which includes Lake Rotokawa, and is cut by the Waikato River and the Parariki stream (Figure 3). Electricity has been generated from the Rotokawa Geothermal Field

since 1997, with a major development in 2010 (Nga Awa Purua), and a present total installed capacity of 174 MW (Quinao and Sirad-Azwar, 2012).

### 1.3.1 Stratigraphy

The surface geology of the Rotokawa Geothermal Field consists predominantly of rhyolite lava flows and domes, alluvium associated with river terraces along the Waikato River, and hydrothermal eruption breccias (Rae, 2007). Hydrothermal eruption vents are aligned along a NE-SW linear trend and include Lake Rotokawa which is the source of one of the largest hydrothermal breccia deposits in the TVZ ($10^7$ $m^3$, Browne & Lawless, 2001). The subsurface geology has been defined by extensive drilling into the Rotokawa Geothermal Field (Figure 2).

The Rotokawa subsurface hydrothermal system is divided into three distinct levels: a high temperature geothermal reservoir; an intermediate aquifer; and a shallow aquifer (Sewell et al., 2012). Discontinuous low-permeability layers, rich in the alteration clay Smectite, separate each aquifer (Figure 2). The oldest rocks present in the Rotokawa geothermal field are Mesozoic in age, consisting of poorly sorted sandstones interbedded with argillites (Rae, 2007), most likely belonging to the Torlesse Terrane (Leonard et al., 2010). These are directly overlain by rocks of Quaternary age. The rocks that are part of the deep reservoir comprise the Rotokawa Andesite, a massive to flow banded porphyritic lava (up to 2100m thick) (Rae, 2007), the Tahorakuri Formation, a succession of ignimbrite-bearing volcaniclastic deposits between 0.7-1.89 Ma (up to 250 m thick at Rotokawa) (Eastwood et al., 2013) and found both above and below the Waikora Formation, a greywacke sandstone and argillite siltstone pebble conglomerate (up to 250 m thick) (Rae, 2007). Above these units, the Nga Awa Purua

Andesite and the Wairakei ignimbrite are also included in the deep reservoir geology (Rae, 2007; Wallis et al., 2013). The Wairakei ignimbrite (up to 390 m) is part of the ~350 ka Whakamaru group of ignimbrites. The younger Quaternary units above the reservoir comprise a thick sequence of rhyolite lavas and, together with a crystal rich hornblende bearing tuff (the Waiora Formation) are ≤ 800 m thick (Wallis et al., 2013). The intermediate aquifer is mostly confined within this sequence (Sewell et al., 2012). The Parariki hydrothermal breccias (up to 200 m thick, Rae, 2007), and the Huka Falls Formation (up to 150 m of tuffs and sediments) are generally impermeable and act as a shallow cap to the intermediate aquifer (Sewell et al., 2012). The Oruanui Formation, a 26 ka pumice-bearing ignimbrite is one of the shallowest units in the Rotokawa Geothermal Field (Wallis et al., 2013).

### 1.3.2 Structure

The tops of the units older than ~350 ka are consistently displaced vertically by NE-SW trending faults that have little surface expression (Wallis et al., 2013), consistent with the alignment of hydrothermal eruption vents at the surface (Browne and Lawless, 2001). It has also been suggested by Wallis et al. (2013) that a significant paleo-topographic valley is present at the upper contact of the Rotokawa Andesite, where a thicker than usual sequence of the younger Tahorakuri and Waikora formations is present. The relationship between the temperature contours and the inferred structures at depth (Rae, 2007), the drawdown pressure gradients (Quinao et al., 2013), and results from microseismic studies (Sewell et al., 2013) suggest that the permeability of the deep reservoir rocks is strongly influenced by faulting and fracturing of host rocks.

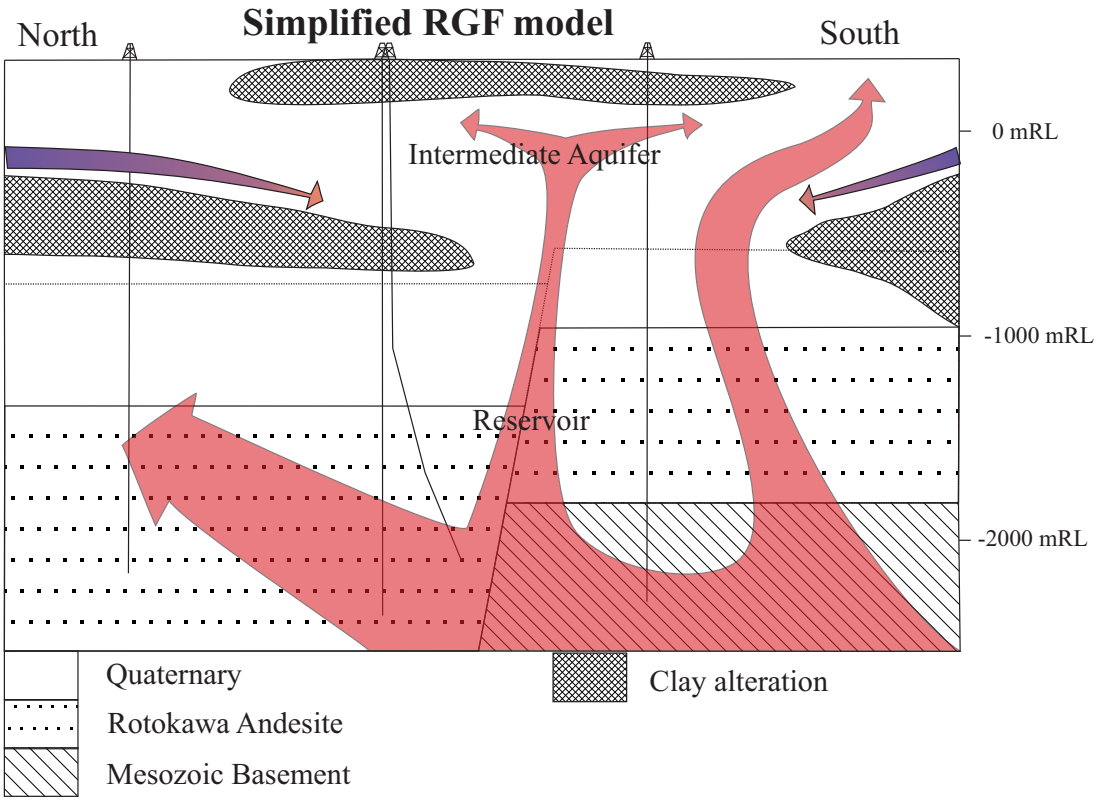


**Figure 2 Simplified cross section of the Rotokawa geothermal field, showing major geological boundaries, clay alteration and fluid flow (red polygons arrow for hot fluid, and blue for cold fluid) (after Winick et al 2009 and Sewell et al 2012). The fault in the centre is the Central Field Fault (see Figure 3); other inferred faults in Figure 3 are not shown here.**

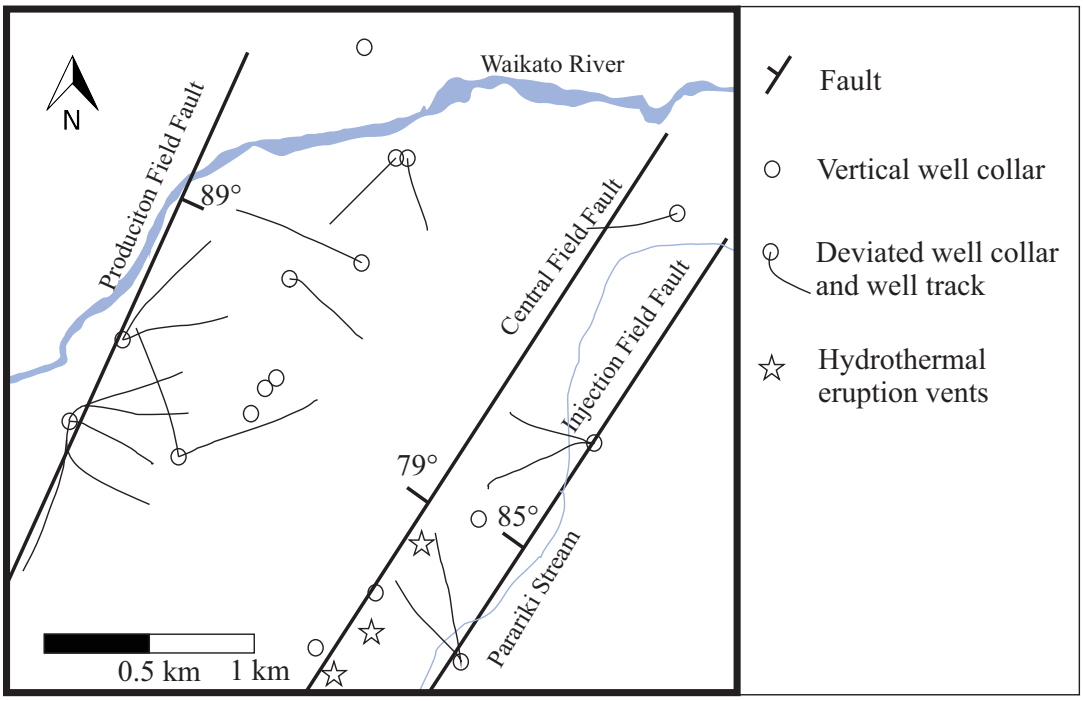


**Figure 3 Map of the Rotokawa Geothermal Field, showing main faults (Wallis 2013), permeability compartments (Quinao 2013) and well locations. Well tracks are shown for wells mentioned in the text only.**

# 2 FRACTURE PERMEABILITY

## 2.1 Controls on fracture permeability

Permeability not only controls the rate at which geothermal fluids, or other economically important fluids such as oil and gas, can be extracted from a reservoir, but is also a crucial parameter for $CO_2$ sequestration (Pollyea and Fairley, 2012), and nuclear waste repository containment (Montazer and Wilson, 1984; Bredehoeft, 1997). Changes in permeability can have a significant impact on surface groundwater levels (Rojstaczer and Wolf, 1992). Although the permeability of rock has wide-ranging economic implications, it can be challenging to assess, as permeability can be spatially and temporally variable. Few studies have managed to measure flow rates along faults, and usually rely on geochemical evidence (Favara et al., 2001), evidence of exhumed paleofluid paths (Caine et al., 1996), or flow rate proxies such as temperature (Fairley, 2004).

Measuring permeability on various scales often gives vastly different results (Brace, 1980). Permeability of rocks can be measured from core (i.e., on a scale of centimetres, referred to as matrix permeability) up to the scale of well interference or tracer tests (i.e., up to kilometres, referred to as bulk permeability). The amount of variability between scales can be related to a range of factors including the type of rock, the presence of fractures, and fracture densities. For example, core of crystalline rock consistently has lower permeability than larger scale tests within the same rock type, such well interference tests (Brace, 1980, 1984; Townend and Zoback, 2000). The

discrepancy between these scales of measurement is evidence that joints that are not present in lab scale experiments play a role in conducting fluids (Brace, 1980). However, scale has less of an effect on permeability measurements in sandstones, as fractures without any offset play a minor hydrological role in these high porosity rocks (Brace, 1980). The effect of scale is also not usually observed in shales, as the plastic behaviour of these rock types tend to seal joints, even at modest pressures (Brace, 1980). This first order appreciation of the effect of fractures on large-scale permeability does not take into account the complexity of fracture permeability, especially when considering the effects arising from the gouge and offset caused by faults.

The rock type in which the faulting occurs will strongly influence the permeability of the fault. In porous sandstones, the permeability of rock produced by faulting processes (e.g. cataclasis) can be reduced by up to seven orders of magnitude (Antonellini and Aydin, 1994). Deformation bands in unlithified sand-dominated sediments also reduce permeability by orders of magnitude (Rawling et al., 2001). The reduction in permeability is typically due to the development of fault rock associated with the destruction of porosity and reduction in grain size or the entrainment of fine-grained material, which creates a low permeability and clay-rich material (Yielding et al., 1997). The high clay content of gouge material means that it will deform plastically and remain unaffected by joints, even if deformed. The continuity and extent of the development of the fault rock will dictate whether it acts as an effective barrier to fluid flow, or allow flow across the fault (Yielding et al., 1997).

Fault gouge can be present in low-porosity, low-permeability crystalline rock. However, faulting in crystalline rock tends to be accompanied with extensive fracturing. The

fracture density can be high approaching the fault core, causing an associated increase in permeability and extremely high permeability gradients within some fault zones (Faulkner et al., 2010). The permeability will be increased near faults only if fractures are developed that promote fluid flow, which can be function of the rock type in which the faulting takes place (Caine et al., 1996; Rawling et al., 2001). The combination of fault core and associated fracturing cause fault zones to have a bipolar hydrological behaviour, where they can behave as effective barriers to across fault fluid flow and/or conduits for along fault fluid flow (Caine et al., 1996).

The permeability of fault zones varies in space and time. Fault zones in crystalline rock have generally have permeability promoting fractures, however the fractures produce an uneven increase in permeability. This means that some parts of fault zones are orders of magnitude more permeable than others and fluid flow tends to be focused or channelized into these small sections along the fault, usually located in complex zones along faults such as fault tips, fault interaction areas and fault intersections (Curewitz and Karson, 1997; Gartrell et al., 2004; Anderson and Fairley, 2008).

The uneven increase in permeability is demonstrated by the qualitative study of Barton et al. (1995). At three different locations (Cajon Pass and Long Valley, California and Yucca Mountain, Nevada) they showed that sharp temperature gradients existed near fractures that have a shear stress to normal stress ratio $\geq 0.6$, inferring that the change in temperature gradient was caused by fluid flow. This ratio of 0.6 is similar to what was derived experimentally for the friction of common crustal rocks (Byerlee, 1978). The fact that friction can be a control on fracture permeability suggests that fractures that most likely to experience slip tend to be open to fluid flow, and that fracture

permeability is mostly independent of fracture architecture (Barton et al., 1995, 1998). However, in the well where fluid flow rates were estimated at the Cajon Pass, the same study found that although many fractures were qualitatively assessed as open to flow, 80% of flow into the well was attributed to a single fracture (Barton et al., 1995). Localised flow along fault planes has been observed in the southern Taupo Volcanic Zone (TVZ) of New Zealand (Seebeck et al., 2014) where, although fluid flow was generally observed on or near faults, a single fault out of 720 contributes 30% of fluid flow into tunnels through crystalline rock. These observations suggests that factors other than slip impact on the fluid flow along fractures.

Although flow is generally restricted to fault planes that experience slip in low permeability rock, some parts of these same faults are orders of magnitude more permeable than other parts. Fracture permeability will be affected by fracture connectivity and density (Faulkner et al., 2010; Seebeck et al., 2014), by fracture dilation (Sibson, 1996) and also the transient nature of fracture permeability (Cox, 2005). The complexities of fracture mesh or fault zone architecture (Caine et al., 1996) cause large variations in fracture permeability, which translates to channelized flow of fluids along segments of faults that have the highest fracture permeability.

## 3 RESEARCH OBJECTIVES

The main goal of this thesis is to investigate the relationship between faults/fractures and bulk permeability of rocks. The variable effect that fractures have on different rock types, as well as the effect of fractures on permeability at different scales, all contribute

to the challenge of defining and understanding permeability. The reader of this thesis will be left with a sense of:

- The processes affecting soil gas flow near faults, including small-scale diffusion and large-scale advection (Chapter 2).
- Stress estimation methods, and pitfalls to avoid when using these methods such as Leak-off Test (Chapter 3).
- The variability in permeability and fluid flow along discontinuities such as faults and fractures, especially when considering the scale of fluid flow (Chapter 4).
- The usefulness of laboratory measurements, such as rock strength and permeability (Chapter 5).
- The shortcomings of laboratory measurements, and how to overcome them (Chapter 5).
- The effect of scale on rock strength caused by fractures, and how to assess rock mass behaviour (Chapter 5).

## 4 THESIS LAYOUT

This thesis has been written with the objective that each chapter presented is a stand-alone manuscript, and consequently there is some repetition between the introductory sections of each chapter. In this chapter, the general context for the research was introduced, and subsequent chapters will provide detailed assessment and discussion of the relevant literature and background. As the chapters have been written as individual manuscripts within a large and coherent body of work, it allows each chapter to be read independently, but it also enables the reader to follow a natural progression from one

chapter to the next in order to better understand fracture permeability in geothermal systems.

After this first introductory chapter, the second chapter focuses on the flow of gases around several faults in the central TVZ rift (including the major Paeroa fault) by means of quantifying the soil gas concentration of radon (Rn). The radioactivity of the radon (Rn) gas means that it is easy to distinguish between Rn isotopes, even at extremely low concentrations. The soil gas surveys found Rn anomalies spatially correlated with the location of faults scarps, however most Rn measured in the soil, even most of the anomalously high Rn, can be related to emanation from the soil itself. However, a small proportion of measurements cannot be explained by soil emanation. These are sometimes spatially correlated with the hot springs and fumaroles, suggesting that the anomalous radon has a deeper source, whose flow is influenced by disparities in the rock (i.e. faults and fractures).

The third chapter in this thesis focuses on a method for estimating the minimum principal stress in rocks at depth: the Leak-off Test (LOT). The LOT is extremely useful as it is able to establish stress at a great distance down wellbore, otherwise unattainable using other methods. Time based pressure data that was collected during drilling of development wells in the Rotokawa Geothermal Field is used to estimate the minimum principal stress. However, care is required when estimating stress using the LOT method, and an extra step is proposed to help eliminate tests in permeable formations where stress estimations are not appropriate. The valid stress results, combined with results for the vertical stress in Chapter 3, show that the stress at depth is roughly in frictional equilibrium if the effects of low friction clays are taken into account.

The fourth chapter delves into several other methods for estimating stress, including the stress caused by the weight of the overburden rock, as well as methods for estimating stress by inferring the conditions required to create drilling induced tensile fractures visible in borehole images. The ultimate goal of this chapter, however, is to infer the relationship between stress and fracture permeability in the main geological unit within the high temperature reservoir. The results show that the fracture permeability is quite complicated, where at times slip on fractures promotes permeability, and other times slip on fractures has a negative effect on permeability.

The fifth and penultimate chapter of the thesis attempts to assess factors that might influence the creation of permeability promoting fractures in the Rotokawa Andesite. In order to achieve this goal, a variety of datasets are gathered, and applied to simple analytical models, as well as empirical failure criteria, to help constrain the conditions that lead to rock failure. The conclusions of the chapter are that fluid overpressure may lead to failure, but only if they are externally driven, and the most likely mode of failure of the Rotokawa Andesite is shear failure.

The final Chapter sums up the conclusion and recommends future work. It is followed by several Appendices, which describe methods and present data mentioned in the Chapters.

## 5 REFERENCES

Anderson, T.R., Fairley, J.P., 2008. Relating permeability to the structural setting of a fault-controlled hydrothermal system in southeast Oregon, USA. J. Geophys. Res. 113, 1–13.

Antonellini, M., Aydin, A., 1994. Effect of Faulting on Fluid Flow in Porous Sandstones: Petrophysical Properties. Am. Assoc. Pet. Geol. Bull. 78, 355–377.

Barton, C.A., Hickman, S.H., Morin, R., Zoback, M.D., Benoit, D., 1998. Reservoir-Scale Fracture Permeability in the Dixie Valley, Nevada, Geothermal Field. Proc. SPE/ISRM Rock Mech. Pet. Eng. 299–306.

Barton, C.A., Zoback, M.D., Moos, D., 1995. Fluid flow along potentially active faults in crystalline rock. Geology 23, 683–686.

Bégué, F., Gravley, D.M., Chambefort, I., Deering, C., Kennedy, B., 2014. Magmatic volatile distribution as recorded by rhyolitic melt inclusions in the Taupo Volcanic Zone, New Zealand. Geol. Soc. London, Spec. Publ. in press.

Bertrand, E.A., Caldwell, T.G., Hill, G.J., Wallin, E.L., Bennie, S.L., Cozens, N., Onacha, S. a., Ryan, G. a., Walter, C., Zaino, A., Wameyo, P., 2012. Magnetotelluric imaging of upper-crustal convection plumes beneath the Taupo Volcanic Zone, New Zealand. Geophys. Res. Lett. 39, 1–6.

Bibby, H.M., Caldwell, T.G., Davey, F., Webb, T.H., 1995. Geophysical evidence on the structure of the Taupo Volcanic Zone and its hydrothermal circulation. J. Volcanol. Geotherm. Res. 68, 29–58.

Boseley, C., Cumming, W., Urzúa-monsalve, L., Powell, T., Grant, M.A., 2010. A Resource Conceptual Model for the Ngatamariki Geothermal Field Based on Recent Exploration Well Drilling and 3D MT Resistivity Imaging, in: Proceedings World Geothermal Congress 2010. Bali, Indonesia, p. 8.

Brace, W.F., 1980. Permeability of crystalline and argillaceous rocks. Int. J. Rock Mech. Min. Sci. Geomech. Abstr. 17, 241–251.

Brace, W.F., 1984. Permeability of crystalline rocks: New in situ measurements. J. Geophys. Res. 89, 4327.

Bredehoeft, J.D., 1997. Fault permeability near Yucca Mountain. Water Resour. Res. 33, 2459–2463.

Browne, P.R.L., 1978. Hydrothermal alteration in active geothermal fields. Annu. Rev. Earth Planet. Sci. 6, 229–250.

Browne, P.R.L., Lawless, J. V, 2001. Characteristics of hydrothermal eruptions, with examples from New Zealand and elsewhere. Earth-Science Rev. 52, 299–331.

Byerlee, J., 1978. Friction of rocks. Pure Appl. Geophys. PAGEOPH 116, 615–626.

Caine, J.S., Evans, J.P., Forster, C.B., 1996. Fault zone architecture and permeability structure. Geology 24, 1025–1028.

Cole, J.W., Lewis, K., 1981. Evolution of the Taupo-Hikurangi subduction system. Tectonophysics 72, 1–21.

Cox, S., 2005. Coupling between deformation, fluid pressures, and fluid flow in ore-producing hydrothermal systems at depth in the crust. Econ. Geol. 100th Anniv. Vol. 39–75.

Curewitz, D., Karson, J.A., 1997. Structural settings of hydrothermal outflow: Fracture permeability maintained by fault propagation and interaction. J. Volcanol. Geotherm. Res. 79, 149–168.

Eastwood, A.A., Gravley, D.M., Wilson, C.J.N., Chambefort, I., Oze, C., Cole, J.W., Ireland, T.R., 2013. U-Pb Dating of Subsurface Pyroclastic Deposits (Tahorakuri formation) at Ngatamariki and Rotokawa Geothermal Fields, in: New Zealand Geothermal Workshop 2013 Proceedings.

Fairley, J.P., 2004. Field observation of fluid circulation patterns in a normal fault system. Geophys. Res. Lett. 31, 1–4.

Faulkner, D.R., Jackson, C. a. L., Lunn, R.J., Schlische, R.W., Shipton, Z.K., Wibberley, C. a. J., Withjack, M.O., 2010. A review of recent developments concerning the structure, mechanics and fluid flow properties of fault zones. J. Struct. Geol. 32, 1557–1575.

Favara, R., Grassa, F., Inguaggiato, S., Valenza, M., 2001. Hydrogeochemistry and stable isotopes of thermal springs: earthquake-related chemical changes along Belice Fault (Western Sicily). Appl. Geochemistry 16, 1–17.

Gartrell, A., Zhang, Y., Lisk, M., Dewhurst, D., 2004. Fault intersections as critical hydrocarbon leakage zones: integrated field study and numerical modelling of an example from the Timor Sea, Australia. Mar. Pet. Geol. 21, 1165–1179.

Giggenbach, W., 1995. Variations in the chemical and isotopic composition of fluids discharged from the Taupo Volcanic Zone, New Zealand. J. Volcanol. Geotherm. Res. 68, 89–116.

Hatherton, T., Macdonald, W., Thompson, G., 1966. Geophysical methods in geothermal prospecting in New Zealand. Bull. Volcanol. 29, 485–497.

Herbert, A.S., 1921. The hot springs of New Zealand. H.K. Lewis, London.

Leonard, G.S., Begg, J.G., Wilson, C.J.N., 2010. Geology of the Rotorua Area: scale 1:250,000. Low. Hutt Inst. Geol. Nucl. Sci. Ltd. 102.

Manville, V., Wilson, C.J.N., 2003. Interactions between volcanism, rifting and subsidence: implications of intracaldera palaeoshorelines at Taupo volcano, New Zealand. J. Geol. Soc. London. 160, 3.

Montazer, P., Wilson, W., 1984. Conceptual Hydrologic Model of Flow in the Unsaturated Zone, Yucca Mountain, Nevada. USGS Water-Resources Invrestigations Rep. 84-4345 55.

O'Brien, J., Mroczek, E., Boseley, C., 2011. Chemical Structure of the Ngatamariki Geothermal Field, Taupo Volcanic Zone, N.Z., in: New Zealand Geothermal Workshop 2011 Proceedings.

Pollyea, R.M., Fairley, J.P., 2012. Implications of spatial reservoir uncertainty for CO2 sequestration in the east Snake River Plain, Idaho (USA). Hydrogeol. J. 20, 689–699.

Quinao, J.J., Sirad-Azwar, L., 2012. Correlation of Reservoir Monitoring and Continuous Production Data to Interpret Unexpected Well Behavior in Rotokawa, in: New Zealand Geothermal Workshop 2012 Proceedings. pp. 1–5.

Quinao, J.J., Sirad-azwar, L., Clearwater, J., Hoepfinger, V., Le Brun, M., Bardsley, C., 2013. Analyses and Modelling of Reservoir Pressure Changes to Interpret the Rotokawa Geothermal Field Response to Nga Awa Purua Power Station Operation, in: Thirty-Eight Workshop on Geothermal Reservoir Engineering.

Rae, A.J., 2007. Rotokawa Geology and Geophysics. GNS Sci. Consult. Rep. 2007/83, 11.

Rawling, G.C., Goodwin, L.B., Wilson, J.L., 2001. Internal architecture, permeability structure, and hydrologic significance of contrasting fault-zone types. Geology 29, 43.

Rojstaczer, S., Wolf, S., 1992. Permeability changes associated with large earthquakes: An example from Loma Prieta, California. Geology 20, 211–214.

Rosenberg, M.D., Bignall, G., Rae, A.J., 2009. The geological framework of the Wairakei–Tauhara Geothermal System, New Zealand. Geothermics 38, 72–84.

Rowland, J. V, Sibson, R.H., 2004. Structural controls on hydrothermal flow in a segmented rift system, Taupo Volcanic Zone, New Zealand. Geofluids 4, 259–283.

Seebeck, H.C., Nicol, A., Walsh, J.J., Childs, C., Beetham, R.D., Pettinga, J., 2014. Fluid flow in fault zones from an active rift. J. Struct. Geol. 62, 52–64.

Sewell, S.M., Cumming, W.B., Azwar, L., Bardsley, C., 2012. Integrated MT and Natural State Temperature Interpretation for a Conceptual Model Supporting Reservoir Numerical Modelling and Well Targeting at the Rotokawa Geothermal Field, New Zealand, in: Proceedings: Thirty-Seventh Workshop on Geothermal Reservoir Engineering. Stanford University, Stanford California.

Sewell, S.M., Cumming, W.B., Bardsley, C.J., Winick, J.A., Quinao, J.J., Wallis, I.C., Sherburn, S., Bourguignon, S., Bannister, S., 2013. Interpretation of Microearthquakes at the Rotokawa Geothermal Field, 2008 to 2012, in: New Zealand Geothermal Workshop 2013 Proceedings.

Sibson, R.H., 1996. Structural permeability of fluid-driven fault-fracture meshes. J. Struct. Geol. 18, 1031–1042.

Townend, J., Zoback, M.D., 2000. How faulting keeps the crust strong. Geology 28, 399–402.

Walcott, R.I., 1978. Geodetic strains and large earthquakes in the axial tectonic belt of North Island, New Zealand. J. Geophys. Res. 83, 4419–4429.

Walcott, R.I., 1998. Modes of oblique compression: Late Cenozoic tectonics of the south island of New Zealand. Rev. Geophys. 36, 1.

Wallis, I.C., Bardsley, C.J., Powell, T., Rowland, J. V, Brien, J.M.O., 2013. A Structural Model for the Rotokawa Geothermal Field, New Zealand, in: New Zealand Geothermal Workshop 2013 Proceedings.

Wallis, I.C., McNamara, D., Rowland, J. V, Massiot, C., 2012. The Nature of fracture permeability in the basement greywacke at the Kawerau Geothermal Field, New Zealand, in: Proceedings, Thirty-Seventh Workshop on Geothermal Reservoir Engineering. pp. 1–9.

Williams, A., Walton, T., 2003. Early landuse patterns in the Lake Taupo area. Sci. Conserv. 222.

Wilson, C.J.N., Houghton, B.F., McWilliams, M.O., Lanphere, M. a., Weaver, S.D., Briggs, R.M., 1995. Volcanic and structural evolution of Taupo Volcanic Zone, New Zealand: a review. J. Volcanol. Geotherm. Res. 68, 1–28.

Winick, J.A., Powell, T., Mroczek, E., 2009. The Natural-State Geochemistry of the Rotokawa Reservoir, in: New Zealand Geothermal Workshop 2009 Proceedings.

Yielding, G., Freeman, B., Needham, D., 1997. Quantitative Fault Seal Prediction. Am. Assoc. Pet. Geol. Bull. 6, 897–917.

# CHAPTER 2:

## Radon activity around faults in a geothermally-active area

# Radon activity around faults in a geothermally-active area

## 1 ABSTRACT

Radon anomalies are commonly measured near faults in various environments. Radon isotopes ($^{220}$Rn and $^{222}$Rn) were measured in soil gas extracted from 1 m depth in two areas where active faults have been mapped in the central Taupo Volcanic Zone (TVZ). Radon concentrations, for both isotopes, tend to be higher near the mapped faults. Soil samples recovered from 1 m depth indicate that the isotopic anomalies are coincident with changes in soil colour, presumably an indication of soil composition. $^{220}$Rn isotope emanation measured from extracted soil samples show a linear correlation with the field concentration measurements ($R^2$=0.90, p-value=$3x10^{-6}$), whereas $^{222}$Rn emanation shows no linear correlation ($R^2$=0.17, p-value=0.17). Yet, the isotopes measured in soil gas show a significant linear correlation of $^{220}$Rn and $^{222}$Rn concentrations ($R^2$ =0.35-0.55 , p-value<$9.1x10^{-3}$). This suggests a constant radon isotopic ratio is emitted from soil, which is supported by emission data measured on extracted soil samples. The distribution of $^{222}$Rn concentration compared to $^{220}$Rn can be explained by small-scale diffusion for >90% of the soil gas measurements. However, diffusion cannot explain all of the observed patterns in the data, and in some specific locations along the fault, $^{222}$Rn concentrations are more likely sensitive to advective flow of sub-surface gases, suggesting channelizing of flow along faults.

## 2 INTRODUCTION

Radon soil gas can occur along faults where it may record gas flow along the fault surfaces (e.g. Caine et al., 1996). Radon can also be produced by radium decay in the soil. This chapter focuses on understanding the processes that cause radon anomalies around faults, with the goal of using radon soil gas surveys to delineate faults that are not visible using geomorphic or geological mapping methods. To achieve this goal, we sampled the natural occurrence of two radon isotopes, $^{220}$Rn and $^{222}$Rn, in soil gas near faults in the central Taupo Volcanic Zone (TVZ).

Radon is the only naturally occurring gas that has no stable isotopes. It is part of the uranium/thorium decay series, and is the product of the alpha-decay of radium. Radon is relatively easy to detect at extremely low concentrations (1000Bq/m$^3$ is equivalent to 1.79x10$^{-13}$ g/m$^3$), due to the energy it emits as it decays to polonium, also by alpha decay. Radon is an inert gas, and thus is unaffected by chemical reactions.

Radon concentration anomalies that are significantly higher than background levels have been identified in areas of active fracturing or faulting (Tanner, 1978; Whitehead, 1984; Ciotoli et al., 1999; Font et al., 2008; Katsanou et al., 2010). The reported causes of these radon anomalies are considered to be due to either an increase in radon emanation in soils, or increased gas flow near faults that carry a radon-rich gas with it.

The “increased emanation” hypothesis is based on variability in radioactivity of soils (Vogler, 1960), co-variation between radon isotopes (Israel and Bjornsson, 1967), and/or the variability of the parent $^{226}$Ra and daughter $^{222}$Rn in soils (Tanner, 1964).

Increases in emanation could be caused by a number of processes (see review by Tanner, 1978), including co-precipitation of parent nuclides in groundwater mixing zones (Tanner, 1964), or increasing the surface area of faulted material by grain-size reduction (Tanner, 1978).

More recently, however, the increased gas flow hypothesis has been favoured. The main argument in favour of this hypothesis is that fault zones include fractures that locally increase permeability. In support of this hypothesis, some authors argue that faults are commonly associated with flow of gases, not exclusively radon. For example, co-variation between $CO_2$ gas flux and radon gas concentration around faults suggests that $CO_2$ might be acting as a carrier gas (King et al., 1996); however, it is worth noting that in one case, an increase in $CO_2$ flux was correlated in a decrease of $^{222}Rn$ concentration (Zarroca et al., 2012). In addition, a study of radon gas and radium soil content showed that radium remained constant over the fault scarp despite the presence of a radon concentration anomaly. Thus, the radon anomaly over the fault was best attributed to advective transport of radon enriched gas along the fault (Katsanou et al., 2010). Some radon anomalies over known faults have been attributed to increased gas flow without further investigation of the cause (Ioannides, 2003; Whitehead, 1984; Al-Tamimi and Abumurad, 2001; Atallah et al., 2001), and some of these authors have concluded that radon soil gas surveys are an effective tool to map blind faults (Whitehead, 1984; King et al., 1996; Burton et al., 2004; Al-Tamimi and Abumurad, 2001).

## 2.1 Radon migration

There are two main naturally occurring isotopes, $^{222}$Rn and $^{220}$Rn. $^{222}$Rn is part of the $^{238}$U decay series, and thus $^{222}$Rn gas is produced naturally in soils that contain $^{238}$U. $^{220}$Rn is part of the $^{228}$Th decay series, and as such is produced naturally in soils that are rich in the thorium parent. Thorium and uranium tend to be found in trace amounts in most soils.

The parent nuclides of radon (uranium, thorium and radium), being solid elements, naturally occur within grains in soils. Most radon that is produced remains within the grain. It is however possible for radon gas to escape from solid grains to the pore space of soils, through the recoil of the daughter nuclide (Rn) during alpha-decay of the parent nuclide (Ra). The proportion of radon nuclides that make it into the pore space is called the emanation power, or the radon emanation coefficient, and is a function of the grain size of the soil (Tanner, 1978), the soil humidity (Huxol et al., 2012) and also where the parent nuclide is contained relative to the grain itself (i.e. in the grain or on the grain as a surface coating) (Semkow and Parekh, 1990).

The two radon isotopes have vastly different half-lives: $^{222}$Rn has a half-life of 3.82 days and $^{220}$Rn, a half-life of 55.6s. $^{220}$Rn is much more abundant in soils than its longer lived counterpart, but its short half-life impedes this gas's ability to diffuse - e.g. its diffusion length in a common soil is estimated to be 20-31mm, compared to 1600-2400mm for $^{222}$Rn (using diffusion coefficients of $D_{eff}$=5x10$^{-6}$ and 12x10$^{-6}$ m$^2$/s, respectively) (Tanner, 1978; Huxol et al., 2012). The diffusion length is equivalent to

the distance that a radioactive gas travels by diffusion until only 1/*e* of the original gas concentration remains, the rest having dropped out due to radioactive decay.

$^{222}$Rn soil gas surveys have been suggested as a method of detecting uranium deposits (Fleischer et al., 1980). However, most radon anomalies linked to uranium deposits were relatively shallow (several meters). Uranium deposits at depths greater than 90 m are not detectable at the surface using radon surveys (Fleischer et al., 1980). Deposits at depths of around 50 m could be detected when 'sporadic puffs of upflowing gas' carried radon to the surface (Fleischer et al., 1980). In an experiment where a uranium bearing rock was buried, anomalies would register only within 4 m right above the buried source, and no anomalies were detected if you sidestepped away from the source rock (Tanner, 1978). These results highlight the small distances that radon gases can travel by diffusion, even when $^{222}$Rn gas is highly concentrated.

It is possible, however, for radon gas to travel by advective transport, in the presence of a "carrier gas". When such conditions exist, the distance that radon gas could cover before decaying is much larger than by diffusion processes alone. Yet, even when assisted by a carrier gas, radon transport remains spatially restricted. For example, a gas flowing through a relatively permeable saturated media can have a velocity on the order of cm/s (by bubble ascent, see Etiope, 2002), and in such a case the $^{220}$Rn gas would travel 80 cm before decaying to 1/*e* of its original concentration. If $^{222}$Rn were carried in the same situation, however, it would travel over 4 km before decaying to 1/*e* of the original concentration. Even at micro-seepage velocities (~0.1 cm/s, Etiope, 2002), the $^{222}$Rn would travel almost 500 m before decaying the same amount.

The difference in migration distance achieved by both isotopes is highly significant when conducting soil gas surveys. The $^{220}$Rn nuclide is unable to travel distances more than 1 m, even in the presence of a carrier gas, unless an extreme flow of gas is achieved (such as a steam fumarole). Any $^{220}$Rn measured in soil gas will have been produced within 1m of the sampling location. This provides a powerful tool to measure radon gas production that occurs within the soil. For example, when the concentration of both isotopes co-vary, it is more likely that an anomaly is due to an increase in the production of radon gases in the soil, rather than radon gases travelling by either diffusion or advection from a deeper source. This allows us to distinguish anomalies that are caused by local variation in soil radon emanation from ones that are caused by a flow of a radon-rich gas from depth.

The two causes of radon anomalies are not mutually exclusive. Yet, dominant process that causes the anomalies is expected since it is generally accepted that anomalous radon concentrations are associated with faults. Unfortunately, determining the cause(s) of these anomalies is complex, involving a variety of site-specific conditions including soil composition, soil permeability, presence/absence of potential carrier gases, gas diffusion, etc. Furthermore, the distance that $^{222}$Rn can migrate by advection is 3 orders of magnitude greater than by diffusion alone, thus the depth at which buried faults can be detected varies greatly depending on the cause of the anomaly and the local radon transport conditions. In an effort to explore the possible mechanisms of radon transport in active faults of the TVZ, the concentration of $^{220}$Rn and $^{222}$Rn in soil gas is measured in the Maleme Fault Zone (MFZ) and the Paeroa Fault of the central TVZ. Radon anomalies of both isotopes were found to exist near faults in both field areas sampled, and based on the relationship between both isotopes, we interpret that the most likely

cause for the anomaly is an increase in radon soil emanation, with patchy localised increase of $^{222}Rn$ transported by a carrier gas.

## 3 GEOLOGICAL SETTING

The central TVZ comprises an active rift (variously referred to as the Taupo Rift or Taupo Fault Belt), which formed during the last 1-2 Ma in association with subduction of the Pacific plate (Wright, 1992; Wilson et al., 1995; Rowland and Sibson, 2001). This rift is coincident with a volcanic arc, which has produced in excess of 15,000 $km^3$ of volcanic material over the past 2 Ma, mostly through caldera forming eruptions (Wilson et al., 1995). The geology of the central TVZ is dominated by Quaternary volcanic and lake deposits (Manville and Wilson, 2003), emplaced on top of the Mesozoic basement rocks, known as the Torlesse Terrane, which comprise poorly sorted sandstones interbedded with argillites (Leonard et al., 2010).

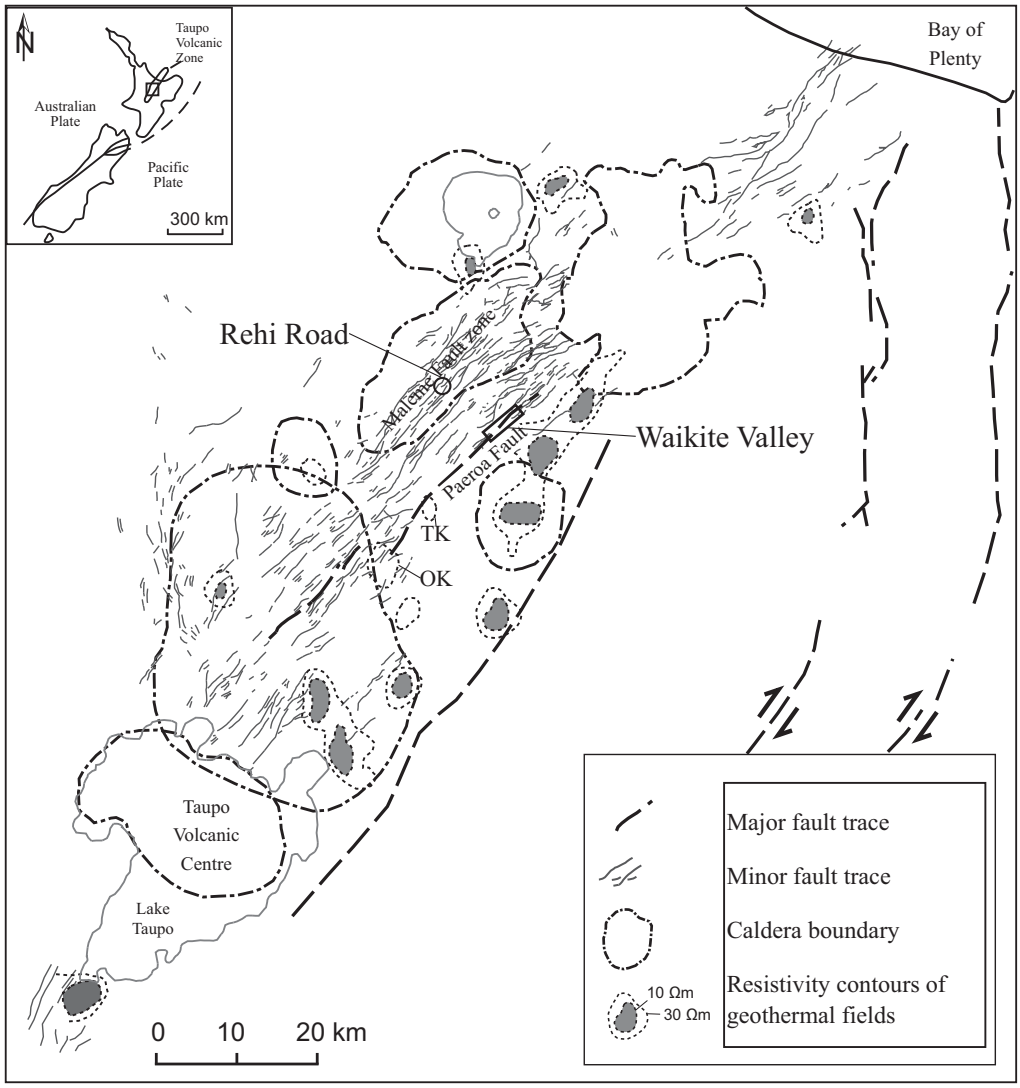


**Figure 1 Map of the central TVZ (after Bégué et al., 2014). Note the absence of mapped fault traces at the surface along the south-eastern edge of the zone, where recent faulting is known to have occurred at depth. OK=Orakei Korako, TK=Te Kopia**

The central TVZ hosts more than 20 geothermal fields. The geothermal activity is only occasionally associated with fault traces visible at the ground surface. The Paeroa Fault, which is studied in this thesis, is a notable exception having three geothermal fields at different locations along its length (Rowland and Sibson, 2004). Many fields are associated with recently active faults at depth, which have been subsequently buried by volcanic deposits (blind faults). In order to detect these faults and their prospectivity for

geothermal energy, soil gas radon surveys have been proposed over areas potentially hosting blind faults.

Radon soil gas surveys have been successfully used to detect buried faults that had gone undetected using traditional mapping methods. An important focus of this study was to assess whether radon surveys can be used as a tool to detect blind faults in the TVZ. We conducted radon soil gas surveys over two areas of known faulting in the Ngakuru graben; 1) Rehi road, which hosts multiple faults within the Maleme Fault Zone, all with several metres of offset at the ground surface, and 2) the Waikite valley area, where the Paeroa Fault, a major fault hosting hot springs and fumaroles, is located. The results are used to assess the potential for detecting blind faults and for refining the location of gas migrating vertically along faults using radon soil gas surveys.

### 3.1 Rehi Road

Rehi road is located on the TVZ rift axis. At Rehi Road, a series of normal faults, known as the Maleme Fault Zone (MFZ), define the rift axis, with an overall trend of 055° (Villamor and Berryman, 2001; Nicol et al., 2010). The MFZ is composed of up to 16 discrete fault strands within 1 km of each other that displace flat lying, ~25 ka old fluvio-lacustrine sediments. Each individual strand accommodates 1 - 15.2 m maximum vertical displacement of the ~25 ka surface, and the total vertical displacement in the MFZ is between 1.85 to 3.55 mm/a (Villamor and Berryman, 2001; Nicol et al., 2010). The area is located on grass farmland being used for dairy production. The relatively consistent vegetation cover and easy access made Rehi Road a good location for a detailed investigation focussing on the variation of radon in soil gas over faults.

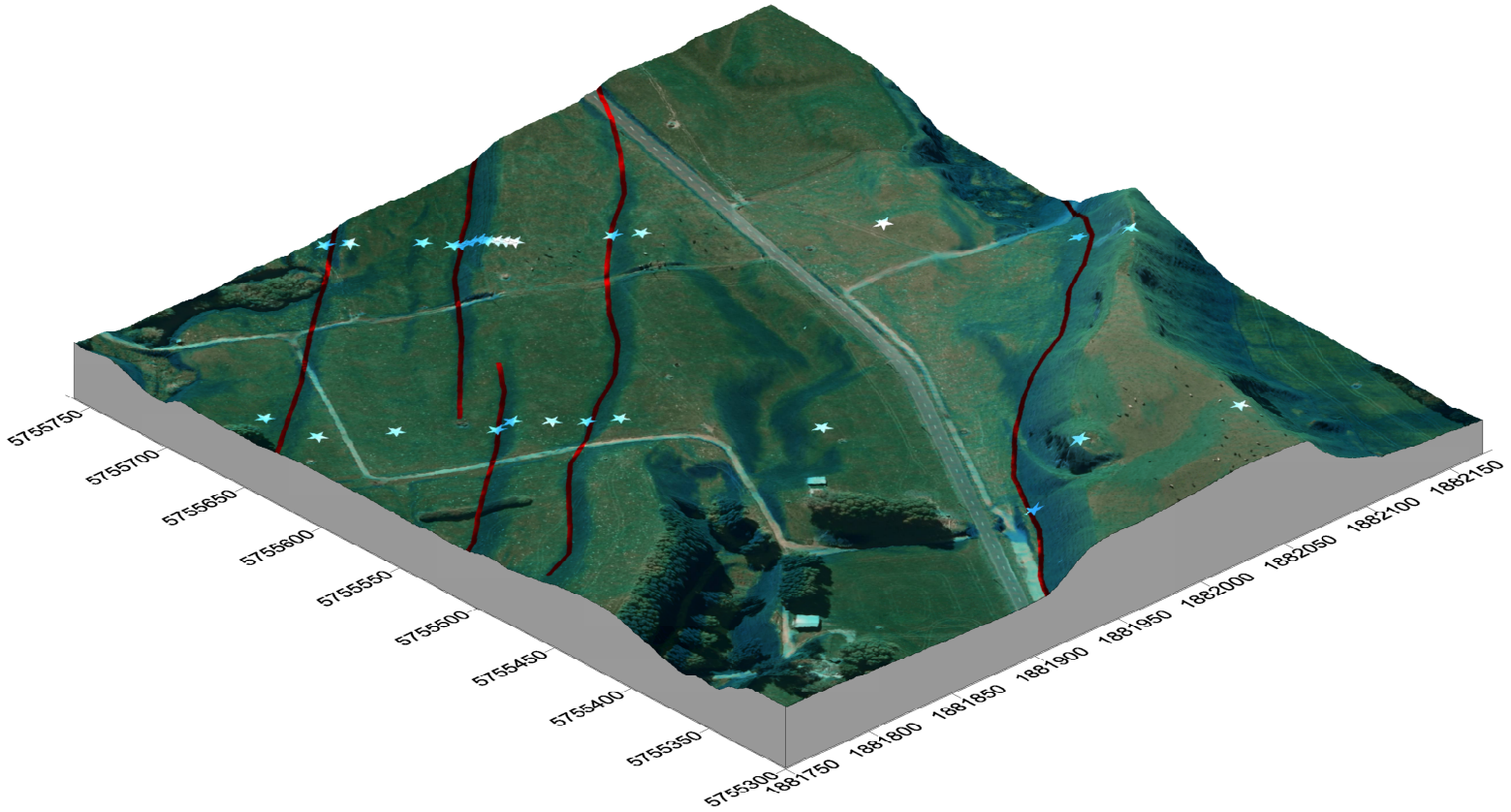


**Figure 2 Three-dimensional surface of Rehi Road site with base of visible fault scarps (dark red) and sample sites (white stars) highlighted. Aerial photography sourced from the LINZ Data Service https://data.linz.govt.nz/layer/1760-bay-of-plenty-025m-rural-aerial-photos-2011-2012/ and licensed by BOPLASS limited for re-use under the Creative Commons Attribution 3.0 New Zealand license.**

## 3.2 Waikite Valley

The Waikite Valley study area is located between Waikite Valley Road and Ngapouri Road, close to the northern end of the Paeroa Fault scarp (Figure 2). Two main Paeroa Fault strands are evident in the study area: the main Paeroa strand, with a scarp of several hundred metres, and a shorter strand in the hanging wall of the main fault, called the Te Waro Fault, with a scarp up to ~20 m (Glover et al., 1992). The Paeroa Fault is ~30 km long, strikes 040-050°, and exposes a series of large ignimbrite units along the Paeroa Range. The vertical displacement of the Paeroa ignimbrite is 550 m near Te Kopia, 10 km south of the study site, with a displacement rate of 1.5 mm/a since deposition of the Whakamaru Group ignimbrites approximately 350 ka (Villamor and Berryman, 2001).

The Paeroa Fault scarp has some of the best exposures of ignimbrites in the TVZ. There are three ignimbrite units that have been mapped in the study area. The Te Weta ignimbrite, up to 240 m thick, and Paeroa ignimbrite, up to 140 m exposed (Keall, 1988), are both considered part of the Whakamaru Group ignimbrites and now believed to have erupted from a local linear vent source at the base of the Paeroa scarp (Downs et al., 2014). The Matahina ignimbrite (~320 ka), erupted from the Okataina caldera, is also partially exposed in the Paeroa scarp.

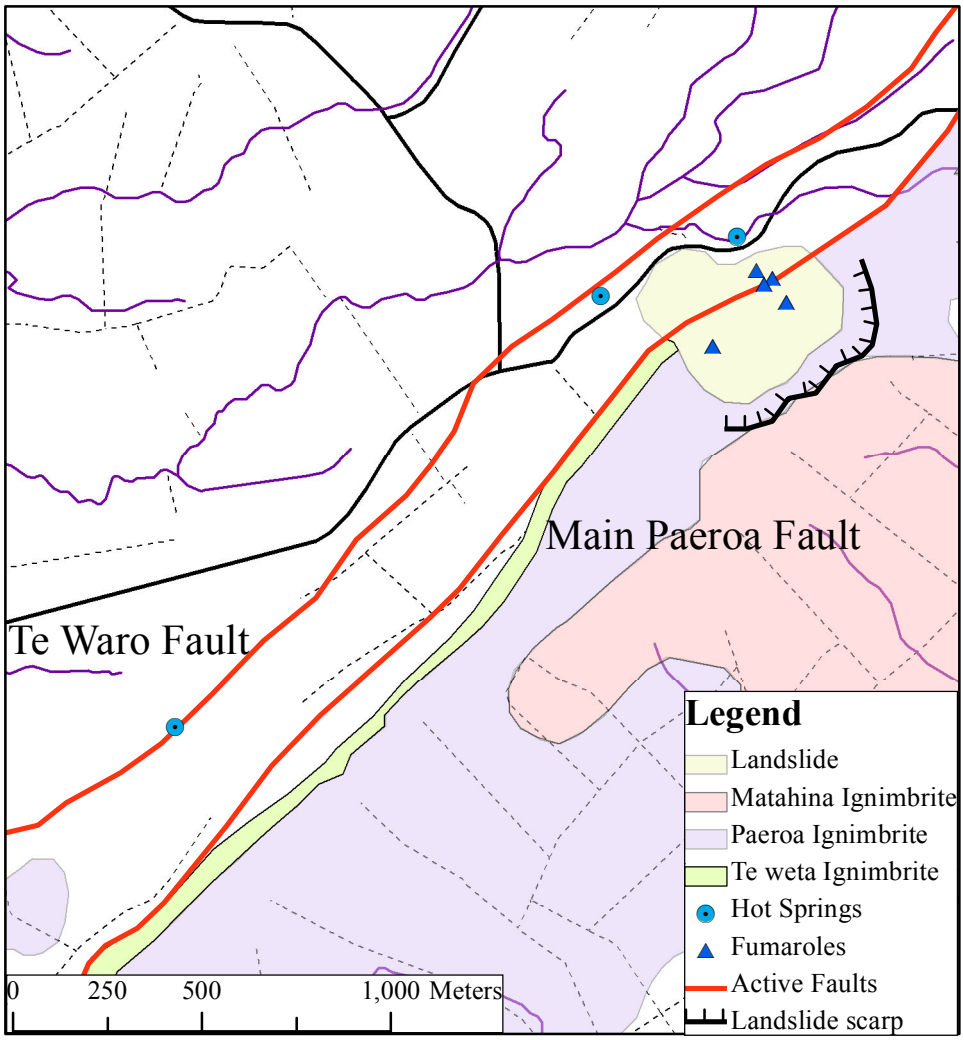


**Figure 3 Geological map of the Waikite Valley area (after Grindley 1994). The areas not coloured are assumed to be late alluvial or tephra deposits.**

Hot springs and fumaroles are located at several locations along the Paeroa scarp. There are two main spring sites within the field area; 1) the Waikite springs located near the base of the Paeroa scarp in the NW end of the field area, and 2) the Te Waro spring further to the SW at the base of the Te Waro Fault scarp. The Waikite spring has several small springs and fumaroles associated with it, but the main source is a 98º boiling spring which flows at a rate of ~40 l/s. There are many small fumaroles located upslope from the Waikite spring, and also a few locations with dead vegetation and hot, clay-rich soil. The Te Waro springs emerge at the surface at a temperature of around 35º.

Both springs are considered to be bicarbonate springs, although they are heavily diluted compared to other New Zealand bicarbonate geothermal waters (Glover et al., 1992).

The hummocky and irregular ground near the Waikite hot springs is evidence of an old landslide deposit, likely a partially disaggregated rotational slide (Figure 2). There are steaming fumaroles, dead vegetation and hot clay-altered ground located within the landslide. The hydrothermal alteration associated with these sites could have weakened the rocks, making them susceptible to slope failure and landsliding. Landslides are common along the Paeroa range, as landslides have been recognised along the scarp at the Te Kopia geothermal field (Newson 2002), and a landslide occurred (at an unknown location along the scarp) during a seismic event of magnitude 5.1 in 1983 (Smith, 1984).

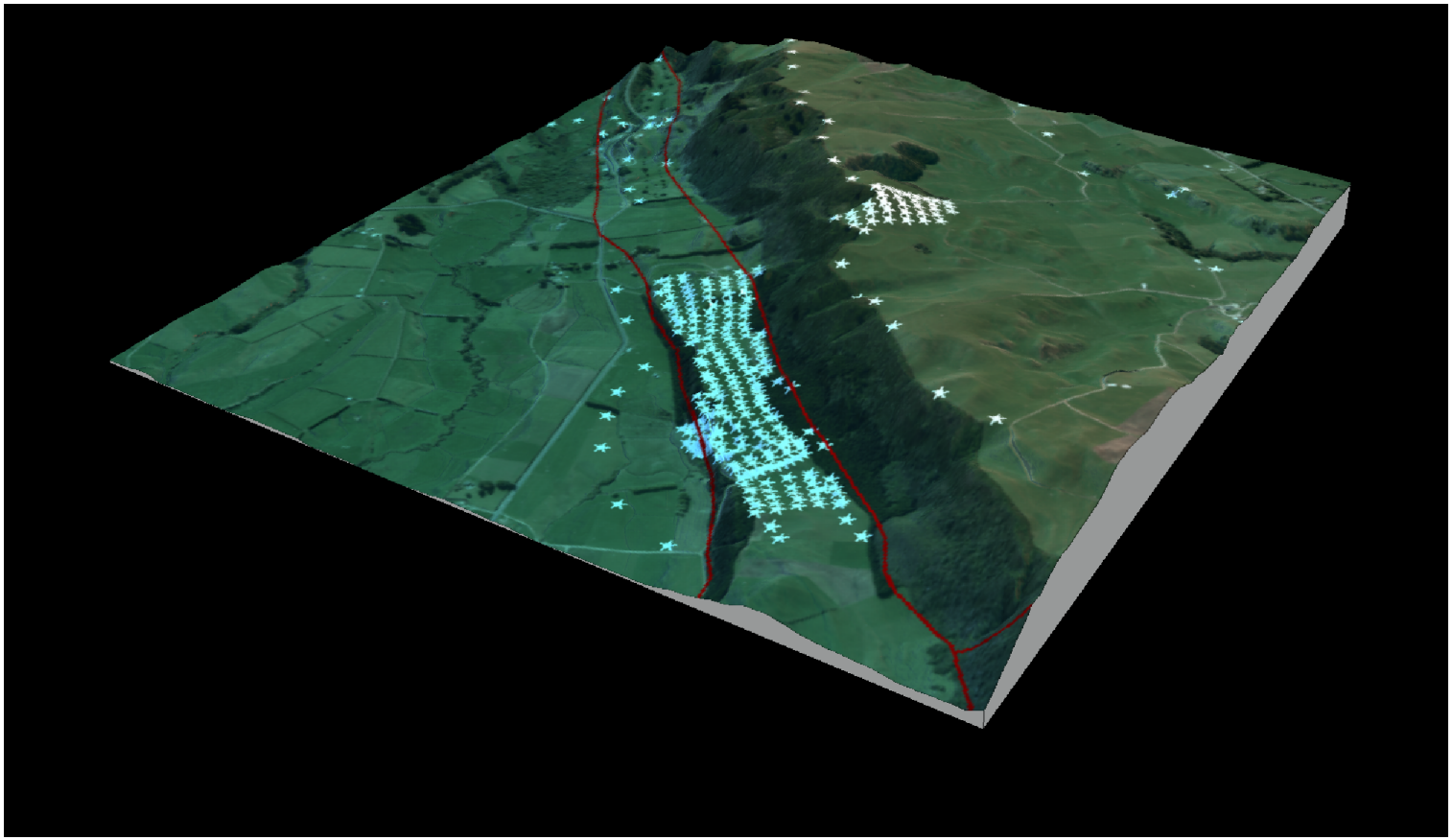

**Figure 4 Three-dimensional surface of the Waikite Valley site with base of visible active (dark red, after Grindley 1994) and sample sites (white stars) highlighted. To improve legibility, not all sample sites are shown. Aerial photography sourced from the LINZ Data Service https://data.linz.govt.nz/layer/1760-bay-of-plenty-025m-rural-aerial-photos-2011-2012/ and licensed by BOPLASS limited for re-use under the Creative Commons Attribution 3.0 New Zealand license.**

# 4 METHODS

## 4.1 Equipment

Soil gas was sampled at 1 m depth using a steel soil probe. This depth was chosen in order to mitigate variations in soil gas compositions due to atmospheric conditions (Clements and Wilkening, 1974; Malczewski and Zaba, 2007). The gas was extracted at a constant rate of 1 l/min using a piston air-pump, and then pumped it through a Durridge RAD7 radon detector. The RAD7 distinguishes between the radon isotopes based on the different alpha emission energies of the radon daughter product, polonium.

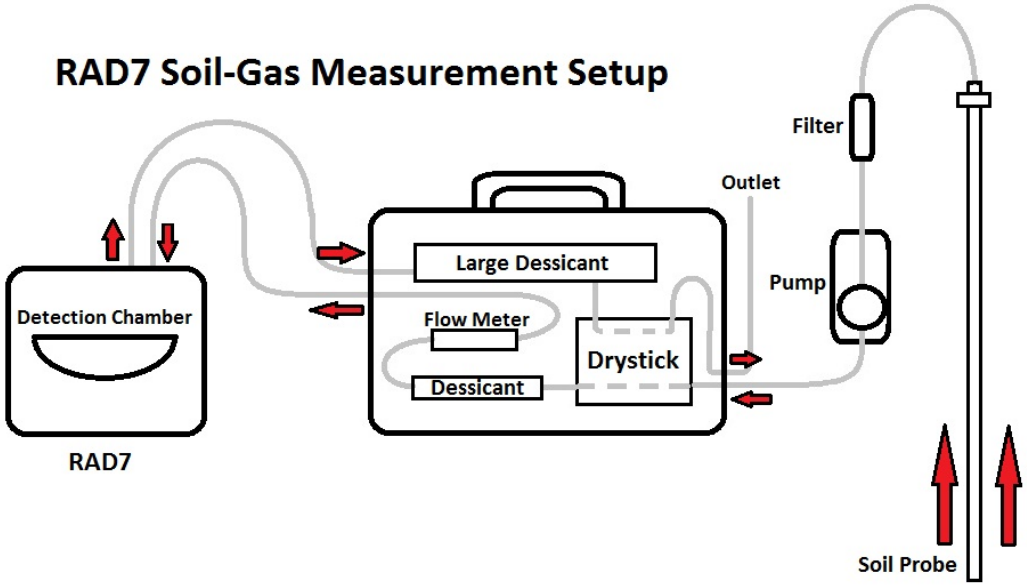


**Figure 5 Diagram of experimental setup for field work gear.**

The accuracy of the RAD7 radon measurement is ±5%, however the precision is time dependent. Therefore we pumped air for 10 min to obtain a $^{220}$Rn reading then stopped

pumping, closed the loop and waited the required time until we obtained a precise $^{222}Rn$ reading.

## 4.2 Sampling strategy

The soil gas surveys were conducted over two separate field seasons (January-February 2012 and November-December 2012). During the first season, widely spaced surveys were conducted on fault scarps at both Rehi Road and Waikite Valley. At Rehi Road, the top, the base of the scarp, and halfway between two successive scarps were sampled (Figure 2). At Waikite Valley, we sampled on both the hanging wall and the footwall of the Paeroa and Te Waro Faults, as well as background samples sites. The fault scarps at Waikite Valley are much higher (>20 m) and have a lot of dense shrub vegetation. All of the sampling locations were taken on grass paddocks to maximise logistics and remaining consistent between sites. No data are available for the fault scarp itself.

In the second season, only the Waikite Valley was sampled, and the survey was confined to a regularly spaced grid near the Paeroa and Te Waro scarps, above the Te Waro Hot Spring. A densely spaced grid (20x50m) was sampled in a 200 by 1000 m area near the Te Waro scarp warm spring, due to the presence of radon anomalies observed during the first field season (Figure 12 & Figure 13). The spacing was determined based on variograms computed from the first season's data, in order to get a representative sample of the spatial variability of radon soil gas.

### 4.3 Measurement reproducibility

In order to establish the reproducibility of the results, two sites that were two metres apart were repeatedly surveyed near the Te Waro Fault Scarp (Waikite) over a period of 3 weeks. Even though only a short distance separates the two sites, the $^{220}$Rn concentrations measured had a difference of one order of magnitude (Figure 6), demonstrating the spatial heterogeneity of soil gas radon. $^{220}$Rn concentration were generally consistent over time (±5%). One $^{220}$Rn result (27 Jan, Site 2; see Figure 6) is 25% lower than measurements made on other days for that site. The concentration measurement at the other site was unaffected on the same day, and therefore it is suggested that it is possible that an experimental error occurred.

The $^{222}$Rn values are less consistent over time. The difference between the largest and smallest measurement is ~25%. The final measurement was taken to test the effect of heavy rainfall on soil gas radon concentration. Both sites show a drop in $^{222}$Rn following a significant precipitation event, while $^{220}$Rn appears to be unaffected by rain.

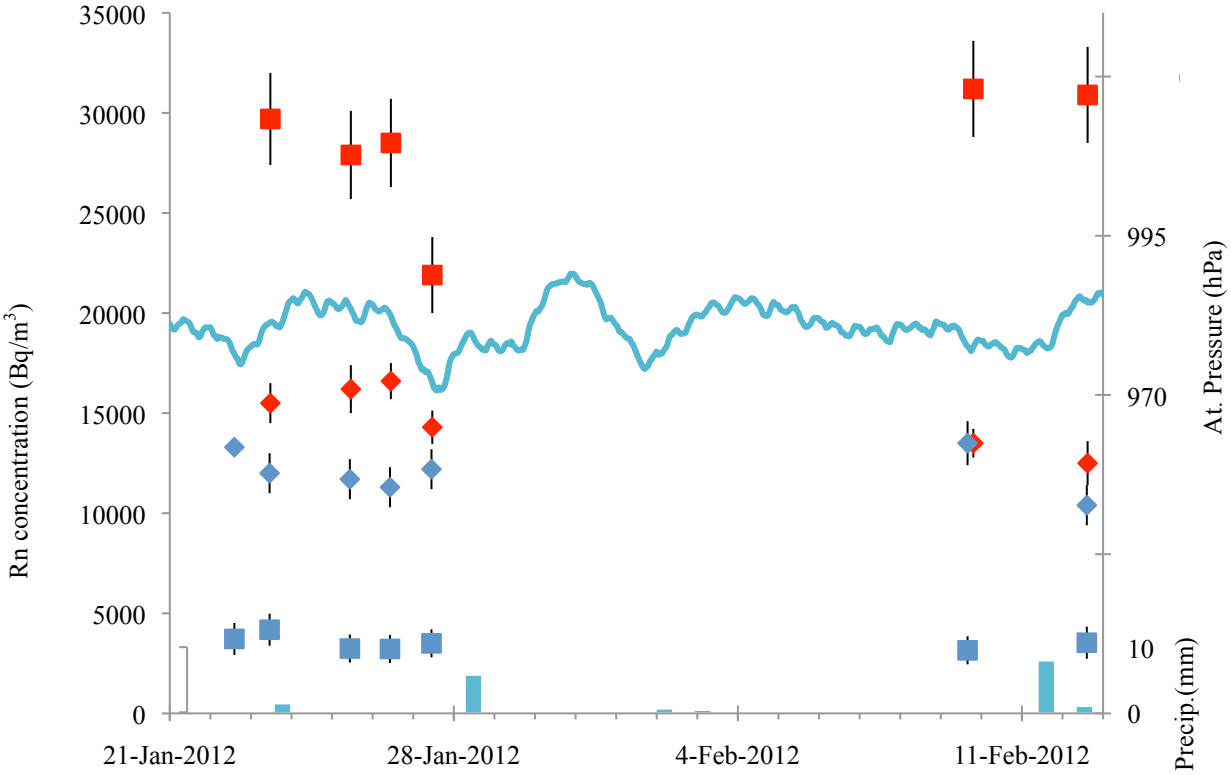


**Figure 6 Repeated measurements over time for two sites (Site 1 in blue, Site 2 in red) located 2 m apart. The squares are the $^{220}$Rn measurements; the diamonds are the $^{222}$Rn measurements. Precipitation (light blue bars) and Atmospheric Pressure (blue line) from nearby Rotorua airport (from NIWAs CliFlo database) presented for reference.**

Several time-dependant factors could explain the variability in $^{222}$Rn measurements such as temperature, soil humidity, or $CO_2$ content. All of these factors change over time due to weather effects or bacterial processes. An increase in soil temperature can cause an increase in radon soil activity, most likely by release of adsorbed radon gas (Shefsky et al., 1993; Iskandar et al., 2004). A variation in soil humidity content can also affect the results. An increase in relative humidity tends to reduce the emanation of $^{220}$Rn more readily than $^{222}$Rn (Huxol et al., 2012). $CO_2$ concentration could affect the RAD7 instrument (Tuccimei and Soligo, 2008), but again this will affect the $^{220}$Rn measurements much more than the $^{222}$Rn measurements (Lane-Smith and Sims, 2013). Repeated measurements over time at the Waikite Valley site suggest that the majority of

the variability is caused by $^{222}Rn$, therefore it is suggested that it is unlikely that the data are affected by the processes described above. In order to mitigate the variability associated with rainfall, we avoided sampling radon soil gas immediately after rainfall.

# 5 RESULTS

## 5.1 Rehi Road

### 5.1.1 Soil gas surveys

The $^{220}Rn$ concentration tended to be higher at the top of the fault scarps, with lower concentrations at the base of and between fault scarps (Figure 7). The variation in $^{222}Rn$ concentrations (Figure 8) shows a pattern relative to the faults, similar to $^{220}Rn$ (although less abrupt or clear-cut).

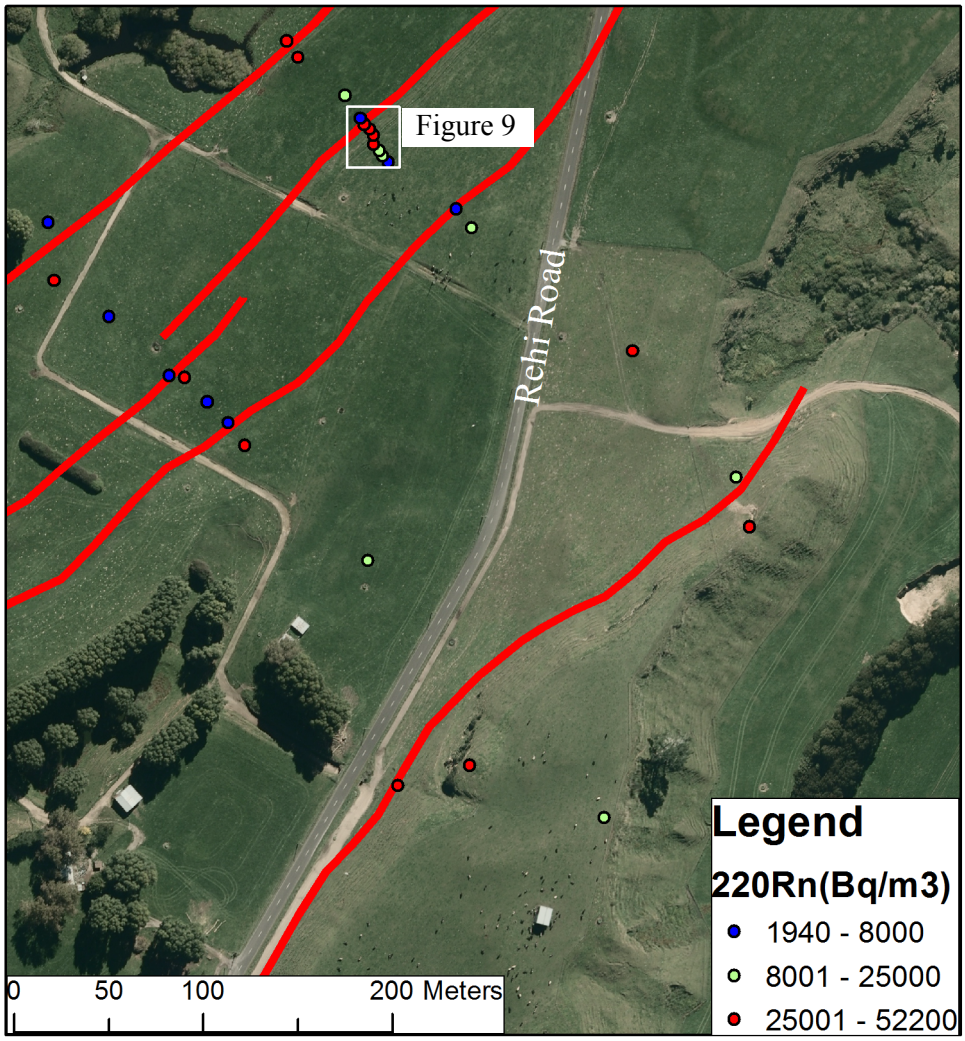


**Figure 7 Map of soil gas survey locations. The dots are coloured according to the $^{220}$Rn activity. Red lines highlight the base of the inferred fault scarps. Aerial photography sourced from the LINZ Data Service https://data.linz.govt.nz/layer/1760-bay-of-plenty-025m-rural-aerial-photos-2011-2012/ and licensed by BOPLASS limited for re-use under the Creative Commons Attribution 3.0 New Zealand license.**

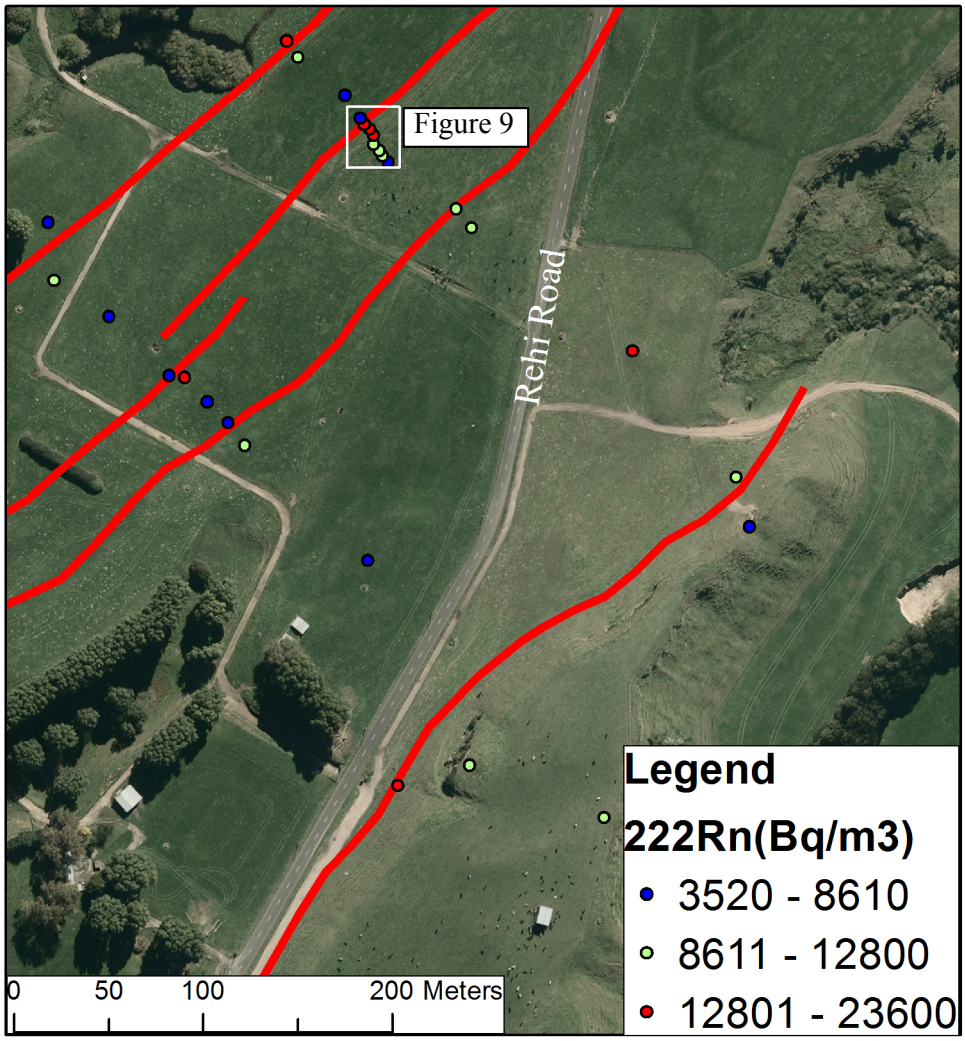


**Figure 8 Map of soil gas survey locations. The dots are coloured according to the $^{222}$Rn activity. Red lines highlight the base of the inferred fault scarp. Aerial photography sourced from the LINZ Data Service https://data.linz.govt.nz/layer/1760-bay-of-plenty-025m-rural-aerial-photos-2011-2012/ and licensed by BOPLASS limited for re-use under the Creative Commons Attribution 3.0 New Zealand license.**

The $^{220}$Rn data in the closely spaced survey (Figure 9) show a strong relationship relative to the fault. The data for this isotope vary between 2960 and 13300 Bq/m$^3$ away from the scarp. There is a sharp change in $^{220}$Rn concentration when crossing from the inferred footwall to the hanging wall, at the base of the scarp. The data vary between 26100 and 37100 Bq/m$^3$ of $^{220}$Rn gas on the scarp itself. The $^{222}$Rn follows the same trend (between 6570 and 12100 away from the scarp, and between 11700-17800 away

from the scarp), however the difference in measurements between the scarp and outside the scarp is less pronounced for $^{220}$Rn.

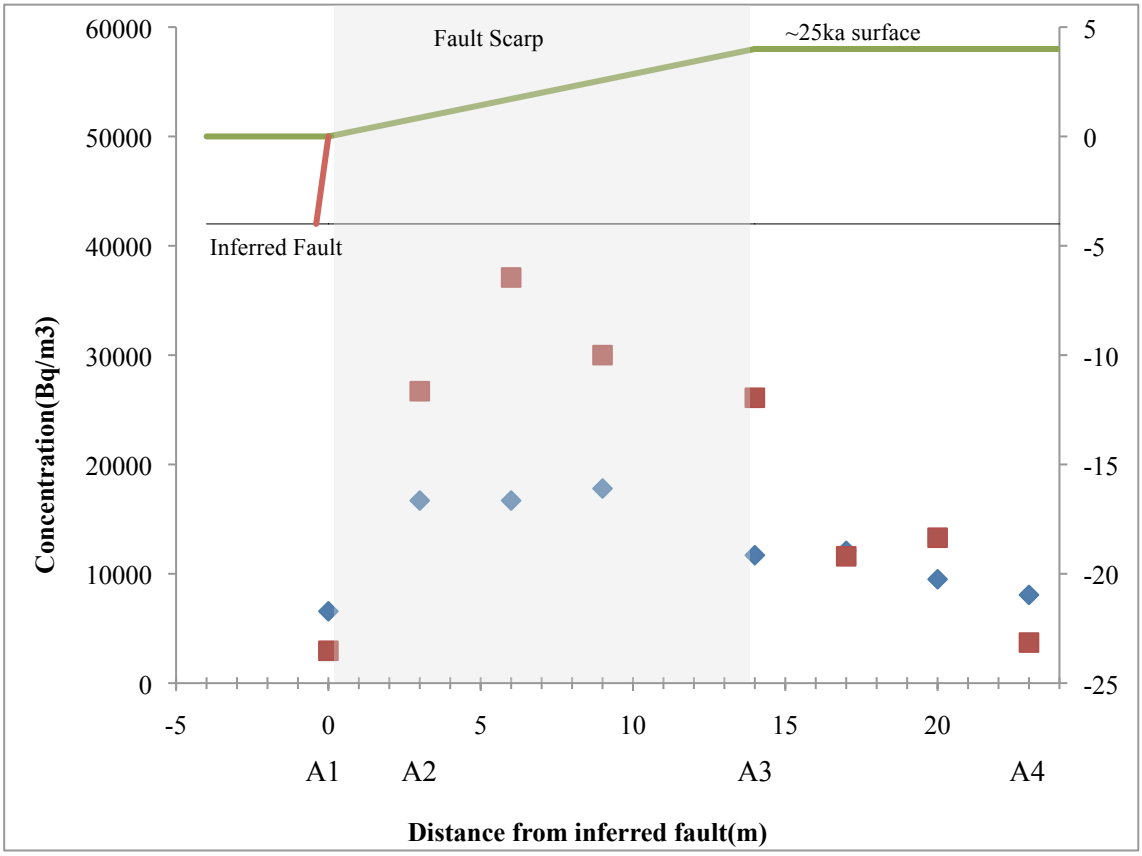


**Figure 9 Schematic cross-section of closely spaced soil gas radon concentrations across one fault scarp. $^{220}$Rn in red, $^{222}$Rn in blue, and the green line represents the scarp itself. A1-A4 shows the locations of Augers. See Figure 6 & 7 for location.**

### 5.1.2 Soil augers

Four augers were dug at the same location as four of the soil gas surveys across the fault at the location of Figure 9 (Symbols A1 to A4 on Figure 9). Soil samples were retrieved and characterised to assess the radon emanation potential of the soil. The soil is mostly composed of fine-grained ash, with variable pumice clast content, ≤2 cm in diameter.

The weathering of the soil is variable, with the top of the holes usually being light grey in colour, indicating a relatively fresh sample, and the bottom of the hole being reddish brown due to oxidation. In hole A2, the auger reached the water table at ~2.8 m, below which the soil looks relatively fresh again.

There is a clear relationship between the colour of the soil at 1 m depth (Figure 10 and Figure 11) and radon concentration measured at that location (Figure 9); where the soil is light grey, the radon values are generally lower (<~10 kBq/m$^3$), and where the colour is red, the radon values are higher (>10 kBq/m$^3$). This observation seems more pronounced with the $^{220}$Rn isotope, compared to the $^{222}$Rn isotope.


**Figure 10 Photograph of augered soil at Site A2. Lengths of augered soil are 1 m. Water table intercepted at 2.9m. See Figure9 for locations of auger relative to fault scarp. See Figure 6 for location in MFZ.**


**Figure 11 Photograph of augered soil at Site A4. Lengths of augered soil are 1 m. See Figure9 for locations of auger relative to fault scarp. See Figure 6 for location in MFZ.**

## 5.2 Waikite Valley

### 5.2.1 Soil gas survey

The sampling locations were split into two groups: 1) measurement near the surface fault expression, and 2) background measurements, based on the distance to the fault scarp itself. Survey results confirm that radon concentrations tend to be higher closer to faults (See Figure 12 and Figure 13).

Steam was sampled from several fumaroles and the hot ground (<30ºC) located near the Waikite Springs (Figure 3). The high temperature and nature of the fumarole required using a cooling coil coupled with a small probe. This setup differed to the one used for the soil gas survey, which means that the results are not directly comparable to the rest of the survey, and were not included in the survey. However, all of the sampled hot ground sites were associated with high $^{222}$Rn concentrations. The fumaroles showed the highest radon activities, at ~258 kBq for $^{222}$Rn, and ~180 kBq for $^{220}$Rn. High radon values reflect the fact that the thermal fluids carry a significant amount of radium, which is common for bicarbonate springs (Leonard and Janzer, 1977; Wollenberg, 1974).

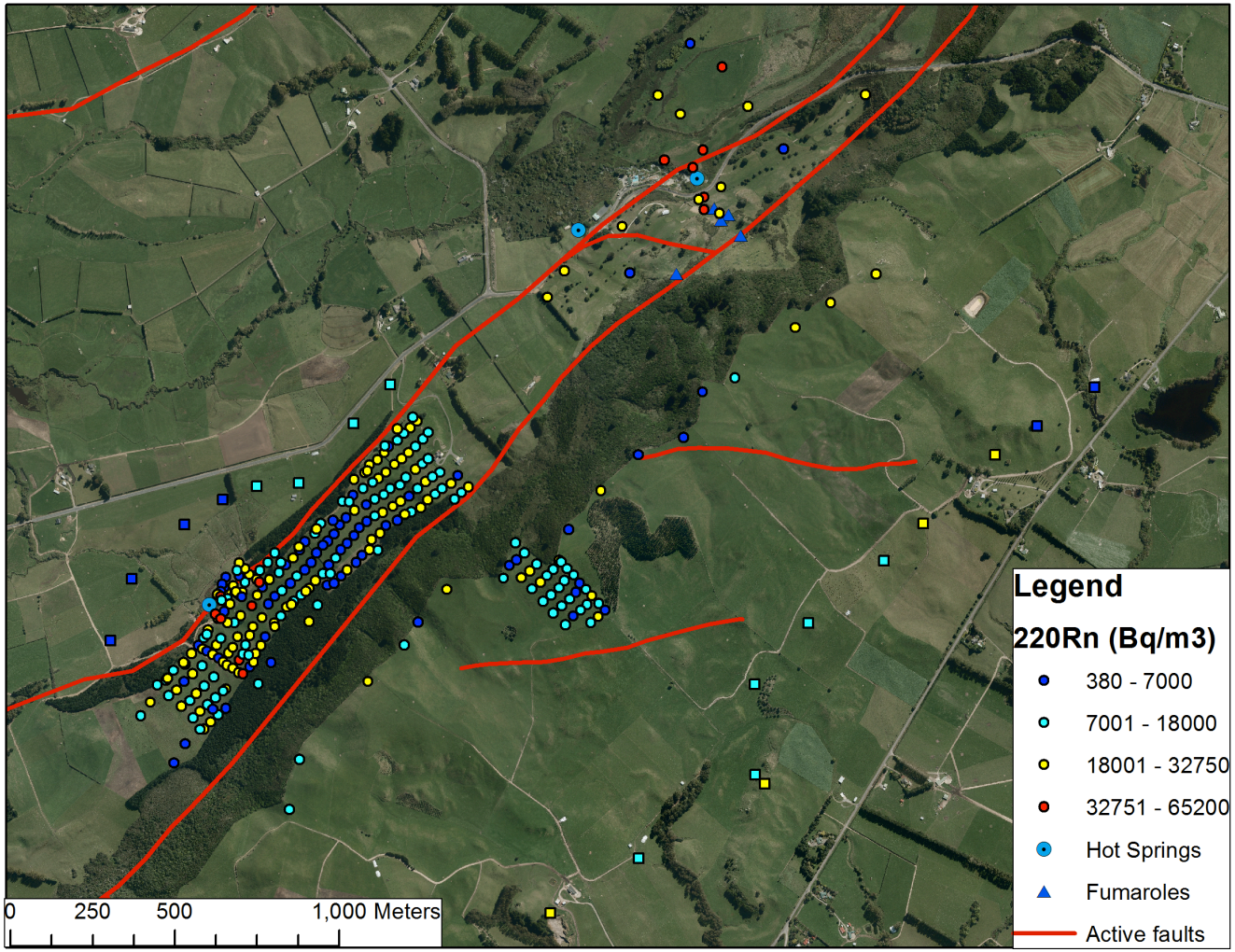


**Figure 12 Map of soil gas survey for $^{220}$Rn. Aerial photography sourced from the LINZ Data Service https://data.linz.govt.nz/layer/1760-bay-of-plenty-025m-rural-aerial-photos-2011-2012/ and licensed by BOPLASS limited for re-use under the Creative Commons Attribution 3.0 New Zealand license.**

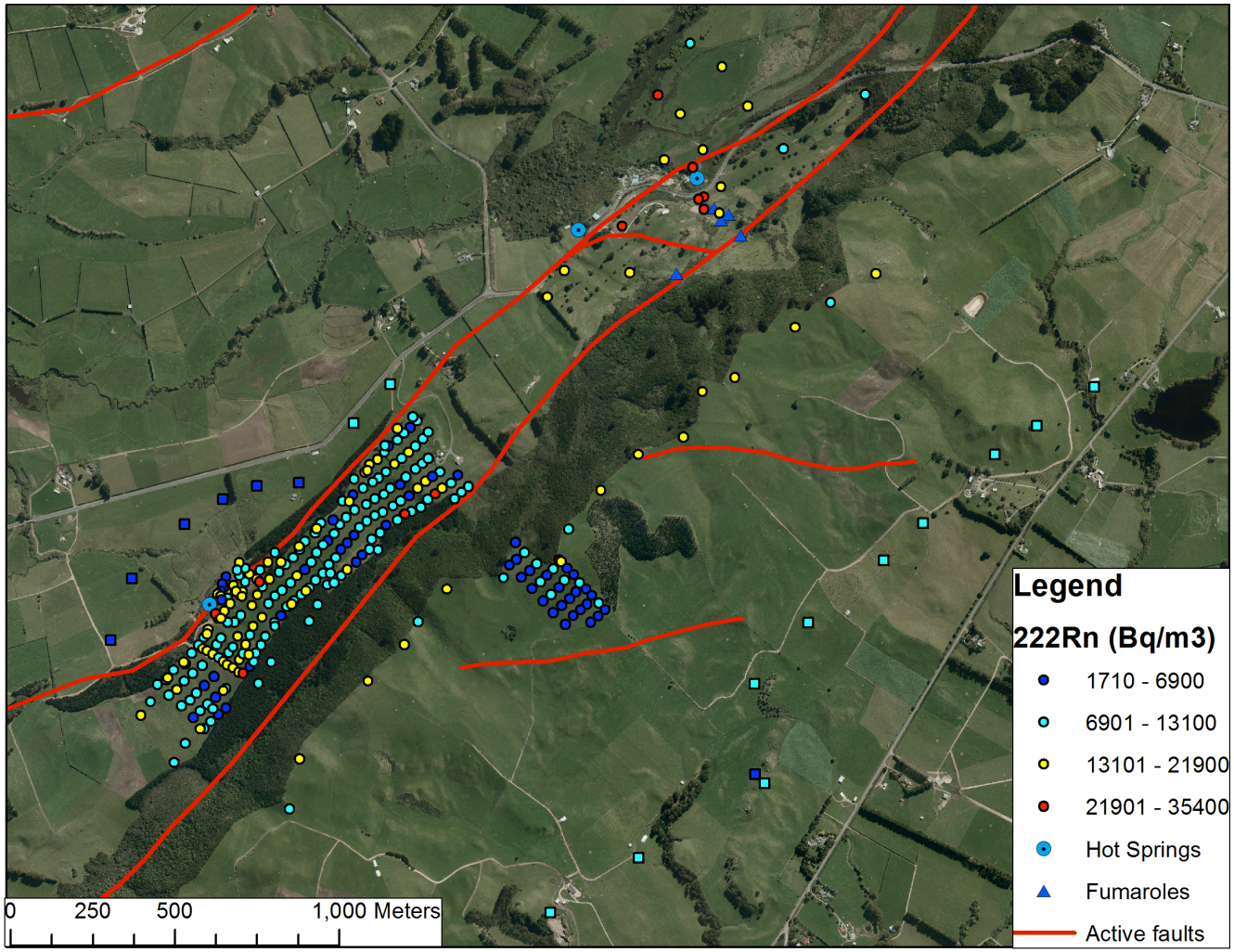


**Figure 13 Map of soil gas survey for $^{222}$Rn Aerial photography sourced from the LINZ Data Service https://data.linz.govt.nz/layer/1760-bay-of-plenty-025m-rural-aerial-photos-2011-2012/ and licensed by BOPLASS limited for re-use under the Creative Commons Attribution 3.0 New Zealand license.**

### 5.2.2 Soil augers and samples

The two repeat-measurement sites (see Section 4.3) were cored to 3 m depth using an auger after the last radon measurement was taken. This revealed an almost identical relationship to that described at Rehi Road. Both sites were soils with varying amounts of pumice and a few lithic fragments visible, with a notable weathering horizon in the soil. At site 1 in Figure 6, the soil does not appear oxidised until 1.5 m depth, well below the point where the soil gas sample was taken. This site had a low $^{220}$Rn measurement (~4 kBq/m$^3$). At site 2 (Figure 6) the oxidised soil is at 0.7 m, which means that the soil gas measurements would have been within the oxidised layer. This site had a significantly higher $^{222}$Rn measurement (~ 29 kBq/m$^3$, Figure 6).

After having completed the soil gas survey, 12 sites were revisited and augered in order to assess the soil composition and retrieve soil samples. The samples were transported back to the laboratory and analysed the radon emission of the soil, in order to compare to the soil gas measurements, where there is likely to be some input of $^{222}$Rn through diffusive or advective processes. The soil sample radon emission was measured by inserting the sample in a small container open on either end. After being purged with fresh, radon-poor air, the container was put in a closed loop with the RAD7. Air was pumped through the loop, and the concentration of both radon isotopes was measured regularly over 24 hours. In such a configuration, the production rate of $^{220}$Rn is matched with the decay rate after ~4 minutes, and therefore in secular equilibrium. The average concentration over 24 hours was used as a measure of the soil emanation of $^{220}$Rn. The $^{222}$Rn isotope will only be in secular equilibrium after ~16 days, and therefore the rate of increase in $^{222}$Rn concentration is a measure of the $^{222}$Rn emanation of the sample.

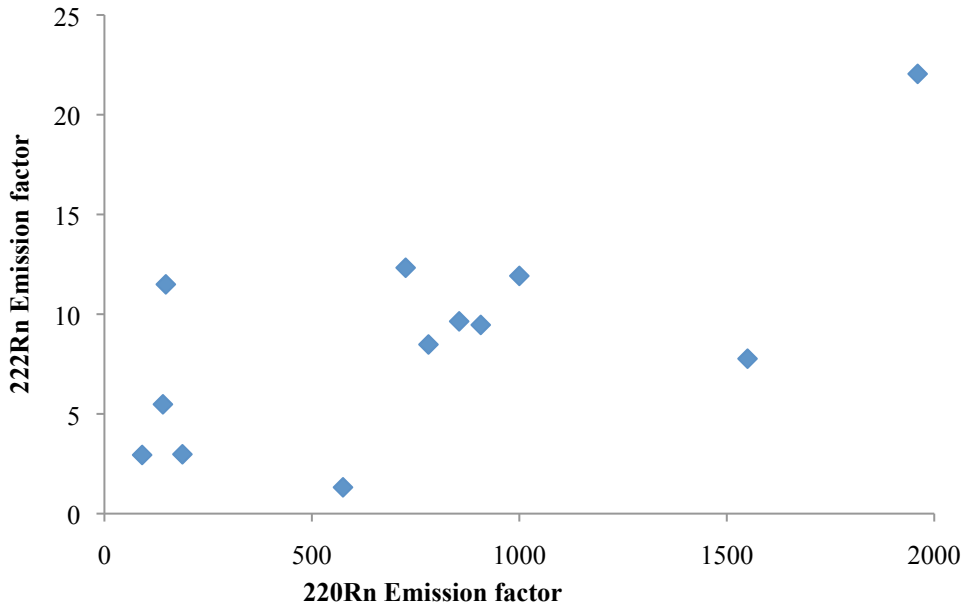


**Figure 14 Results of the lab emission sampling for the 12 samples collected. The emission factors are dimensionless. See Appendix B for method.**

## 6 DATA ANALYSIS

The results from two study areas where the soil gas investigations took place illustrate that the same processes are occurring close to faults, albeit at a different scale. In the Rehi Road area, the fault scarps are smaller (1-10 m high) compared to the Waikite site, where the fault scarp is up to 500 m high. A similar scale difference is observed in our results: the data showing that, in general, the processes governing radon variation proximal to faults are similar in both study areas, except on a smaller scale around the smaller Rehi Road faults. In this discussion, both data sets are used to illustrate the processes causing the anomalies around faults.

When analysing the relationship between variables in the data analysis, two tests are used to assess the relationship between two datasets; the Pearson product-moment correlation coefficient, also known as coefficient of determination ($R^2$), and the Pearson correlation test p-value. In the former, $R^2$ estimates the fraction of the variance of the independent variable that can be explained by the dependent variable. A value over 0.90 is usually accepted as a good correlation. However, this method can be susceptible to outliers and therefore it is good to also complement this with the test p-value. The Pearson correlation test p-value measures the probability of the true correlation coefficient being 0, and therefore the two datasets are linearly independent. A high p-value (usually above 0.05) suggests that the probability of the two datasets being linearly dependent is not significant. However, when the p-value is below 0.05, the two data sets are likely to be linearly correlated. If the correlation coefficient is low and the p-value is below 0.05, then it is likely that the data are linearly correlated, but that there is a significant amount of noise in the data.

## 6.1 Behaviour of radon isotopes

The soil radon emission data from the extracted soil, the Quantile-Quantile plots of the field data, and repeated measurements of soil gas at one location illustrate that 222Rn is being transported through soil gas.

### 6.1.1 Quantile-Quantile plots

Quantile-Quantile (Q-Q) plots are used to identify trends in the distribution of large populations of data. For example, they can be used to identify whether a population is

normally distributed or whether the population has a bimodal distribution. They are equivalent to histograms, but are more powerful than histograms in that they do not require bin-widths to be specified.

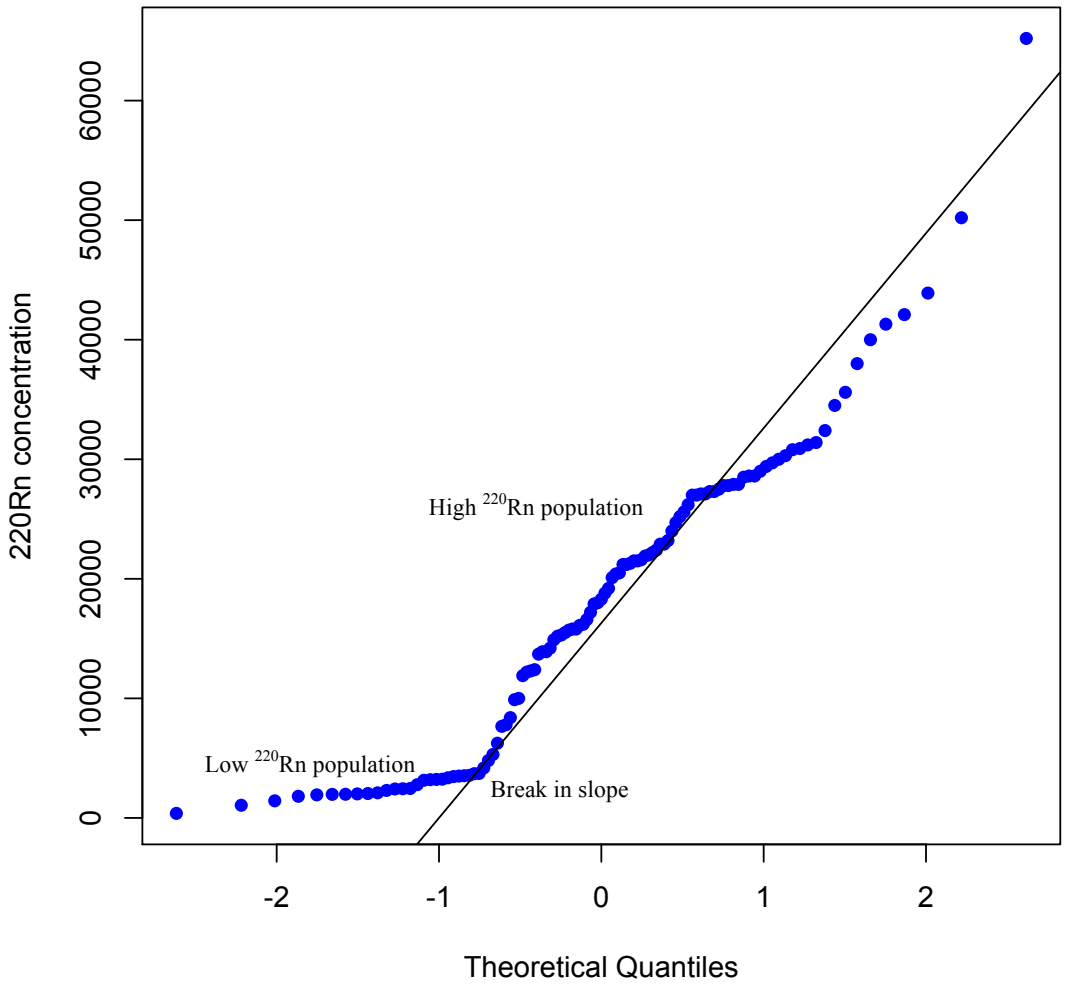


**Figure 15 Waikite soil gas $^{220}$Rn concentration Quantile-Quantile plot. The line represents the distribution of a normal population.**

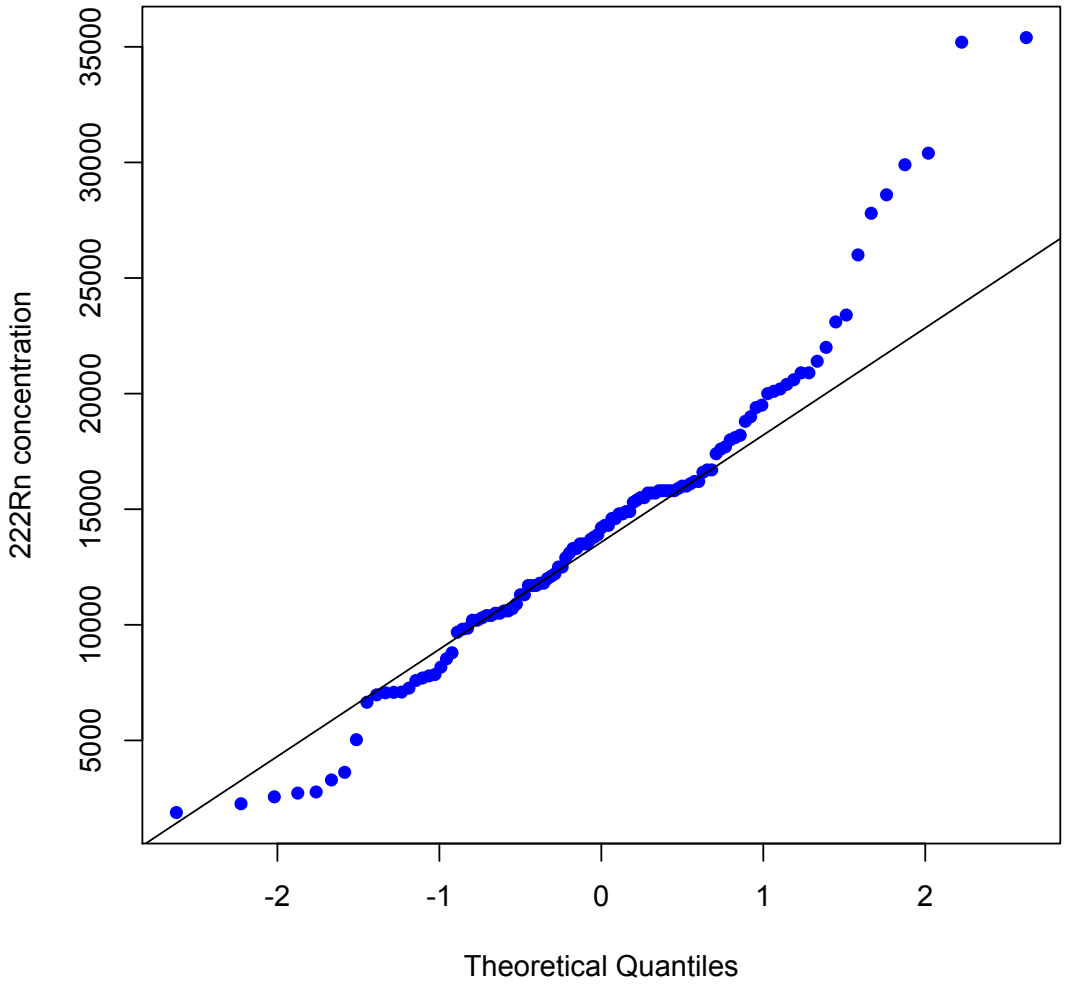


**Figure 16 Waikite soil gas $^{222}$Rn concentration Quantile-Quantile plot. The data largely follows the normal distribution trendline.**

The quantile-quantile plot for the $^{220}$Rn data (Figure 15) shows a bimodal distribution. One group clusters around an average value of 5000 Bq/m$^3$, and the other around an average of 25000 Bq/m$^3$. The $^{222}$Rn distribution follows more a normal trend (Figure 16). These two plots highlight the fundamental difference between the isotopes and the underlying processes that give rise to their concentration distributions. The $^{220}$Rn is unable to diffuse over significant distances and controlled by the local production of the isotope in the soil. The bimodal distribution for $^{220}$Rn reflects the two types of soil that influence radon emanation, the light grey soil (lower emanation) and the oxidised soil

(higher emanation). The underlying process which gives rise to the $^{222}$Rn distribution is clearly different, and is caused by the ability of $^{222}$Rn to migrate as gas. As the gas migration process is similar throughout the soil, this gives rise to the normal distribution of the data for $^{222}$Rn.

### 6.1.2 Soil gas radon emission results

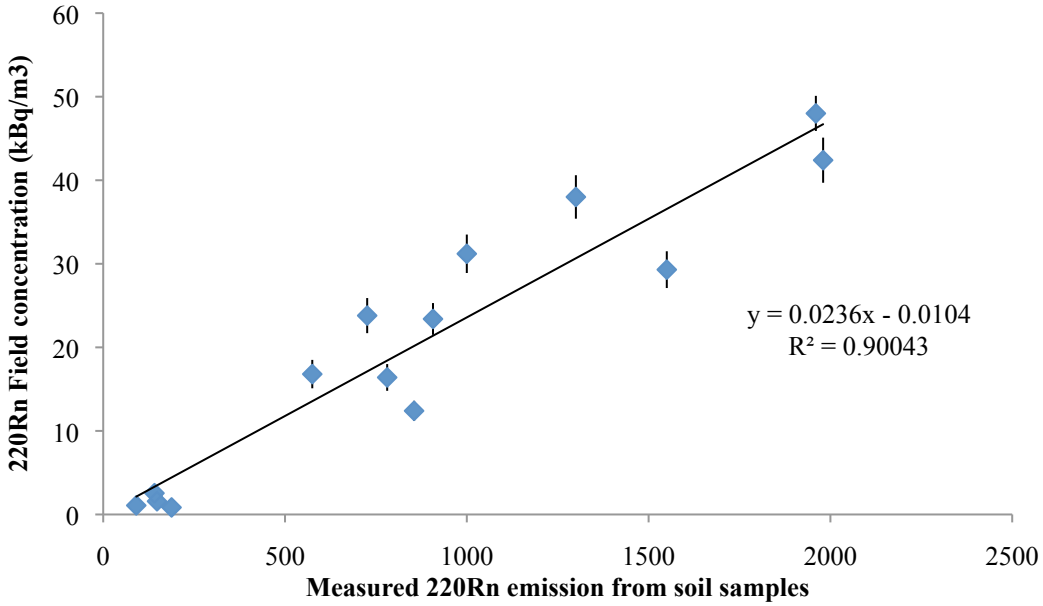


**Figure 17 Field $^{220}$Rn measurements compared to the lab emission results. Equation and $R^2$ for line of best fit indicated on graph.**

First measurements of $^{220}$Rn for the same site, made in the field and in the lab, are compared to assess whether there is a linear correlation. The radon emission results show a good correlation between the $^{220}$Rn data collected in the field and the lab test results ($R^2$=0.90, p-value=3x10$^{-6}$; Figure 17). This good fit shows that $^{220}$Rn data measured in the field is a measure of the $^{220}$Rn emission of the soil where the measurement took place.

The emission data for $^{222}$Rn is not in good agreement with the same isotope measured in the field ($R^2$=0.17, p-value= 0.17; Figure 18). The lack of linear correlation is an indication that the $^{222}$Rn we are measuring in the field is not related to the emanation of the soil. This is due to the fact that $^{222}$Rn gas is able to travel through the soil, so the concentration of gas produced locally is either depleted by diffusion to areas of lower concentration, or is modified by advection of gas with a different $^{222}$Rn concentration (see discussion on radon migration in Section 1).

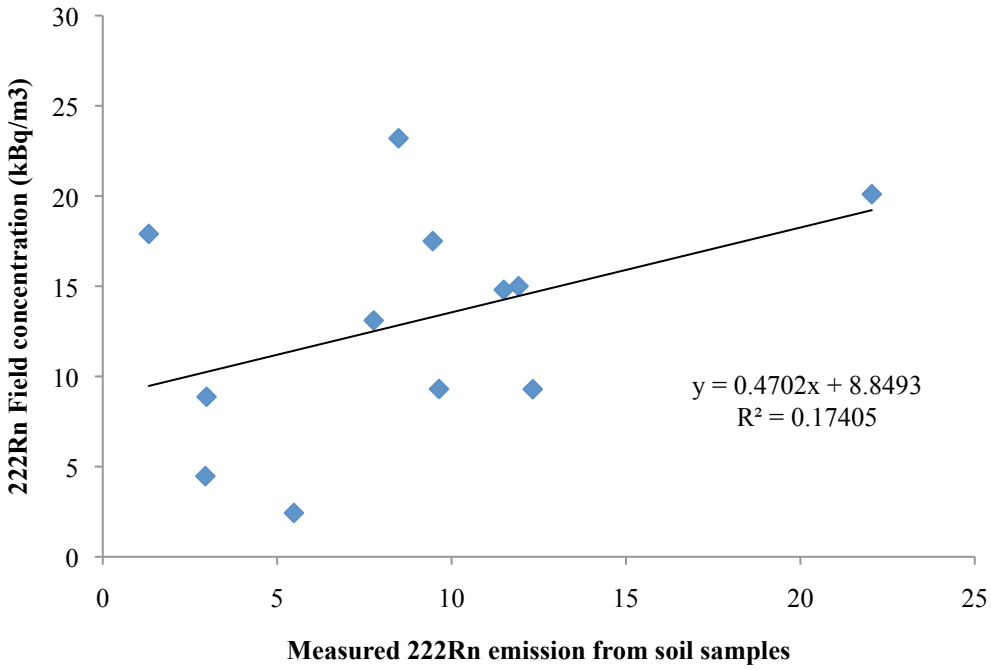


**Figure 18 Field $^{222}$Rn measurements compared to the lab emission results. Equation and $R^2$ for line of best fit indicated on graph.**

## 6.2 $^{222}$Rn and $^{220}$Rn relationship- evidence for local production of $^{222}$Rn

To summarise thus far, the bimodal population distribution of $^{220}$Rn (Figure 15), the $^{220}$Rn soil emission tests (Figure 17), as well as the relationship between soil type and $^{220}$Rn concentration (Figure 9) indicate that $^{220}$Rn measurements that were made in the field are related to the local production of $^{220}$Rn gas in the soil where the measurement was made. Another important observation is that the $^{220}$Rn concentration does not vary much over time (Figure 6).

The concentration of $^{222}$Rn has a similar relationship relative to the position of faults as $^{220}$Rn (see Figure 9). However, the population distribution of $^{222}$Rn concentration (Figure 16) suggests a different underlying generating process, which is not related to the emanation of $^{222}$Rn in the soil (Figure 18). This evidence is all consistent with $^{222}$Rn gas migrating through soil gas, but it gives no indication of how it migrates (i.e. diffusion or advection). In order to better understand the radon anomalies around faults, the relationship between $^{220}$Rn and $^{222}$Rn soil gas concentrations at both study areas are further examined here. The data is split between "near fault" (i.e. within 200 m of a fault scarp) and "background" domains at Waikite Valley, based on the distance to the closest fault scarp. Linear regression models of the radon isotopes for the three datasets (Rehi Road, Waikite near fault, and Waikite background; Table 1 and Figure 18) have been produced in order to assess the relationship between both isotopes in the field and in the lab.

### 6.2.1 Field data

The positive correlation between $^{220}$Rn and $^{222}$Rn isotopes in the linear regression models (Figure 17) indicates that their concentration may be related; this is supported by the low p-value (Table 1), which shows a significant linear dependence between $^{220}$Rn and $^{222}$Rn. The slopes for each of the linear models are very similar with the exception of a subtle difference in the Waikite near fault model. Therefore an increase of $^{220}$Rn concentration, and hence an increase in the radon emanation of the soil, generally leads to a similar increase in $^{222}$Rn across all sites. The inference is that there is a consistent isotopic ratio between radons parent's ($^{224}$Ra and $^{226}$Ra), in soils across the field areas. Further, since the short half-life of $^{220}$Rn means that the gas is produced locally, then it is logical to assume a proportion of the $^{222}$Rn concentration measured at each location is produced locally, which has to be within centimetres of the sampling location.

**Table 1 Linear regression model for $^{220}$Rn vs. $^{222}$Rn for each of the 3 sites. The ± value is 1.96 times the standard error.**

| | Waikite near fault | Waikite Background | Rehi Road |
|---|---|---|---|
| Intercept | 6113±877 | 3881±2318 | 6136 ±2294 |
| Slope | 0.337±0.090 | 0.254±0.172 | 0.268 ± 0.096 |
| $R^2$ | 0.41 | 0.34 | 0.54 |
| p-value | $<2.2\times10^{-6}$ | $9.1\times10^{-3}$ | $8.5\times10^{-6}$ |

A consistent parent ratio across all soils implies that the ratio of $^{222}$Rn and $^{220}$Rn emanated from the soil should remain the same, even if the emanation coefficient of radon gas changed. This, however, contradicts the observation from above in Figure 16

that the $^{222}$Rn concentration measured in the field is unrelated to the emanation potential measured in the lab. It is important to recognise that the $R^2$ score for the $^{220}$Rn linear regression suggests that only 34-54% of the variance of the $^{222}$Rn population is accounted for (i.e. only 30-50% of $^{222}$Rn is likely to be locally produced). The fraction of the $^{222}$Rn variance that is not accounted for by the linear model is caused by $^{222}$Rn that was produced and came from somewhere else, either by diffusion or advection.

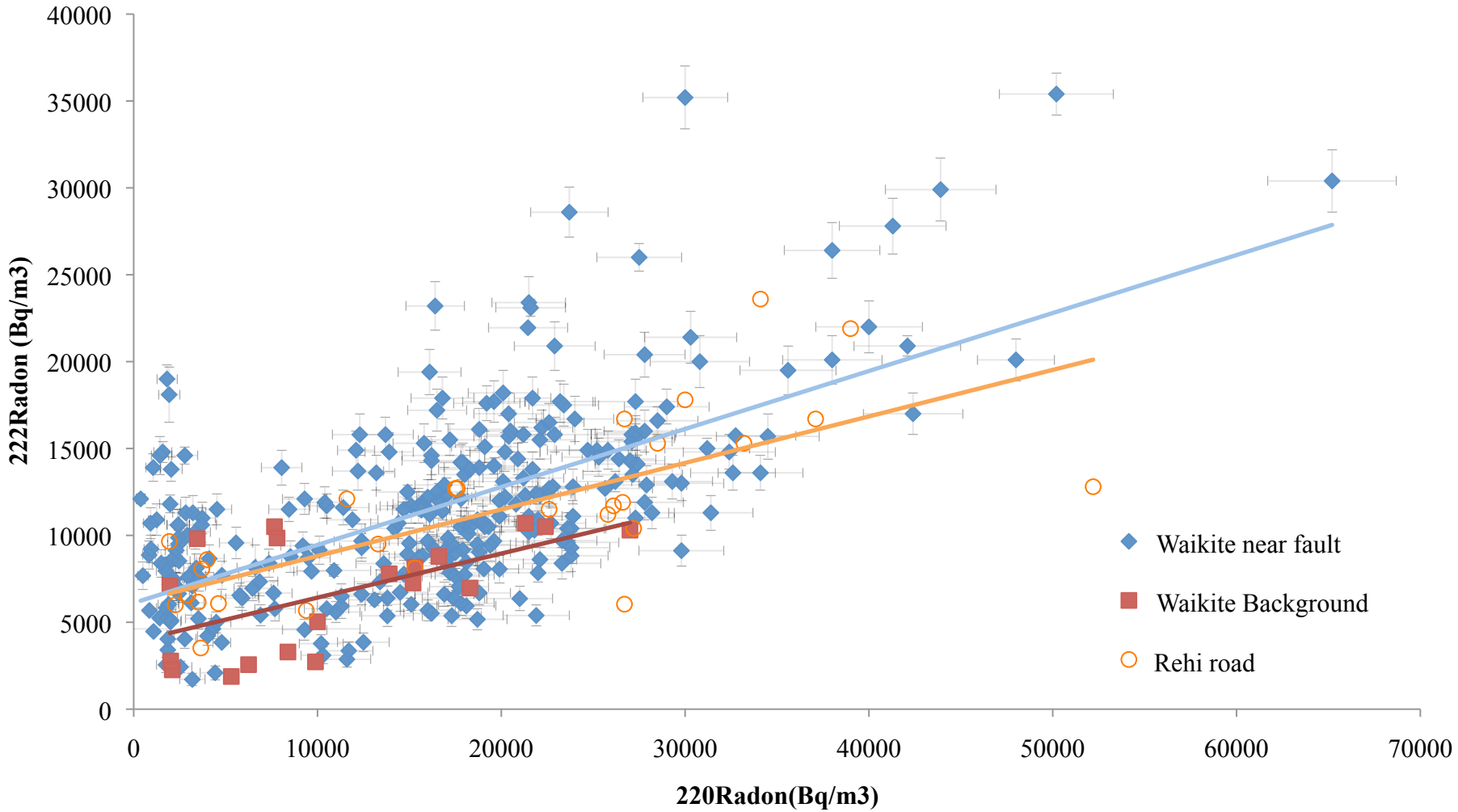


**Figure 19 $^{220}$Rn vs. $^{222}$Rn plot for all data from Waikite valley and Rehi Road. The lines are the linear regression models for each dataset (Table 1), coloured same as the symbol colour.**

An additional interesting point arising from the linear regression model of the field data is that the intercept for the Waikite data near the fault is significantly higher than the background data intercept in the same area (see Table 1). This means that overall, higher $^{222}$Rn concentrations occur near faults, as corroborated by the data for the Rehi Road faults (Figure 8 and Table 1), albeit at a smaller scale. This is probably due to the fact that the soil near faults has a higher emanation potential, as observed at the Waikite Valley sites that have a higher $^{220}$Rn concentration compared to the background data. The processes occurring around faults, such as erosion of the scarp due footwall uplift, possibly cause intensely weathered soil to be present at shallower depths around faults, and therefore the weathered, higher radon emanation soil are regularly measured near faults.

### 6.2.2 Laboratory data

The field data show that there might be a consistent radon parent ratio across both field areas. From the soil samples collected in the field, the hypothesis that the emission rate of both isotopes is linearly correlated can be tested in the lab. The soil emission lab data of both isotopes are plotted against each other (Figure 19B) and compared with the same plot for in situ soil gas measurements taken in the field before the samples were extracted (Figure 19A, see Table 2 for summary of comparison).

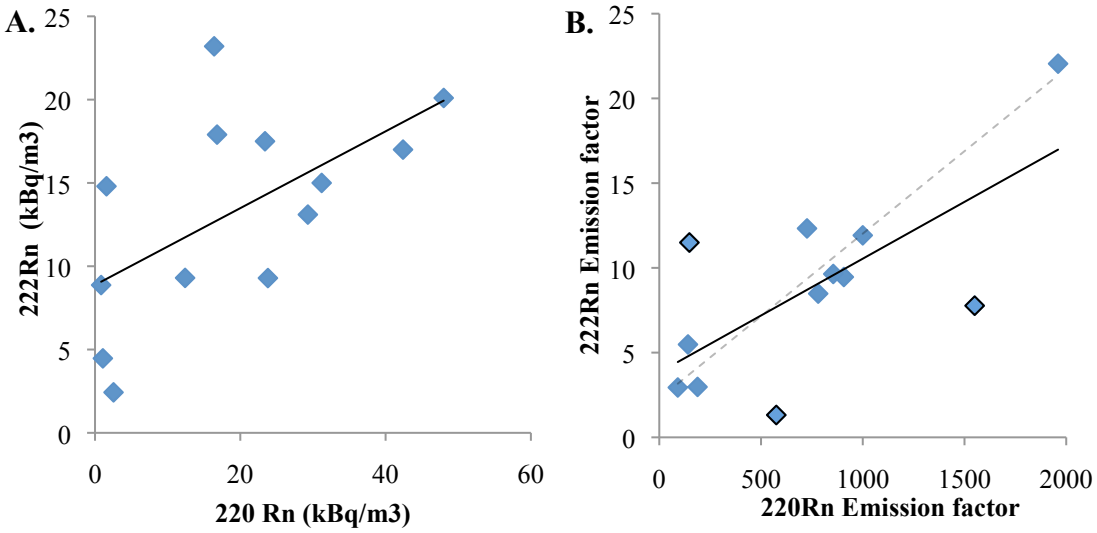


**Figure 20 Comparison of field radon concentration (A, left) and lab soil emission results (B, right). The solid lines are the linear regression models (see Table 2). The dashed line is the linear regression line for the points excluding the three outliers, highlighted with a black outline (see text)**

**Table 2 Linear regression model for field and lab data (± is 1.96 times the standard error).**

| | Field data | Lab data |
|---|---|---|
| Intercept | 8.71±4.7 | 3.84±3.94 |
| Slope | 0.24±0.21 | $6.71 \times 10^{-3} \pm 4.26 \times 10^{-3}$ |
| $R^2$ | 0.34 | 0.488 |
| p-value | 0.048 | 0.011 |

The field data in Figure 20 are similar to the overall Waikite dataset, although the intercept is significantly higher. The lab data in Figure 20, on the other hand, are very different. The linear model derived from the lab data show that there is a significant relationship between the two isotopes (low p-value) and that the intercept (3.84±3.94, see Table 2) could be 0. A majority of the lab data plot on or near the linear trend; however, there are three outliers. These three points may have had a different parent isotopic ratio compared to the rest of the population. It should be noted that the augers

were done after the radon gas sampling was finished, and outliers in Figure 19 were preferentially chosen as locations to sample with the auger. The outliers may therefore be overrepresented in Figure 20B, due to the method in choosing auger sampling locations.

In summary, the lab data indicate that there is a prevalent isotopic ratio between radon and its parent radium, across all field areas, but there are also some samples that deviate from this trend. The scatter and associated low $R^2$ values for the linear models in Table 1 could therefore be caused by the migration of $^{222}Rn$ through soil gas, or by a minority population with a different radon parent ratio.

# 7 DISCUSSION

## 7.1 Increase in soil emanation in weathered zones

The relationship between soil weathering and radon emanation (see 5.1.2 and 5.2.2) indicates that radon concentration may be linked to near-surface weathering processes. This could be either related to soil forming processes, where clays are leached from a higher permeable horizon and deposited in a deeper lower permeability horizon (Easterbrook, 1999). The leached clays could possibly coat grains in the lower horizon, increasing radon emanation.

Another possibility is that the weathering is related to a fluctuating water table. The zone of a fluctuating water table is one of intense weathering (Taylor and Eggleton, 2001), which could be the cause of the apparent oxidation of the soil. The weathering

might reduce the grain size of minerals, increasing the relative surface area, and increasing the radon emanation.

The fact that weathered soil is consistently observed closer to the surface is likely to be to erosional processes on the scarp. This would make the weathered zone appear shallower than it originally was. If the top of the weathered zone were originally horizontal, erosion associated with footwall uplift would explain why the weathered zone is consistently observed to be shallower in the footwall of the Rehi Road faults.

It seems that faults generally have two types of radon anomalies associated with them. Although there is evidence that radon anomalies could be associated with advective flow, the flow is spatially discontinuous, and not as common as anomalies caused by in increase in soil emanation. An anomaly caused by the increase in soil radon emanation is more common around faults. Processes associated with faulting, including footwall uplift, footwall/scarp erosion are likely to be a direct cause of the association of faults with radon anomalies.

## 7.2 Diffusion or advection of $^{222}$Rn?

Radon anomalies are associated with faults in both study areas, and $^{222}$Rn is affected by flow to some degree. The data do not conclusively show however whether a carrier gas induces the flow of $^{222}$Rn advectively over large distances, or whether it is caused by diffusion of $^{222}$Rn, the latter being restricted to a few metres. A flux of radon rich gas from depth, which is significantly different than background values, would be required

in order to use radon surveys as a fault-tracing tool, due to the short diffusion distance of $^{222}Rn$.

Soil in the study areas has variable emanation potential based on the $^{220}Rn$ measurements. Therefore $^{222}Rn$ gas would be expected to migrate from sites that have a high $^{220}Rn$ concentration to low $^{220}Rn$. The fact that there is a positive intercept in the $^{220}Rn$ vs. $^{222}Rn$ graphs suggests that there is higher $^{222}Rn$ at low emanation potential sites. This is consistent with the hypothesis that the $^{222}Rn$ gas migrates through diffusion. This is true for the both the 'near fault' and background datasets.

The scatter of data (low $R^2$ value) and positive intercept could be caused by advectively flowing gas. The gas would need to contain a $^{222}Rn$ concentration of the same order of magnitude or less than the concentration of the gas in the soil. However, since the background data do not produce a zero intercept, the advective flow of $^{222}Rn$ gas would be also occur in background areas, and not only restricted to faulted areas.

The fact remains that the positive intercept of the Waikite near fault dataset is significantly higher than the background values. It is possible that this is caused by either: 1) the presence of soils with a higher emanation potential near faults, 2) the advective flow of a gas with a $^{222}Rn$ concentration higher than background values, or 3) soils that have a different radon-parent ratio compared to the majority of the soils.

The question of whether the $^{222}Rn$ isotope is migrating by diffusion or by advective flow of gases can be addressed by analysing the relative concentration of the radon isotopes and comparing this behaviour to that expected for diffusion. Diffusion would

cause $^{222}$Rn gas produced in the soil to migrate from sites of higher concentration to sites of lower concentration. When $^{222}$Rn gas diffuses from high to low emanation soils, the $^{222}$Rn concentration measured at low emanation potential sites would be higher than production at these sites. The excess of $^{222}$Rn would vary depending on the proximity of the highly emanating soil, the magnitude of the difference, and the diffusion coefficient for the soil.

The diffusion profile for $^{222}$Rn gas from $^{222}$Rn producing soil was modelled using the diffusion equation presented in Appendix A. The highest concentration of $^{222}$Rn produced by soil in the study areas, based on the highest $^{220}$Rn measurement (65200 Bq/m$^3$) in these areas and multiplied it by the dominant parent ratio (0.337), gives us a value of 22000 Bq/m$^3$. The extreme diffusion case, which would produce the highest $^{222}$Rn diffusion, is where $^{222}$Rn was being produced at 1.2 m (i.e. just below the horizon we sampled in our soil gas measurements) at the highest rate measured in our field area. By doing this, we make the assumption that the soil across the whole field area has a constant radon emanation ratio between both isotopes.

The initial concentration at 1.2 m is set to 22000 Bq/m$^3$, and the expected $^{222}$Rn concentration at our measured depth, 1m, modelled based on the emanation potential of the soil (i.e. the $^{220}$Rn concentration). This gave us the maximum value expected at 1 m depth, if the $^{222}$Rn was entirely produced in the soil and migrated solely through diffusion. Any value above this would have to be explained by either 1) a variation in the parent ratio and/or 2) input of $^{222}$Rn by advection.

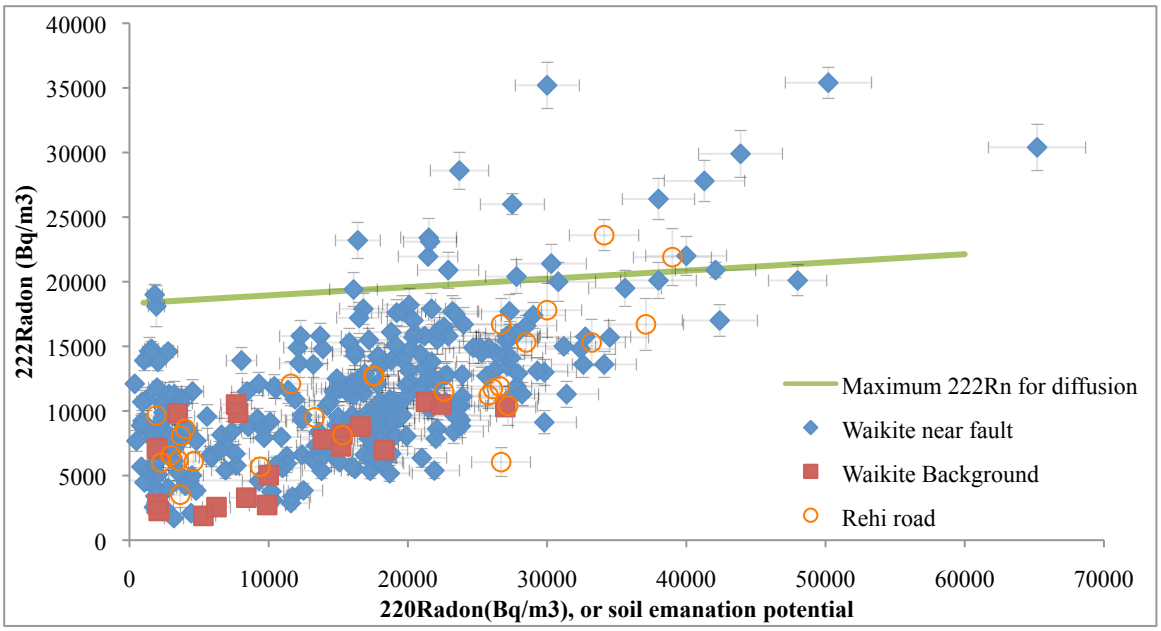


**Figure 21: Same plot as in Figure 20, with the addition of the maximum possible concentration of $^{222}$Rn if affected by diffusion.**

The highest possible $^{222}$Rn concentration for diffusion is plotted against the emanation potential of the soil (Figure 21). This shows that all but twelve points could be explained solely by diffusion within the soil. This means that as little as 4% of the observations cannot be explained based solely by diffusion of $^{222}$Rn gas using a single emanation ratio.

One possible explanation for the samples that cannot be explained by diffusion is that the soil at the location sampled has a different parent ratio, with the $^{222}$Rn parent more enriched than the $^{220}$Rn parent, and thus showing a higher emanation potential. The other explanation is that these locations are affected by the input of $^{222}$Rn through advective flow of a radon-rich gas.

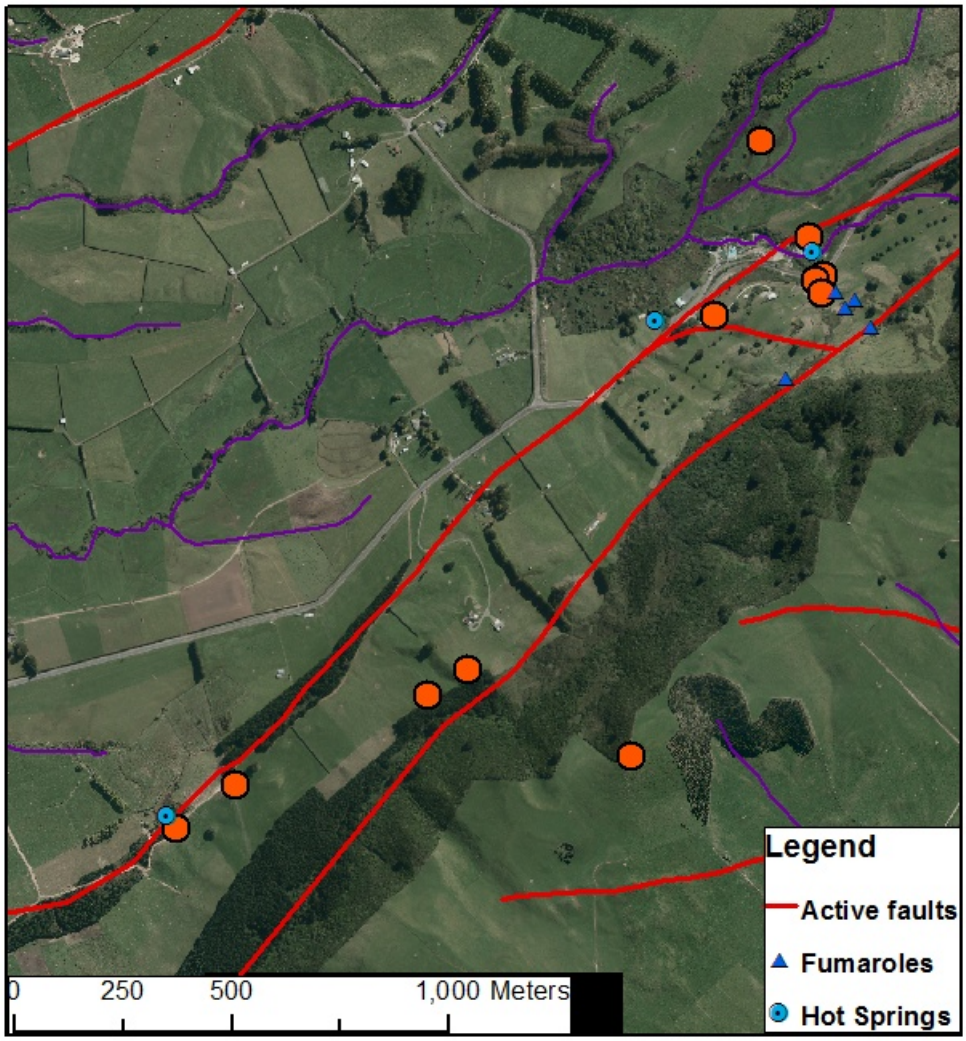


**Figure 22 Map showing location of points (in orange) that have a higher $^{220}$Rn than can be accounted for by diffusion.**

The locations of the 12 points with a higher $^{220}$Rn are plotted in Figure 22. It is worth noting that 6 out the 12 points plot within 100 m of a known thermal feature, such as a hot spring or a fumarole. These features are advectively flowing fluids. It would be reasonable to assume that the $^{222}$Rn could also be affected by the visible flow of the nearby fluids. The anomalies shown in Figure 22 document in some cases the spatial distribution of permeable pathways within fault zones.

The Waikite Valley hot springs together with the Te Kopia (TK) and the Orakei Korako (OK) geothermal fields are located on the Paeroa Fault (see Figure 1). Given the size of the fault (~28 km long and maximum throw of ~1100 m), it probably extends to the base of the continental crust (e.g., at 10-16 km depth) and intersects the fluid convective system in the rift. The coincidence of the fault and the geothermal areas is consistent with the fault being a conduit for the upward movement of hot geothermal fluids (e.g., Rowland and Sibson, 2004). At the Orakei Korako geothermal field, there is also evidence that low permeability fault rock locally provide barriers to water flow and compartmentalises the near surface hydrology, as mapped normal faults produce a series of sinter-covered terraces that host perched boiling springs emanating from the bases of 5–10 m high scarps.

The results from Figure 22 suggest that the actual flow of fluids along the Paeroa is restricted to specific locations, instead of the fault providing a continuous permeable pathway along its strike. The channelizing of fluids along faults is a phenomenon that has been observed elsewhere in the TVZ (Seebeck et al 2014).

## 8 CONCLUSIONS

The results of this study are consistent with the hypothesis that radon anomalies around faults are mainly due to an increase in the emanation potential of soils. $^{222}$Rn migrates through soil, and in >90% of cases can be attributed to the diffusion of $^{222}$Rn gas from sites of low to high radon emanation potential within the soil. There is some evidence of advective flow of $^{222}$Rn, however this is at specific locations along the Paeroa Fault,

most of which are associated with advectively flowing features such as hot springs and fumaroles.

$^{222}$Rn anomalies are spatially related to faults on various scales. At Rehi Road, anomalies are observed located on the fault scarp, and $^{222}$Rn concentration is close to background values within 4 m of the scarp. At Waikite, higher $^{222}$Rn values are located closer to the fault scarp. However, at both sites, we also observed higher $^{220}$Rn values near the faults.

An important outcome of this research is that $^{222}$Rn soil gas concentration cannot be related to the emanation potential of the soil due to the diffusion of radon gas. Hence it is not possible to use the lack of a correlation between $^{222}$Rn and $^{226}$Ra as evidence for advective flow of $^{222}$Rn gas.

Even though it is possible that there are some $^{222}$Rn anomalies associated with advective flow near faults, these anomalies are restricted to small areas within zones of high flux. The increase of radon emanation of the soil causes $^{222}$Rn anomalies that are spatially associated with faults.

With this in mind, if a fault was buried by a new geological formation, such as sedimentary or volcanic deposit, the radon anomalies associated with the fault are likely to be undetectable if the deposit was thicker than several meters. It is therefore unlikely that ‘blind’ faults will be detectable using radon soil gas surveys if they are buried at significant depths (e.g. >2 m).

# 9 REFERENCES

Al-Tamimi, M.H., and Abumurad, K.M., 2001, Radon anomalies along faults in North of Jordan: Radiation Measurements, v. 34, no. 1-6, p. 397–400.

Atallah, M.Y., Al-Bataina, B.A., and Mustafa, H., 2001, Radon emanation along the Dead Sea transform (rift) in Jordan: Environmental Geology, v. 40, no. 11-12, p. 1440–1446.

Bégué, F., Gravley, D.M., Chambefort, I., Deering, C., and Kennedy, B., 2014, Magmatic volatile distribution as recorded by rhyolitic melt inclusions in the Taupo Volcanic Zone, New Zealand: Geological Society, London, Special Publications, v. in press.

Burton, M., Neri, M., and Condarelli, D., 2004, High spatial resolution radon measurements reveal hidden active faults on Mt. Etna: Geophysical Research Letters, v. 31, no. L07618, p. 1–4.

Caine, J.S., Evans, J.P., and Forster, C.B., 1996, Fault zone architecture and permeability structure: Geology, v. 24, no. 11, p. 1025–1028.

Ciotoli, G., Etiope, G., Guerra, M., and Lombardi, S., 1999, The detection of concealed faults in the Ofanto Basin using the correlation between soil-gas fracture surveys: Tectonophysics, v. 301, no. 3-4, p. 321–332.

Clements, W.E., and Wilkening, M.H., 1974, Atmospheric pressure effects on 222Rn transport across the earth-air interface: Journal of geophysical research, v. 79, no. 33, p. 5025–5029.

Downs, D.T., Wilson, C.J.N., Cole, J.W., Rowland, J. V, Calvert, A.T., Leonard, G.S., and Keall, J.M., 2014, Age and eruptive center of the Paeroa Subgroup ignimbrites

(Whakamaru Group) within the Taupo Volcanic Zone of New Zealand: Geological Society of America Bulletin, , no. X, p. 1–14.

Easterbrook, D.J., 1999, Surface processes and landforms:.

Etiope, G., 2002, Migration of carrier and trace gases in the geosphere: an overview: Physics of The Earth and Planetary Interiors, v. 129, no. 3-4, p. 185–204.

Fleischer, R.L., Hart, H., and Mogro-Campero, A., 1980, Radon emanation over an ore body: Search for long-distance transport of radon: Nuclear Instruments and Methods, v. 173, no. 1, p. 169–181.

Font, L., Baixeras, C., Moreno, V., and Bach, J., 2008, Soil radon levels across the Amer fault: Radiation Measurements, v. 43, no. Supplement 1, p. S319–S323.

Glover, R., Klyen, L., and Crump, M., 1992, Spring Chemistry of the Waikite-Paukohurea Thermal Area: Proc. 14th New Zealand Geothermal,, p. 63–72.

Huxol, S., Brennwald, M.S., Hoehn, E., and Kipfer, R., 2012, On the fate of 220Rn in soil material in dependence of water content: Implications from field and laboratory experiments: Chemical Geology, v. 298-299, p. 116–122.

Ioannides, K., 2003, Soil gas radon: a tool for exploring active fault zones: Applied Radiation and Isotopes, v. 59, no. 2-3, p. 205–213.

Iskandar, D., Yamazawa, H., and Iida, T., 2004, Quantification of the dependency of radon emanation power on soil temperature: Applied Radiation and Isotopes, v. 60, no. 6, p. 971–973.

Israel, H., and Bjornsson, S., 1967, Radon (Rn-222) and Thoron (Rn-220) in soil air over faults: Zeitschrift für Geophysik, v. 33, no. 1, p. 48–64.

Katsanou, K., Stratikopoulos, K., Zagana, E., and Lambrakis, N., 2010, Radon Changes Along Main Faults in the Broader Aigion Region, NW Peloponnese: Bulletin of the Geological Society of Greece, 2010, , no. 4, p. 1726–1736.

Keall, J.M., 1988, Volcanology and Ignimbrite Stratigraphy Along the Paeroa Fault, Taupo Volcanic Zone: Victoria University of Wellington.

King, C.-Y., King, B.-S., Evans, W.C., and Zhang, W., 1996, Spatial radon anomalies on active faults in California: Applied Geochemistry, v. 11, no. 4, p. 497–510.

Lane-Smith, D., and Sims, K.W.W., 2013, The effect of CO2 on the measurement of 220Rn and 222Rn with instruments utilising electrostatic precipitation: Acta Geophysica, v. 61, no. 4, p. 822–830.

Leonard, G.S., Begg, J.G., and Wilson, C.J.N., 2010, Geology of the Rotorua Area: scale 1:250,000: Lower Hutt: Institute of Geological & Nuclear Sciences Limited,, p. 102.

Leonard, R.B., and Janzer, V.J., 1977, Natural Radioactivity in Geothermal Waters, Alhambra Hot Springs and Nearby Areas, Jefferson County, Montana:, 20 p.

Malczewski, D., and Zaba, J., 2007, 222Rn and 220Rn concentrations in soil gas of Karkonosze-Izera Block (Sudetes, Poland).: Journal of Environmental Radioactivity, v. 92, no. 3, p. 144–164.

Manville, V., and Wilson, C.J.N., 2003, Interactions between volcanism, rifting and subsidence: implications of intracaldera palaeoshorelines at Taupo volcano, New Zealand: Journal of the Geological Society, v. 160, no. 1, p. 3.

Nicol, A., Walsh, J.J., Villamor, P., Seebeck, H.C., and Berryman, K.R., 2010, Normal fault interactions, paleoearthquakes and growth in an active rift: Journal of Structural Geology, v. 32, no. 8, p. 1101–1113.

Rowland, J. V, and Sibson, R.H., 2001, Extensional fault kinematics within the Taupo Volcanic Zone, New Zealand: soft-linked segmentation of a continental rift system: New Zealand Journal of Geology and Geophysics, v. 44, no. 2, p. 271–284.

Rowland, J. V, and Sibson, R.H., 2004, Structural controls on hydrothermal flow in a segmented rift system, Taupo Volcanic Zone, New Zealand: Geofluids, v. 4, no. 4, p. 259–283.

Seebeck, H.C., Nicol, A., Walsh, J.J., Childs, C., Beetham, R.D., and Pettinga, J., 2014, Fluid flow in fault zones from an active rift: Journal of Structural Geology, v. 62, p. 52–64.

Semkow, T.M., and Parekh, P.P., 1990, The Role of Radium Distribution and Porosity in Radon emanation from Solids: Geophysical Research Letters, v. 17, no. 6, p. 837–840.

Shefsky, S.I., Rose, D., and Parsons, C.G., 1993, A Study of Radon adsorption on Activated Carbon as a Function of Temperature, *in* The 1993 International Radon Conference, p. 12–18.

Smith, W.D., 1984, Principal New Zealand Earthquakes in 1983: Bulletin of the New Zealand National Society for Earthquake Engineering, v. 17, no. 1, p. 56.

Tanner, A.B., 1964, Physical and chemical controls on distribution of radium-226 and radon-222 in ground water near Great Salt Lake, Utah, *in* Adams, J.A.S. and Lowder, W.M. eds., The Natural Radiation Environment, p. 253–276.

Tanner, A.B., 1978, Radon Migration in the Ground: A Supplementary Review, *in* Third International Symposium on the Natural Radiation Environment, Houston, Texas, p. 63.

Taylor, G., and Eggleton, R.A., 2001, Regolith geology and geomorphology:.

Tuccimei, P., and Soligo, M., 2008, Correcting for CO2 interference in soil radon flux measurements: Radiation Measurements, v. 43, no. 1, p. 102–105.

Villamor, P., and Berryman, K.R., 2001, A late Quaternary extension rate in the Taupo Volcanic Zone, New Zealand, derived from fault slip data: New Zealand Journal of Geology and Geophysics, v. 44, no. 2, p. 243–270.

Vogler, G., 1960, Ursachen emanometrischer Anomalien (Origins of emanometric Anomalies): Zeitschrift für Geophysik, v. 26, no. 2, p. 57–71.

Whitehead, N., 1984, Geothermal prospecting by ground radon measurements: Journal of volcanology and geothermal research, v. 20, p. 213–229.

Wilson, C.J.N., Houghton, B.F., McWilliams, M.O., Lanphere, M. a., Weaver, S.D., and Briggs, R.M., 1995, Volcanic and structural evolution of Taupo Volcanic Zone, New Zealand: a review: Journal of Volcanology and Geothermal Research, v. 68, p. 1–28.

Wollenberg, H.A., 1974, Radioactivity of Nevada Hot-Spring Systems: Geophysical Research Letters, v. 1, no. 8, p. 359–362.

Wright, I.C., 1992, Shallow structure and active tectonism of an offshore continental back-arc spreading system: the Taupo Volcanic Zone, New Zealand: Marine Geology, v. 103, no. 1-3, p. 287–309.

Zarroca, M., Linares, R., Bach, J., Roqué, C., Moreno, V., Font, L., and Baixeras, C., 2012, Integrated geophysics and soil gas profiles as a tool to characterize active faults: the Amer fault example (Pyrenees, NE Spain): Environmental Earth Sciences,.

# CHAPTER 3:

## Stress estimation in the Rotokawa Geothermal Field, New Zealand: Evidence for crustal weakening caused by clay alteration

# Stress estimation in the Rotokawa Geothermal Field, New Zealand: Evidence for crustal weakening caused by clay alteration

## 1 ABSTRACT

A methodology is presented to estimate the magnitude minimum principal stress from Leak-off Tests (LOTs) conducted in boreholes in the Rotokawa Geothermal Field in the Taupo Volcanic Zone (TVZ) New Zealand. Tests that were run in a permeable formation, where fluid loss to the formation prohibits fracture formation, are distinguished from tests that efficiently opened pre-existing or new fractures. The results of the stress interpretation in the Rotokawa Geothermal Field show a relationship between the minimum principal stress and alteration zones containing smectite, where the presence of smectite lowers the strength of the crust. This confirms a well-recorded relationship between the friction of rocks, and the strength of the crust. The fact that friction controls stress magnitude in the shallow crust shows that shear slip is a controlling factor for stress magnitude at shallow depth (<1500 m) at Rotokawa.

## 2 INTRODUCTION

Accurately determining the state of stress in the Earth's crust is challenging. To date, focal mechanism inversions are the only type of stress estimations published in New Zealand (e.g.; Reyners, 2010). There are no published direct stress measurements for any of the geothermal fields in the TVZ. Yet the state of stress is important for inferring the overall strength of the crust (Townend and Zoback, 2000), for considering the likelihood of fault reactivation (Sibson, 1985; Morris et al., 1996), and for predicting such parameters as permeability (Barton et al., 1995). For these reasons, a robust stress model would be a useful resource for geothermal exploration and development. The goal of this study was to estimate the magnitude of the minimum principal stress at depth in the Rotokawa Geothermal Field using LOTs.

### 2.1 Stress estimation method

Several methods exist for estimating the magnitude of stress imposed on rocks, such as the flat-jack method (e.g. Doe and Korbin, 1987), the overcoring method (e.g., Haimson, 1983) or the fracture opening (HF) method. The flat-jack method measures the pressure required to jack open a slot cut into rock. The overcoring method involves inserting a device into a borehole, and then removing the device by coring the surrounding rock. Stress is estimated from the deformation experienced by the removed rock, once it is relieved of stresses. The HF method isolates a section of rock exposed down a borehole and then increases the hydraulic pressure until a fracture is opened. Stress is estimated from the fluid pressure required to open and/or close the fracture.

Unlike the first two methods, which usually require a tunnel face to attempt measurements, the HF method is unique in that it can be used to estimate stress at great depths in boreholes, at locations that are otherwise unattainable.

In order to determine the complete state of stress using the flat jack method, the test has to be repeated in 6 different orientations. To determine the complete stress tensor from the HF method, a minimum of 8 tests need to run on pre-existing fractures, and the orientation of these fractures needs to be known (Haimson and Cornet, 2003). However, a single test that opens a fracture is enough to estimate the minimum principal stress, and the other stress components can be estimated using other methods.

The HF method has been used to estimate stress for over 50 years, (Scheiddeger, 1962) and has been a main-stream stress estimation method since at least 1981, when a conference on the subject was organised (Zoback and Haimson, 1983). Some notable experiments from this conference compared the HF stress determination method to other stress-determinations methods (Haimson, 1983), and showed that stress estimations using the HF method gave results that are consistent with other methods. In 2003, the International Society for Rock Mechanics (ISRM) produced a series of papers with recommended methods on rock stress estimation, including one method for HF (Haimson and Cornet, 2003), with the aim of standardising the procedure. This method covered in detail the series of steps required in order producing precise estimations of stress. There remains some controversy over the best method to estimate stress from HF data, but the variation in the results obtained by the different methods is minimal compared to measurement uncertainty (Zoback et al., 2003; Raaen et al., 2006; Couzens-Schultz and Chan, 2010).

## 2.2 Leak-off Tests

The Leak-off test (LOT) is a variation of the HF test. The two differ in that HF tests use packers to isolate the borehole section of interest, whereas LOT are run after a well casing has been cemented in place, and a short section of rock (~5 m) has been exposed by drilling. Once the borehole wall has been exposed, fluid is pumped down the borehole at a constant rate, and the pressure change is observed (Figure 1). Once the curve deviates from a linear trend (LOP), the test is continued for a pre-determined amount of time, at which point the pump is turned off and the borehole is shut-in (indicated by the flow rate dropping to zero). After shut-in, the well pressure is monitored for a set amount of time. LOTs are frequently run during drilling operations, and therefore LOTs are an attractive and convenient way to acquire data for the purposes of stress estimation (Raaen et al., 2006; Couzens-Schultz and Chan, 2010; Haimson et al., 2010).

In some cases, tests run in the same conditions as LOT are stopped after the pressure has reached a pre-determined level. This type test is referred to as a Formation Integrity Test (FIT, Figure 1) or Limit Test (LT, Figure 1) if the test did not open a hydraulic fracture. By carefully interpreting the time-based pressure data of a LOT, it is possible to distinguish fracture opening to estimate the minimum principal stress accurately.

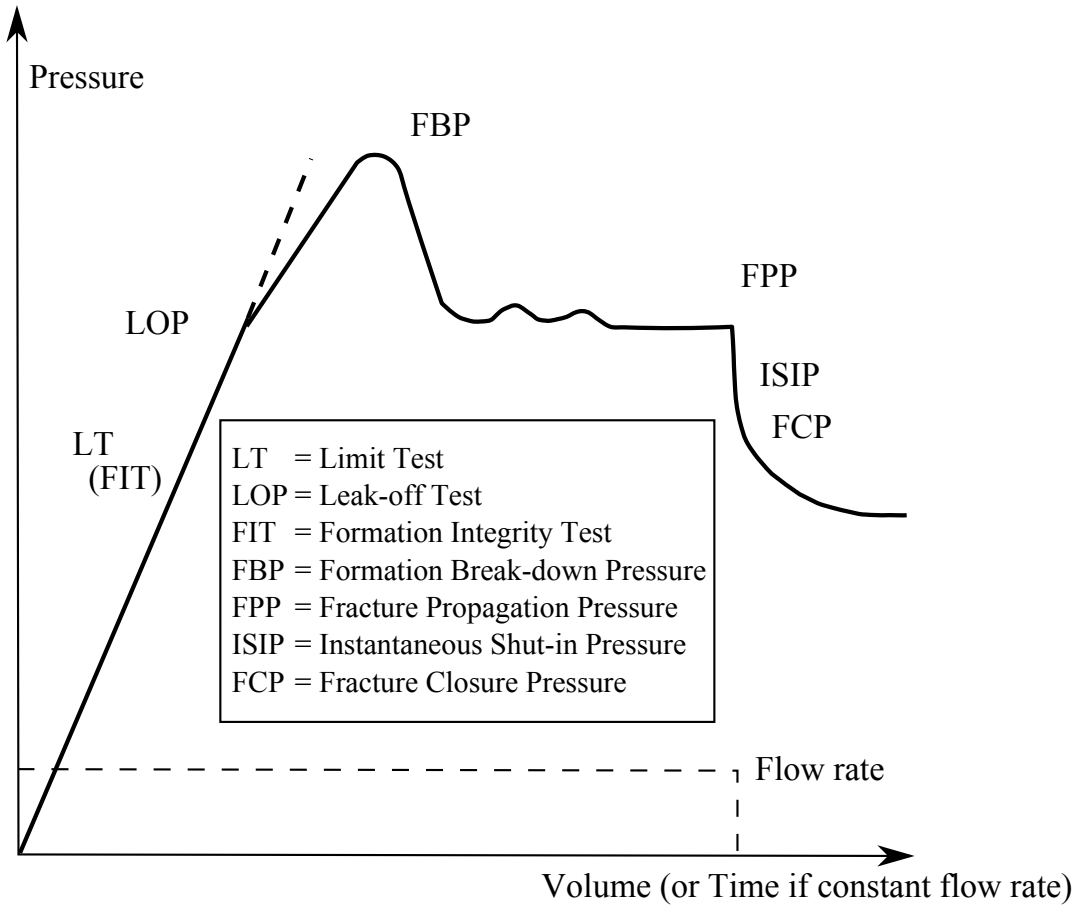


**Figure 1 Typical LOT surface pressure vs. time curve (from Gaarenstroom 1993). Flow rate indicates shut-in time.**

An important point to make is that LOTs are run to determine the pressure at which fractures form, which will help set safe drilling limits and aid with well casing design. They do not have the explicit goal of opening a fracture in order to measure stress. The pressure at which fractures form during leak-off tests can be affected by the tensile strength if the exposed rock in the wellbore is intact (Haimson, 1983). However, stress can be still be determined from affected tests by using the data points obtained from the shut-in curve.

In theory, deviation from the linear trend (LOP in Figure 1) signifies a fracture opening, and thus the minimum principal stress acting on the fracture has been overcome. Once

evidence for fracture opening is evident, it is possible to use the LOP, the instantaneous shut in pressure (ISIP, Figure 1), or the Fracture Closure Pressure (FCP, see Figure 1) to estimate the minimum principal stress, depending on conditions during the LOT (see Raaen et al., 2001; and Zoback et al., 2003 for more details). Often the three points mentioned above will offer repeatable and redundant estimates of the minimum principal stress (Zoback et al., 2003). In this case, the Instantaneous Shut-in Pressure (ISIP) is used as an equivalent to the minimum principal stress (Zoback et al., 2003). Using this avoids problems associated with the tensile strength of the rock, or with near-borehole stress modifications, caused either by the void of the borehole, or by near-borehole plastic deformation (Hickman and Zoback, 1983; Zhou and Wojtanowicz, 2002).

In this paper, the procedure that was used to estimate the minimum principal stress in the Rotokawa Geothermal Field of the TVZ of New Zealand is described. This procedure allowed to distinguish between valid LOT tests that have overcome the minimum principal stress and opened a fracture, and tests that have lost fluid to a permeable rock formation without opening fractures, solely based on the pressure time data. This allowed for the estimation of a minimum principal stress model for the Rotokawa Geothermal Field. The resulting model suggests that the minimum principal stress imposed on rock does not increase linearly with depth. This can be explained by presence of the alteration clay mineral smectite in some parts of the Rotokawa Geothermal Field.

## 3 GEOLOGICAL BACKGROUND

The Rotokawa Geothermal Field is located approximately 10 km northeast of Taupo, on the eastern edge of the central TVZ (Figure 2). The central TVZ comprises an active rift which formed during the last 1-2 Ma in association with subduction of the Pacific plate (Wright, 1992; Wilson et al., 1995; Rowland and Sibson, 2001). This rift is coincident with a volcanic arc, which has produced in excess of 15,000 $km^3$ of volcanic material over the past 2 Ma, mostly through caldera forming eruptions (Wilson 1995). The geology of the central TVZ is dominated by these Quaternary volcanic and sedimentary deposits (Manville and Wilson, 2004), emplaced on top of the Mesozoic basement rocks, known as the Torlesse Terrane, composed of poorly sorted meta-sandstones variably interbedded with argillites (Leonard et al., 2010).

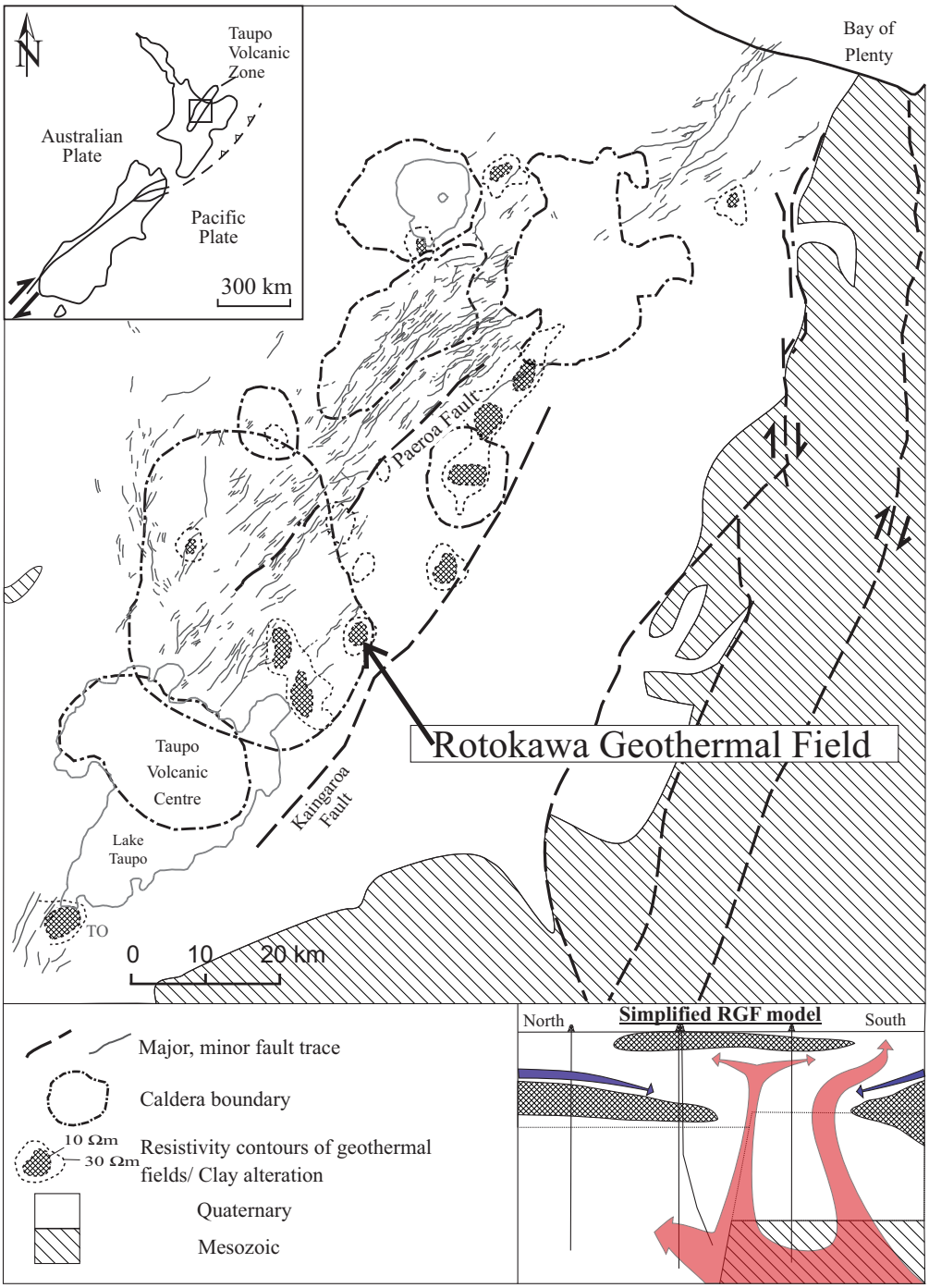


**Figure 2 Map of TVZ showing location of Rotokawa Geothermal Field (modified from Leonard et al., 2010; Bégué et al., 2014), and simplified Rotokawa conceptual model (Winick et al., 2009; Sewell et al., 2012).**

The TVZ has numerous geothermal fields located throughout the whole of the volcanic area (Figure 2). The hydrology of these fields is composed of large convecting cells of fluid. Cold meteoric water circulates to depth and, once heated, rises buoyantly back to

surface (Bibby et al., 1995; Bertrand et al., 2012). Zones of intense clay alteration tend to form through the interaction of the hot rising hydrothermal fluids with the surrounding rocks (Browne, 1978). These clay alteration zones are detectable using resistivity and magneto-telluric surveys, as they are less resistive compared to the surrounding rocks (Hatherton et al., 1966; Bibby et al., 1995; Bertrand et al., 2012).

The Rotokawa geological units can be broadly subdivided into the basement rocks, and the Quaternary deposits. The tops of the units older than ~330 ka are consistently offset by either faults that have little surface expression, or by paleo-topographical features (Wallis et al., 2013).

The Rotokawa hydrothermal system is divided into three distinct levels: a hot geothermal reservoir; an intermediate aquifer; and a shallow aquifer (Sewell et al., 2012). Each aquifer is separated by discontinuous and low-permeability layers, rich in the alteration clay smectite. The intermediate aquifer is mainly constrained within two geological units, indicating a primary control on permeability (Rae, 2007; Sewell et al., 2012). The permeability of the deep reservoir rocks, however, is thought to be strongly influenced by faulting and fracturing of host rocks, based on the relationship between the temperature contours and the inferred structures at depth (Rae, 2007), and the drawdown pressure gradients (Quinao et al., 2013). Estimating the magnitudes of the principal stresses is a critical step to understand the processes that govern fracture permeability in the Rotokawa reservoir (Barton et al., 1995; Rowland and Simmons, 2012).

# 4 DATA AND METHODOLOGY

41 LOTs conducted during drilling at the Rotokawa Geothermal Field over the period of August 2004 to November 2010 have been interpreted, in order to estimate the magnitude of stress at various depth and locations in the Rotokawa Geothermal Field. The pressure vs. time curves of the tests were obtained, classified the tests based on the curve morphology, and determined the ISIP of the tests that opened fractures. All tests were conducted as water-only injections, or with light mud (max 9.0ppg).

In order to determine the minimum principal stress from LOTs, it is necessary to observe a change in the pressurization rate after a linear increase (see LOP in Figure 1). As mentioned earlier, this observation is usually interpreted as an increase in the volume available to the fluid inside the well, and hence a fracture forming (Zoback, 2007). However, fitting a line through LOT data can be subjective and can be a function of the frequency of the pressure acquisition (see Figure 13 in Raaen et al., 2006). This can lead to difficulties in interpretation when the break in slope is subtle, or when the slope imitates a linear trend when in reality the slope is gradually changing throughout the test. This is why it was necessary to include an extra step in the methodology- by analysing the pressure change over time (which is the equivalent of the slope of the pressure vs. time curve, or dP/dt), and comparing it to the pressure itself.

## 4.1 Fluid loss to the formation

Several LOT results from the Rotokawa Geothermal Field could be interpreted as tests during which the pressure deviated from an initial linear trend (and hence a test in

which a fracture opened) using pressure vs. time curves alone (Figure 3). However, by plotting the rate of pressurization (dP/dt) as a function of pressure itself, the two variables were found to form a linear relationship. This linear relationship is a crucial characteristic to determine from LOT data, as it reveals the fact that the change in pressurization is due to fluids being lost to the formation during the test (Altun et al., 1999; Song et al., 2001).

Fluid loss to the formation is a crucial characteristic to classifying LOT results, and a simple theoretical analysis can show how the dP/dt vs. P plots show that fluids are lost to the formation. While injecting fluid into the borehole, a permeable exposed rock will allow for a certain amount of fluid to escape through the exposed borehole wall. The rate at which the fluid escapes the borehole can be described according to a version of Darcy's Law:

$$Q = \frac{kA\Delta P}{\mu L} \quad , \tag{1}$$

where $Q$ is the flow rate, $k$ is the permeability, $A$ the cross-sectional area, $\mu$ the viscosity of the fluid and $L$ the length of the medium over which the pressure drop ($\Delta P$) takes place.

During a LOT, all parameters remain constant except for $L$, and $\Delta P$, as long as a fracture is not opened. At the beginning of a test, the pressure of the fluid inside the rock is the same as the pressure of the fluid itself, and $\Delta P$ is equal to zero. As the pressure is increased in the borehole, there is an increase in the difference in fluid pressure between the borehole and the rock formation ($\Delta P$), and consequently the flow

rate Q of the fluid escaping into the formation is increased. Where a relatively impermeable formation is exposed (i.e. where *k* is very small), the loss of fluid to the formation is negligible; even at high pressure, the rate at which fluid is lost to the formation is very small. In a permeable formation (*k* is large), however, the rate at which fluid is lost can become significant. The most important conclusion though is that the rate at which fluids are lost is function of the difference in pressure between the wellbore and the surrounding formation pressure.

Since the flow rate of fluids escaping the borehole is a function of the pressure difference, the rate of fluid loss will increase as the pressure increases during a LOT. At the same time, the flow rate of the fluid being pumped into the borehole is kept constant. The difference between the flow into the wellbore, and the flow out of the wellbore and into the formation (i.e. the rate at which the pressure increases over time, dP/dt), will decrease as the pressure increases. dP/dt and P form a linear relationship. The slope of the relationship is almost horizontal in low permeability situations, and becomes more negative in high permeability situations.

The pressure will increase inside the borehole until the point where the rate at which fluid escapes into the formation is equal to the rate at which fluid is pumped into the borehole (Song et al., 2001). At this point, the rate of pressure increase will be zero (see Figure 4).

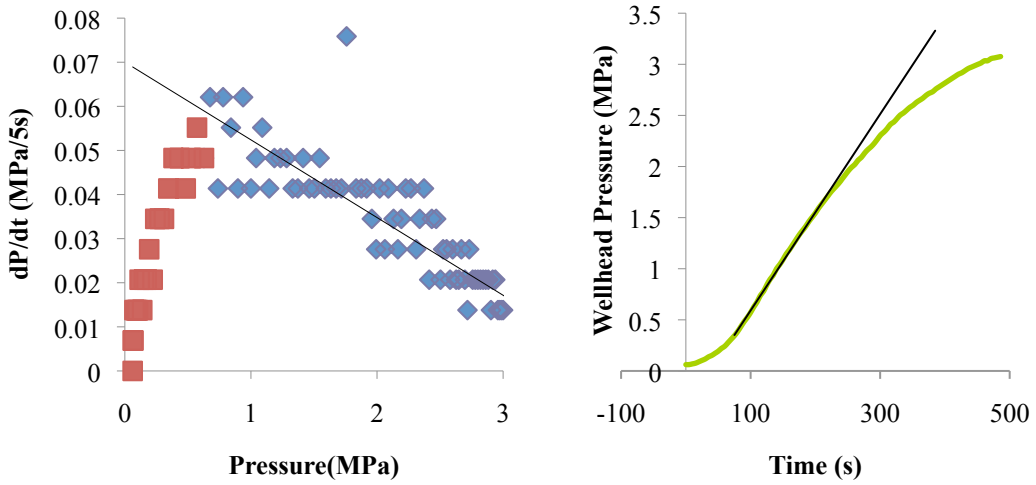


**Figure 3 Left: LOT dP/dt graph from borehole RK21 at 404 m vertical depth. Black line of best fit is added for blue diamonds, showing a linear relationship. Right: P vs. t graph for same test. Pump rate is steady throughout test at 0.25 bpm. Line is added for reference (see text).**

In Figure 3, the red squares represent measurements taken during the initial borehole pressurisation (see Section 5). The blue diamonds are measurements showing the linear relationship between pressure and rate of pressure increase. This linear relationship, or any deviation from it, is easy to recognise in the data. The use of dP/dt vs. P plots allowed to clearly establish whether a non-linear rate of pressurization in P vs. t plots is due to a loss of fluids to the rock formation, or if a fracture has opened.

The creation and/or opening of a fracture is required in order to estimate stress from LOT data. When data from a LOT shows that no fracture was created, it cannot be used for stress estimation purposes, since it is the pressure required to open and/or close the fracture that is used for stress estimation. Plotting dP/dt vs. total pressure graphs of the pressure build-up improves interpretation and can be used to remove some ambiguity from several LOTs results. Since this distinction is crucial to determining whether a specific LOT is appropriate for stress estimations, the use of dP/dt graphs are highly recommended while interpreting LOTs.

# 5 LOT RESULTS

LOT results have been divided into three different categories, based on the interpretation of the physical processes affecting the borehole. By using the dP/dt vs. P and P vs. t curve morphologies of each LOT, the tests are separated into one of three categories. The three categories represent the interpretation of the process operating between the fluid and the rock at the borehole wall interface.

The first category, named permeable fluid loss, is characterised by a linear trend in the dP/dt vs. P graph, with no sharp breaks or changes in the slope of the line. This translates to a curve that is continuously changing slope in the P vs. t graph, until it reaches a plateau pressure, if the test has not been halted before it reaches this stage. The second category, referred to as fracture reactivation, differs in that the dP/dt vs P curve is linear until a sudden sharp change occurs, while the pumping continues. The P vs. t curve looks similar to the previous category, also reaching a plateau, although there is a subtle difference. Importantly though, there is no significant drop in pressure as pumping continues. The characteristic feature of the last category, designated as new fracture formation, is that there is a significant drop in the pressure measured in the borehole, even as the pumping continues. The results in the second and third categories can be used to deduce information about the magnitude of the least principal stress.

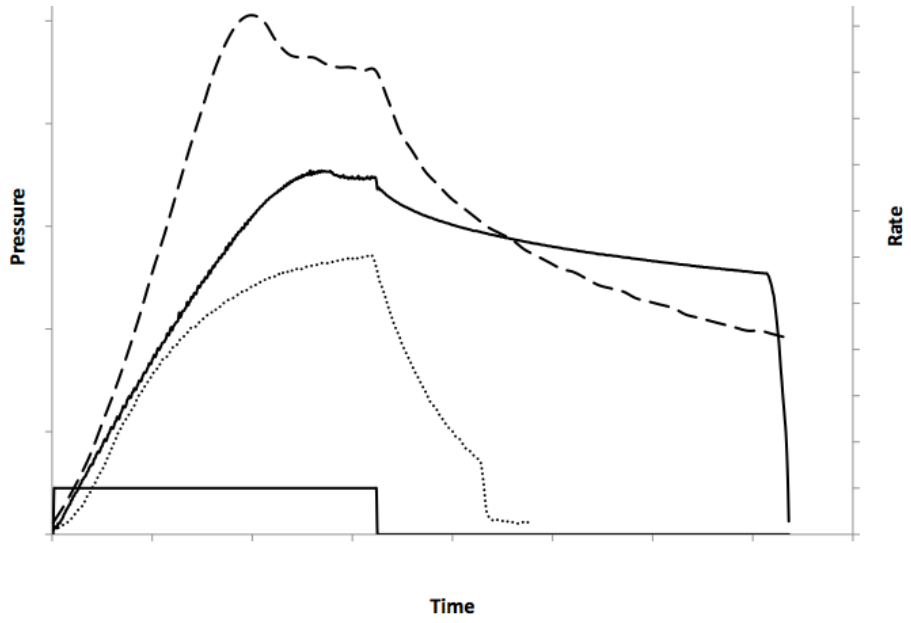


**Figure 4 Cartoon diagram of the three LOT categories: Dotted line represents the permeable fluid loss category, the solid line represents the fracture reactivation category, and the dashed line represents the fracture formation category.**

One common feature to most LOTs is that for the initial part of the P vs. t curve gradually curves upwards (see red part of dP/dt vs. P curve in Figure 5 and Figure 7). This is observed predominantly below wellhead pressures of 0.5 MPa, and is likely related to borehole expansion in response to the increased pressure (Altun et al., 1999) and/or to poroelastic effects (Detournay et al., 1989). After this initial part, the curve morphology eventually settles into several distinct patterns, described in the text below, that are used to distinguish between tests. The initial part of the curve is ignored when classifying the tests, as it is a common low-pressure feature of most tests.

## 5.1 Permeable fluid loss

As mentioned above, the example of the permeable fluid loss type of test in Figure 5 is characterised by a dP/dt vs. P curve that is linear. The P vs. t time does not display any

obvious sharp change, and almost reaches its plateau value of 1.72 Mpa before the test is stopped.

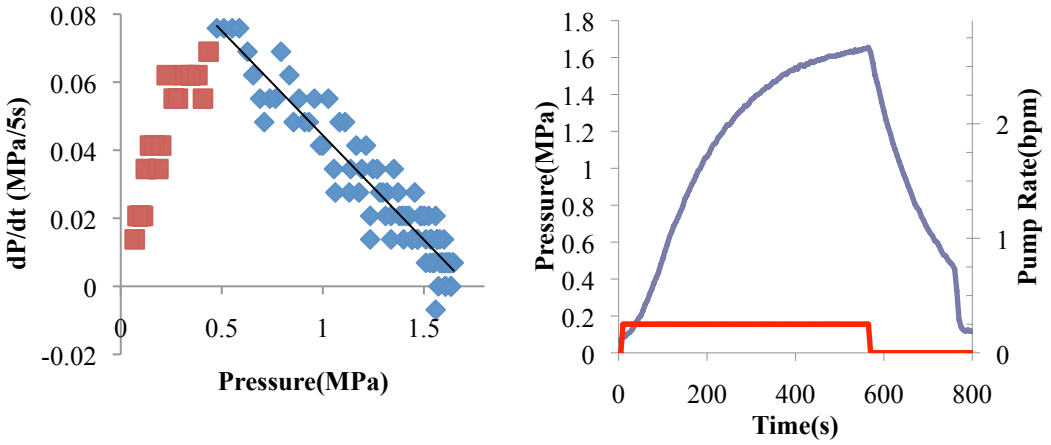


**Figure 5 Left: LOT dP/dt graph from borehole RK21 at 1277m vertical depth. Right: P vs. t graph for same test. Pump rate in red (right axis), indicating shut-in time.**

This linear relationship was observed in many LOTs at Rotokawa (see example in Figure 3), and is one that would be characteristic of a permeable formation (Song et al., 2001). The effect that permeable rock has on LOTs is not discussed much in the scientific literature (with the exceptions of Altun et al., 1999; and Song et al., 2001). This could be due to the fact that the overwhelming majority of LOTs in the oil and gas industry are performed in low permeability mudrocks (Couzens-Schultz and Chan, 2010). The LOTs at the Rotokawa Geothermal Field were performed in formations having a wide range of permeability.

In the permeable fluid loss type of test, there is no evidence that a fracture was opened. The negative linear relationship between dP/dt and P suggests that fluid is lost to a permeable formation through Darcian flow. The fact that the pressure rapidly drops to 0 (hydrostatic) after the test has been shut-in confirms this suggestion. The exposed rock

in not able to retain fluid and the pressure is rapidly dissipated as the fluid flows relatively quickly into the formation.

In this type of test, there is no change in either graphs, such as a break in the dP/dt linear relationship, or a sudden decrease in P as pumping continues, which could indicate that there is a change in downhole conditions, and hence a fracture opening due to the pressure increase. Since a fracture was not opened, the pressure in the borehole was either not sufficient to overcome the minimum principal stress, the exposed rock has a significant tensile strength which is not overcome, or that a fracture opening does not affect the bulk permeability of the well. The LOT that display these types of results do not provide information suitable for determining the minimum principal stress magnitude.

A LOT that has been terminated before forming a fracture is commonly called a Formation Integrity Test (FIT). It is likely that the permeable fluid loss test gives the same amount of information as a FIT test.

### 5.2 Fracture reactivation

In fracture reactivation LOTs, the defining characteristic is a change in the dP/dt vs. P relationship as pumping continues. In Figure 6, the borehole appears to be pressurising at a constant rate, until ~6.5 MPa.

Soon after this point, the pressure in the P vs. t stops increasing. In a permeable formation, it might be difficult to unambiguously identify the exact pressure at which

the change occurs on a P vs. t graph; however, the change should be clear in a dP/dt vs. P graph (Figure 6).

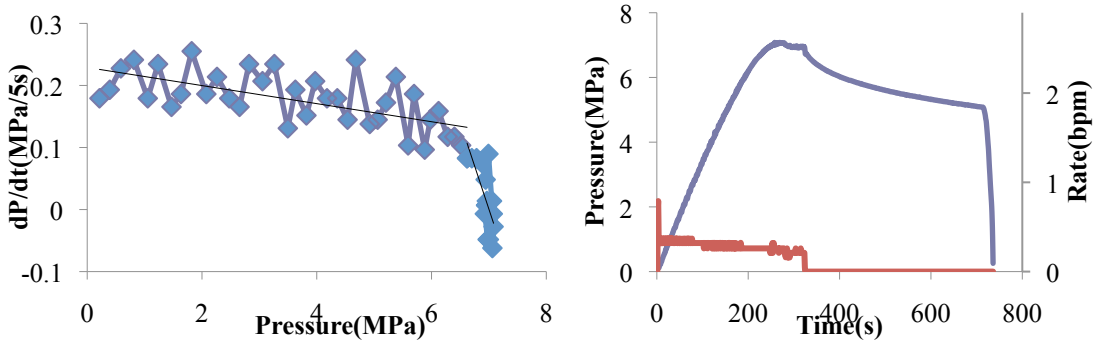


**Figure 6 Left: LOT dP/dt graph from well RK17 at 946 m vertical depth. Right: P v t graph for same test. Pump rate in red (right axis), indicating shut-in time.**

Although the P vs. t graph of this type of test appears similar to the graph from the permeable fluid loss type in the section above, there is an important difference. The dP/dt graph suggests that the rate at which fluids escape the borehole is relatively low until approximately 6.5 MPa. At this point, a change in borehole conditions occurs and the rate at which fluid escape the borehole increases dramatically. The change in slope in the dP/dt graph at ~6.5 MPa is interpreted as an indication of fracture opening due to the pressure of the fluid in the wellbore.

After the well is shut-in, the curve in the P vs. t graph initially drops and then quickly levels off as the pressure becomes insufficient to maintain the fracture open. Once the fracture is closed, the fluid is lost through primary permeability of the formation, which is relatively low in this formation. This behaviour is different from that shown in Figure 5, where the pressure rapidly drops after shut-in.

The break in slope on the dP/dt vs. P plot could be related to a change in the formation permeability and/or a sudden change in borehole volume, with both of these processes likely to be occurring in response to a fracture opening under fluid pressure. The behaviour after shut-in is also consistent with the hypothesis that a fracture opened. As the exposed rock is relatively impermeable, little fluid is lost to the formation until a fracture is opened. This occurs only once the fluid pressure is great enough to overcome the minimum principal stress. After shut-in, the pressure drops relatively quickly on the P vs. t graph until it reaches a pressure where the fracture closes again (~6.5 MPa), at which point the rate at which fluids are lost decreases dramatically.

### 5.3 New fracture formation

In this category, the pressure in the P vs. t drops as pumping continues at a steady rate (i.e.: before shut-in of the well). This is in stark contrast to the other test types, where the pressure always increases or remains at a steady value as pumping continues.

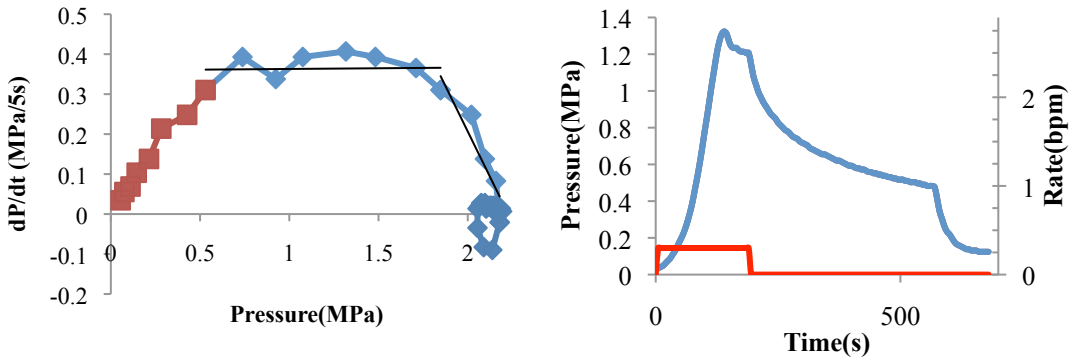


**Figure 7 Left: LOT dP/dt graph from well RK32 at 159 m vertical depth. Note that the pressure decreases as pumping is continued and this causes the negative values of the slope. Right: P v t graph for same test. Pump rate in red (right axis), indicating shut-in time.**

This drop in pressure signifies that the rate at which the fluid exits the borehole is greater than the pump rate. This is interpreted as a rapid increase in the volume

available to the fluid in the borehole. This leaves little ambiguity in the interpretation, as the only way to rapidly increase the volume available to the fluid is by the unstable propagation of a new tensile fracture at the borehole wall (Zoback et al., 2003). Newly created hydraulic fractures propagates normally to the least principal stress (Hubbert and Willis, 1957), which means that this type of test is the most desirable when it comes to interpreting the stress magnitudes from LOT data.

## 5.4 Minimum Principal Stress Magnitudes at Rotokawa

Figure 8 displays the data from all categories of LOTs conducted in boreholes drilled into the Rotokawa Geothermal Field. In this case, the Instantaneous Shut-in Pressure (ISIP) of the two LOT groups that opened fractures to be the equivalent of the minimum principal stress (Zoback 2006). The maximum pressure reached for the permeable fluid loss and FIT test have also been displayed for reference. The two black dashed lines in Figure 8 represent minimum principal stress values at which Coulomb frictional failure would occur, based on two different coefficient of friction(μ), using the following (Jaeger and Cook, 1969):

$$S_{\min} = \frac{S_{\max} - P_f}{\left(\sqrt{\mu^2 + 1} + \mu\right)^2} + P_f \quad , \tag{2}$$

where $S_{\min}$ and $S_{\max}$ are the minimum and maximum (in this case, vertical) principal stresses, $P_f$ is the pore fluid pressure, and μ is the coefficient of friction. The term 'coefficient of friction' is used here as defined by Lockner and Beeler (2002).

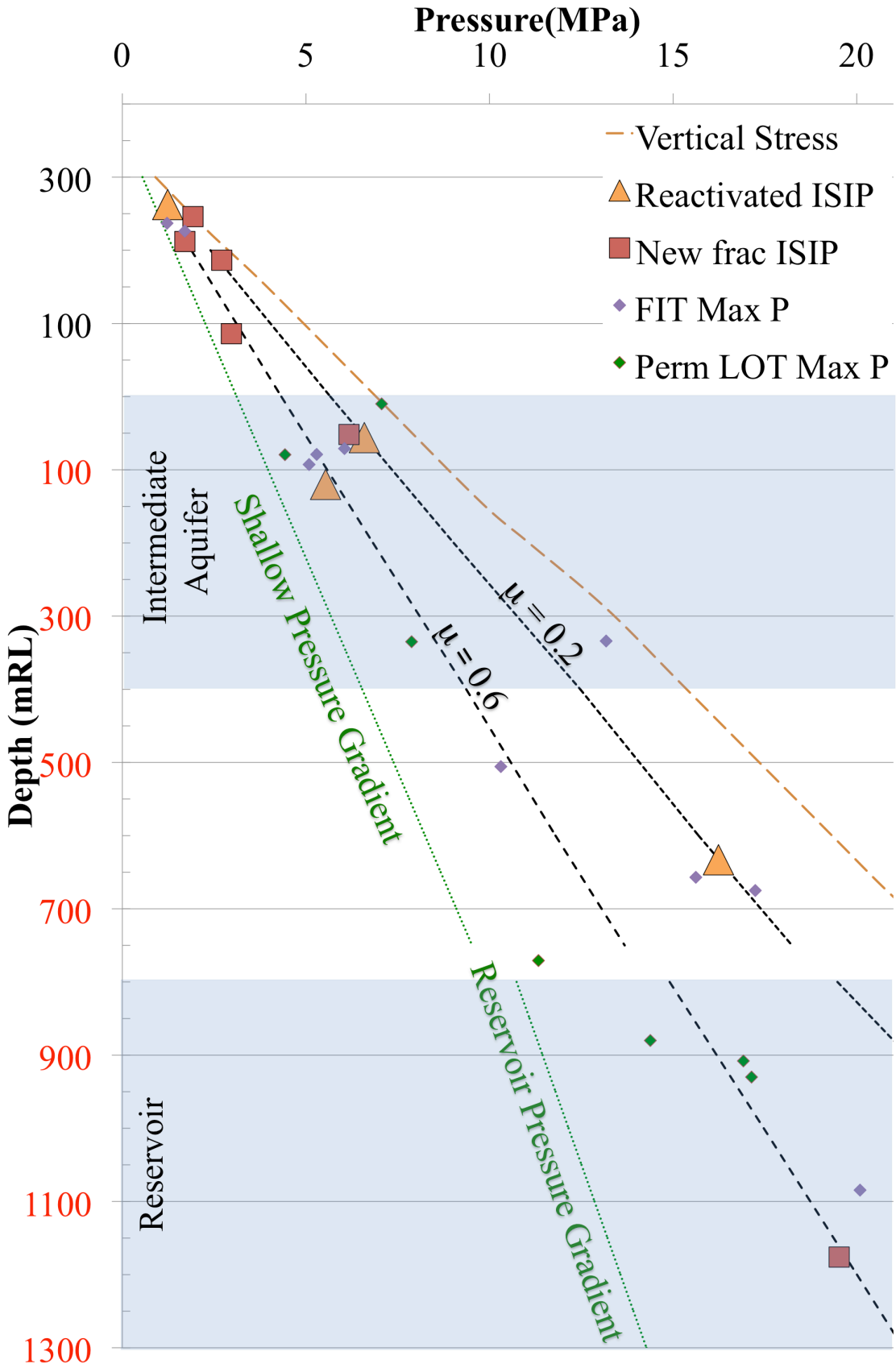


**Figure 8 Depth vs pressure graph for the Rotokawa Geothermal Field, showing LOT values for different test types (refer to Section 5), vertical stress (Chapter 4) and natural state fluid pressure gradient (Chapter 5).**

# 6 DISCUSSION

## 6.1 Fracture reactivation

LOTs interpreted as belonging to the fracture reactivation category are likely to be opening an existing fracture during the LOT, as the lack of a sharp drop in P vs. t graph shows there is no unstable fracture propagation (Zoback et al., 2003). A pre-existing fracture is not necessarily normal to the minimum principal stress, and therefore the normal stress imposed on that fracture could be higher than the minimum principal stress. In such a case, the stress estimation result would be an over-estimation of the minimum principal stress.

The prevalent interpretation method suggests that the presence or absence of unstable growth does not affect the stress interpretation (Zoback, 2007), due to the fact that if a defect such as a fracture exists, once the fracture begins to propagate under fluid pressure, it will be normal to the minimum principal stress. The cold drilling fluids used to drill through the high natural temperatures of the geothermal field tend to cause ubiquitous tensile fractures along the borehole wall, which further supports the interpretation method suggested above (see Chapter 4). However, this might be a source of errors, and a more conservative approach would be to use the results as an upper limit on the minimum principal stress.

## 6.2 FIT, permable fluid loss test results, and reservoir permeability

Figure 8 shows the approximate depth at which it is likely to encounter the permeable formations or structures that characterise the geothermal reservoir and intermediate aquifer. All of the LOTs that show evidence for fluid loss (green diamonds) plot in or near the aquifers, whereas the tests run in the aquitards tend to not show evidence for fluid loss (blue diamonds, Figure 8). The impermeable nature of the aquitards is consistent with the lack of evidence for fluid loss during LOT.

It is sometimes suggested that the highest pressure reached in FITs can be used to determine the lower limit to the minimum principal stress. This method of determining the minimum principal stress assumes that the tensile strength is always negligible, which essentially means that a tensile fracture already exists. However, some rock types in the Rotokawa Geothermal Field have a high tensile strength, with an average of 15 MPa (Siratovich et al., 2012). Also, there are several points belonging to the permeable fluid loss LOT group that plot higher than any minimum principal stress estimations, near the estimated vertical stress for the Rotokawa Geothermal Field (see points plotting to the right of the 0.2 Frictional eq. line in Figure 9). It is likely that these values are unexpectedly high because the exposed rock was intact, and the pressure achieved during those tests was not sufficient to overcome the tensile strength of the rock. Therefore, assuming that FIT can be used as a lower limit to the minimum principal stress can lead to errors in interpretation in some special cases.

## 6.3 Evidence for a clay 'weakened' crust

As far as the actual stress magnitudes are concerned, several data points plot near the 0.6 line, which is consistent with stress magnitude observations made at other locations (see Townend and Zoback, 2000). However, three measurements plot closer to the 0.2 line. These results suggest that the differential stress is lower than expected for common crustal rocks. A sharp variability in the mineralogy of rocks in Rotokawa Geothermal Field, modifiying the coefficient of friction of the rock, might be the cause of lowered differential stress observed. A reduced coefficient of friction lowers the ability of rocks to sustain differential stress, and can be interpreted as a form of crustal 'weakening'.

Laboratory experiments show that for most common crustal rocks, the coefficient of friction falls in a restricted range of 0.6 to 1.0 (Byerlee, 1978). Frequently, in-situ stress measurements show that the brittle crust is likely to be in "frictional equilibrium", as the coefficient of friction predicted by Coulomb frictional failure of rocks is often between ~0.6 and 1.0 (Townend and Zoback, 2000). The implication is that the frictional properties of crustal rocks control the magnitude of stress that the crust can withstand, before slip on these rocks relieve the stress imposed on them.

The laboratory experiments collated by Byerlee (1978) highlighted two other important points. The first was that, unlike at higher normal stress values, the coefficient of friction of most rocks is highly irregular when the normal stress is less than 5 MPa. This could be linked to the fact that joint roughness has a larger effect on the coefficient of friction measured on rocks at low stresses (Barton, 1976). This means that at stresses

less than 5 MPa, the stress that these rocks can withstand would be highly dependent on the fracture geometry.

The second point raised by the laboratory experiments (Byerlee, 1978) was that above 5 MPa, experimental results using certain clays had a significantly lower coefficient of friction compared to the range of coefficient demonstrated by majority of rocks (~0.6). These clays demonstrated a coefficient of friction much lower than 0.6. In some cases, research has shown that montmorillonite (a member of the smectite group of clay minerals) has a coefficient of friction as low as 0.2 (Figure 9). It can be concluded that rocks in the crust containing significant amounts of clay would be significantly weaker, as they are not able to withstand as large of a differential stress before slipping. Indeed, the presence of smectite has been flagged as the possible cause for the apparent weakness of the San Andreas fault (Zoback et al., 1987; Carpenter et al., 2012), and the frictional properties of smectite have been the subject of extensive studies (e.g.: Moore and Lockner, 2007).

Given the potential impact of clay minerals on the frictional strength of rocks, the stress estimation results have been divided into two groups. The first one, Group 0.2, plots close to the Mohr-Coulomb frictional failure stress values, if the stress in the crust were in frictional equilibrium using a value of 0.2 for the coefficient of friction. The second group, Group 0.6, which has a larger differential stress, plots near values of 0.6. The location at which these tests were conducted is plotted on a cross-section of the Rotokawa Geothermal Field showing the magneto-telluric (MT) resistivity data. The MT cross section shows the resistivity of the subsurface of the Rotokawa Geothermal

Field. The low resistivity areas (warm colours) in Figure 10 indicate areas of pervasive smectite alteration (Sewell et al., 2012).

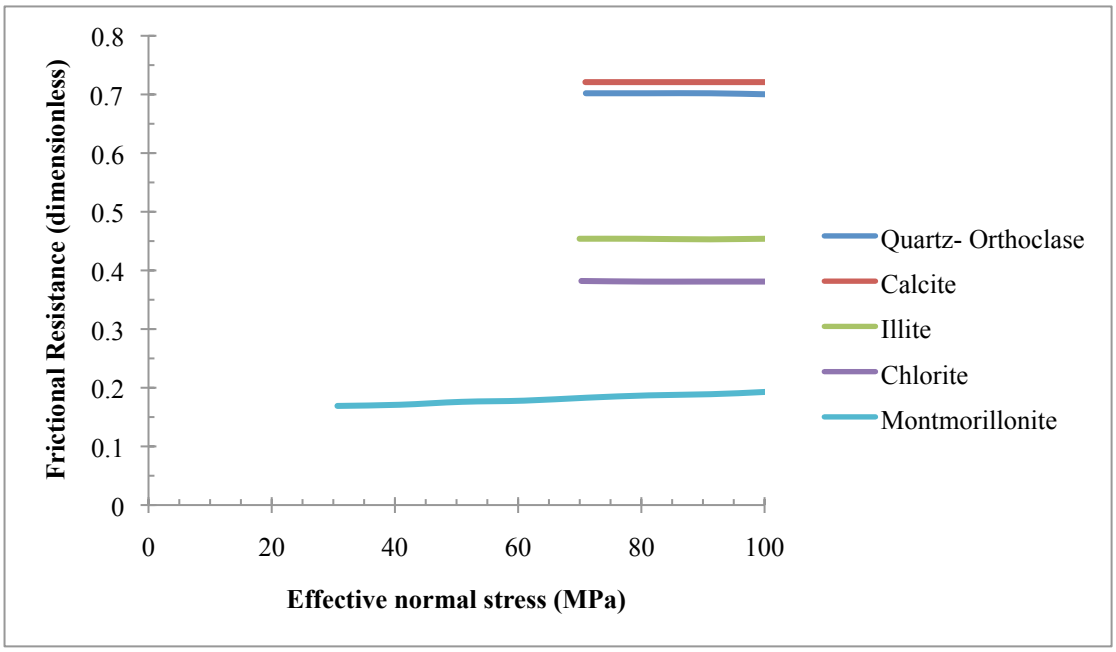


**Figure 9 Frictional resistance for minerals that occur commonly in the Rotokawa Geothermal Field (modified from Lockner and Beeler, 2002)**

The square symbols in Figure 10, which represent the location of the second group (Group 0.6), plot in high resistivity areas as shown by the magneto-telluric (MT) image. The round symbols represent the location of stress estimation belonging to Group 0.2, and they tend to plot in or near areas of low resistivity. This indicates that and that the lower differential stress is caused by the presence of significant amounts of smectite. Although the data seem to be contradicting the results presented by Townend & Zoback (2000), if the presence of smectite significantly reduces the strength of the crust, then these results correlate well.

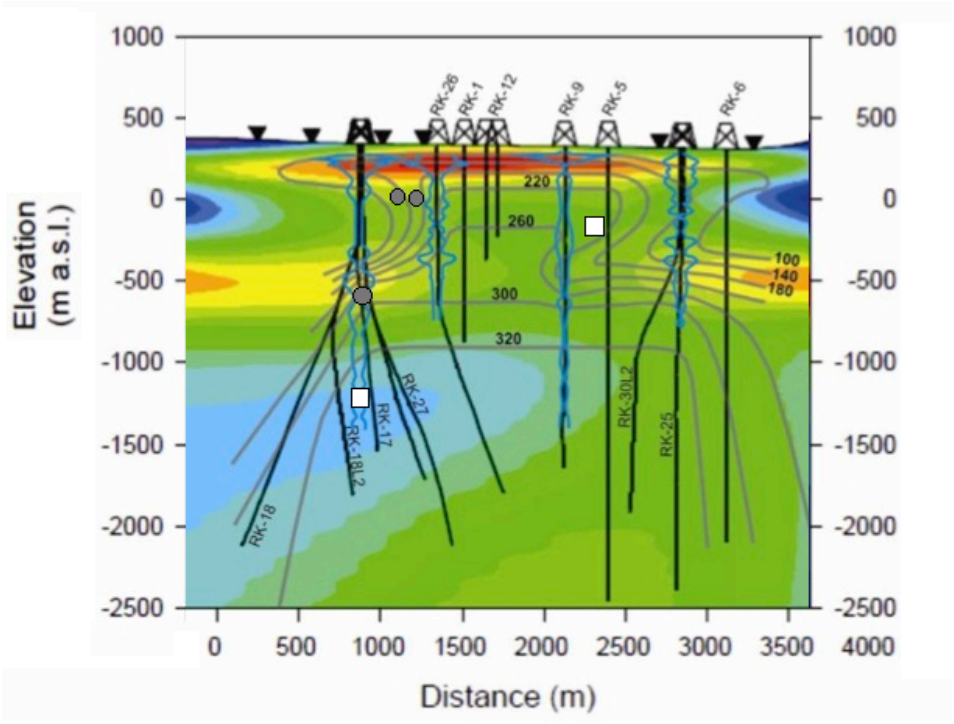


**Figure 10: A cross-section of the Rotokawa field, displaying resistivity features from MT, and various wells drilled into the Field. Low resistivity zones (warm colours) are associated with higher smectite content. Dark grey circles and white squares show approximate locations of LOTs (see Figure 8). Figure modified from Sewell et al. (2012).**

## 6.4 Implications of crustal weakening

The relationship between the frictional properties of the subsurface rocks and the stress magnitude highlights the fact that slip is on faults control the magnitude of stress imposed on the rock in the Rotokawa Geothermal Field. Shear failure is an important process controlling the stress magnitude.

Shear failure also contributes to overall permeability of rock (Barton et al., 1995). It is unlikely to affect permeability at shallow depths (above the reservoir level), since main control on permeability intermediate aquifer is lithological (Sewell et al., 2012). However, at deeper levels, there is independent evidence that fracture permeability

affects bulk permeability, and it is likely that shear failure is an important process contributing to the bulk permeability of rock.

The effect of crustal weakening on stress magnitudes has a profound effect on the pressure required to create fractures. When no smectite is present, the coefficient of friction for the rock tends to be higher, and therefore the differential stress that the rock can withstand before slipping is higher. Conversely, in the weaker, clay-rich rocks, the rocks are unable to withstand large differences between the maximum and minimum principal stresses. As in this case, the maximum principal stress is equal to the weight of the overburden, then a smaller differential stress in the weaker rocks requires the minimum principal stress to be higher.

When attempting to create hydro-fractures, the difference between the hydrostatic gradient and the minimum principal stress is the pressure required to open the fracture. Since that difference is higher in clay-rich rocks due to the higher minimum principal stress, the pressure required would be higher to open a fracture will be higher, and these rocks will appear ‘stronger’ compared to rock with little clay. In essence, the low coefficient of friction of the rock causes an increase the pressure required to create fractures.

## 7 CONCLUSIONS

This chapter addresses the issues around interpreting the minimum principal stress magnitude from LOTs, and outline a method using the slope of the pressure build up

over time (dP/dt) versus the magnitude of the pressure itself, in order to differentiate between tests where fractures were 1) opened, 2) reactivated, or 3) where fluid was lost to a permeable formation. The results of LOTs have been categorised into three groups, based on the interpretation of their plots.

The LOT results are consistent with a crust in frictional equilibrium, where the magnitude of stress in the crust is defined by the frictional properties of the rocks. This means that where the minerals known to reduce the rock coefficient of friction (such as smectite) are present, the differential stress that the rock can withstand is seriously reduced. Conversely, where clays are absent, the rock is able to withstand a larger differential stress. A general linear stress gradient is inappropriate for the Rotokawa Geothermal Field, as the gradient is dependent on the rock mineralogy. The strong dependence of stress magnitude on alteration and clay content highlights the fact that frictional processes affect the shallow parts of hydrothermal systems.

## 8 REFERENCES

Altun, G., Shirman, E., Langlinais, J.P., Bourgoyne, A.T., 1999. New Model to Analyze Nonlinear Leak-Off Test Behavior 121.

Barton, C.A., Zoback, M.D., Moos, D., 1995. Fluid flow along potentially active faults in crystalline rock. Geology 23, 683–686.

Barton, N., 1976. The shear strength of rock and rock joints. Int. J. Rock Mech. Min. Sci. Geomech. Abstr 13, 255–279.

Bégué, F., Gravley, D.M., Chambefort, I., Deering, C., Kennedy, B., 2014. Magmatic volatile distribution as recorded by rhyolitic melt inclusions in the Taupo Volcanic Zone, New Zealand. Geol. Soc. London, Spec. Publ. in press.

Bertrand, E.A., Caldwell, T.G., Hill, G.J., Wallin, E.L., Bennie, S.L., Cozens, N., Onacha, S. a., Ryan, G. a., Walter, C., Zaino, A., Wameyo, P., 2012. Magnetotelluric imaging of upper-crustal convection plumes beneath the Taupo Volcanic Zone, New Zealand. Geophys. Res. Lett. 39, 1–6.

Bibby, H.M., Caldwell, T.G., Davey, F., Webb, T.H., 1995. Geophysical evidence on the structure of the Taupo Volcanic Zone and its hydrothermal circulation. J. Volcanol. Geotherm. Res. 68, 29–58.

Browne, P.R.L., 1978. Hydrothermal alteration in active geothermal fields. Annu. Rev. Earth Planet. Sci. 6, 229–250.

Byerlee, J., 1978. Friction of rocks. Pure Appl. Geophys. PAGEOPH 116, 615–626.

Carpenter, B.M., Saffer, D.M., Marone, C., 2012. Frictional properties and sliding stability of the San Andreas fault from deep drill core. Geology 40, 759–762.

Couzens-Schultz, B.A., Chan, A.W., 2010. Stress determination in active thrust belts: An alternative leak-off pressure interpretation. J. Struct. Geol. 32, 1061–1069.

Detournay, E., Cheng, A., Roegiers, J.-C., McLennan, J.D., 1989. Poroelasticity considerations in In Situ stress determination by hydraulic fracturing. Int. J. Rock Mech. Min. Sci. Geomech. Abstr. 26, 507–513.

Doe, T.W., Korbin, G.E., 1987. A Comparison Of Hydraulic Fracturing And Hydraulic Jacking Stress Measurements, in: The 28th U.S. Symposium on Rock Mechanics (USRMS). Tucsan, AZ.

Haimson, B.C., 1983. A Comparative Study of Deep Hydrofracturing and Overcoring Stress Measurements at Six Locations with Particular Interest to the Nevada Test Site, in: Hydraulic Fracturing Stress Measurements Proceedings.

Haimson, B.C., Cornet, F.H., 2003. ISRM Suggested Methods for rock stress estimation—Part 3: hydraulic fracturing (HF) and/or hydraulic testing of pre-existing fractures (HTPF). Int. J. Rock Mech. Min. Sci. 40, 1011–1020.

Haimson, B.C., Lin, W., Oku, H., Hung, J., Song, S., 2010. Integrating borehole-breakout dimensions, strength criteria, and leak-off test results, to constrain the state of stress across the Chelungpu Fault, Taiwan. Tectonophysics 482, 65–72.

Hatherton, T., Macdonald, W., Thompson, G., 1966. Geophysical methods in geothermal prospecting in New Zealand. Bull. Volcanol. 29, 485–497.

Hickman, S.H., Zoback, M.D., 1983. The interpretation of hydraulic fracturing pressure-time data for in-situ stress determination, in: Hydraulic Fracturing Stress Measurements Proceedings.

Hubbert, M.K., Willis, D., 1957. Mechanics of Hydraulic fracturing. Trans. Soc. Pet. Eng. AIME 210, 153–168.

Jaeger, J.C., Cook, N.G.W., 1969. Fundamentals of Rock Mechanics.

Leonard, G.S., Begg, J.G., Wilson, C.J.N., 2010. Geology of the Rotorua Area: scale 1:250,000. Low. Hutt Inst. Geol. Nucl. Sci. Ltd. 102.

Lockner, D.A., Beeler, N.M., 2002. Rock Failure and Earthquakes, in: International Handbook of Earthquake and Engineering seismology, Volume 81A. pp. 0–12.

Manville, V., Wilson, C.J.N., 2004. The 26 . 5 ka Oruanui eruption , New Zealand : a review of the roles of volcanism and climate in the post-eruptive sedimentary response. New Zeal. J. Geol. Geophys. 47, 525–547.

Moore, D.E., Lockner, D.A., 2007. Friction of the Smectite Clay Montmorillonite, in: Dixon, T., Moore, C. (Eds.), The Seismogenic Zone of Subduction Thrust Faults. pp. 317–345.

Morris, A.P., Ferrill, D.A., Henderson, D.B., 1996. Slip-tendency analysis and fault reactivation. Geology 24, 275.

Quinao, J.J., Sirad-azwar, L., Clearwater, J., Hoepfinger, V., Le Brun, M., Bardsley, C., 2013. Analyses and Modelling of Reservoir Pressure Changes to Interpret the Rotokawa Geothermal Field Response to Nga Awa Purua Power Station Operation, in: Thirty-Eight Workshop on Geothermal Reservoir Engineering.

Raaen, a. M., Horsrud, P., Kjørholt, H., Økland, D., 2006. Improved routine estimation of the minimum horizontal stress component from extended leak-off tests. Int. J. Rock Mech. Min. Sci. 43, 37–48.

Raaen, A.M., Skomedal, E., Kjørholt, H., 2001. Stress determination from hydraulic fracturing tests: the system stiffness approach. Int. J. Rock Mech. Min. Sci. 38, 529–541.

Rae, A.J., 2007. Rotokawa Geology and Geophysics. GNS Sci. Consult. Rep. 2007/83, 11.

Reyners, M., 2010. Stress and strain from earthquakes at the southern termination of the Taupo Volcanic Zone , New Zealand. J. Volcanol. Geotherm. Res. 190, 82–88.

Rowland, J. V, Sibson, R.H., 2001. Extensional fault kinematics within the Taupo Volcanic Zone, New Zealand: soft-linked segmentation of a continental rift system. New Zeal. J. Geol. Geophys. 44, 271–284.

Rowland, J. V, Simmons, S.F., 2012. Hydrologic, Magmatic, and Tectonic Controls on Hydrothermal Flow, Taupo Volcanic Zone, New Zealand: Implications for the Formation of Epithermal Vein Deposits. Econ. Geol. 107, 427–457.

Scheiddeger, A.E., 1962. On the Stresses in the Earth's Crust as determined from Hydraulic Fracturing Data. Geol. und Bauwes. 27, 1.

Sewell, S.M., Cumming, W.B., Azwar, L., Bardsley, C., 2012. Integrated MT and Natural State Temperature Interpretation for a Conceptual Model Supporting Reservoir Numerical Modelling and Well Targeting at the Rotokawa Geothermal Field, New Zealand, in: Proceedings: Thirty-Seventh Workshop on Geothermal Reservoir Engineering. Stanford University, Stanford California.

Sibson, R.H., 1985. A note on fault reactivation. J. Struct. Geol. 7, 751–754.

Siratovich, P.A., Davidson, J., Villeneuve, M., Gravley, D.M., Kennedy, B., Cole, J.W., Wyering, L., Price, L., 2012. Physical and mechanical properties of the Rotokawa Andesite from production wells RK 27_L2, RK28 and RK30, in: New Zealand Geothermal Workshop 2012 Proceedings. Auckland, New Zealand.

Song, I., Suh, M., Won, K.S., Haimson, B.C., 2001. A laboratory study of hydraulic fracturing breakdown pressure in table-rock sandstone. Geosci. J. 5, 263–272.

Townend, J., Zoback, M.D., 2000. How faulting keeps the crust strong. Geology 28, 399–402.

Wallis, I.C., Bardsley, C.J., Powell, T., Rowland, J. V, Brien, J.M.O., 2013. A Structural Model for the Rotokawa Geothermal Field, New Zealand, in: New Zealand Geothermal Workshop 2013 Proceedings.

Wilson, C.J.N., Houghton, B.F., McWilliams, M.O., Lanphere, M. a., Weaver, S.D., Briggs, R.M., 1995. Volcanic and structural evolution of Taupo Volcanic Zone, New Zealand: a review. J. Volcanol. Geotherm. Res. 68, 1–28.

Winick, J.A., Powell, T., Mroczek, E., 2009. The Natural-State Geochemistry of the Rotokawa Reservoir, in: New Zealand Geothermal Workshop 2009 Proceedings.

Wright, I.C., 1992. Shallow structure and active tectonism of an offshore continental back-arc spreading system: the Taupo Volcanic Zone, New Zealand. Mar. Geol. 103, 287–309.

Zhou, D., Wojtanowicz, A., 2002. Analysis of Leak-off tests in shallow marine sediments. J. energy Resour. Technol. 124.

Zoback, M.D., 2007. Reservoir geomechanics: Earth stress and rock mechanics applied to exploration, production and wellbore stability.

Zoback, M.D., Barton, C.A., Brudy, M., Castillo, D., Finkbeiner, T., Grollimund, B., Moos, D., Peska, P., Ward, C., Wiprut, D., 2003. Determination of stress orientation and magnitude in deep wells. Int. J. Rock Mech. Min. Sci. 40, 1049–1076.

Zoback, M.D., Haimson, B.C., 1983. Hydraulic Fracturing Stress Measurements, Proceedings of a Workshop, December 2-5, 1981.

Zoback, M.D., Zoback, M., Mount, V., Suppe, J., Eaton, J.P., Healy, J.H., Oppenheimer, D., Reasenberg, P., Jones, L., Raleigh, C.B., Wong, I.G., Scotti, O., Wentworth, C., 1987. New Evidence on the State of Stress of the San Andreas Fault System. Science (80-. ). 238, 1105–1111.

# CHAPTER 4:

## Using Stress Estimates to Evaluate Fracture Permeability in an Active Geothermal Field

# Using Stress Estimates to Evaluate Fracture Permeability in an Active Geothermal Field

## 1 ABSTRACT

The variability of stress magnitude in the Rotokawa Geothermal Field is assessed using density and borehole televiewer logs. The range of the vertical stress magnitude is delimited by estimating the weight of the overburden. An attempt to constrain the maximum horizontal stress magnitude by modelling drilling induced failure observed in image logs yields no result, due to a lack of physical constraints. The magnitude and orientation of the principal stress axes is acquired and used to predict the fracture orientations prone to slip in the Rotokawa reservoir. The precise range of fracture orientations prone to slip is critically dependent on the poorly constrained maximum horizontal stress magnitude. Analysis of stresses, together with fracture orientations from borehole televiewer logs, and permeability estimates from temperature/pressure/spinner logs for three wells, reveals a complex relationship between fractures slip tendency, and permeability. In one well, there is a positive correlation between the frequency of fractures prone to slip, and known zones of permeability, confirming that these structures are contributing to fluid flow. In another well, there is a negative correlation between slip on fractures and known permeability. In this case, the data suggest that slip on fractures reduce permeability, indicating that perhaps other controls on permeability exist in this well.

## 2 INTRODUCTION

Faults and fractures can be important in controlling the bulk permeability of geothermal reservoirs. The rock type in which the fractures occur largely dictates their hydraulic behaviour (Brace, 1980), influencing their contribution to bulk permeability. Fractures in crystalline rock with low matrix permeability tend to increase bulk permeability (Brace, 1980), however the development of a continuous gouge along the fracture plane can instead decrease permeability (Caine et al., 1996; Yielding et al., 1997). In porous sandstones, permeability of rocks in close proximity to faults is reduced by up to seven orders of magnitude (Antonellini and Aydin, 1994). Deformation bands in unlithified sediments also reduce permeability (Rawling et al., 2001). The bulk permeability of rock that mainly deforms by ductile processes (such as clay-rich rocks at low temperatures) is unaffected by fractures (Brace, 1980).

In rock types where fractures increase bulk permeability; such as low-porosity, low-permeability, crystalline rock, the spatial configuration of faults and fracture networks can impact the bulk permeability. In a qualitative study at three separate locations, Barton et al. (1995) showed that large temperature gradients existed near fractures that have a shear stress to normal stress ratio $\geq 0.6$, inferring that the change in the temperature gradient was caused by fluid flow. This ratio of 0.6 is similar to that derived experimentally for the friction of common crustal rocks (Byerlee, 1978). Friction, as a major control of fracture permeability, implies that the main mechanism that keeps fractures open to fluid flow is fault slip induced dilation (Barton et al., 1995, 1998), and that fracture permeability is mostly independent of the spatial configuration of fractures. However, not all fault zones are equally permeable. Permeable fault zones

tend to have an uneven distribution of fluid flow, usually concentrated in complex zones such as at fault tips, fault interaction areas and fault intersections (e.g. Curewitz and Karson, 1997; Gartrell et al., 2004; Anderson and Fairley, 2008). Direct evidence for fluid flow rates along faults is rare in the literature, and estimates for the flow rates usually rely on interpretation of geochemistry (Favara et al., 2001), exhumed paleofluid paths (Caine et al., 1996), or flow rate proxies such as temperature (Fairley, 2004).

The few studies that have been able to measure flow rates directly have emphasized an uneven spatial distribution of flow in fault zones. For example, in a well at Cajon Pass, California, although many fractures were qualitatively assessed as open to flow 80% of flow into the well was attributable to a single fracture (Barton et al., 1995). Localised flow along fault planes has been observed in the southern Taupo Volcanic Zone (TVZ) of New Zealand (Seebeck et al., 2014) where, although fluid flow was generally observed in, or near fault zones in low permeability rock, a single fault out of 720 contributes 30% of fluid flow. Although flow is mostly restricted to faults in low permeability rock, some parts of the faults are orders of magnitude more permeable than others. Fault and fracture permeability will be affected by connectivity and density, (Faulkner et al., 2010; Seebeck et al., 2014), fracture dilation (Sibson, 1996), and by transient changes in fluid pressures through time (Cox, 2005). The complexities of fracture mesh or fault zone architecture (Caine et al., 1996) cause large variations in permeability along the structure, which translates to channelized flow of fluids along segments of fault or fracture that have the highest permeability.

In this chapter the relationship between fracture permeability and the stress imposed on rocks within the main reservoir formation (Rotokawa Andesite) of the Rotokawa

Geothermal Field is assessed. To do this, the magnitude of the three principal stresses imposed on reservoir rocks for the Rotokawa Geothermal Field are quantified to determine which fracture orientations are mostly likely to experience slip. To then test the hypothesis that 'fault slip induced dilation is an important control on permeability and fluid flow', the shear/normal stress ratio imposed on fractures is considered (fracture slip/reactivation, Barton et al., 1995) observed on acoustic images acquired using borehole televiewer (BHTV) logs. Finally, fracture reactivation results from three wells within the Rotokawa Geothermal Field are compared to independent permeability measurements made of the Rotokawa Andesite. This shows that the permeability in the Rotokawa Andesite is relatively complex, with some locations suggesting that fractures prone to slip coincide with permeable zones, and other locations showing that slip on fracture has a negative effect on bulk permeability of the rock.

## 3 GEOLOGICAL SETTING

The Rotokawa Geothermal Field is located approximately 10 km northeast of Taupo, on the eastern edge of the central TVZ (Figure 1). The central TVZ comprises an active rift which formed 1 to 2 Ma in association with subduction of the Pacific plate (Wright, 1992; Wilson et al., 1995; Rowland and Sibson, 2001). This rift is coincident with a volcanic arc, which has produced in excess of 15,000 $km^3$ of volcanic material over the past 2 Ma, mostly through caldera forming eruptions (Wilson et al., 1995). The geology of the central TVZ is dominated by Quaternary volcanic and lake deposits (Manville and Wilson, 2004), emplaced on top of Mesozoic basement rocks, known as the Torlesse Terrane (poorly sorted sandstones with variably interbedded argillites; Leonard et al., 2010).

There are 23 geothermal fields across the TVZ. The hydrology of these fields is composed of large convecting cells of fluid whereby cold meteoric water circulates to depth and, once heated, rises buoyantly back to surface (Bibby et al., 1995; Bertrand et al., 2012). Zones of intense clay alteration tend to form through the interaction of the hot rising hydrothermal fluids with the surrounding rocks (Browne, 1978). These clay alteration zones are identifiable using resistivity and magneto-telluric surveys, as they are less resistive than the surrounding rocks (Hatherton et al., 1966; Bibby et al., 1995; Bertrand et al., 2012). The Rotokawa geological units can be broadly subdivided into two units: the basement rocks, and the Quaternary deposits. The tops of those units older than ~330 ka are consistently offset by faults that have little surface expression (Wallis et al., 2013).

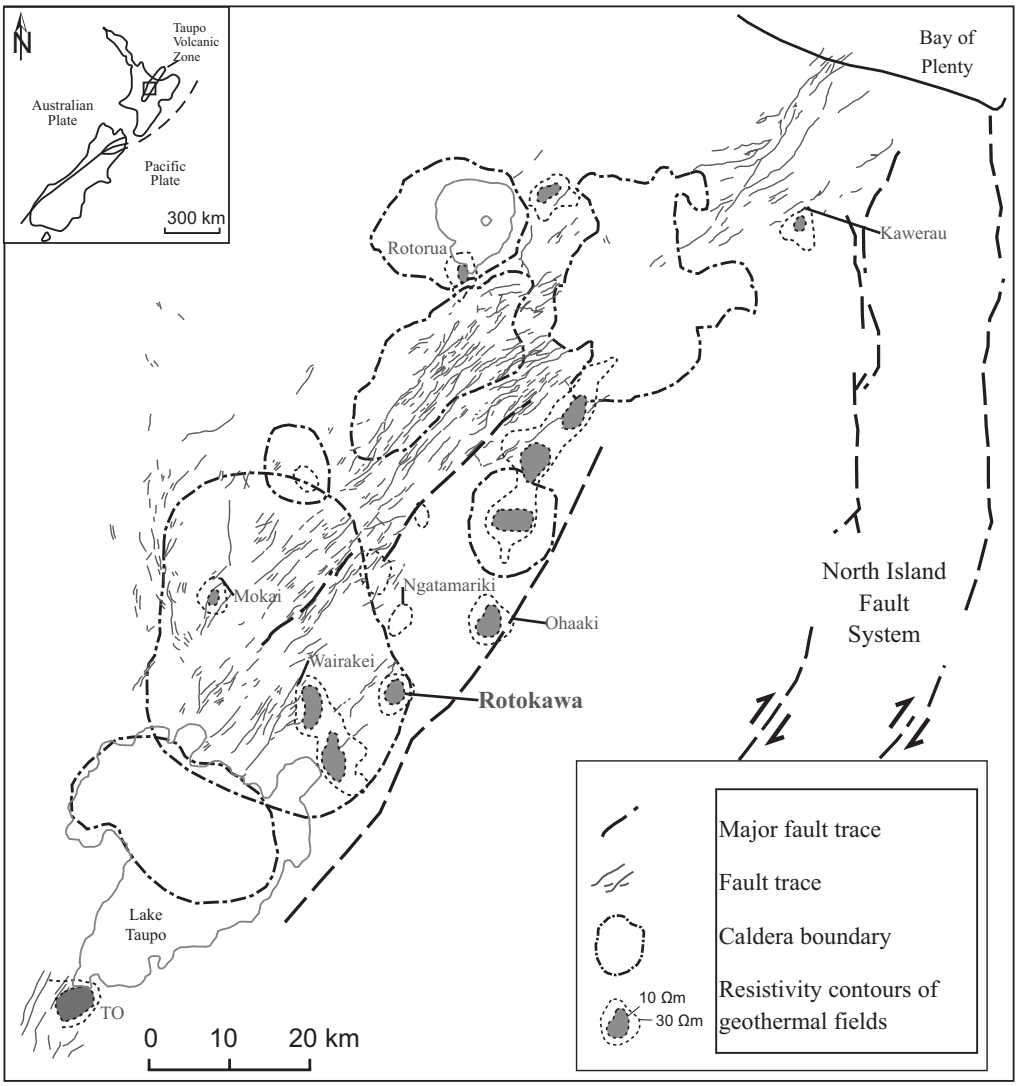


**Figure 1 Map of TVZ showing location of Rotokawa Geothermal Field and currently producing geothermal fields (modified from Bégué et al., 2014).**

The Rotokawa hydrothermal system has three distinct levels: a hot geothermal reservoir; an intermediate aquifer; and a shallow aquifer (Sewell et al., 2012). Each aquifer is separated by discontinuous, low-permeability layers, which are rich in hydrothermal, smectite clay. The intermediate aquifer is mainly constrained within two geological units (Rae, 2007; Sewell et al., 2012). The permeability of the deep reservoir rocks is thought to be strongly influenced by faulting and fracturing based on: 1) the relationship between temperature gradients and inferred structures at depth (Rae, 2007), 2) drawdown pressure gradients from production monitoring (Quinao et al., 2013), and

3) patterns of microseismic activity (Sewell et al., 2013). Estimating the magnitudes of the principal stresses may be critical to understanding the processes that govern fracture permeability in the Rotokawa reservoir (Barton et al., 1995; Rowland and Simmons, 2012), as fractures thought to be permeable have a restricted range of orientations with regards to the stress field orientation (McLean and McNamara, 2010; Wallis et al., 2012).

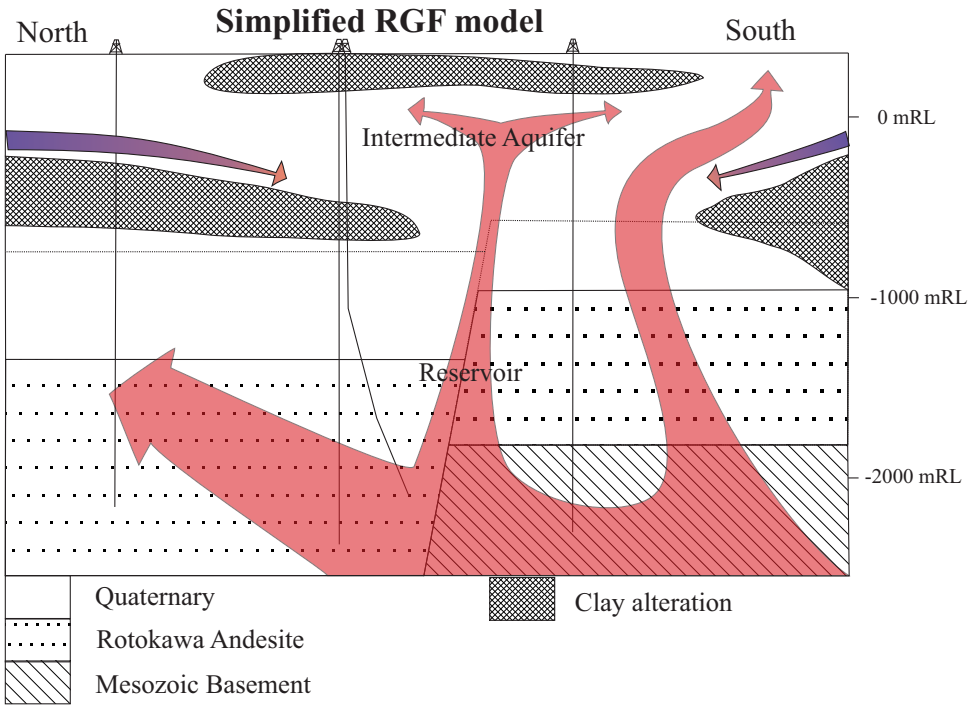


**Figure 2 Simplified cross section of the Rotokawa Geothermal Field, showing major geological boundaries, clay alteration and fluid flow** (modified from Winick et al., 2009; Sewell et al., 2012)**. The fault in the centre is the Central Field Fault; other inferred faults are not shown.**

The major geological unit of the deep Rotokawa reservoir is the Rotokawa Andesite, a flow banded porphyritic sequence of lavas and breccias. It is up to 2100 m thick, directly overlies the Mesozoic basement (Rae 2007), and is overlain by ignimbrite deposits dated at 1.8 Ma (Eastwood et al., 2013), making it one of the oldest andesites

in the central TVZ. The physical properties of the Rotokawa Andesite have been extensively studied, and therefore properties such as porosity, density, permeability and rock strength are well constrained (Pochee, 2010; Siratovich, 2014).

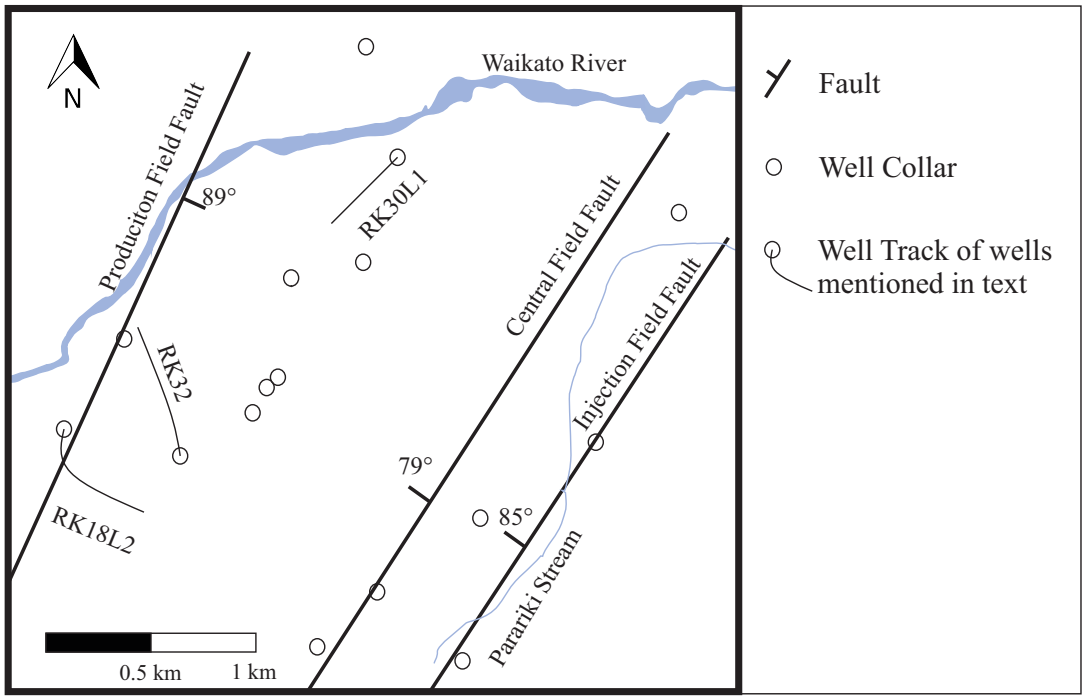


**Figure 3 Map of Rotokawa with main structures, location of well collars, and well tracks of wells mentioned in text. Map reproduced from Wallis (2013). Map oriented north.**

## 4 METHODS & DATA

The amount of shear and normal stress imposed on fractures is dependent on three factors: (1) the orientation of the fractures with respect to the orientation of the principal stress axes; (2) the relative magnitude of the principal stresses; and (3) pore pressure (Zoback et al., 2003). In every stressed rock body, there are three planes (principal planes), orthogonal to each other, where there are no shear stresses. The orientation of these three planes can be characterised by three vectors normal to the planes. These

vectors are called the principal stresses, with orientations orthogonal to each other, and magnitudes equal to the normal stress on the principal plane. The convention where $\sigma$ represents the stress axis (with orientation and magnitude), whereas S represents the magnitude of the normal stress only is follwed. $\sigma_1$, the maximum principal stress axis, $\sigma_2$, the intermediate principal stress axis, and $\sigma_3$, the least (or minimum) principal stress axis are ordered by the stress magnitude associated with the vector, such that $S_1 > S_2 > S_3$.

Anderson (1951) proposed that, since the surface of the earth is a free surface, one of the stress axes will coincide with the vertical, and therefore the other two will be horizontal. For this reason it is useful to use the terms vertical stress, maximum horizontal stress, and minimum horizontal stress in special cases. This allows the definition of the three main tectonic regimes (extensional, strike-slip, or compressional) by defining which of the three principal stress axes corresponds to the vertical. At the Rotokawa Geothermal Field the $\sigma_1$ is assumed to correspond to the vertical stress axis, as expected from an extensional regime. To constrain uncertainty on stress magnitudes at depth, the weight of the overburden rock is estimated, corresponding to the $S_1$. An attempt to constrain the $S_2$ is made using observed, stress induced, wellbore features (drilling induced tensile fractures (DITFs)). $S_3$ is measured using Leak-off Tests (see Chapter 3).

## 4.1 Vertical stress

The vertical stress is dependent on the weight of the overburden, as the surface of the Earth acts as a free surface that cannot sustain shear stress. The assumption that the vertical stress is dependent on the weight of the overburden is generally supported by

data from underground excavations (Brown and Hoek, 1978). The magnitude of the vertical stress can be defined by the following equation:

$$S_1 = \int_0^z \rho(z) g dz, \quad (1)$$

where $g$ (m/s$^2$) is the gravitational constant and $\rho$ (kg/m$^3$) is the density at depth $z$ (m).

The shallow rock units in the TVZ (<1.5 km) exhibit a wide range of densities (Stern, 1986). Different geological units however only have a small range of densities, even within a variably altered rock such as the Rotokawa Andesite (Pochee, 2010). Figure 4 depicts the density ranges for some of the geological units that occur within the Rotokawa Geothermal Field, measured from drill-core retrieved from Rotokawa Geothermal Field wells, as well as from nearby geothermal fields (Wairakei and Ngatamariki).

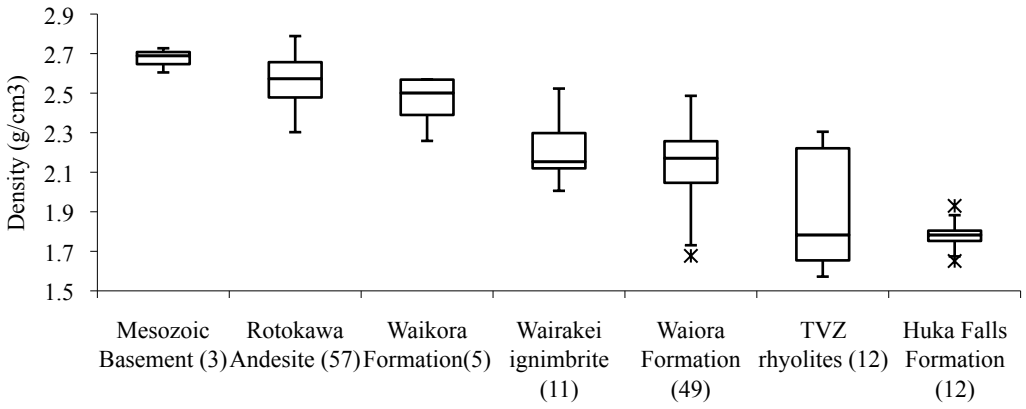


**Figure 4 Box plot of density measurements of drill-core. Geological units shown are known to occur at depth at the Rotokawa Geothermal Field (number of measurements in brackets). The TVZ rhyolite has been referred to as Haparangi Rhyolite in the past. Data from** Pochee, (2010), Siratovich et al., (2012), Mielke, (2009), and Whitford and Lumb, (1978**).**

To compute the vertical stress at Rotokawa the average saturated density of each geological unit is integrated with respect to the known thicknesses of each unit as derived from well data. Where density data was absent, values from a geologically similar lithology have been used to estimate the vertical stress.

## 4.2 Minimum Horizontal Stress

The magnitude of the minimum horizontal stress ($S_3$) was estimated from Leak-off Tests at several depths between the surface and -1176 mRL (depth relative to sea level). The results (in chapter 3) show that values of $S_3$ are consistent with the frictional properties of the rock. At the Rotokawa reservoir level, the frictional coefficient of the rocks is likely to be consistently ~0.6 due to the lack of smectite clays at depth, and therefore $S_3$ will increase as a function of $S_1$ with depth.

## 4.3 Maximum Horizontal Stress

The most common method for calculating the magnitude of the maximum horizontal stress uses the width of borehole breakouts observed on BHTV logs. Borehole breakouts occur when the compressive stress is greater than the borehole wall can withstand. This leads to curvilinear shearing from the borehole wall where the compressive stresses are highest and this spalling is observable on BHTV logs. However they are rarely observed in wellbore images of Rotokawa wells (McNamara et al., in prep), and therefore this method cannot be applied here.

A second method makes use of the presence of drilling induced tensile fractures (DITF) in the borehole (Moos and Zoback, 1990; Wiprut et al., 1997) and has been used in this

study to estimate $S_2$. Under certain stress conditions, the borehole wall rock will experience tension and DITFs are formed. The pressure and temperature conditions during drilling and the mechanical properties of the rock in which they form have a significant influence on the creation of DITFs. The presence of DITFs can be used to infer the stress conditions that led to their formation, which can help constrain $S_2$. DITFs are common in the walls of boreholes in the Rotokawa Geothermal Field (McNamara et al., in prep).Therefore, it is appropriate to investigate the stress conditions around the borehole in order to understand how DITFs formed. Here observed DITFs from BHTV logs are used to estimate the stress conditions required to create these structures, which can be modelled using the Kirsch equations (Zoback et al., 2003).

### 4.3.1 Review of Kirsch equations and their effect on wellbore wall

The Kirsch equations have been applied extensively to the problem of wellbore deformation in the literature, where they have been successful at describing the observed features such as DITFS and borehole breakouts (e.g. Wiprut et al., 1997). The Kirsch equations describe elastic stress modification caused by a circular void inside an infinite plane (in two dimensions), where a principal stress orientation coincides with the borehole orientation (such as vertical wells). In the Rotokawa Geothermal Field however, very few wells coincide with a principal stress direction, as most wells are deviated from vertical. The Kirsch equations are briefly reviewed here, however, the failure modeling is done using the more generalized forms (Peska and Zoback, 1995).

For the method used here, stress at a point in space is best-described using polar coordinates (r,θ), due to the shape of the void. The three main equations applied here are:

$$\sigma_{rr} = \frac{\sigma}{2}\left(1 - \frac{a^2}{r^2}\right) + \frac{\sigma}{2}\left(1 + 3\frac{a^4}{r^4} - 4\frac{a^2}{r^2}\right)\cos(2\theta) \quad (2)$$

$$\sigma_{\theta\theta} = \frac{\sigma}{2}\left(1 + \frac{a^2}{r^2}\right) - \frac{\sigma}{2}\left(1 + 3\frac{a^4}{r^4}\right)\cos(2\theta) \quad (3)$$

$$\tau_{r\theta} = -\frac{\sigma}{2}\left(1 - 3\frac{a^4}{r^4} + 2\frac{a^2}{r^2}\right)\sin(2\theta) \quad (4)$$

Where $\sigma$ is the differential stress, $a$ is the radius of the void, and $\theta$ is the angle measured from the direction of the smaller of the two stresses (Zoback et al., 2003). At the borehole wall (where $a=r$) $\sigma_{rr}$ (stress normal to the borehole wall) and $\tau_{r\theta}$ (shear stress) are both equal to zero. This is due to the fact that the borehole wall acts as a free surface, and cannot sustain any shear stress, or stress normal to the surface. The stress parallel to the borehole wall ($\sigma_{\theta\theta}$) however, does not reduce to zero. It varies symmetrically in magnitude according to its position around the borehole, with the maximum being at the position of the maximum far-field stress (at $\theta = \pi/2$, $\sigma_{\theta\theta} = 3\ \sigma$) and the minimum at the position of the minimum stress (at $\theta = 0$ , $\sigma_{\theta\theta} = -\ \sigma$).

If the stress imposed on the borehole wall leads to failure of the rock, the compressive features would form at the orientation of the maximum compressive stress (breakouts), and tensile features would form at the orientation of the minimum compressive stress (DITFs). Thus, since the maximum and minimum values of $\sigma_{\theta\theta}$ are a function of the

differential stress, then a large difference between stresses promotes drilling induced failure.

When using the generalised form of the Kirsch equations, deviation of the borehole from vertical, in a given stress field, must be taken into account (Peska and Zoback, 1995). In order to define the stress at the borehole wall in a deviated well, the orientation of the borehole, the orientation and magnitude of the far field stress field, the Poisson's ratio of the rock, and the pore pressure of the fluid in the rock need to be known.

### 4.3.2 Effect of mud weight on borehole failure

The density of the fluid used during drilling can vary significantly, and therefore can cause a notable difference in pressure between the formation and the borehole itself. An increase in the borehole pressure causes a reduction of the overall stress at the borehole wall. This could lead to the formation of tensile fractures (Zoback et al., 2003). The density of the fluid used at Rotokawa is constantly recorded during drilling and was usually kept between 1.00 and 1.06 g/cm$^3$. The formation pressure has a lower gradient (see Chapter 5), which can result in overpressures up to 5 MPa at depth. However, in practice these overpressures rarely exceed 1.2 MPa at depths shallower than ~1100 mRL.

### 4.3.3 Effect of temperature on borehole failure

The temperature of the drilling fluid can also have an effect on borehole failure. Cooling of the borehole causes a reduction in the compressive stress at the borehole wall due to contraction. This increases the likelihood of tensile failure. The drilling fluid temperature records are used, as well as an estimated maximum and minimum rock temperature to estimate the stress induced by cooling the wellbore at the wellbore face, and estimate the stress induced by cooling of drilling fluids using the model by Stephens and Voight (1982):

$$\sigma_{\theta\theta} = \frac{\alpha_t E \Delta T}{1 - \nu} \tag{5}$$

Where $\alpha_t$ is the coefficient of thermal expansion, $E$ is Youngs modulus, $\Delta T$ is the change in temperature, and $\nu$ is Poissons ratio. The effect of cooling during drilling is taken into account using equation (5) when modelling the stress condition causing DITFs.

## 4.4 Well data

### 4.4.1 Borehole televiewer data

BHTV logs are acquired using the AFIT (Acoustic Formation Imaging Technology tool), a high temperature BHTV tool. The AFIT tool records the travel time and amplitude attenuation of a returning sonic pulse from the geothermal borehole wall. This information is collated and processed allowing the observation of both natural

geological and induced features at the borehole wall surface, making it possible to obtain data relating to the orientation of features exposed in the rock at the borehole wall (Massiot et al., 2012). The interpretation and analysis of acoustic images from three wells in the Rotokawa Geothermal Field (RK18L2, RK30L1, and RK32, see Figure 3) reveals a wealth of low-amplitude and several high-amplitude planar surfaces intersecting the wellbore. These are described as discordant within the host rock and interpreted as fractures, both open and sealed (veins) (McNamara et al., in prep).

It is important to note that several processes, including image quality, and the borehole sampling, will affect the final dataset. The fact that the fracture orientation data is collected along the wellbore wall means that there is a sampling bias (Massiot et al., submitted; Terzaghi, 1965). This bias can be statistically corrected in order to gain a more accurate picture of the density of fracture orientation populations for a given well. In this chapter visible fractures are related to identified flow within wells, which requires direct observation and so an orientation bias correction is not necessary.

Variability in the acoustic image quality has been identified and assumed to be the result of poor well conditions, where an irregular wellbore can partially obscure wellbore images, make feature identification difficult and affecting confidence in the interpretation (Massiot et al., submitted). A major part of logs from wells RK18L2 and RK30L1 are considered to have poor quality imaging. Well RK32 has the highest quality imaging, with just over half the well is considered to have moderate quality image quality, or better.

**Table 1 AFIT imaging quality. Quality estimates are from** (McNamara et al., in prep)

| Well | Poor image quality (<50% image interpretable) | Moderate image quality (<75% image interpretable) | Good image quality (>75% image interpretable) |
|---|---|---|---|
| RK18L2 | 66% | 34% | 0% |
| RK30L1 | 72% | 28% | 0% |
| RK32 | 49% | 36% | 15% |

### 4.4.2 Feed zones and performance tests from RK18L2, RK30L1 and RK32

The permeability of the three imaged wells is characterised by discrete feed zones providing the majority of the flow into the wellbore. The feed zones were located based on temperature, pressure and fluid velocity logs, often refined to 10 m intervals (I. Wallis pers. Comms., 2014), and are separated into major/minor feed zones. Table 2 marks the feedzone intervals that are located in the Rotokawa Andesite. There are feed zones identified in other formations that provide a minor flow contribution.

**Table 2 Feed zone data in the Rotokawa Andesite**

| Well | Depth from(mRF) | Depth to (mRF) | Feed Type |
|---|---|---|---|
| RK18L2 | 1831 | 2019 | Major |
| RK30L1 | 2145 | 2155 | Minor |
| RK30L1 | 2165 | 2175 | Minor |
| RK32 | 1833 | 1843 | Major |
| RK32 | 2109 | 2119 | Major |
| RK32 | 2608 | 2618 | Minor |

Permeability can also be measured by assessing the overall well performance data. The Productivity Index (PI, tonnes/hr/bar of wellhead pressure) is the most wide ranging measure of performance for production wells; however, since RK30 has multiple legs coming off a common wellhead (RK30L1 and RK30L2), it is not possible to use the PI for comparative purposes, as both well legs contribute to the available PI value (Wallis pers. comm., 2014). However, injection testing was done when only the RK30L1 leg was complete and therefore the Injectivity Index (II) data is a better measure for comparing the three wells, as data is available for each particular leg (Table 3). Both the II and PI are defined by the following equation (Grant and Bixley, 2011):

$$II \text{ or } PI = \frac{W}{(P_f - P_w)} \tag{6}$$

with $W$ being the flow rate, $P_f$ the flowing pressure and $P_w$ the well pressure. During injection, the cold water pressure gradient favours injection in deeper feed zones, which is one reason why the PI and II do not correlate perfectly (Grant and Bixley, 2011). However, the II can be used as an indication of well potential.

**Table 3 Injectivity Index for the three imaged wells. (Wallis, pers. comms. 2014)**

| Well | Injectivity Index (t/hr/bar) |
|---|---|
| RK18L2 | 13.5-17.1(average 15.5) |
| RK30L1 | 9 |
| RK32 | 11-13 |

# 5 RESULTS

## 5.1 Vertical stress

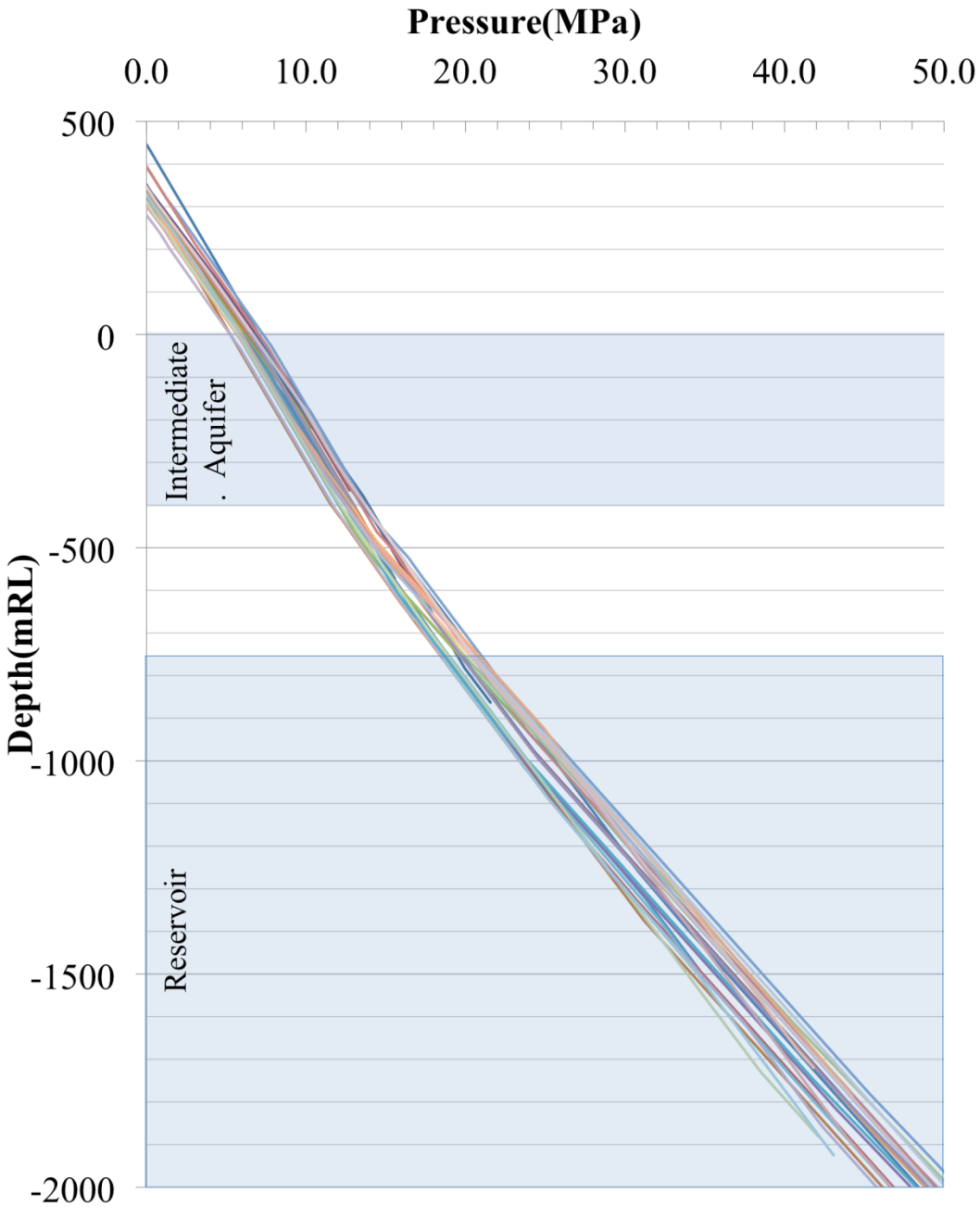


**Figure 5 Vertical stress model for all wells in the Rotokawa Geothermal Field. Each colour represents a different well.**

Calculations of the vertical stress profiles for each well shows that the effect of varying thicknesses of geological units has an impact on its magnitude that is as significant as

topographic impact (Figure 5). This is illustrated by the stress profile of the well drilled from the highest elevation (highest RL). If the stress increased at a constant rate, the well drilled from the highest elevation would have the highest vertical stress at depth. However, that well has a modeled vertical stress profile several MPa lower than other wells drilled from a lower elevation. The lower stress is caused by a variation in rock density across the field. In general, the difference between the highest and lowest vertical stress modeled at sea level is 2.4 MPa, where most of the divergence between wells would be caused by topography. The difference in vertical stress between wells, at -1500 mRL, is 5.1 MPa. These observations suggest that thick, low-density formations may have a significant effect on the vertical stress at depth.

There are several shortcomings associated with the application of rock densities and thicknesses to a vertical stress model. Fractures, brecciated rock, and voids would cause the overall density of the lithologies to be lower than that measured from discrete rock laboratory testing (Figure 5). This means that the results may overestimate the vertical stress. Also, although most units have a near normal distribution of density measurements (Figure 4), the TVZ rhyolites do not. The density data this rock type has a bimodal distribution. This is likely to be inherent in rhyolite dome lavas due to their heterogeneous nature from the obsidian-rich, coherent regions of the dome to the more pumiceous, brecciated carapaces (Rissmann et al., 2011; Ashwell, 2013). Using the mean density to represent these rhyolites in vertical stress calculations might not reflect the true stress magnitude.

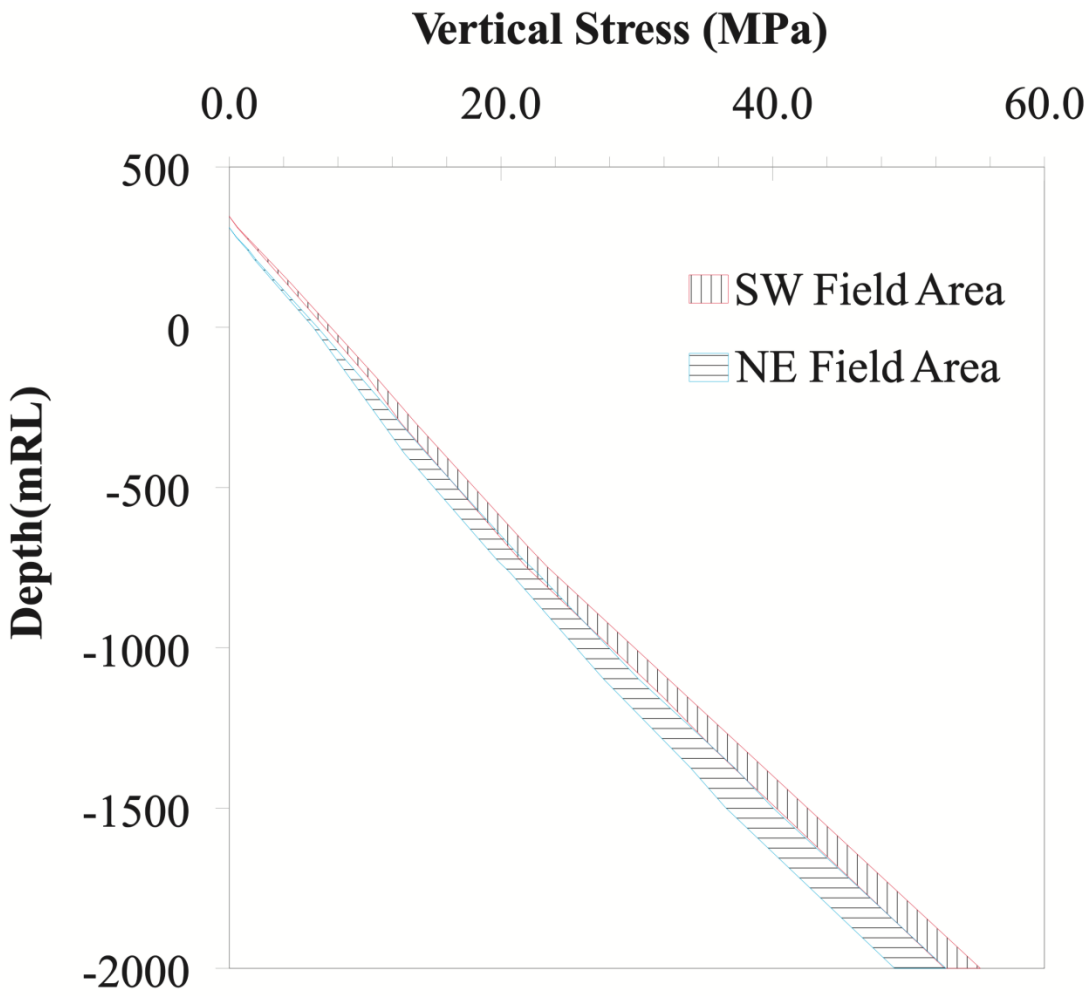


**Figure 6 Graph shows the variability in the vertical stress with depth, for the NE and SW quadrants of the Rotokawa Geothermal Field. The range in magnitude for each quadrant represents error in the vertical stress estimate. The range is defined by the average value of density, ±1.96 times the standard error of the average.**

Figure 6 depicts the vertical stress as a function of depth for two wells with similar wellhead elevations, but sited in different sectors of the field (NE and SW). Each well penetrates a significantly different stratigraphy. As described in Section 2.1, density data is limited and calculations may not represent the true vertical stress magnitude. In order to convey this uncertainty, a range of "realistic" vertical stress profiles is computed for each well. These are derived from the 95% confidence limits on the mean formation densities (Figure 4) and assume that the populations are normally distributed. There is some overlap in the range of vertical stress for the two wells due to the

uncertainty in formation densities. However, results suggest that for a given depth, the difference in the vertical stress between the well in the NE and the well in the SW field area is up to ~6 MPa at a depth of -2000 mRL, a difference which in the extreme could be entirely attributable to differential loading (Figure 6). The depth to the 20 MPa vertical stress isosurface is used to illustrate the variabililty of the vertical stress in the Rotokawa Geothermal Field (Figure 7).

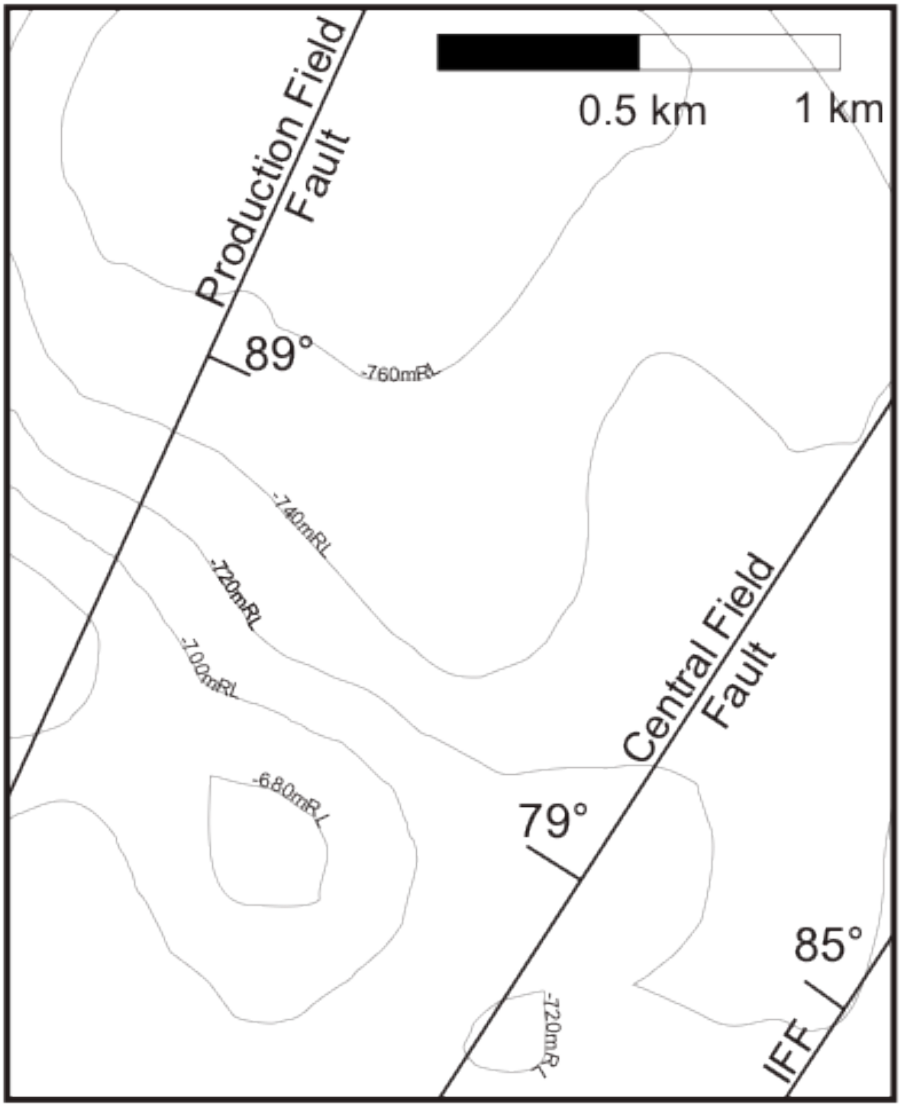


**Figure 7 Map of contours of the 20 MPa isosurface, showing the depth where the vertical stress equals 20MPa.**

## 5.2 Maximum Horizontal stress

Due to the prevalence of DITFs in the borehole, modelling the stress conditions required to create tensile failure and DITFs orientations estimated from acoustic images can help constrain the maximum horizontal stress (see Figure 8). The DITF model was run in Matlab using the method by Peska & Zoback (1995) (see Appendix D). The coloured lines in Figure 8 show the stress conditions required for the borehole wall to go into tension at a depth of -1500 mRL, for a range of temperature differentials and tensile strength of rock. The dashed black lines constrain the range of likely stress magnitudes at the modelled depth, assuming the stress is in frictional equilibrium, using a coefficient of friction between 0.6 and 1.0. The parameters used in Figure 8 are summarized in Table 4. The range of temperature changes, $\Delta T$, is derived from the expected differences between the temperature of the formation rocks and the temperature of the drilling mud. Values for $E$, $\nu$, and tensile strengths used in Table 4 are sourced from Siratovich et al. (2012).

**Table 4 Summary of parameters used in Figure 8**

| | |
|---|---|
| Vertical stress | 35.9 MPa |
| Pore pressure | 16.14 MPa |
| Well Azimuth | 355º |
| Well Deviation | 22.5º |
| Drilling mud temperature | 70º C |
| Maximum formation T | 350º C |
| Minimum formation T | 170º C |
| Range of $\Delta T$ | 100º - 290º |
| Coeff. of thermal exp. | $5.00 \times 10^{-6}\ K^{-1}$ |
| Youngs modulus | 29.5 GPa |
| Poissons ratio | 0.21 |
| Range in tensile strength | 15.3 MPa - 24.2 |

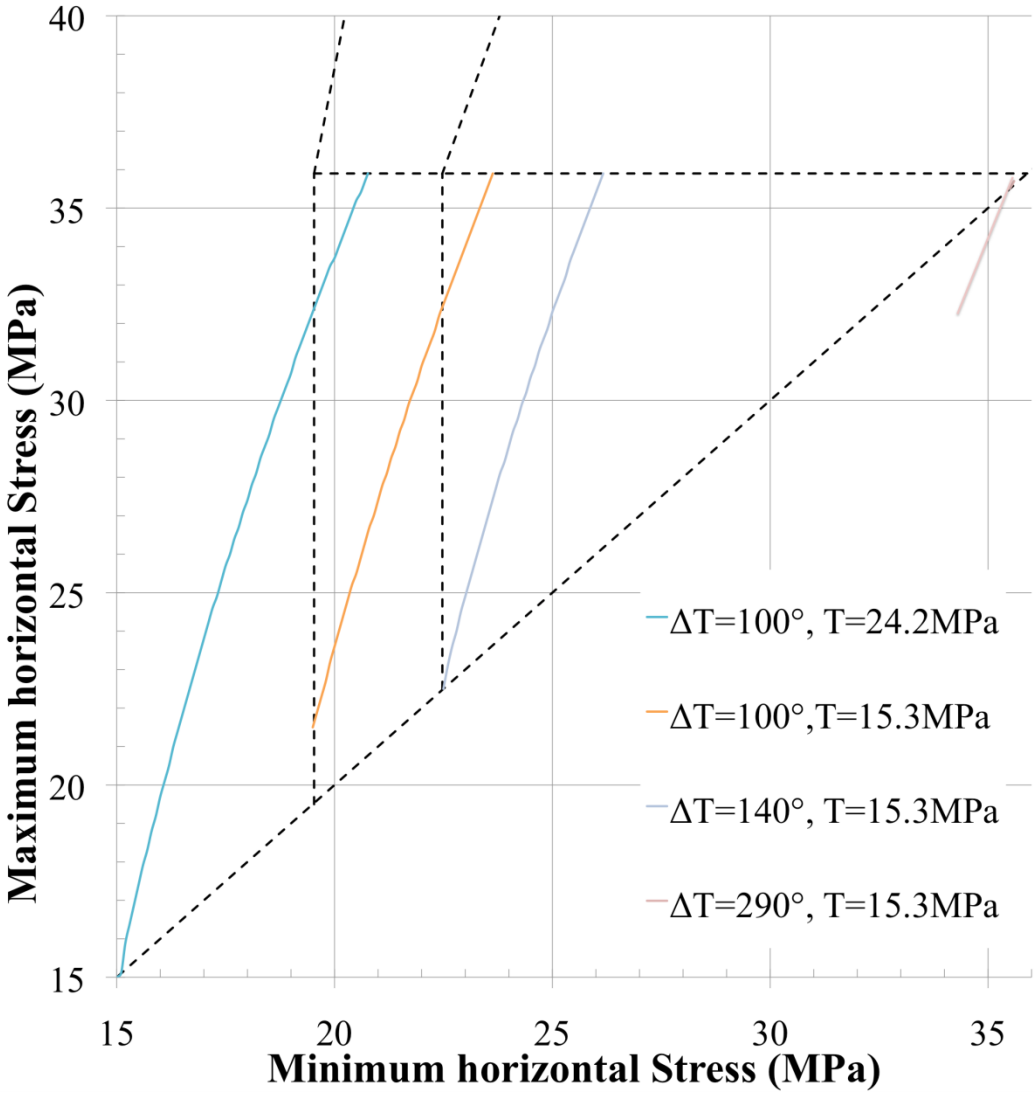


**Figure 8 Maximum horizontal stress vs. minimum horizontal stress at a given depth where DITFs are known to occur. The coloured lines are the stress conditions required for the wellbore to go into tension as predicted by the Peska & Zoback method, for various cooling temperatures (ΔT) and tensile strength (T).**

The DITF model shows that cooling of the formation rock by drilling fluids is a major factor in creating DITFs, as a change in temperature greatly decreases the stress required to induce failure (Figure 8). Another important factor influencing the formation of DITFs is the tensile strength of the rock. The variability in the tensile strength of the Rotokawa Andesite formation is large enough (Siratovich et al., 2012) to influence whether or not DTIFs will form. The modeling indicates that there are not enough constraints on the degree of cooling, or on the mechanical properties of the rock, to

estimate the magnitude of the maximum horizontal stress (Figure 8). However, for an extensional setting, it is reasonable to assume that the magnitude of the maximum horizontal stress must be between the magnitude of the minimum horizontal stress and the vertical stress (Anderson, 1951).

# 6 DISCUSSION

## 6.1 Shear and normal stress imposed on fractures

As discussed previously, repeated slip on fractures is likely to keep fractures open to fluid flow. The magnitudes for vertical stress (Section 4.1) and minimum horizontal stress (derived in Chapter 3) are used to estimate the normal and shear stresses that could act on fractures, as the highest ratio is the most likely to experience slip. The Mohr circles in Figure 9 show the shear and normal stresses for all fracture orientations containing $\sigma_2$, as fractures in this orientation experience the largest shear stress. Two Mohr circles are drawn, using the lowest and highest estimate of vertical stress, and the minimum horizontal stress at a depth where $S_3$ was confidently interpreted (Figure 6, also see Chapter 3). The Mohr circle plots in Figure 9 illustrate the uncertainty associated with the stress modelling, as well as the effect of variation in vertical stress caused by differential loading, on normal and shear stresses. The area that plots above the 0.6 shear/normal ratio represents the strike orientations of fractures likely to experience slip (Barton et al., 1995). A significant portion of fracture orientations plot above the 0.6 ratio, showing that some fracture orientations are prone to slip. A larger vertical stress results in a wider range of fracture orientations above the 0.6 ratio.

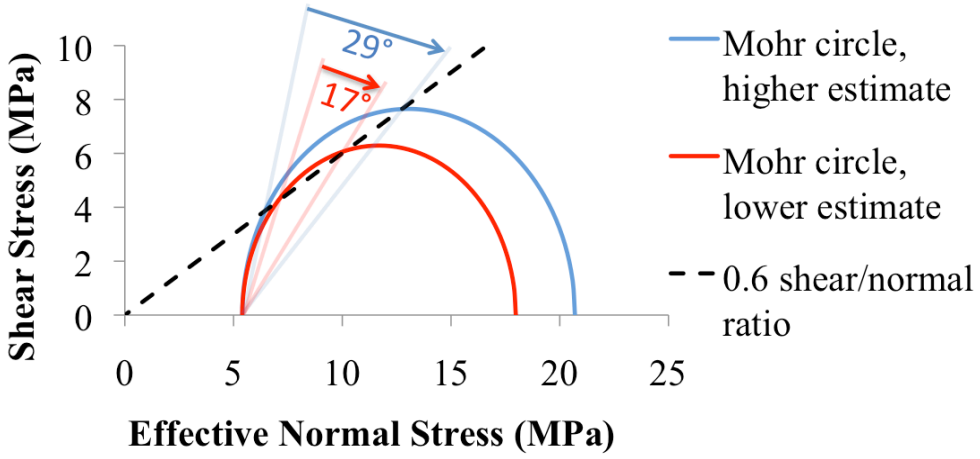


**Figure 9 Mohr Circle for stress estimation in the Rotokawa Andesite at -1176 mRL. The range of fractures with shear/normal stress above 0.6 is shown for both the lower (red Mohr circle) and higher (blue Mohr circle) estimate of vertical stress. A decrease in the vertical stress reduced the range of fracture orientations likely to experience slip from 29º to 17º.**

## 6.2 Effect of the maximum horizontal stress on the orientation of fractures prone to slip

As $S_2$ was not constrained through modelling methods, in this section the effect of a variable $S_2$ on shear/normal stress is shown by allowing it to take any value between $S_1$ and $S_3$. The effect of $S_2$ is significant, even when using fixed values of $S_1$ and $S_3$, on the orientation of fracture plane poles that have a shear to normal stress ratio higher than 0.6 (i.e., are likely to experience slip) (Figure 10).

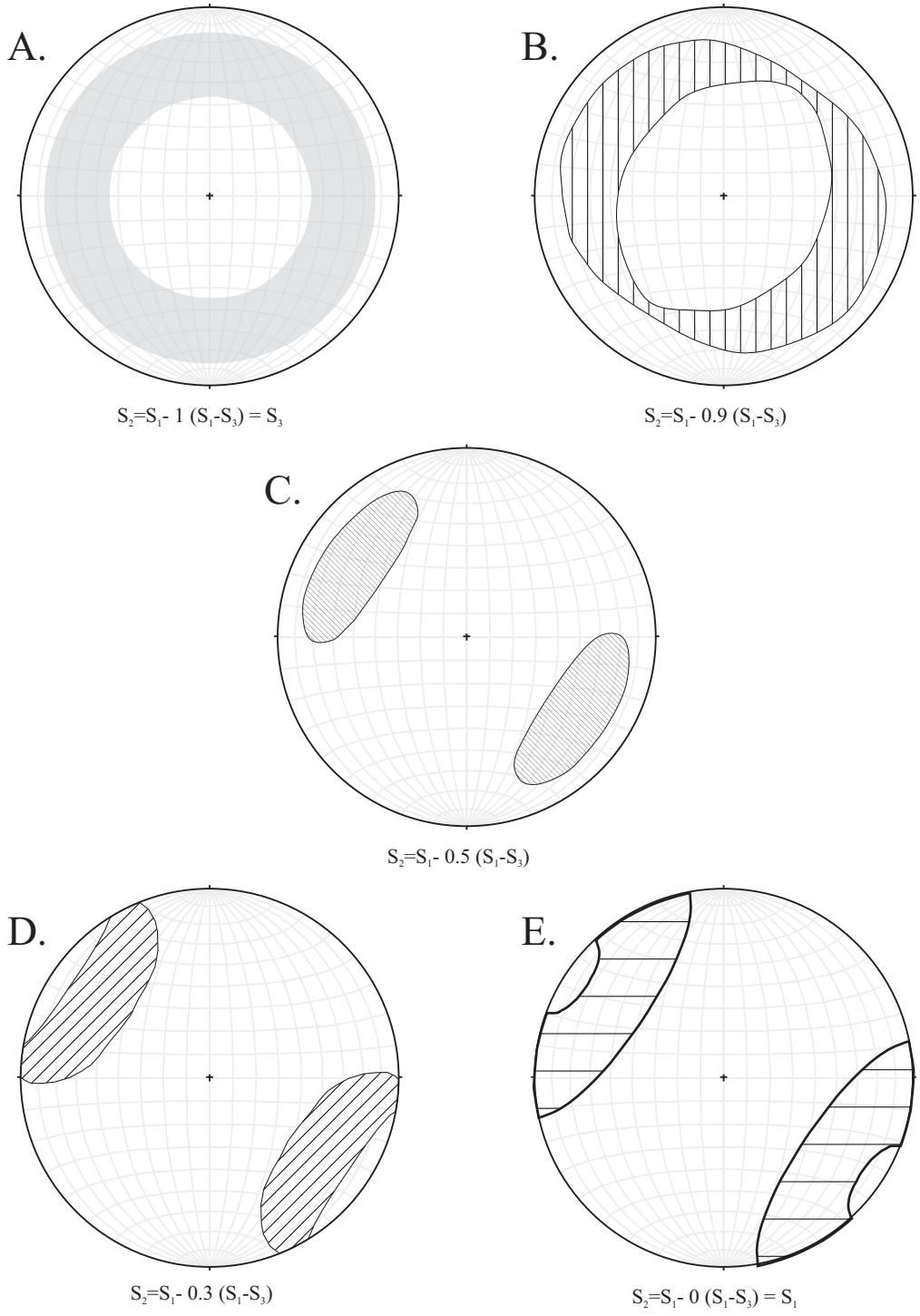


**Figure 10 Equal-area lower hemisphere stereonets (Allmendinger et al., 2012) with shaded regions representing poles of fractures with a shear/normal stress ratio above 0.6, for stress conditions similar to those at -1176 mRL, but with variable maximum horizontal stress. The trend of the minimum horizontal stress ~130°.**

For example, where $S_2$=$S_3$ (Figure 10a), the fracture strike orientations that are likely to experience re-shear is unconstrained. In this situation there is no relationship between strike of faults/fractures and slip; only the dip of fractures is constrained. The strike of fracture reactivation is the most constrained when $S_2$ takes a value halfway between $S_1$ and $S_3$ (Figure 10c). As the value of $S_2$ approaches that of $S_1$, the orientation of fractures prone to slip can be defined solely by the angle between the fracture and $\sigma_3$ (Figure 10e). The stereonets in Figure 10 show that the relative magnitude of principal stress has a large influence on the orientation of fractures prone to slip. Therefore, it is important to note that without information on the relative magnitude of stresses, it can be misleading to only use the strike of fractures as a means of assessing fracture slip (McLean and McNamara, 2010; Seebeck et al., 2014).

### 6.3 Fracture characterisation in the Rotokawa Andesite

The effect of stress-controlled permeability is evaluated by estimating the shear and normal stress on fractures observed using a borehole televiewer tool in three wells in the Rotokawa Geothermal Field. The three imaged wells (RK18L2, RK30L1 and RK32) are all located on the NW production side of the geothermal field (Figure 3). Fractures imaged in the Rotokawa Andesite (the reservoir formation and a geological unit common to all three wells) is the only geological unit considered, in order to avoid factors related to variable lithology.

In order to assess which fracture orientations are prone to slip, and which are not, the magnitude of $S_2$ is required (Figure 10). Seismic inversion studies of microseismicity in the Rotokawa Geothermal Field show that the most likely value for $S_2$ is halfway

between $S_3$ and $S_1$ (Rawling et al., 2001). This is consistent with most faults in the TVZ that are oriented NE-SW and show little strike-slip (Seebeck, 2012). Without any additional data, the most likely value of $S_2$ as determined by seismic inversion, halfway between $S_3$ and $S_1$, is assumed to be correct (Figure 10c) and used fracture orientation to distinguish fractures that are likely and unlikely to slip (Barton et al., 1995) Since the BHTV data allows the imaging fracture aperture, the fracture population of the Rotokawa andesite from the three wells is separated into three groups: 1) all the fractures imaged 2) all fractures that have a shear/normal ratio greater than 0.6 (using a stress ratio $\nu$=0.5), and 3) the fracture from group 2 that were opened greater than 12 mm. The frequency of these fractures is plotted at the depth at which they were measured, along with the depths of permeable feed zones (Figure 11 to Figure 13; refer to Table 2 for specific feed zone depths).

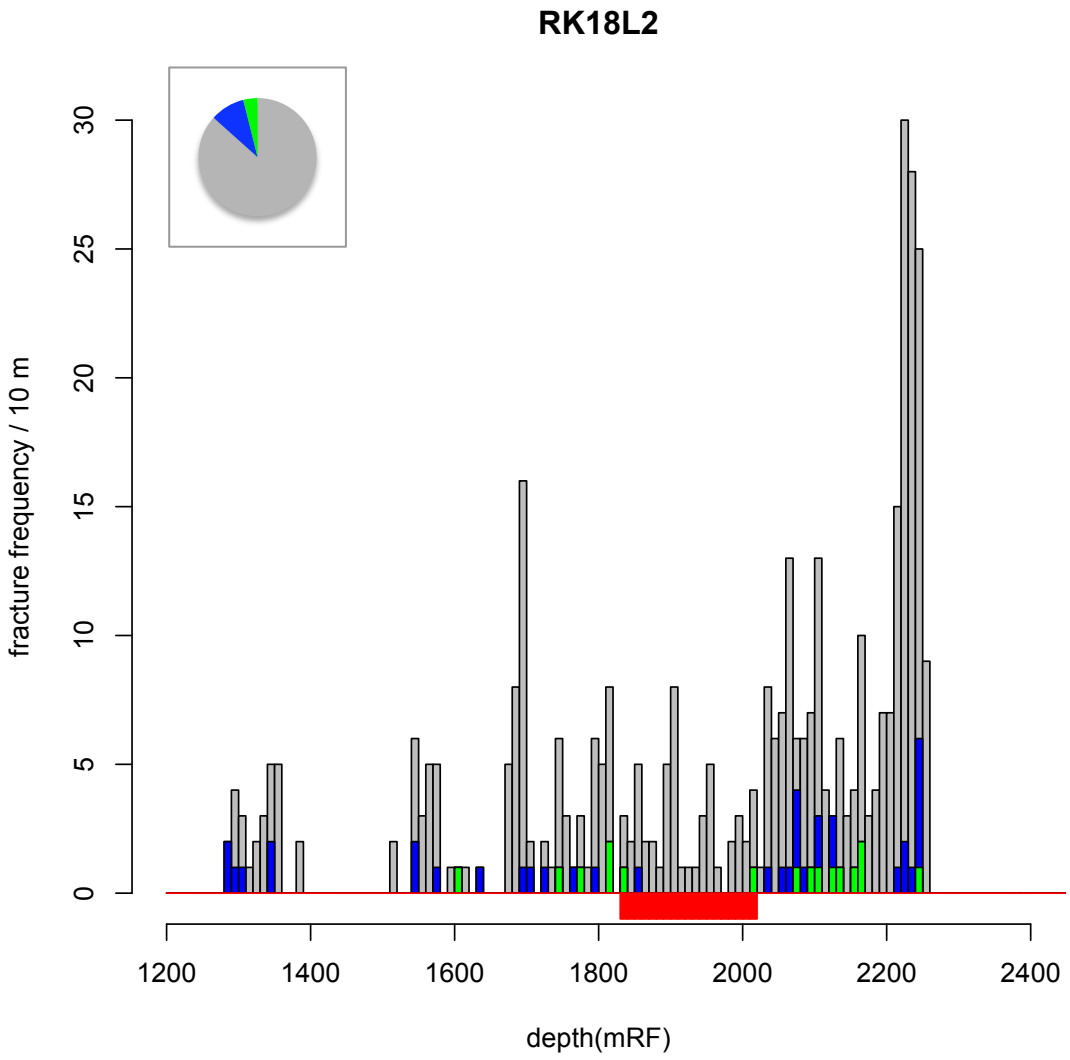


**Figure 11 Histogram of fracture frequency/10 m, compared to depth in well RK18L2. The zone in red is the depth at which fluid feeder zones have been identified in the well. The grey color represents all fracture orientation at the specified depth. The blue bars show the number of fractures with a shear/normal stress ratio above 0.6. The green bars are the subset of the fractures in blue, that have an imaged aperture greater then 12 mm. Pie chart shows relative frequency of each fracture population.**

The Rotokawa Andesite in the well RK18L2 has a relatively low incidence for fractures with orientations prone to slip (13%, Figure 11). Well RK18L2 also has a skewed distribution of fractures, with fractures occurring at a very high frequency below 2200 mRF (i.e. >75 fractures over a 30 m interval). There are no exceptional zones with a high concentration of fractures prone to slip in this well (Figure 11), with only three fractures prone to slip within the interval. In fact, the feed zone identified in the well

seems to coincide with a notable lack of fractures with orientations prone to slip, compared to the rest of the borehole. This latter observation is not likely to be due to image quality, as the frequency of all fracture orientations does not drop through the interval of the feed zone. The negative correlation between the feed zone and fractures with a shear/normal stress ratio > 0.6 suggests that in this case it is not possible to estimate the location of the high-flowing section of the well by estimating the stress imposed on fractures. In fact, Figure 11 suggests that slip might have a negative effect on permeability. In addition, it seems that the density of wide aperture (>12 mm) open fractures (as inferred from the acoustic logs) do not permit prediction of the feed zone location.

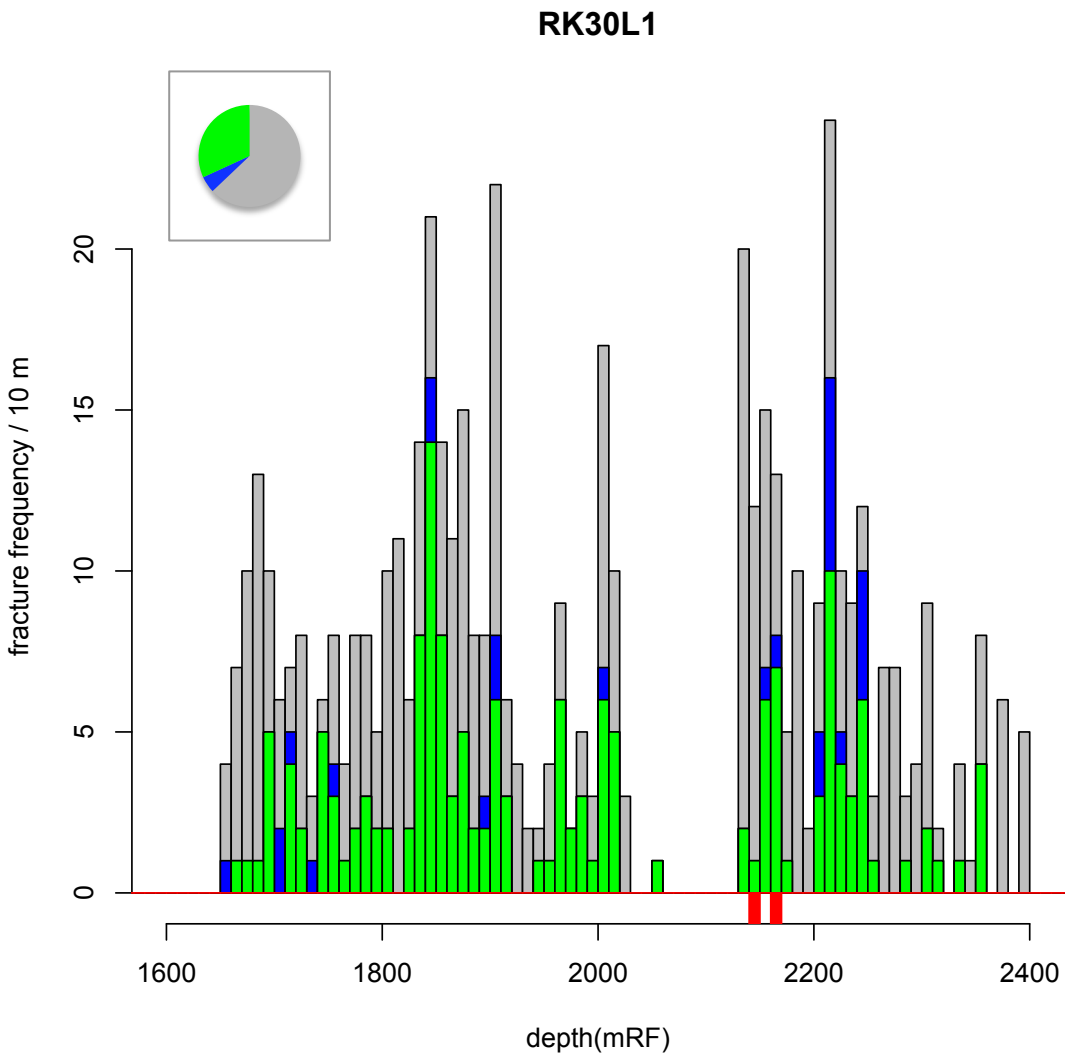


**Figure 12 Histogram of fracture frequency/10 m, compared to depth in well RK30L1. The zones in red are the depth at which fluid feeder zones have been identified in the well. The grey color bars represent all fractures over a specified 10 m depth range. The blue bars represent the number of fractures with a shear/normal stress ratio above 0.6. The green bars are the subset of blue-bar fractures, that have an imaged aperture greater then 12 mm. Pie chart shows relative frequency of each fracture population.**

A large number of fractures in well RK30L1 have orientations prone to slip (37%) most of which (~86%) are imaged as being open >12 mm (Figure 12). The intervals 1830-1910 mRF, and 2200-2250 mRF, have a relatively larger incidence of fractures prone to slip. Two minor feed zones were identified in the Rotokawa andesite and are relatively close to each other, one at 2145-2155 mRF, and one at 2165-2174 mRF. The lower feed zone corresponds to a slight increased occurrence of fractures prone to slip and the

higher one has one fracture oriented prone to slip within the interval. The poor correlation between the feed zone and fractures with a normal/shear stress ratio > 0.6 suggests that again it is not possible to estimate the location of the higher-flowing section of the well by using the stress imposed on fractures. In addition, the densities of wide aperture (> 12 mm) open fractures (as inferred from the acoustic logs) do not permit prediction of the feed zone location.

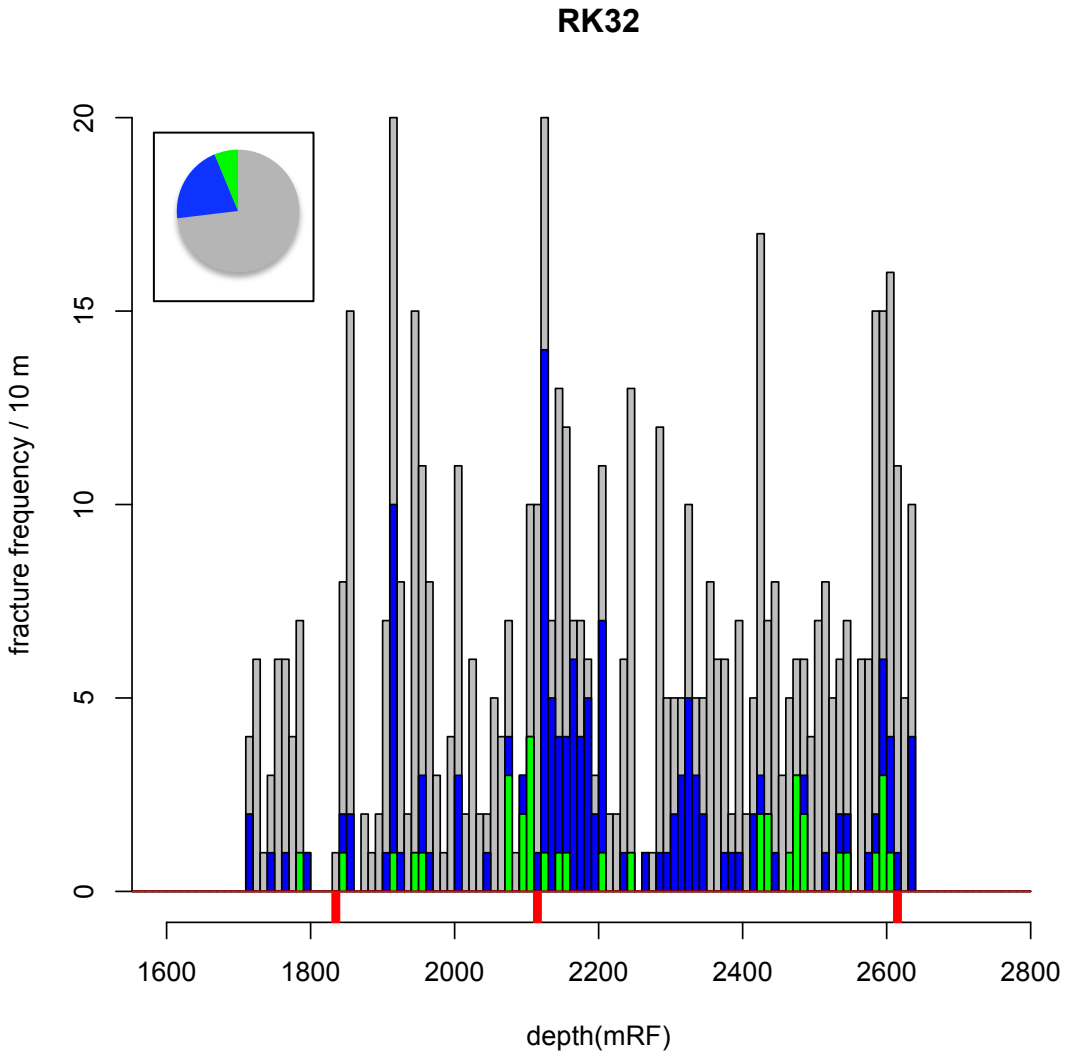


**Figure 13 Histogram of fracture frequency/10 m for depth in well RK32. The zone in red is the depth at which fluid feeder zones have been identified in the well. The grey color bars represent all fractures within a specified 10 m depth range. The blue bars represent the number of fractures with a shear/normal stress ratio > 0.6. The green bars show a subset of the blue bar, that have an imaged aperture > 12 mm. Pie chart shows relative frequency of each fracture population.**

Of all fractures imaged in RK32, 27% are oriented prone to slip, 6% of which are open more than 12mm (Figure 13). There are 3 main zones in RK32 that have a significant population of fractures prone to slip: 1) from 1910-1920 mRF; 2) a relatively large zone from 2070-2210mRF, with a peak population at 2120-2130 mRF, and a high frequency of open fractures from 2070-2110 mRF, and 3) from 2580-2610 mRF. The two latter zones are associated with feed zones - a major one at 2109-2119 mRF, and a minor one at 2608-2618 mRF. The major feed zone at 1833-1843 mRF does not appear to be related to any extraordinary fracture patterns, however few fractures have been identified in this interval, which may be due to poor image quality. The major feed zone at 2109-2119 mRF occurs just after the highest incidence of open fractures prone to slip (2100-2010 mRF), and just before the highest incidence of all fractures prone to slip (2120-2130 mRF). The minor feed zone at 2608-2618 mRF occurs just after an interval that has a high frequency of both open and overall fracture prone to slip (2590-2600 mRF). It is possible that the flow identified at these depths could be associated with the high frequency zones, as discrepancies are common between different types of logs (in this case the BHTV log and the logs defining the feed zones).

## 6.4 Permeability of the Rotokawa Andesite

Well RK32 has two zones with a large number of fractures oriented prone to slip that are associated with the feeder zones, however, many of those same fractures are also located outside the feed zones (Figure 13). Although RK30L1 does have fractures prone to slip imaged in the intervals associated with flow, these do not match up with the frequency of fractures prone to slip (Figure 12). Most of RK18L2 has fractures oriented prone to slip imaged throughout, but the interval associated with flow, on the other

hand, has a clear lack of slip-prone fractures (Figure 11). In one well zones of high fluid flow into the wellbore are associated with a high incidence of fractures prone to slip, but in another well, the flow into the well occurs where there is a lack of fractures prone to slip. This mixed result suggests that slip on fractures can be an important process that increases bulk permeability of rock (e.g.: RK32), but that it is not always the case.

The general lack of a correlation between the shear/normal stress ratio and fluid flow could be attributed to the tool resolution. It is possible that the imaged 'open' fractures are poorly connected to the fracture network, and the flow associated with the fracture is too small to be identified by wellbore logs. Due to the high temperature of fluid, dynamic pressure gradients and the existence of cross flows in geothermal wells (Grant and Bixley, 2011), only the permeable zones with the highest flow associated with them would be identified with the downhole logs. It is also possible that the fractures imaged are filled with material that has a different acoustic signal, which would be picked up by the BHTV as an 'open' fracture (McNamara et al., submitted).

Most of the feed zones listed in Table 2 are restricted to a 10 m interval. The relatively focussed intervals are consistent with fracture permeability. However, the feed zone identified in RK18L2 is relatively wide. Although this might be a resolution issue with the tool used to identify the feed zone, it could also signify that a different underlying process is generating permeability. The fact that there is a notable lack of fractures prone to slip also indicates that a different underlying process is a possibility; it might suggest that slip has a negative effect on permeability.

As mentioned in the introduction, faults do not always increase permeability in all rock types. In the case of high porosity sandstones, faults tend to decrease the permeability of the rock (Antonellini and Aydin, 1994), as the deformation associated with faulting tends to destroy the porosity and permeability. This type of effect would not be expected in a dense, low porosity andesite such as the one found at Rotokawa, yet the data from well RK18L2 suggests that there is a negative correlation between fracture prone to slip and permeability.

A detailed study of the effect of alteration on the mechanical properties of the Rotokawa Andesite was done by Adam Pochee in 2010. He used core samples of only this rock type, from wells across the field and paying attention to avoid fractures, and estimated the degree of alteration based on the chemistry of low-mobility elements. He showed that the Rotokawa andesite is a low porosity rock when unaltered, but when it is highly altered, the porosity is increased (Figure 14). For example, the highest porosity measured in Rotokawa Andesite that has a low Alteration Index (AI<50) is 5.14 vol% (Figure 14), however, the porosity can be up to 18.81 vol% when altered; i.e. porosity values that are more common to sandstones than andesites.

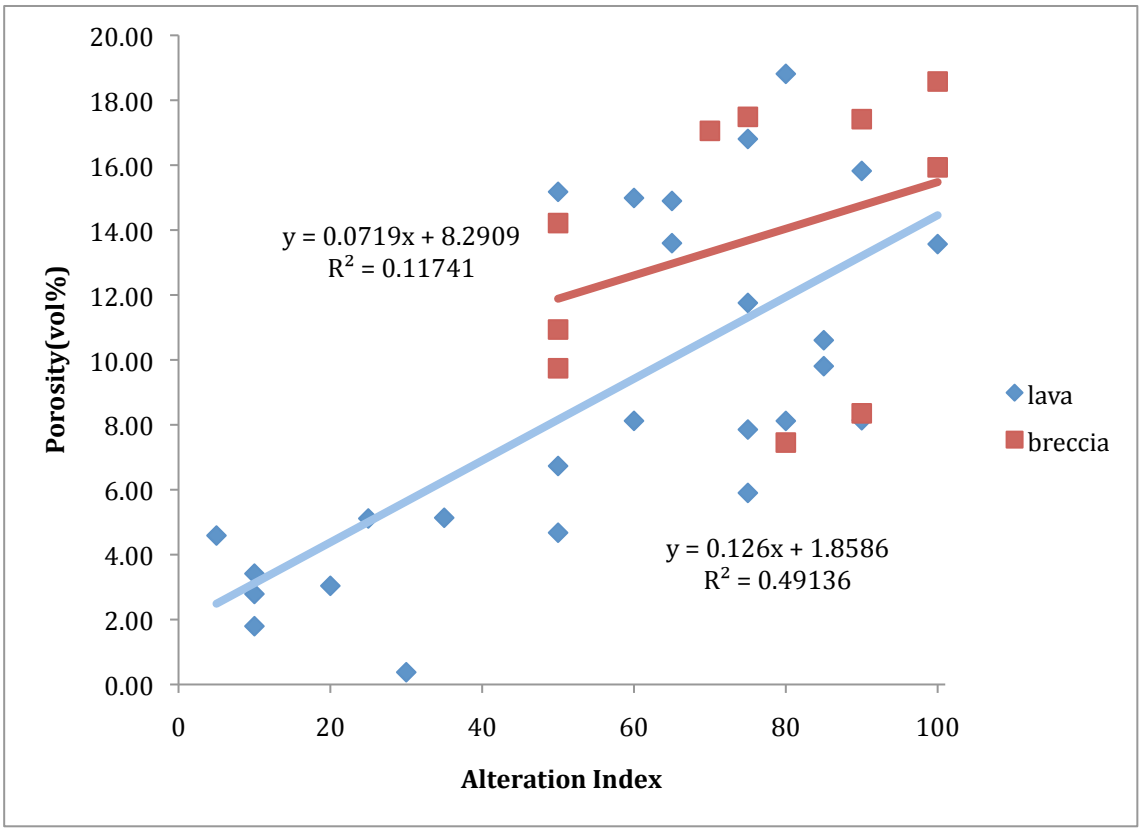


**Figure 14 Alteration Index plotted against the porosity of the Rotokawa Andesite. The Alteration Index is based on the mobility of chemical elements within the Rotokawa Andesite. The lines are linear regression models for the two separate rock types (lava and breccia) within the Rotokawa Andesite, showing a general positive trend. Figure modified from Pochee (2010).**

The wide feed zone in RK18L2 could be due to a wide zone of alteration which has increased the porosity, and possibly bulk permeability (Pochee, 2010). If such was the case, then it is possible that slip would have a negative effect on permeability, as is the case in high porosity rocks such as sandstones (Antonellini and Aydin, 1994).

The method of assessing fractures based on the shear and normal stress shows that the permeability of the Rotokawa Andesite can be quite complex. In some cases, there is a relationship between the frequency of fractures prone to slip and high fluid flow rates into geothermal wells. In other examples, fractures oriented prone to slip could possibly have a negative effect on fluid flow. Therefore, the stress imposed on fractures might be

a useful tool to elucidate the processes that affect the zones of high fluid flow in geothermal wells, such as flow fractures, or a lack of fractures prone to slip implying other methods of bulk permeability creation. However, the method of assessing fractures based on the shear and normal stress is not an effective method for locating zones of highest fluid flow on its own, as many fractures prone to slip do not contribute significantly to the flow of wells.

## 7 CONCLUSION

A stress model for the Rotokawa Geothermal Field has been constructed. The overburden model in a volcanic and volcaniclastic terrain contains more uncertainty than those constructed for sedimentary basins due to the inherent variation in the density of volcanic rock. However, at Rotokawa the density variation between stratigraphic units is greater than within. A better understanding of rock density variation, such as density profiles from wireline logging, would improve the accuracy of vertical stress model.

Standard methods of modeling the maximum horizontal stress have not constrained this principal stress beyond the range that can be defined by theory alone. This is because thermal effects at the wellbore wall have not been sufficiently quantified, and the range of mechanical properties of the rocks is too great.

Simple two-dimensional Mohr circles have been used to demonstrate the impact uncertainty in the overburden model has on hydraulically conductive fracture orientation. However, to precisely quantify the fracture population that will be

orientated for slip at Rotokawa, the magnitude of the maximum horizontal stress must be constrained and the fracture planes assessed in three dimensions.

The permeability structure in the Rotokawa Andesite is complex, as in some cases there is a positive correlation between frequency of fractures prone to slip, and permeable zones, however, in one example, there is a negative correlation. In the latter case, permeability might be enhanced by alteration. Shear and normal stress ratios imposed on fractures is not an effective method for independently determining zone of high fluid flow on its own, and neither is the aperture of fractures; however, it might be an effective tool to combine with other datasets, in order to draw conclusions on the nature of permeability in geothermal wells.

## 8 REFERENCES

Allmendinger, R.W., Cardozo, N.C., Fisher, D., 2012. Structural Geology Algorithms: Vectors & Tensors, First. ed. Cambridge University Press, Cambridge, England.

Anderson, E.M., 1951. Dynamics of Faulting and Dyke Formation with Applications to Britain.

Anderson, T.R., Fairley, J.P., 2008. Relating permeability to the structural setting of a fault-controlled hydrothermal system in southeast Oregon, USA. J. Geophys. Res. 113, 1–13.

Antonellini, M., Aydin, A., 1994. Effect of Faulting on Fluid Flow in Porous Sandstones: Petrophysical Properties. Am. Assoc. Pet. Geol. Bull. 78, 355–377.

Ashwell, P., 2013. Controls on rhyolite lava dome eruptions in the Taupo Volcanic Zone.

Barton, C.A., Hickman, S.H., Morin, R., Zoback, M.D., Benoit, D., 1998. Reservoir-Scale Fracture Permeability in the Dixie Valley, Nevada, Geothermal Field. Proc. SPE/ISRM Rock Mech. Pet. Eng. 299–306.

Barton, C.A., Zoback, M.D., Moos, D., 1995. Fluid flow along potentially active faults in crystalline rock. Geology 23, 683–686.

Bégué, F., Gravley, D.M., Chambefort, I., Deering, C., Kennedy, B., 2014. Magmatic volatile distribution as recorded by rhyolitic melt inclusions in the Taupo Volcanic Zone, New Zealand. Geol. Soc. London, Spec. Publ. in press.

Bertrand, E.A., Caldwell, T.G., Hill, G.J., Wallin, E.L., Bennie, S.L., Cozens, N., Onacha, S. a., Ryan, G. a., Walter, C., Zaino, A., Wameyo, P., 2012. Magnetotelluric imaging of upper-crustal convection plumes beneath the Taupo Volcanic Zone, New Zealand. Geophys. Res. Lett. 39, 1–6.

Bibby, H.M., Caldwell, T.G., Davey, F., Webb, T.H., 1995. Geophysical evidence on the structure of the Taupo Volcanic Zone and its hydrothermal circulation. J. Volcanol. Geotherm. Res. 68, 29–58.

Brace, W.F., 1980. Permeability of crystalline and argillaceous rocks. Int. J. Rock Mech. Min. Sci. Geomech. Abstr. 17, 241–251.

Brown, E., Hoek, E., 1978. Trends in Relationships between Measured In-Situ Stresses and Depth. Int. J. Rock Mech. Min. Sci. Geomech. Abstr 15, 211–215.

Browne, P.R.L., 1978. Hydrothermal alteration in active geothermal fields. Annu. Rev. Earth Planet. Sci. 6, 229–250.

Byerlee, J., 1978. Friction of rocks. Pure Appl. Geophys. PAGEOPH 116, 615–626.

Caine, J.S., Evans, J.P., Forster, C.B., 1996. Fault zone architecture and permeability structure. Geology 24, 1025–1028.

Cox, S., 2005. Coupling between deformation, fluid pressures, and fluid flow in ore-producing hydrothermal systems at depth in the crust. Econ. Geol. 100th Anniv. Vol. 39–75.

Curewitz, D., Karson, J.A., 1997. Structural settings of hydrothermal outflow: Fracture permeability maintained by fault propagation and interaction. J. Volcanol. Geotherm. Res. 79, 149–168.

Eastwood, A.A., Gravley, D.M., Wilson, C.J.N., Chambefort, I., Oze, C., Cole, J.W., Ireland, T.R., 2013. U-Pb Dating of Subsurface Pyroclastic Deposits (Tahorakuri formation) at Ngatamariki and Rotokawa Geothermal Fields, in: New Zealand Geothermal Workshop 2013 Proceedings.

Fairley, J.P., 2004. Field observation of fluid circulation patterns in a normal fault system. Geophys. Res. Lett. 31, 1–4.

Faulkner, D.R., Jackson, C. a. L., Lunn, R.J., Schlische, R.W., Shipton, Z.K., Wibberley, C. a. J., Withjack, M.O., 2010. A review of recent developments concerning the structure, mechanics and fluid flow properties of fault zones. J. Struct. Geol. 32, 1557–1575.

Favara, R., Grassa, F., Inguaggiato, S., Valenza, M., 2001. Hydrogeochemistry and stable isotopes of thermal springs: earthquake-related chemical changes along Belice Fault (Western Sicily). Appl. Geochemistry 16, 1–17.

Gartrell, A., Zhang, Y., Lisk, M., Dewhurst, D., 2004. Fault intersections as critical hydrocarbon leakage zones: integrated field study and numerical modelling of an example from the Timor Sea, Australia. Mar. Pet. Geol. 21, 1165–1179.

Grant, M.A., Bixley, P.F., 2011. Geothermal Reservoir Engineering. Academic Press.

Hatherton, T., Macdonald, W., Thompson, G., 1966. Geophysical methods in geothermal prospecting in New Zealand. Bull. Volcanol. 29, 485–497.

Leonard, G.S., Begg, J.G., Wilson, C.J.N., 2010. Geology of the Rotorua Area: scale 1:250,000. Low. Hutt Inst. Geol. Nucl. Sci. Ltd. 102.

Manville, V., Wilson, C.J.N., 2004. The 26 . 5 ka Oruanui eruption , New Zealand : a review of the roles of volcanism and climate in the post-eruptive sedimentary response. New Zeal. J. Geol. Geophys. 47, 525–547.

Massiot, C., McNamara, D., Lewis, B., n.d. Processing and analysis of high temperature geothermal acoustic borehole image logs, New Zealand. submitted.

Massiot, C., Mcnamara, D., Lewis, B., Price, L., Bignall, G., 2012. Statistical Corrections of Fracture Sampling Bias in Boreholes from Acoustic Televiewer Logs, in: New Zealand Geothermal Workshop 2012 Proceedings.

McLean, K., McNamara, D., 2010. Fractures interpreted from acoustic formation imaging technology: correlation to permeability, in: Thirty-Sixth Workshop on Geothermal Reservoir Engineering. Stanford, California.

McNamara, D., Massiot, C., Lewis, B., Wallis, I.C., n.d. Heterogeneity of structure and stress in the Rotokawa Geothermal Field, New Zealand. prep.

Mielke, P., 2009. Properties of the Reservoir Rocks in the Geothermal Field of Wairakei/New Zealand.

Moos, D., Zoback, M.D., 1990. Utilization of observations of well bore failure to constrain the orientation and magnitude of crustal stresses: application to continental, Deep Sea Drilling Project, and Ocean Drilling Program boreholes. J. Geophys. Res. 95, 9305–9325.

Peska, P., Zoback, M.D., 1995. Compressive and tensile failure of inclined well bores and determination of in situ stress and rock strength. J. Geophys. Res. 100, 12791–12811.

Pochee, A., 2010. Mass transfer and hydrothermal alteration in the Rotokawa Andesite , Rotokawa geothermal field , New Zealand .

Quinao, J.J., Sirad-azwar, L., Clearwater, J., Hoepfinger, V., Le Brun, M., Bardsley, C., 2013. Analyses and Modelling of Reservoir Pressure Changes to Interpret the Rotokawa Geothermal Field Response to Nga Awa Purua Power Station Operation, in: Thirty-Eight Workshop on Geothermal Reservoir Engineering.

Rae, A.J., 2007. Rotokawa Geology and Geophysics. GNS Sci. Consult. Rep. 2007/83, 11.

Rawling, G.C., Goodwin, L.B., Wilson, J.L., 2001. Internal architecture, permeability structure, and hydrologic significance of contrasting fault-zone types. Geology 29, 43.

Rissmann, C., Nicol, A., Cole, J.W., Kennedy, B., Fairley, J.P., Christenson, B., Leybourne, M., Milicich, S., Ring, U., Gravley, D., 2011. Fluid flow associated with silicic lava domes and faults, Ohaaki hydrothermal field, New Zealand. J. Volcanol. Geotherm. Res. 204, 12–26.

Rowland, J. V, Sibson, R.H., 2001. Extensional fault kinematics within the Taupo Volcanic Zone, New Zealand: soft-linked segmentation of a continental rift system. New Zeal. J. Geol. Geophys. 44, 271–284.

Rowland, J. V, Simmons, S.F., 2012. Hydrologic, Magmatic, and Tectonic Controls on Hydrothermal Flow, Taupo Volcanic Zone, New Zealand: Implications for the Formation of Epithermal Vein Deposits. Econ. Geol. 107, 427–457.

Seebeck, H.C., 2012. Normal Faulting, Volcanism and Fluid Flow, Hikurangi subduction Plate Boundary, New Zealand.

Seebeck, H.C., Nicol, A., Walsh, J.J., Childs, C., Beetham, R.D., Pettinga, J., 2014. Fluid flow in fault zones from an active rift. J. Struct. Geol. 62, 52–64.

Sewell, S.M., Cumming, W.B., Azwar, L., Bardsley, C., 2012. Integrated MT and Natural State Temperature Interpretation for a Conceptual Model Supporting Reservoir Numerical Modelling and Well Targeting at the Rotokawa Geothermal Field, New Zealand, in: Proceedings: Thirty-Seventh Workshop on Geothermal Reservoir Engineering. Stanford University, Stanford California.

Sewell, S.M., Cumming, W.B., Bardsley, C.J., Winick, J.A., Quinao, J.J., Wallis, I.C., Sherburn, S., Bourguignon, S., Bannister, S., 2013. Interpretation of Microearthquakes at the Rotokawa Geothermal Field, 2008 to 2012, in: New Zealand Geothermal Workshop 2013 Proceedings.

Sibson, R.H., 1996. Structural permeability of fluid-driven fault-fracture meshes. J. Struct. Geol. 18, 1031–1042.

Siratovich, P.A., Davidson, J., Villeneuve, M., Gravley, D.M., Kennedy, B., Cole, J.W., Wyering, L., Price, L., 2012. Physical and mechanical properties of the Rotokawa Andesite from production wells RK 27_L2, RK28 and RK30, in: New Zealand Geothermal Workshop 2012 Proceedings. Auckland, New Zealand.

Stephens, G., Voight, B., 1982. Hydraulic fracturing theory for conditions of thermal stress. Int. J. Rock Mech. Min. Sci. Geomech. Abstr. 19, 279–284.

Stern, T., 1986. Geophysical studies of the upper crust within the Central Volcanic Region, New Zealand. R. Soc. New Zeal. Bull.

Terzaghi, R., 1965. Sources of error in joint surveys. Geotechnique 15, 287–304.

Wallis, I.C., Bardsley, C.J., Powell, T., Rowland, J. V, O'Brien, J.M., 2013. A Structural Model for the Rotokawa Geothermal Field, New Zealand, in: New Zealand Geothermal Workshop 2013 Proceedings.

Wallis, I.C., McNamara, D., Rowland, J. V, Massiot, C., 2012. The Nature of fracture permeability in the basement greywacke at the Kawerau Geothermal Field, New

Zealand, in: Proceedings, Thirty-Seventh Workshop on Geothermal Reservoir Engineering. pp. 1–9.

Whitford, C.M., Lumb, J.T., 1978. A catalogue of physical properties of rocks, Geophysics Division Report 106. Wellington.

Wilson, C.J.N., Houghton, B.F., McWilliams, M.O., Lanphere, M. a., Weaver, S.D., Briggs, R.M., 1995. Volcanic and structural evolution of Taupo Volcanic Zone, New Zealand: a review. J. Volcanol. Geotherm. Res. 68, 1–28.

Winick, J.A., Powell, T., Mroczek, E., 2009. The Natural-State Geochemistry of the Rotokawa Reservoir, in: New Zealand Geothermal Workshop 2009 Proceedings.

Wiprut, D., Zoback, M., Hanssen, T., Peska, P., 1997. Constraining the Full Stress Tensor from Observations of Drilling-induced Tensile Fractures and Leak-off Tests: Application to Borehole Stability and Sand Production on the Norwegian Margin. Int. J. Rock Mech. Min. Sci. 34, 3–4.

Wright, I.C., 1992. Shallow structure and active tectonism of an offshore continental back-arc spreading system: the Taupo Volcanic Zone, New Zealand. Mar. Geol. 103, 287–309.

Yielding, G., Freeman, B., Needham, D., 1997. Quantitative Fault Seal Prediction. Am. Assoc. Pet. Geol. Bull. 6, 897–917.

Zoback, M.D., Barton, C.A., Brudy, M., Castillo, D., Finkbeiner, T., Grollimund, B., Moos, D., Peska, P., Ward, C., Wiprut, D., 2003. Determination of stress orientation and magnitude in deep wells. Int. J. Rock Mech. Min. Sci. 40, 1049–1076.

# CHAPTER 5:

## Mechanical Behaviour of the Rotokawa Andesite

# Mechanical Behaviour of the Rotakawa Andesite

## 1 ABSTRACT

The conditions leading to failure in the Rotokawa Andesite, a major fluid-bearing rock unit of the Rotokawa geothermal reservoir, Taupo Volcanic Zone (TVZ), are investigated. Two failure processes are investigated: 1) the constant tectonic strain and 2) the increase in fluid pressure. Mathematical models show that if failure occurs through increase in fluid pressure, it is unlikely that the overpressures required to induce rock mass failure would be solely generated by porosity/permeability reduction in the Rotokawa geothermal reservoir. However a constant external flux of fluids could induce failure through fluid overpressure. The large-scale failure of the Rotokawa Andesite is modelled as a rock mass using the Hoek-Brown failure criterion. Two examples show that shear failure is the current dominant mode of failure for the Rotokawa Andesite at depths where it is located. However, small scale changes in stress, or an increase in rock mass strength would favour tensile failure. High densities of fractures observed in three wells of the Rotokawa Andesite are mostly oriented within 26º of the minimum principal stress. These orientations are consistent with fractures formed in shear mode during pure triaxial deformation of rock, confirming the results from the Hoek-Brown failure criterion. It is proposed that 'Healy' faulting is the main mode of fracture formation in the Rotokawa Andesite, promoting fluid flow within the rock.

## 2 INTRODUCTION

Fracture dilation caused by brittle failure of rocks is a process that can maintain high bulk permeability in low permeability rocks. The dilation is induced by slip (Sibson, 1987; Barton et al., 1995; Blenkinsop, 2008; Rowland and Simmons, 2012; Seebeck et al., 2014) or by pressurised pure extension of fractures (Sibson, 1996, 2000; Rowland and Simmons, 2012). In geothermal fields with low matrix permeability rocks, continued brittle failure, which increases bulk permeability, can be important for geothermal convection. This is not only because convection requires relatively high bulk permeability (Cathles et al., 1997; Manning and Ingebritsen, 1999; Rowland and Sibson, 2004), but also because fracture permeability can be transient due to mineralisation and episodic fault rupture (Rowland and Sibson, 2004; Cox, 2005). This chapter discusses the physical conditions required for failure and the common modes of failure, for the Rotokawa Andesite, a low permeability, low porosity, fluid producing geological unit within the Rotokawa Geothermal Field.

Permeability of rock has wide-ranging economic implications. Permeability not only controls the rate at which oil and gas, or geothermal fluids can be extracted from a reservoir, but it is also a crucial parameter for $CO_2$ sequestration (Pollyea and Fairley, 2012) and nuclear waste repository containment (Montazer and Wilson, 1984; Bredehoeft, 1997). Permeability is also a controlling factor in the creation of fluid overpressures (Neuzil, 1995).

Permeability of a porous medium can be assessed on various scales, with often vastly different results (Brace, 1980). Permeability of rocks can be measured from core (i.e.,

on a scale of centimetres) up to the scale of well interference tests (i.e., up to kilometres). Data collected from many sites indicate that the scale of observation can have a profound effect on the measured permeability, with the amount of variability being related to a range of factors including the type of rock. For example, core in "crystalline" rock consistently has lower permeability than well interference tests from this rock type (Brace, 1980, 1984; Townend and Zoback, 2000). The discrepancy between these scales of measurement is evidence that fractures not present in lab scale experiments play a role in conducting fluids (Brace, 1980).

There are several crucial parameters when considering the mechanical failure of rock, including tectonic stresses, fluid pressure and flow rates, matrix and bulk permeability, rock strength, and pre-existing fracture density and orientation. The continued development of the Rotokawa Geothermal Field has increased the quality and quantity of these types of data. For example, pressure drawdown (Quinao et al., 2013) and microseismicity (Sewell et al., 2013) have provided information on the uneven permeability distribution within the Rotokawa Geothermal system.

Mechanical studies of rocks in the TVZ lack data and, as a consequence, the conclusions have large uncertainty (Rowland and Simmons, 2012). By contrast, mechanical constraints from the Rotokawa Geothermal Field including, rock strength properties, bulk and matrix permeability, fracture frequency and orientation, stress, and fluid pressure, permit a detailed study of the mechanical behaviour of the Rotokawa Andesite. The data from the Rotokawa Andesite suggests that if rock failure was driven by fluid pressures above hydrostatic pressures, an external source of fluid forcing would be required (e.g. upward convection of fluid into the field). Regardless of the cause of

failure, shear failure is likely to be the main failure mode in the Rotokawa Andesite, consistent with the orientation of failure observed in borehole images.

## 3 GEOLOGICAL CONTEXT

The Rotokawa Geothermal Field is located approximately 10 km northeast of the Taupo urban area, on the eastern edge of the central TVZ (Figure 1). The central TVZ is occupied by an active rift which formed during the last 1-2 Ma in association with roll-back of the subducting Pacific plate (Wright, 1992; Wilson et al., 1995; Rowland and Sibson, 2001; Seebeck, 2012). Volcanic activity within the rift has produced in excess of 15,000 $km^3$ of volcanic material over the past 2 Ma, mostly through caldera forming eruptions (Wilson et al., 1995). The geology of the central TVZ is dominated by these Quaternary volcanic and sedimentary deposits (Manville and Wilson, 2004; Leonard et al., 2010), emplaced on top of the Mesozoic basement rocks, known as the Torlesse Terrane, composed of meta-sandstones variably interbedded with argillites (Leonard et al., 2010).

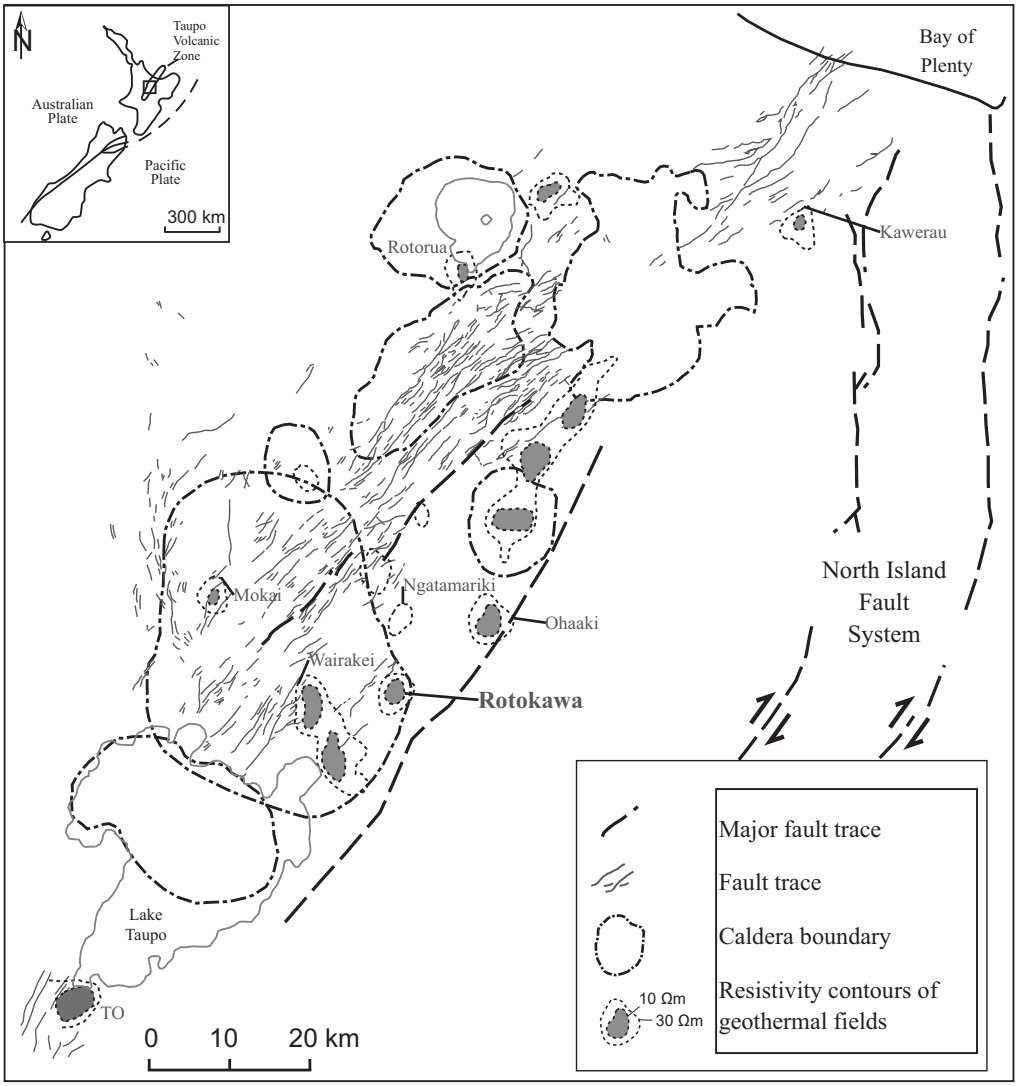


**Figure 1 Geological map of the Taupo Volcanic Zone (after Bégué et al., 2014), with the producing geothermal fields named. The location of the Rotokawa Geothermal Field is shown. Fault traces indicate the location of the active rift.**

## 3.1 TVZ Geothermal Fields

The TVZ contains numerous geothermal fields mainly along the margins of, or outside, the active rift (Figure 1). All of the currently commercially developed high temperature (> 250º C) geothermal fields in the TVZ are charged by convective fluid flow. The hot fluids in these geothermal systems are derived mostly from cold meteoric water which circulates at depth and, once heated, rise under buoyancy towards the ground surface

(Bibby et al., 1995; Bertrand et al., 2012). The convection is induced by the difference in density of the hot- and cold-water column (see Figure 2). These convective geothermal systems are examples of abnormal pressures gradients (see section 4.3). On top of the variation in fluid pressure caused by temperature, convective fluid flow induces changes in pressure gradients, referred to as 'dynamic pressure gradients'. The dynamic contribution in the TVZ to the pressure gradient is usually less than 10%, even in zones of high upflow (Grant and Bixley, 2011).

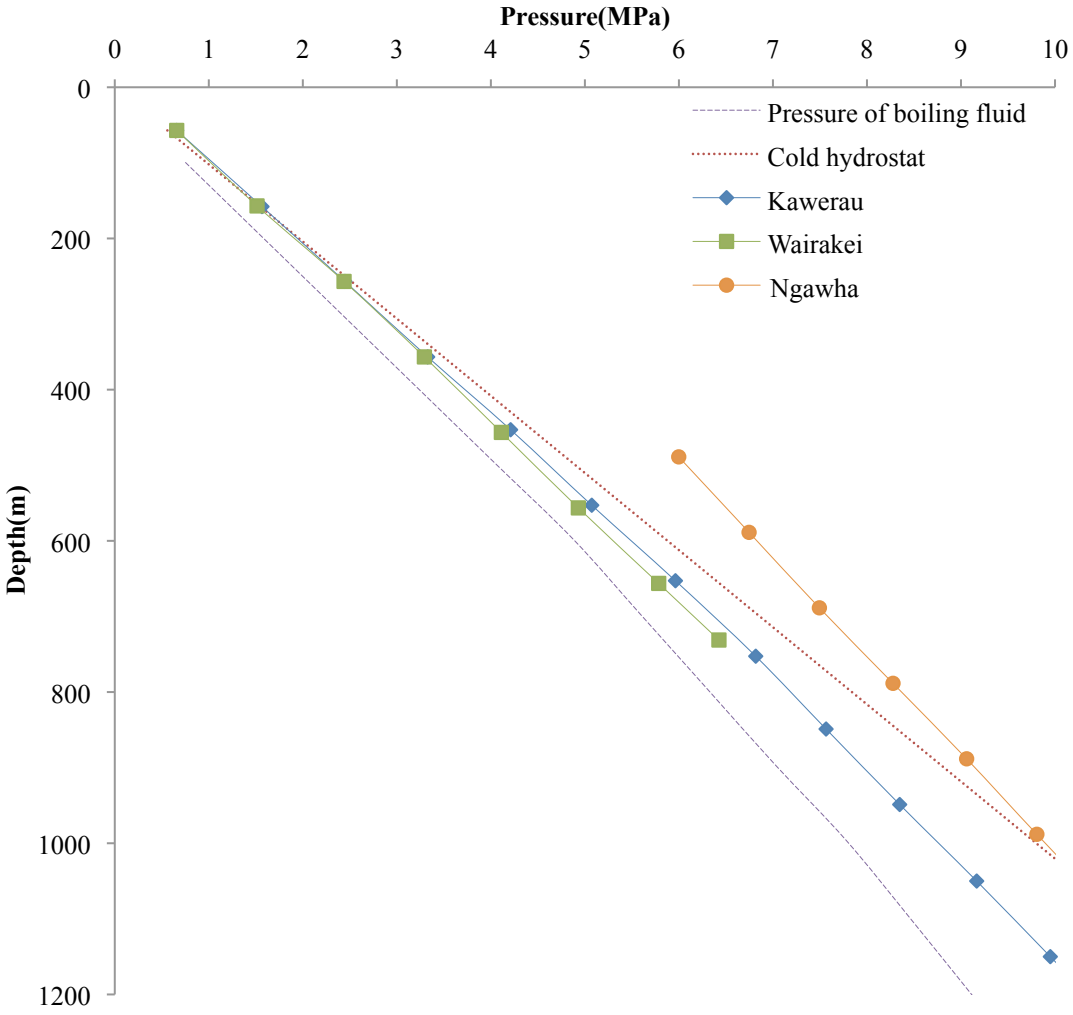


**Figure 2 Shallow pressure gradients for three New Zealand geothermal fields plotted relative to pressure of boiling fluid and cold fluid at hydrostatic pressures. Modified from Browne & Lawless (2001) and Grant & Bixley (2011).**

Not all abnormal pressure gradients in geothermal systems are caused by temperature. In the Ngawha Geothermal Field, which in located in Northland (outside the TVZ), it is not possible to reconcile the observed pressures with temperature-induced changes in fluid density and/or the effect of upflow (Figure 2) (Grant and Bixley, 2011). In such cases, the overpressure is caused by a low permeability rock formation, which retards fluid flow to the ground surface (see section 4.3).

The TVZ geothermal systems have a similar vertical permeability structure within most systems. The main hydrological feature of most TVZ geothermal systems is a well-developed, although discontinuous, clay cap acting as a barrier to vertical fluid flow (Winick et al., 2009; Boseley et al., 2010; O'Brien et al., 2011). These clay caps are typically zones of intense clay alteration which tend to form through the interaction of the hot rising hydrothermal fluids with the surrounding rocks (Browne, 1978), detectable using resistivity and magneto-telluric surveys, as they are less resistive compared to the surrounding rocks (Hatherton et al., 1966; Bibby et al., 1995; Bertrand et al., 2012). These clay caps separate the high temperature geothermal reservoir from shallower aquifers.

The permeability within reservoirs and aquifers can be complicated, and differs between geothermal fields (Rosenberg et al., 2009). Permeability can be lithologically controlled (Rosenberg et al., 2009; Rissmann et al., 2011; Sewell et al., 2012), with certain geological units being the primary reservoir facies in geothermal systems (Rosenberg et al., 2009). However, some lithological units have a wide variability in permeability (Rosenberg et al., 2009), and this complexity can be due to the fracture/fault control on permeability (Seebeck et al., 2014), and alteration of rocks (Pochee, 2010). Permeability

measurements of reservoir rocks in TVZ geothermal fields are rare outside the Rotokawa field. Rock retrieved from outcrop and shallow core (up to -500 masl) at the Wairakei geothermal field have permeabilities that range from $2.1x10^{-17}$ $m^2$ to $2x10^{-14}$ $m^2$ (Mielke, 2009). These values are relatively low compared to the bulk permeability of the Waiora aquifer at Wairakei, which has an estimated permeability of $1.0x10^{-13}$ $m^2$ (Pritchett et al., 1979). Other geothermal fields have similar bulk permeabilities; well tests suggest a horizontal permeability of $1.1x10^{-13}$ $m^2$ for the deep reservoir of the Ohaaki geothermal field, however, the vertical permeability is inferred to be $3x10^{-15}m^2$ (Leaver, 1986). The Kawerau Reservoir has a variable transmissivity, with recent results of ~400 Darcy meters (Grant and Wilson, 2007). This is roughly equivalent to ~$0.4x10^{-13}$ $m^2$ in the case of a 1000 m thick reservoir.

### 3.2 Rotokawa Geothermal Field

The Rotokawa geothermal system is divided into three distinct levels: a hot geothermal reservoir; an intermediate aquifer; and a shallow aquifer (Sewell et al., 2012). Each aquifer is separated by discontinuous low-permeability layers that are rich in the alteration clay smectite (Figure 3). The intermediate aquifer is mainly constrained within two geological units (Rae, 2007; Sewell et al., 2012).

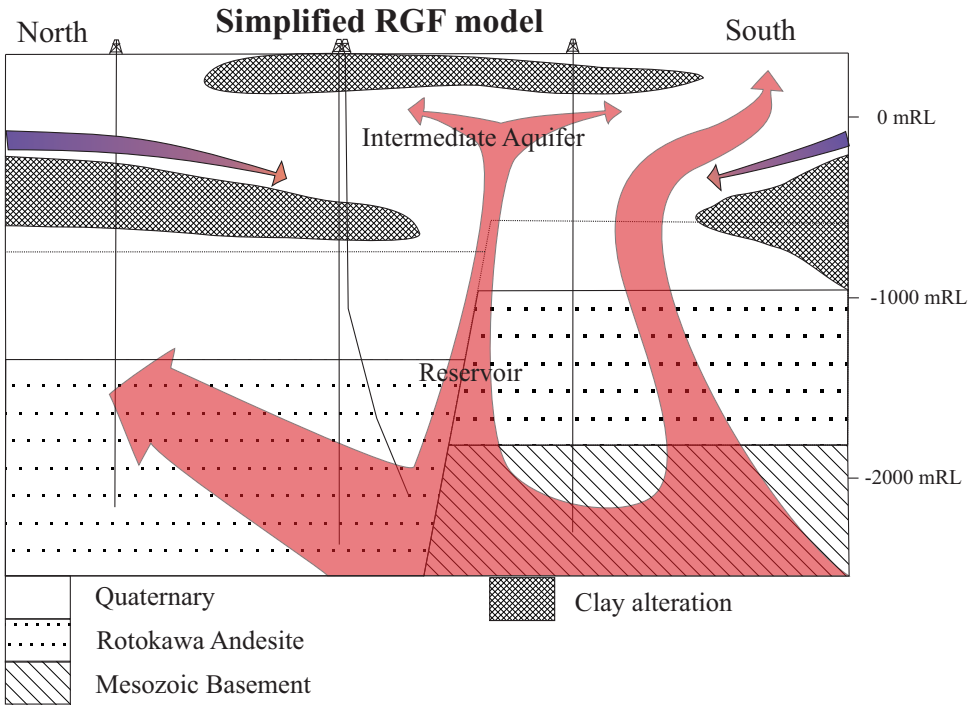


**Figure 3 Simplified cross section of the Rotokawa Geothermal Field, showing major geological boundaries, clay alteration and fluid flow (after Winick et al 2009 and Sewell et al 2012). The fault in the centre is the Central Field Fault; other inferred faults are not shown.**

The reservoir rocks of the Rotokawa Geothermal Field comprise the Rotokawa Andesite (up to 2100 m thick), the 1.8 Ma Tahorakuri Formation (a crystal-lithic vitric tuff, or ignimbrite, of variable thickness up to 250 m), and the Waikora Formation, a greywacke sandstone and argillite siltstone pebble conglomerate (up to 250 m thick) (Rae, 2007). The tops of the units older than ~330 ka are consistently offset by either faults that have little surface expression, or are modified by paleo-topography (Wallis et al., 2013). The relationship between the temperature contours and the inferred structures at depth (Rae, 2007), the drawdown pressure gradients (Quinao et al., 2013), and microseismic studies (Sewell et al., 2013) suggest that the permeability of the deep reservoir is strongly influenced by faulting and fracturing of host rocks.

The magnitude of the vertical stress in an extensional environment, such as the TVZ, is dependent on the weight of the overburden (see Chapter 3). The magnitude of the minimum horizontal stress in the shallower levels of the Rotokawa Geothermal Field (< -1150 mRL depth) is positively correlated with the rock frictional properties (see Chapter 3). This correlation provides a means of estimating minimum horizontal stress required to induce rock failure. For further details on the stresses in the Rotokawa Geothermal Field refer to Chapter 3 & 4.

### 3.2.1 Natural State Fluid Pressure

The Rotokawa Geothermal Field was drilled by 7 exploration wells before major exploitation commenced (Quinao et al., 2013). Pressure data obtained from these wells permitted the interpretation of the natural geothermal system pressure gradients. The data show two distinct pressure gradients; a shallower gradient (≥ -800 mRL) attributed to the intermediate aquifer at Rotokawa, and a deeper gradient (≤ -800 mRL) corresponding to the high temperature reservoir.

Obtaining data on the natural rock pore pressure at depth to populate profiles like those presented for the Rotokawa Geothermal Field in Figure 4 can be very difficult. Opportunities to obtain pressure data while drilling are rare. They can only be obtained once zones of lost circulation are encountered; however, during events of lost circulation, drilling conditions can be difficult and the focus of operators is usually on maintaining borehole integrity rather than obtaining accurate pressure measurements (Grant and Bixley, 2011). It is also possible to obtain formation pressure measurements from completion testing. The fluid pressure in the wellbore is seldom in equilibrium

with formation pressure, due to temperature differences between the natural fluid and the fluid in the wellbore. However, when a good fluid connection between the well and the reservoir is achieved, formation pressure can be determined from downhole measurements. Determining pressure is complicated if flows between connections (crossflows) exist within the well. Once field operation has begun, it is likely that the natural pressure gradient will be affected by the extraction or injection of fluids, and therefore the natural state pressure gradient will be altered. Unless future drilling is performed in areas that remain unaffected by production, it will be impossible to obtain data on the natural state formation fluid pressure. Due to the relatively few opportunities to obtain pressure measurements during field development, the resulting pressure gradient can be a gross simplification of the actual reservoir pressure. These simplified gradients may not incorporate the subtle pressure variations occurring within geothermal fields due to variation in natural flow and complicated permeability structures.

The shallower pressure gradient follows the hydrostatic pressure gradient for a fluid just below boiling, although the pressure gradient is slightly modified due to substantial upflow. The pressure is roughly atmospheric at the surface, and there is no evidence for the existence of disequilibrium overpressure in the shallow parts of the geothermal system.

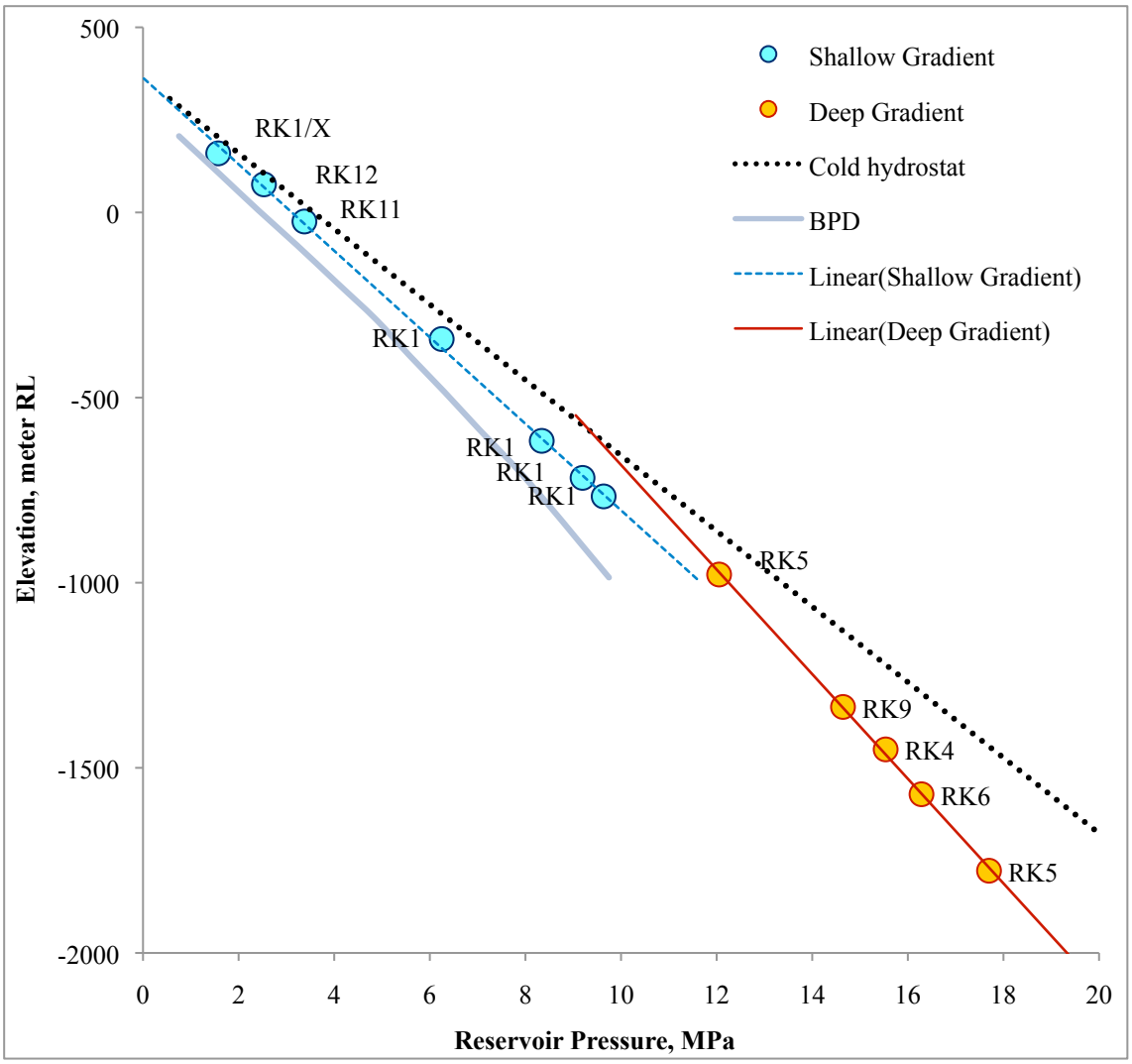


**Figure 4 Fluid Pressure for depth at the Rotokawa Geothermal Field. Points represent successful formation pressure measurements in well, which are named. Lines are lines of best fit. BDP = Pressure for Depth of a continuously boiling fluid (refer to Grant & Bixley 2011).**

The deep reservoir gradient (≤ -800 mRL) has a steeper slope, implying that the density of the fluid is lower at depth, consistent with the presence of a hot fluid at depth. Part of the reservoir pressure gradient in the deeper reservoir is overpressured compared to the shallow gradient, as defined by the measurement in RK5 at -978 mRL (Figure 4). The misfit of deep and shallow pressure gradients at -978 m indicates a disequilibrium overpressure is present, likely caused by changes in the permeability structure, or perhaps by capillary seals (Bjørkum1998, Rodgers 1999).

### 3.2.2 Permeability Structure

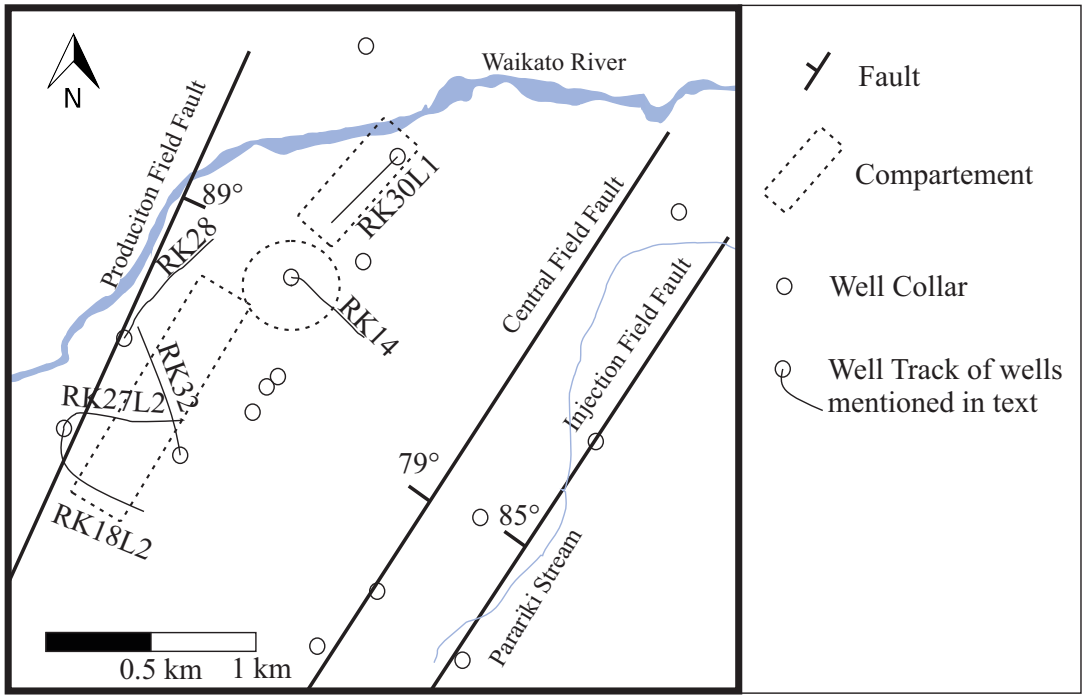


**Figure 5 Map of the Rotokawa Geothermal Field, showing major faults (Wallis et al., 2013), permeability compartments (Quinao et al., 2013) and well locations. Tracks are shown for wells mentioned in the text.**

Well and tracer tests, as well as pressure drawdown patterns show that bulk permeability varies spatially within the Rotokawa reservoir (Figure 5, see Quinao et al., 2013). The bulk of production fluid comes from the western side of the Rotokawa Geothermal Field. The spent geothermal fluids are injected to the SE of the major fault in the reservoir, known as the central field fault (CFF). Pressure drops associated with production of certain wells (e.g., RK14 and RK5) are larger than expected for the amount of fluid that is returned to the reservoir by injection (Quinao et al., 2013). This drop in pressure is consistent with the suggestion that the CFF is a barrier to fluid flow on production timescales. The hypothesis that there is restricted flow across the CFF, is supported by the location of microseismic events associated with the reinjection of the fluids (Sewell et al., 2013). In addition, on the production side of the fault there is

variable pressure drawdown, leading to the conclusion that the reservoir of the production field has a spatial variability of bulk permeability, and is compartmentalised (Figure 5). The low permeability separation between compartments can be transient. For example, after years of pressure decline associated with fluid production, the mass flow rate from production well RK14 suddenly increased 60-70% in March 2011. The increased flow from the well is attributed to the formation pressure returning close to pre-production levels which could have been achieved by pressure equilibration between previously separate pressure cells or compartments (Quinao and Sirad-Azwar, 2012).

A reservoir flow model, characterised by a permeable reservoir divided into several compartments separated by low permeability boundaries, is used to assess and calibrate the bulk permeability of the reservoir (Figure 6). The model also has a discontinuous low permeability layer above the reservoir, with leakage occurring where the layer is absent; the exact size and permeability of the leak is uncertain, but is constrained by MT and measured temperature and pressure data (J. Clearwater, pers. comms. 2014). The permeability inferred from the reservoir model, ranges in the order of $10^{-15}$ to $10^{-13}$ $m^2$ (Figure 6). By comparison, core from the main reservoir rock, the Rotokawa Andesite, has a measured permeability on the order of $10^{-17}$ $m^2$ at low pressures under ambient laboratory conditions (Siratovich et al., 2014). The discrepancy in permeability between these different scales of measurements confirms that fractures are important hydraulic connections in the Rotokawa Andesite.

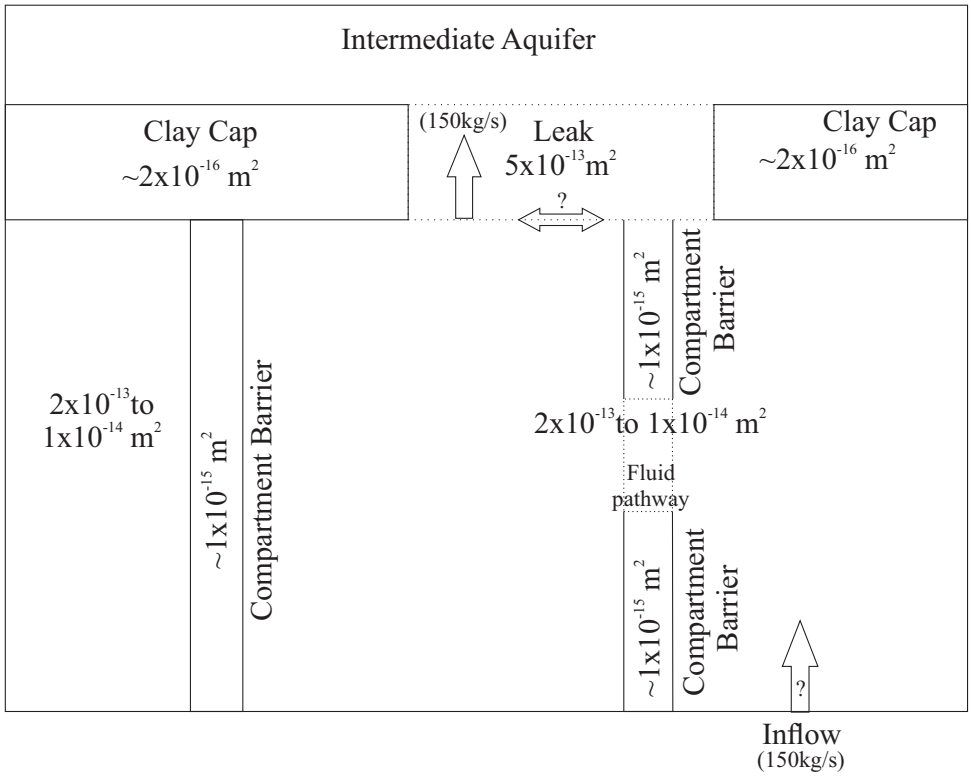


**Figure 6: Diagram simplifying the 3d flow model used for the Rotokawa Geothermal Field. This diagram attempts to display all the complexities present in the model (e.g. discontinuous lower permeability compartment barriers, and variable size of the connection between reservoir and intermediate aquifer). Permeability data from J. Clearwater (pers comms, 2014).**

# 4 FRACTURES AND PERMEABILITY- THEORY AND MEASUREMENTS

## 4.1 Mechanical behaviour of rocks

Brittle rock deformation has been studied extensively over the past 250 years (Coulomb, 1773; Griffith, 1921; Fairhurst, 1964; Hoek and Brown, 1980; Sibson, 1998; Healy et al., 2006). The fundamental processes that affect rock failure are inherently difficult to characterise, because of the heterogeneous and anisotropic nature of rock (Ashby and Sammis, 1990). This is certainly why theoretical criteria are still relied upon to describe rock failure, developed from years of experiments and experience.

Coulomb suggested the earliest brittle failure criterion (Coulomb, 1773) now known as the Mohr-Coulomb failure criterion. This criterion takes into account cohesion (stress independent), as well as friction (stress dependent, using Amontons law) to deduce the angle of the plane of failure of a column under an axial load. Although it was a significant achievement to recognise the effects of cohesion and friction, the Mohr-Coulomb failure criterion is still an empirical formula. The cohesion is unique to each rock sample and is affected by scale, and the angle of internal friction not only varies between rocks, but can also vary depending on the magnitude of stress.

Nearly 150 years after Coulomb, Griffith proposed that microcracks were important for rock failure (Griffith, 1921). Griffith recognised that the stress required to break glass was orders of magnitude smaller than the theoretical stress required to break atomic bonds. He proposed that failure occurred at stresses lower than expected due to the glass not being perfectly isotropic, containing many micro-scale imperfections, known as 'Griffith cracks'. To test his hypothesis, Griffith introduced macroscopic flaws into his samples, and was able to show that the size of the flaw was proportional to the stress required to propagate the flaw. Traditional linear elastic theory was unable to resolve the stresses at the crack tip, so Griffith developed a thermodynamical approach to explain the propagation of flaws, suggesting that the new surfaces required work to be created. Using this approach, he showed that the relationship between the stress and crack length was controlled by Young's modulus and also by the 'surface energy' of the cracks. This mechanistic approach is fundamentally different from the Mohr-Coulomb failure criteria in that once the physical properties of a brittle material are known; the stress required to propagate a fracture can be predicted. However, several challenges

still remained in its application to rocks, as it is difficult to establish the surface energy of cracks in rocks, due to the large inherent variability in composition and texture. Surface energy varies between rock types (Friedman et al., 1972), and is likely to be an individual mineral property (e.g.: Santhanam and Gupta, 1968)

Two modes of brittle failure are recognised in rock mechanics; 1) tensile failure and 2) shear failure. The Griffith criterion adequately describes the phenomena observed with pure tensile fracture propagation (Hoek and Bieniawski, 1965; Ashby and Sammis, 1990). However, the Griffith criterion was not as successful at describing shear failure as the Mohr-Coulomb criterion, as frictional forces become important (Brace, 1960; Sibson, 1998). Many failure criteria have been proposed to improve on the classical criteria (Brace, 1960; Fairhurst, 1964; Hoek and Brown, 1980; Sibson, 1998; Healy et al., 2006). Frequently, these newer criteria incorporate both Coulomb and Griffith theory to describe rock failure. These newer criteria attempt to address two main issues that the classical criteria have not adequately addressed: 1) the orientation of shear failure in intact rock and, 2) the effect of pre-existing fractures on the cohesion of rocks. These issues are discussed below.

Mohr diagrams can be used to illustrate the theoretical orientation at which fractures will form. Figure 7 is a Mohr diagram with two failure envelopes generated by merging the Griffith and Coulomb failure criteria: one with no cohesion (reshear), and one where the cohesion is equal to twice the tensile strength of the sample (T) (Intact rock) (Sibson, 1998). Shear failure will occur at the angles $\theta_s$ or $\theta_r$, only if the intersection of the stress circle with the respective failure envelopes occurs in the positive normal stress field. Here, failure occurring in the negative normal stress field is considered to

be tensile, usually at point –T, the tensile strength of the rock (Figure 7), although some observations of a transitional state of failure exist (Brace, 1960; Ramsey and Chester, 2004).

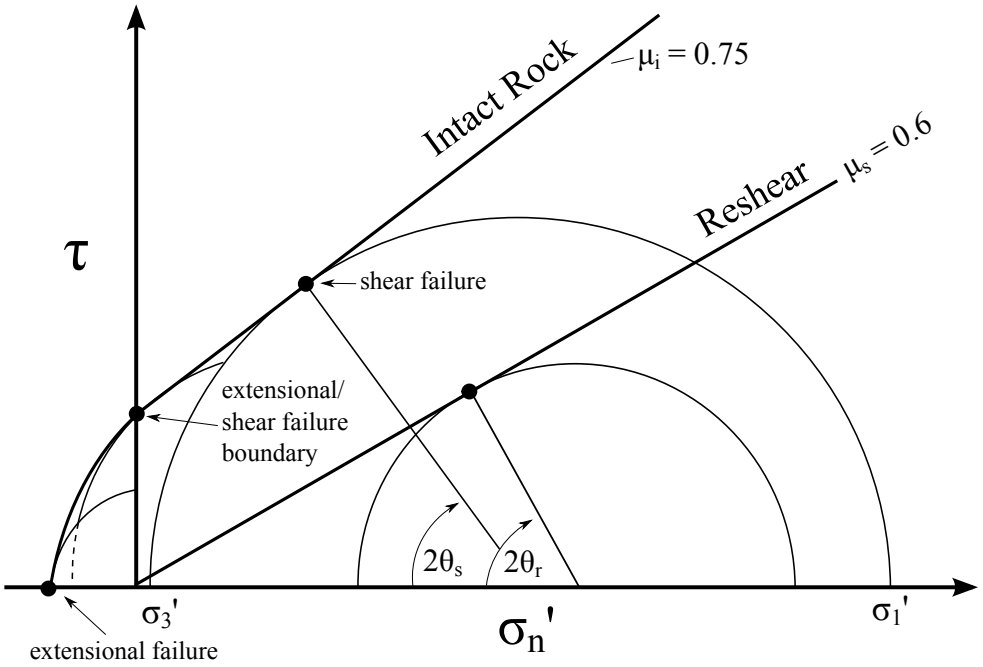


**Figure 7 Generic failure criteria in Mohr space for two conditions: Intact rock and reshear. Reproduced from Sibson (1998).**

One important concept, illustrated by Figure 7, is that cohesion is a pre-requisite condition for tensile failure, as the failure envelope extends into the negative normal stress (tensile) regime. Where a pre-existing failure plane exists, it is not possible for a rock to sustain tensile stresses, regardless of stress conditions, due to a lack of cohesion. In these circumstances the condition for shear failure will always be met before tensile stresses are generated.

Experimental data show that tensile failure occurs when a single fracture propagates unstably, exploiting small-scale weaknesses, such as along grain boundaries and mineral cleavages (Ramsey and Chester, 2004). However, experience from modelling

and experiments show that processes affecting shear failure are more complicated than the Coulomb failure criterion implies (Reches, 1978; Healy et al., 2006). Prior to the formation of a macroscopic shear failure, opening of tensile micro-fractures has been observed (Brace et al., 1966). In many laboratory studies, these tensile micro-fractures have been observed as micro-cracks in the samples prior to failure (Lockner, 1993; Reches and Lockner, 1994). Micro-cracking continues until eventually some of the micro-cracks amalgamate into a larger shear fracture (Reches and Lockner, 1994).

The small-scale tensile fracturing preceding failure results in an anisotropic rock fabric (Healy et al., 2006). The interaction of these tensile micro-fractures leads to the formation of a macroscopic shear fracture whose poles can take any orientation within an angle of 26º to minimum principal stress axis (Healy et al., 2006). This phenomenon has been named 'Healy faulting' (Blenkinsop, 2008) and the orientation of failure is in stark contrast to the Mohr-Coulomb failure criterion, which predicts a single orientation of failure. The discrepancy between Coulomb and 'Healy' shear failure orientation is attributed to the fact that most experimental data are not conducted in true triaxial conditions (i.e., where $S_1 \neq S_2 \neq S_3$), but often, like in the case of Coulombs column, with the two lesser principal stress magnitudes equal to each other ($S_1 > S_2 = S_3$) (Healy et al., 2006). Although the orientation of failure might not be appropriate, various forms of the Mohr-Coulomb criterion are still widely used due to its success at describing the stress required to induce shear failure.

When considering Figure 7, there are two possible end members: 1) intact rock with high cohesion, and 2) a rock with no cohesion, where the ability of the rock to withstand failure is dominated by the frictional properties of the rock. When considering a large-

scale fractured rock mass, it is difficult to predict how the rock will respond to stress. The rock in between fractures behaves cohesively, but the fractures within the mass have no inherent cohesion, and will slip once friction is overcome on the surface. Experiments have shown that increasing the size of samples causes the cohesion of the sample to be reduced (Hoek and Brown, 1980). This relationship implies that the larger the rock mass studied, the greater the likelihood that there are weaknesses, such as fractures, that exist at various scales. This means that in order to predict failure of a larger rock mass, it is necessary to assess the properties of discontinuities that could act as planes of weakness.

The Hoek-Brown criterion (Hoek and Brown, 1980) was developed to address the issue of cohesion within a rock mass containing discontinuities. It is used to solve engineering problems such as large-scale rock mass failure encountered during tunnelling operations. The criterion takes into account the properties of intact rock, measured on the small scale in the laboratory, as well as the effect caused by discontinuities (joints and fractures) in the rock mass itself, based on qualitative and quantitative data. This is then used to compute a modified Griffith criterion.

The scale of application of the Hoek-Brown criterion is essential, as it assumes that the discontinuities contained within the rock mass results in isotropic rock mass behaviour. If the area or volume of interest is relatively small compared to the spacing of discontinuities (joints/fractures), the rock mass behaviour will be anisotropic and will not behave as a Hoek-Brown body. In these circumstances, it is inappropriate to use the failure criterion to assess the strength of the rock. For the Hoek-Brown criterion to be applicable, the minimum dimension of the area of interest should be a factor of 10

larger than the discontinuity spacing, in order to guarantee isotropic behaviour (Hoek and Brown, 1980).

## 4.2 Stress in an extensional environment

Stress is a key controlling factor for the brittle failure of rock. Two main mechanisms can lead to failure in an extensional environment; 1) strain driven, where tectonic strain in rock drives changes in stress (Sibson, 1992), and 2) fluid pressure driven- where increase in fluid pressure modifies stress. Strain-driven failure will be induced by a decrease in horizontal stress, assuming that the vertical stress is entirely controlled by gravity and the weight of the overburden rock (Anderson, 1951). The failure will cause a sudden increase in the horizontal stress, with little change to the vertical stress (Dempsey, Ellis, et al., 2012). This cycle is continued as long as the strain rate on the system remains constant (Sibson, 1992).

Changes in fluid pore pressure in rocks have a critical effect on brittle rock failure. The difference between the total stress and the fluid pressure in a homogeneous rock is termed the 'effective stress' (Terzaghi, 1925; Hubbert and Rubey, 1959), as pore pressure counteracts the effect of compressive stress imposed on rocks at depth. An increase in pore pressure causes the effective normal stress on fractures to be reduced; however shear stresses remain unchanged. The resulting increase in the shear/normal stress ratio increases the possibility of rock failure. The effect of fluid pressure can be amplified in rocks with anisotropic distributions of porosity, as changes in fluid pressure can also cause changes in shear stresses imposed on rocks, depending on the porosity anisotropy (Chen and Nur, 1992; Healy, 2009).

Not only does fluid overpressure induce failure, but also temporal variations of fluid pressure have been recognised as an effective mechanism to promote permeability. An increase in pore pressure can induce pure extensional dilation in fractures normal to the least principal stress (Sibson, 2000). The resulting gaping void will promote fluid flow in low porosity, low-permeability rocks, and the aperture of the fracture will dominate the resulting bulk permeability (Klimczak et al., 2010). The multiple effects of fluid pressure on permeability warrant further investigation, and the conditions that may affect fluid pressure in the Rotokawa reservoir are investigated in detail in this chapter.

## 4.3 Generating Overpressure in a Geothermal Field

Normal (hydrostatic) fluid pressure gradients with increasing depth are defined by the weight of the fluid column using the regional geothermal gradient. The term 'overpressured' in the geological context is used when pressures are observed to be higher than hydrostatic at a given depth (i.e., overpressure is the difference between the overpressured fluid and expected hydrostatic pressure). A variety of mechanisms cause pore pressures to deviate from the expected hydrostatic gradient and can be broadly separated into two categories: 1) equilibrated pressures and, 2) dis-equilibrated pressures (Neuzil, 1995).

Equilibrated overpressures can be caused by topographical expression, as seen in artesian wells, where the influx of water into a constrained aquifer at a high altitude causes the water to flow out where the aquifer is exposed at lower altitudes. Chemical gradients can also induce flow of fluid, causing abnormal pressures where large

chemical gradients exist (Hanshaw and Hill, 1969). The most common overpressure exhibited in a geothermal system is through density gradients in geofluids where hotter fluids are naturally less dense than colder changes of the fluid (Grant and Bixley, 2011). This can arise from a fluid temperature difference, which induces the upward flow of a lower density fluid due to density gradients (Grant and Bixley, 2011). Phase changes are also a cause for density differentials, such as in the case of hydrocarbons where fluid can be layered from heavier oil to lighter gas (Wiprut and Zoback, 2000).

Dis-equilibrated overpressures are documented where a reduction of pore space or an increase in fluid volume occurs at a rate faster than the fluids can be dissipated (Neuzil, 1995). This dis-equilibration typically occurs in situations where low permeability seals isolate regions of rock from the hydrostatic gradient and these volumes are then subject to changes in the fluid regime such as could be produced by compaction, diagenesis, kerogen formation or devolatilisation (Neuzil, 1995). The most common examples of a dis-equilibrated overpressure would be of a porous sedimentary sequence containing fluid and isolated on all sides by a low permeability formation (Gaarenstroom et al., 1993). As this sequence is buried, overpressures will occur if the rate of compaction of the pore space, or production of fluids (such as kerogen production or mineral dehydration) is greater than the rate at which the fluid can escape (Gaarenstroom et al., 1993). Another example is the dehydration of a subducting slab into a low permeability lower crust (Screaton et al., 1990).

Time scales are a crucial component when considering overpressures and permeability. For example, a typical geothermal development will require production flows of around 1000 kg/s (Grant and Bixley, 2011). These flow rates are around an order of magnitude

higher than estimates of natural flow rate through geothermal systems (Grant and Bixley, 2011). The total volume of fluid moved by production will be much larger than the volume of recharge during the production of a geothermal field (~ 30 - 50+ years), which will greatly affect the fluid pressure within the geothermal system. However, geothermal fields in the TVZ are known to have existed in their current position for over 100,000 years (Browne, 1979; Arehart et al., 2002). The total volume to flow through a geothermal reservoir during its long life will therefore easily eclipse the volume used for geothermal power generation.

In addition to considering permeability contributions over various time scales, it is important to recognise that permeability is dynamic and can vary over time. Processes such as, fracturing of rock, and dissolution and precipitation of minerals can affect permeability over short time-scales, certainly within the lifetime of a geothermal field (Titley, 1990; Dempsey, Rowland, et al., 2012), if not on the timescale of field production itself (Quinao and Sirad-Azwar, 2012). The variation of permeability with time is likely to be a crucial factor when considering natural fluid pressures with time.

## 4.4 Method for evaluating overpressures

Transient dis-equilibrated overpressures in geothermal systems can occur due to the dynamic nature of these systems. Changes to rock properties caused by processes such as diagenesis and mineral devolatilisation (Neuzil, 1995), porosity reduction (Walder and Nur, 1984) or (forced) fluid flux (Hanshaw and Bredehoeft, 1968) could cause temporary changes in fluid pressures in the hydrothermal system. Two simple one-dimensional mathematical formulae are defined that will help assess what processes are

likely to cause disequilibrium overpressures. The formulae are defined in terms of the maximum relative head, given that the system has infinite time to equilibrate. A non-dimensionalised time factor is given, which permits the assessment of the time required for the pressure to reach its final value.

### 4.4.1 Overpressure caused by changes within the layer

Fluid pressure modifications can be driven by changes in the host rock, such as porosity reduction or fluid sources (i.e. kerogen formation or devolatilisation) within the layer. In order to assess the conditions and processes that could lead to such overpressures, simple one-dimensional flow models of the flow of fluids (after Neuzil, 1995) are used:

$$\nabla \cdot \left(\kappa \nabla h\right) = S_s \frac{\partial h}{\partial t} + \Gamma \qquad (1)$$

where $\kappa$ (m/s) is the hydraulic conductivity, $h$ is the hydraulic head relative to the surface (m), $S_s$ is the specific storage capacity ($l^{-1}$) and $\Gamma$ is the rate of geological forcing (essentially the rate at which the total porous volume of the rock changes compared to the volume of the fluid, $s^{-1}$). As the fluid source in this model is within the layer, this model has been named the 'internal forcing' model.

If a region $-l < x < l$ with a constant $\Gamma$ for $t > 0$ and zero initial head is considered ($h(t=0)=0$) , given enough time for the system to equilibrate ($t \rightarrow \infty$) the solution of (1) is (after Carslaw and Jaeger, 1959, p.130):

$$h = \frac{\Gamma l^2}{2\kappa}\left(1 - \frac{x^2}{l^2}\right) \tag{2}$$

The highest head will be at x=0, and therefore in order to assess the largest possible overpressure, equation (2) reduces to:

$$h = \frac{\Gamma l^2}{2\kappa} \tag{3}$$

The hydraulic conductivity (κ) is sensitive to changes in the viscosity and density of the fluid. In a geothermal environment, processes such as boiling and the presence of multiple phases change fluid properties and might have an effect on the generation of overpressures. Assuming that $\kappa = k\rho_f g/\mu_f$, equation (3) can be rewritten as the following:

$$h = \frac{\Gamma l^2 \mu_f}{2kg\rho_f} \tag{4}$$

with $k$ the permeability ($m^2$) , $\rho_f$ the density of the fluid ($kg/m^3$), $\mu_f$ the fluid viscosity (kg/ms), and $g$ is the gravitational constant ($9.81 m/s^2$). If the density of a fluid increases, or the viscosity decreases, the system departs from the overpressure generating condition.

The non-dimensionalised time factor for equation (4) is:

$$t_D = \kappa t / S_s l^2 \tag{5}$$

When $t_D$=1 the head reaches > 90% of its final value (Carslaw and Jaeger, 1959). Therefore, the time required for *h* in equation (4) to reach ~90% of its final value is:

$$t=S_s l^2/\kappa \quad (6)$$

Equation (4) simplifies fluid flow induced by geological forcing which allows the assessment of the conditions for significant deviations from a hydrostatic gradient to occur. The main controlling factor, the rate of geological forcing, is influenced by changes caused to porosity due to stress and diagenesis, by thermomechanical changes, and by fluid sinks/sources. Although these are difficult to quantify, the benefit of using this flow model is that Neuzil (1995) has shown that for a wide variety of situations and environments, the rate of geological forcing falls in the range of $10^{-20}$ $s^{-1} < \Gamma < 10^{-13}$ $s^{-1}$.

### 4.4.2 Overpressures occurring due to fluid flux

Fluid pressure can be affected by constant flow of fluids into a layer (Hanshaw and Bredehoeft, 1968). This type of situation might be comparable to the Rotokawa Geothermal Field, due to the constant flow of fluids through the system. Here, it is assumed that there is a constant flux of fluid from a source layer and use the following governing equation:

$$\frac{\partial^2 h}{\partial z^2} = \frac{S_s}{\kappa}\frac{\partial h}{\partial t} \quad (8)$$

The solution to the governing equation is given considering the domain 0≤z≤l. No initial excess head is assumed ( $h(z,t=0)=0$), with h (z=0,t) = 0. The head gradient ( $\frac{\partial h}{\partial z}$) at z = *l* is equal to $-q_0/\kappa$, and given enough time for the system to equilibrate (t -> ∞) (after Carslaw and Jaeger, 1959, p.113; Hanshaw and Bredehoeft, 1968) the solution is:

$$h(z)=\frac{q_0 z}{\kappa} \tag{9}$$

The highest head will be reached at z = *l*, so equation (9) reduces to:

$$h=\frac{q_0 l}{\kappa} \tag{10}$$

In this situation, the non-dimensionalised time factor is:

$$t_D=\kappa t/S_s l^2, \tag{11}$$

the same as for the geological forcing equation. When $t_D$=1, the head reaches > 90% of its final value (Hanshaw and Bredehoeft, 1968). Therefore, the time to reach 90% of the highest head is:

$$t=S_s l^2/\kappa \tag{12}$$

### 4.5 Rotokawa Datasets

The Rotokawa Andesite is the main geological unit of the Rotokawa geothermal reservoir. A summary is given of the rock properties and rock mass characteristics that are relevant to the discussion of the mechanical behaviour of the andesite. This includes permeability and uniaxial compressive strength (UCS) from three wells (RK27L2, RK28 and RK30L1), rock mass ratings (RMR) from five wells (RK32, RK30L1, RK29, RK18L2, RK27L2), and fracture orientation data from three wells (RK18L2, RK30L1 and RK32).

The permeability of the Rotokawa Andesite measured from cores ranges between $0.98x10^{-17}$ $m^2$ and $4.44x10^{-17}$ $m^2$ (Figure 8) if samples with macro-fractures are excluded (Siratovich et al., 2014). These were measured on cores using Argon gas permeability. It may be worth noting that matrix permeability decreases under increased confining pressures in the lab (Nara et al., 2010), however this effect is likely to be of limited significance in the Rotokawa reservoir (up to half an order of magnitude).

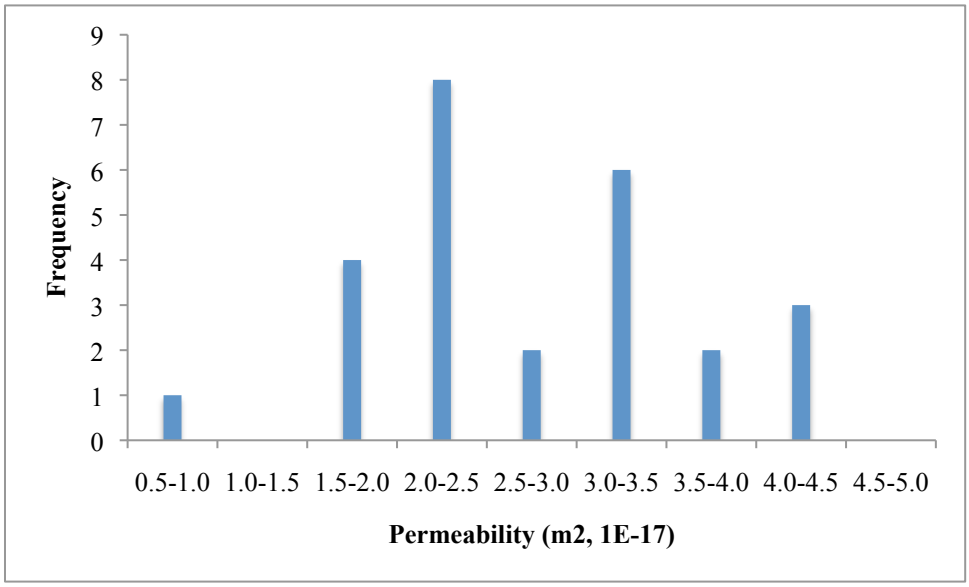


**Figure 8 Rotokawa Andesite permeability, excluding samples that containing visible macrofractures. The total number of measurements is 25 and the data are from Siratovich et al. (2014).**

The most important rock property required to assess rock failure is the uniaxial compressive strength (UCS) of the rock. The UCS, measured using rock cores, has an average of about 124 MPa (Siratovich et al., 2014), however one plug from RK27 measured as high as 211 MPa (Figure 9). For the purposes of the analysis in this chapter 211 MPa is used as an upper bound of intact rock strength for the Rotokawa Andesite.

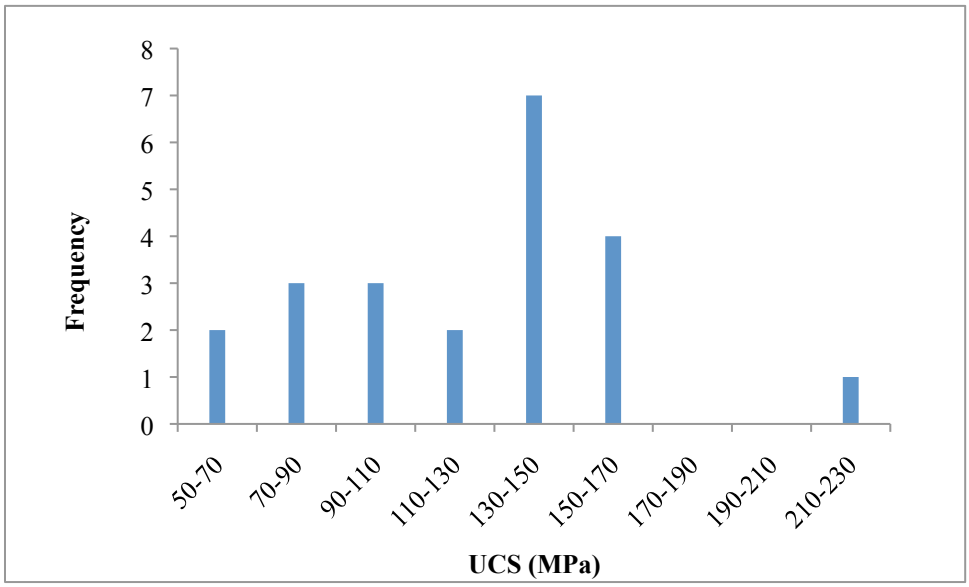


**Figure 9 Histogram of UCS measurements for the Rotokawa Andesite. The total number of measurements is 22 and the data are from Siratovitch et al. (2014).**

Core descriptions and photos were used to estimate the Rock Mass Rating (RMR) of 6 cores from the Rotokawa Andesite (Hoek and Brown, 1980). As all descriptions showed that the RMR was < 40, the RMR was converted to the Geological Strength Index (GSI, see Table 1) (Marinos et al., 2005).

In order to assess the strength of the rock mass using the Hoek-Brown criterion, strength determination triaxial compression data are required, which allows to the estimate the Hoek-Brown constant ($m_i$). However, no triaxial tests were available for the

Rotokawa Andesite, and the $m_i$ value has been estimated using values from Hoek (2006). The rock mass strength has a low sensitivity to $m_i$, and therefore it is acceptable to estimate the value of $m_i$ (Marinos et al., 2005).

Table 1 is a summary of four rock mass conditions for Rotokawa Andesite. The first rock mass condition represents the properties of a hypothetical intact rock mass, with no discontinuities, using the strongest UCS recorded for the Rotokawa Andesite. The remaining three conditions represent the properties for the strongest, average and weakest rock mass of the Rotokawa Andesite.

**Table 1 Summary of rock properties for the Rotokawa Andesite. * denotes inferred value. GSI - Geological Strength Index, UCS – Unconfined Compressive Strength, $m_i$ – Hoek-Brown constant.**

| Rock mass description | GSI | UCS | $m_i$ |
|---|---|---|---|
| Strongest, intact rock | 100* | 211* | 20* |
| RK27L2, strongest recorded mass | 75 | 211 | 20* |
| RK30L1 average recorded rock mass | 61 | 124 | 20* |
| RK32, weakest recorded mass | 35 | 60* | 20* |

The rock strength data in Table 1 was used to produce multiple failure envelopes for the Rotokawa Andesite rock mass. The Hoek-Brown failure criterion is used, as the Rotokawa Andesite is a naturally fractured rock type. Four envelopes have been created (left to right in Figure 10): 1) failure in the strongest intact rock; hypothetical situation if no joints were visible in core, 2) failure for the strongest observed rock mass from well RK27L2, 3) failure for the average rock mass (well RK30L1) and, 4) failure for the weakest rock mass (well RK32). The UCS for RK32 rock is noted as inferred, as no

rock testing was done on core from RK32. The value chosen for the UCS of this core is the weakest UCS from Figure 9.

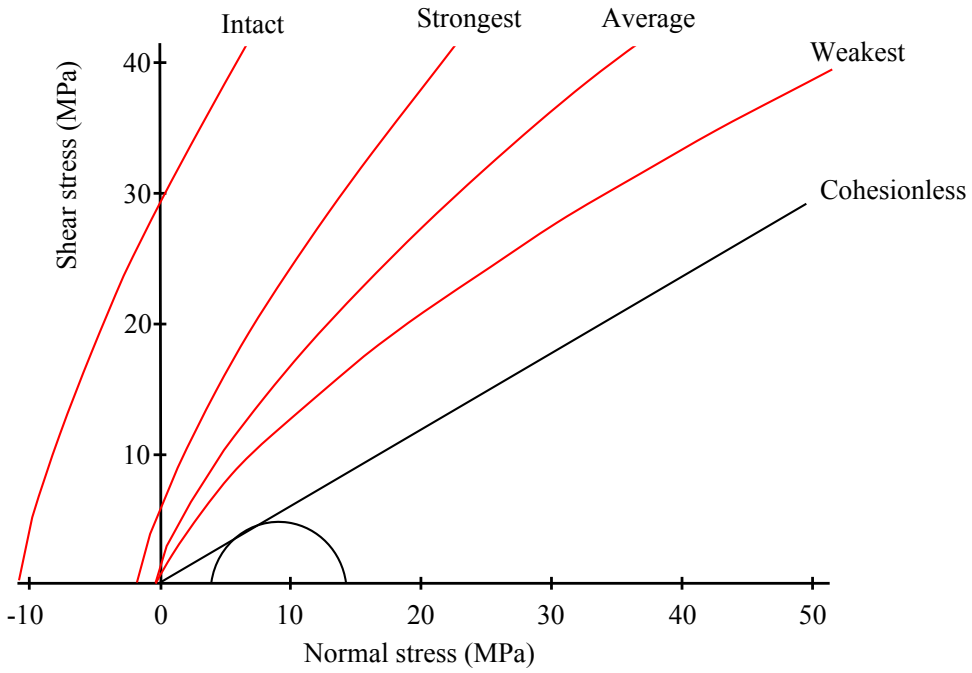


**Figure 10 Hoek-Brown failure criteria, in Mohr space, generated for four rock mass properties of the Rotokawa Andesite (see Table 1). The black line is the failure for a perfectly oriented fracture (mu=0.6), and the black circle represents stress conditions at -800 mRL for reference (top of the Rotokawa reservoir). Refer to text for further discussion of failure envelopes.**

Imaged fracture orientation data from wells provide an alternative way to characterise the Rotokawa Andesite rock mass. These data were collected using the acoustic formation imaging technology (AFIT) tool, which is a high-temperature borehole televiewer (BHTV) that has been commonly employed in the Taupo Volcanic Zone to image the rock formations exposed in geothermal wells. The AFIT tool records the travel time and amplitude attenuation of a returning sonic pulse from the geothermal borehole wall. This information is collated and processed allowing the observation of both natural geological and induced features at the borehole wall surface (Massiot et al., submitted). The interpretation and analysis of acoustic imaging from three wells in the

Rotokawa Geothermal Field has revealed a wealth of low-amplitude and several high-amplitude planar features intersecting the wellbore. These are described as discordant within the host rock and interpreted as fractures, both open and sealed (veins) (McNamara et al., in prep).

It is important to note that several processes, including image quality, and the borehole sampling, will affect the final dataset. The fact that the fracture orientation data is collected along the wellbore wall means that there is a sampling bias (Massiot et al., submitted). This bias can be statistically corrected in order to gain a more accurate picture of the density of fracture orientation populations for a given well. (Massiot et al., submitted; Terzaghi, 1965). The red great circles in Figures 10, 11 and 12 contain all poles to planes parallel to the borehole axis, highlighting the orientation of planes that are likely to be undersampled. The fracture density contouring in the three figures is corrected in order to mitigate the undersampling bias.

It is generally not possible to account for the lack of acoustic contrast and the poor image quality with the available dataset. It is worth noting that there is variability in the quality of the imaging, as poor quality imaging can affect the confidence in interpretation, however it is still possible to confidently resolve orientation data with a poor quality image (Massiot et al., submitted).

**Table 2 AFIT imaging quality. Quality estimates are from (McNamara et al., in prep)**

| Well | Poor image quality (<50% image interpretable) | Moderate image quality (<75% image interpretable) | Good image quality (>75% image interpretable) |
|---|---|---|---|
| RK18L2 | 66% | 34% | 0% |
| RK30L1 | 72% | 28% | 0% |

| | | | |
|---|---|---|---|
| RK32 | 49% | 36% | 15% |

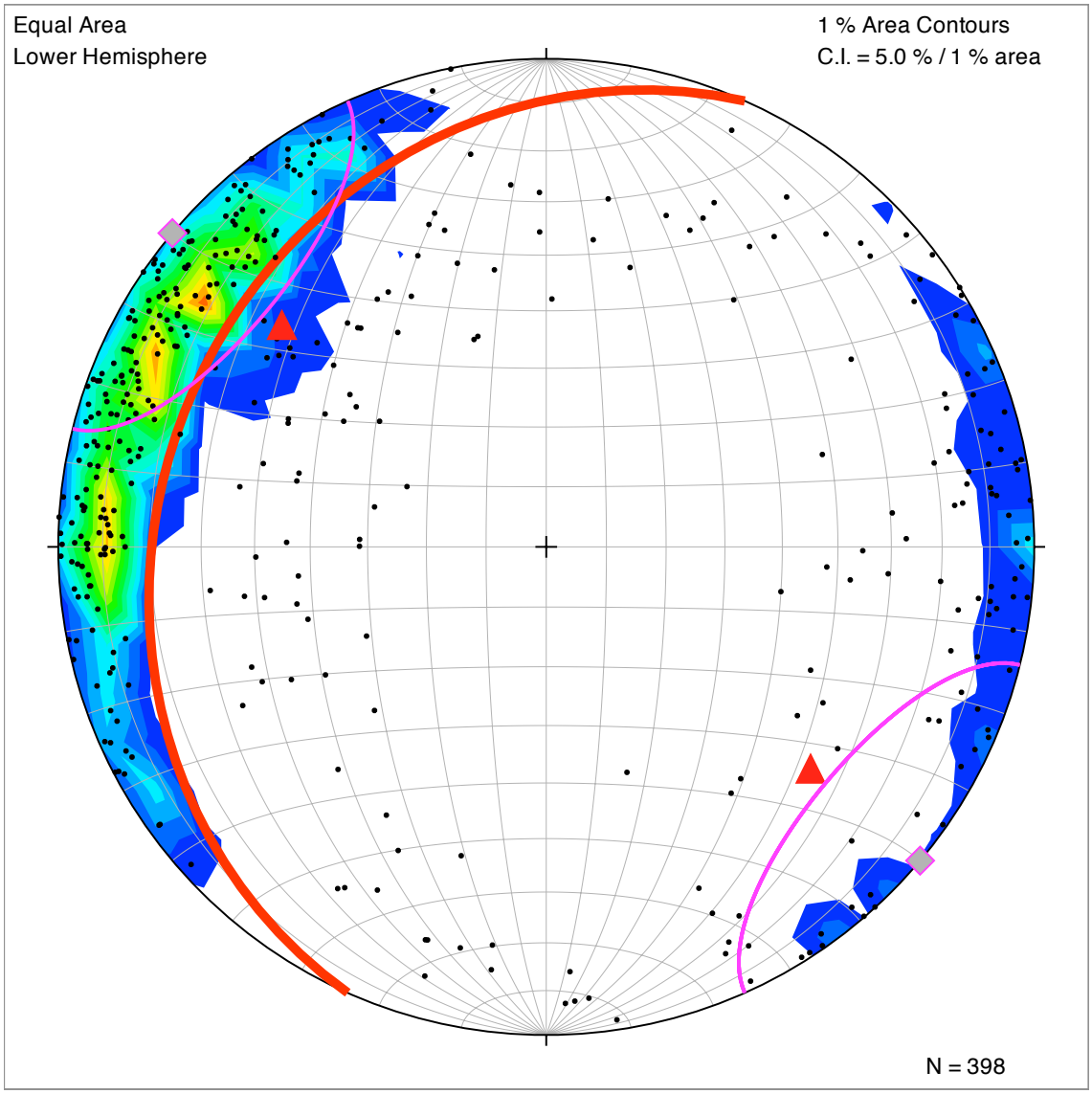


**Figure 11 Lower hemisphere equal-area stereonet (Allmendinger et al., 2012) showing poles to fractures imaged by AFIT in well RK18L2. Contouring is corrected to take sampling bias into account. Red great circle highlights planes parallel to the borehole axis. The pink small circles show the planes that are within 26° to the minimum principal stress axis (diamonds). The diamond shape and triangle represent the predicted orientation of tensile and shear failure respectively, according to Mohr-Coulomb theory.**

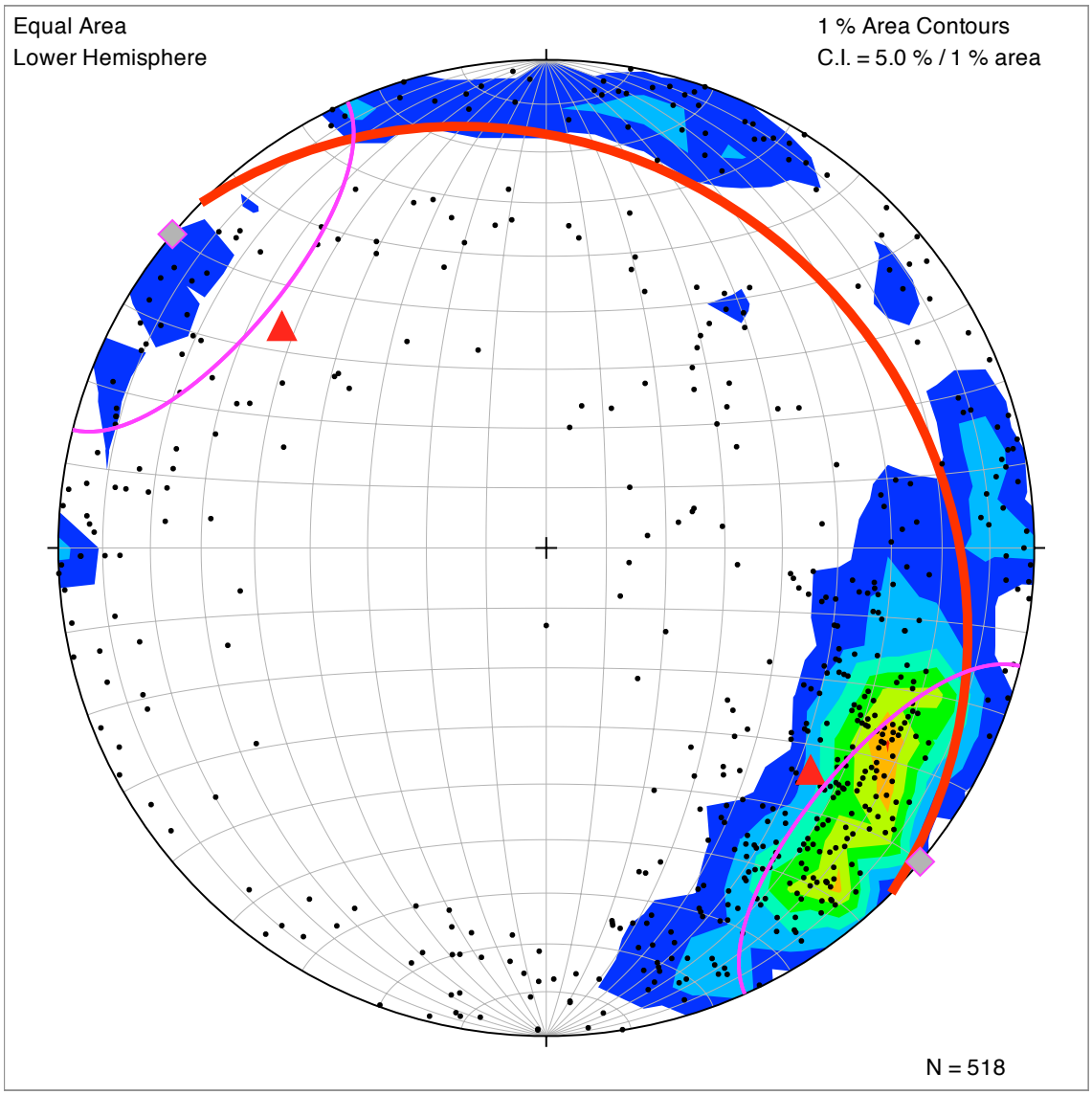


**Figure 12 Lower hemisphere equal-area stereonet (Allmendinger et al., 2012) showing poles to fractures imaged by AFIT in well RK30L1. Contouring is corrected to take imaging bias into account. The red great circle highlights planes parallel to the borehole axis. The pink small circles show the planes that are within 26º to the minimum principal stress axis (diamonds). The diamond shape and triangle represent the predicted orientation of tensile and shear failure respectively, according to Mohr-Coulomb theory.**

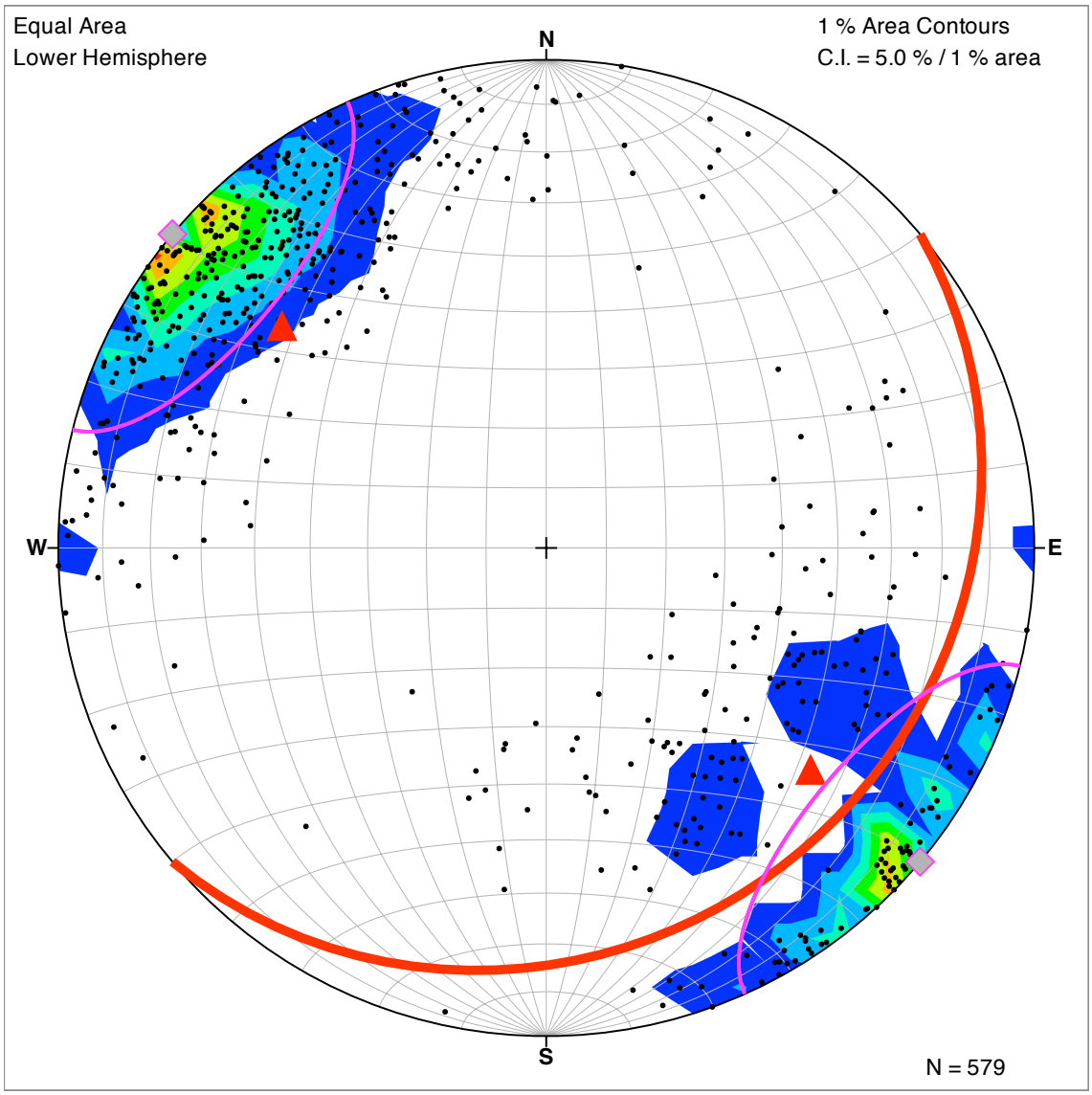


**Figure 13 Lower hemisphere equal-area stereonet (Allmendinger et al., 2012) showing poles to fractures imaged by AFIT in well RK32. Contouring is corrected to take imaging bias into account. The red great circle highlights planes parallel to the borehole axis. The pink small circles show the planes that are within 26º to the minimum principal stress axis (diamonds). The diamond shape and triangle represent the predicted orientation of tensile and shear failure respectively, according to the Mohr-Coulomb theory.**

# 5 DISCUSSION

## 5.1 Disequilibrium Overpressure Generation in the Rotokawa Reservoir

Stress estimations for the Rotokawa Geothermal Field suggest that pressures in excess of 4.2 MPa are required to open pre-existing tensile fractures ($S_3$-$P_p$) near the top of the reservoir (see chapter 3). The required pressure will be even higher in order to initiate tensile fractures, depending on the tensile strength of the rock. In this case, 4.16 MPa corresponds to roughly 600 m of hydraulic head, based on the reservoir pressure gradient. This value represents the minimum overpressure in the system that will lead to tensile mode of failure. Overpressures required for failure of rock mass in shear mode, as seen in Section 5.2, are similar in magnitude to the overpressures required for tensile failure, unless pre-existing fault planes are present.

### 5.1.1 Overpressures due to changing reservoir conditions

To assess the conditions required to generate the overpressures necessary for failure by internal forcing, equation (4) has been used. The extreme case has been assumed where mineral deposition removes all fracture permeability over a domain the size of $l$ (the length of the blocked pathway), reducing the bulk permeability $k$ to the matrix permeability of the rock. Laboratory small-scale permeability of the Rotokawa andesite is on the order of $10^{-17}$ $m^2$. Using a saturated reservoir fluid at 295ºC ($\rho_f$ = 726 kg/$m^3$ and $\mu_f$ = 8x$10^{-5}$ kg/ms) to estimate the size of the sealing required, a minimum seal thickness of 2310 m is required to create the overpressures necessary to open pre-

existing tensile fractures, at the highest rate of geological forcing reported ($10^{-13}$ $s^{-1}$), for more than 19 years (Figure 14).

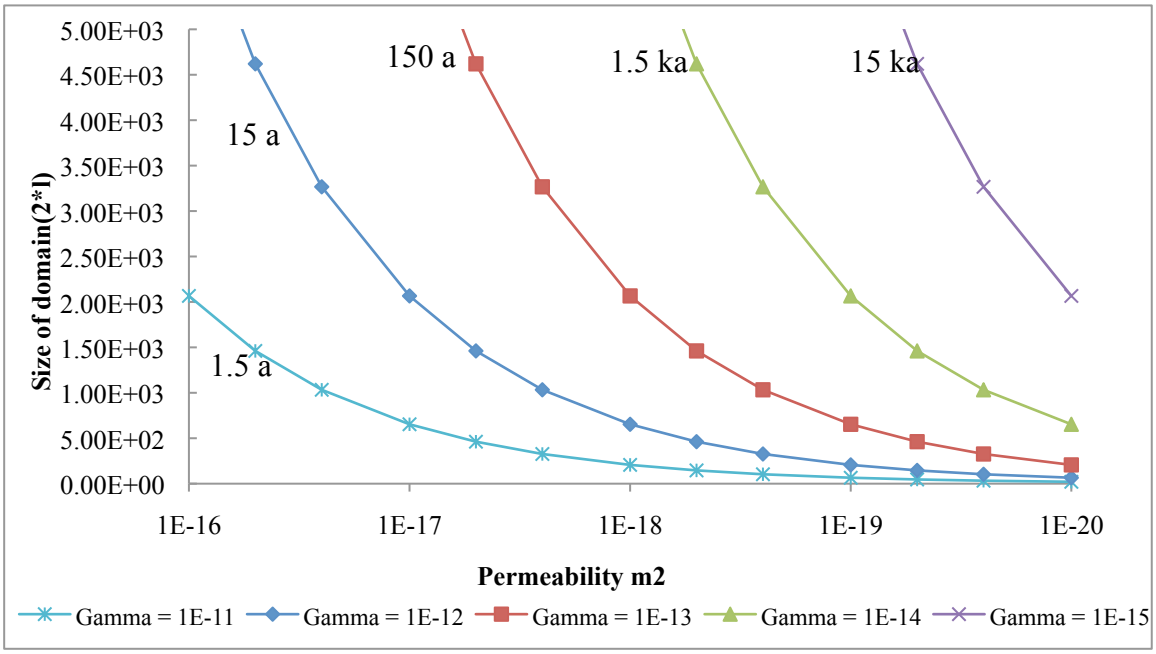


**Figure 14 Size of domain required to create 600 m of head, relative to rock permeability, for a range of rates of geological forcing. The time required to near completion is a function of the rate of forcing, therefore the time required to reach 90% of the hydraulic head (using a specific storage of $10^{-7}m^{-1}$) are indicated for each curve.**

The known physical parameters of the Rotokawa Andesite require a relatively large domain size to force overpressures using internal forcing. Two scenarios could reduce the size of the domain to more realistic values (e.g., ≤ 200 m: Dempsey, Rowland, et al., 2012): 1) increase the rates of geological forcing above the reported values, or 2) reduce the permeability of the Rotokawa Andesite. The highest rate of geological forcing reported in the literature is on the order of $10^{-13}$ $s^{-1}$ .The TVZ is known for its exceptional heat flow (Bibby et al., 1995), and it is possible that the rate of porosity change could also be extreme. However, further work would have to be conducted in order to assess this possibility.

It is common for rocks to have permeability on the order of $10^{-20}$ $m^2$ or lower (Neuzil, 1995). If the mineral deposition in fracture networks was accompanied by 'whole-sale' alteration of the host rock, it is likely that the permeability of the rock could be affected. Lower permeability ($< 10^{-20}$ $m^2$) would allow significant overpressures for smaller sized domains (> 75 m), to create the overpressures required to open tensile fractures. Even the presence of extremely low permeability material, such as fault gouge which can be as low as $10^{-22}$ $m^2$, (Manning and Ingebritsen, 1999) would have to be 7.5 m large to force overpressures required for failure, which is unrealistically large for fault gouge material.

It is important to note though that reducing the bulk permeability of rock below $10^{-16}$ $m^2$ is likely to impede hydrothermal convection (Cathles et al., 1997; Manning and Ingebritsen, 1999; Rowland and Sibson, 2004). If the size of the domain required to force overpressure were on the same order of magnitude as the size of the geothermal field, then the convection of the geothermal system would have to be effectively stopped for a minimum of 19 years, in order to generate overpressure significant enough to induce failure of the Rotokawa Andesite.

### 5.1.2 Disequilibrium overpressure in the Rotokawa reservoir generated by a constant flux of fluid

The effect that a constant flux of fluids would have on the head generated in the Rotokawa reservoir is examined in this section. When using this model, it is assumed that the constant flow of fluid into the Rotokawa reservoir domain is due to the convective flow of fluids. However, roughly 6 to 9% of the convecting fluids are

magmatic in origin (Giggenbach, 1995). This scenario would also be applicable if fluid flux was entirely due to magmatic fluids.

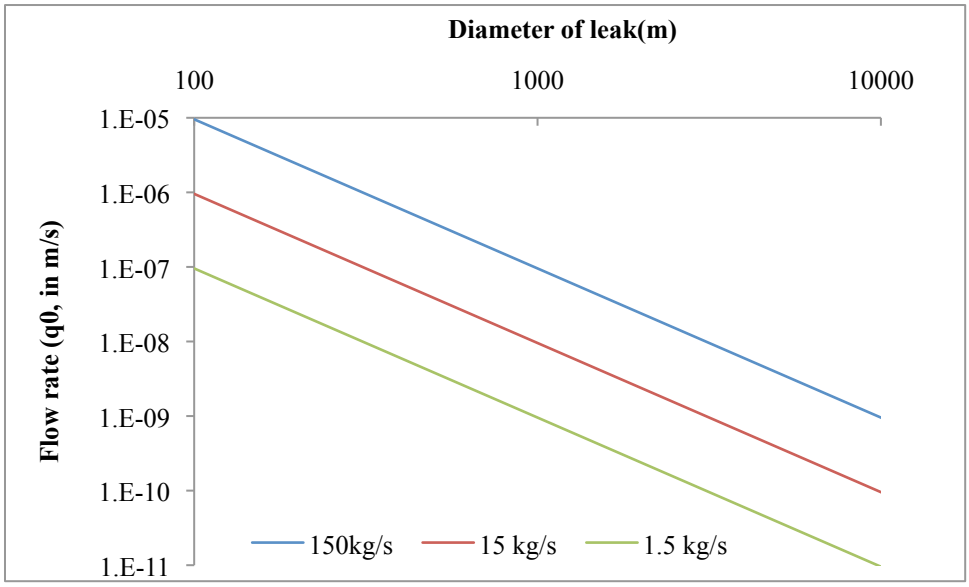


**Figure 15 Estimate of $q_0$ depending on the diameter of the area through which the flow is allowed. Based on a constant total flow rate of 150, 15 and 1.5 kg/s, and a molar mass of 18015 mol/kg. The flow rate is halved, as the model assumes a flow in both directions from the slab.**

The three parameters that can influence overpressures in such a situation are the permeability of the medium, the size of the domain and the flow rate into the domain (see equation 10). The total mass flow is roughly known for the Rotokawa Geothermal Field for the current bulk permeability. However a change in either the bulk permeability or the effective size of the area through which mass flow is allowed would have a profound effect on the one-dimensional flow-rate (Figure 15). Reducing bulk permeability will reduce the mass flow rate. A focussed flow, for the same volume will naturally induce a larger flow rate; assuming that processes that could focus flow will not affect the total volume of fluid flow.

Domain size is critical for reservoir pressures. In general, Figure 16 shows that relatively small domains can be overpressured at realistic flow rates, even for high

permeabilities. The size of the domain is extremely sensitive to permeability at larger domain sizes, for a given flow rate.

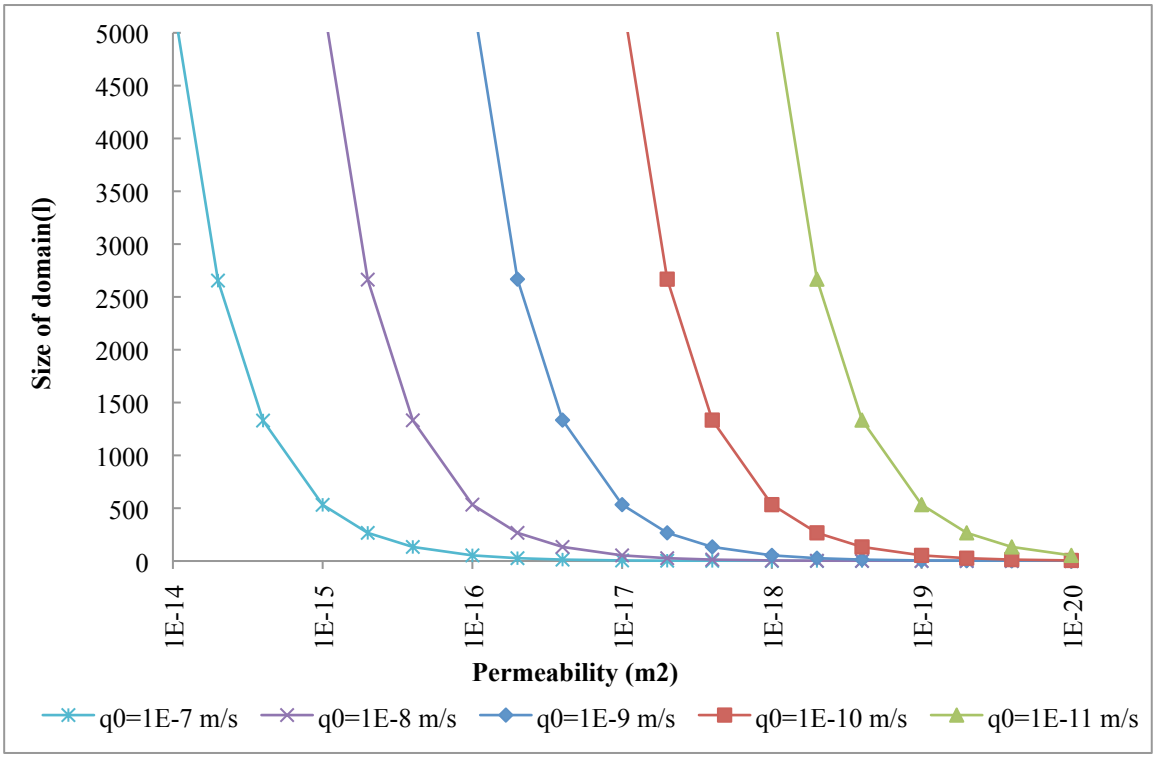


**Figure 16 Domain size vs. permeability graph required for creating overpressures that will open tensile fractures for a range of flow rates ($q_0$).**

The times required to generate the overpressures vary enormously depending on the given conditions. At high flow rates ($10^{-7}$ m/s), the time required to generate overpressures is almost instantaneous compared to the surroundings. Even at lower flow rates the time required is relatively short at lower permeabilities (Figure 17).

1

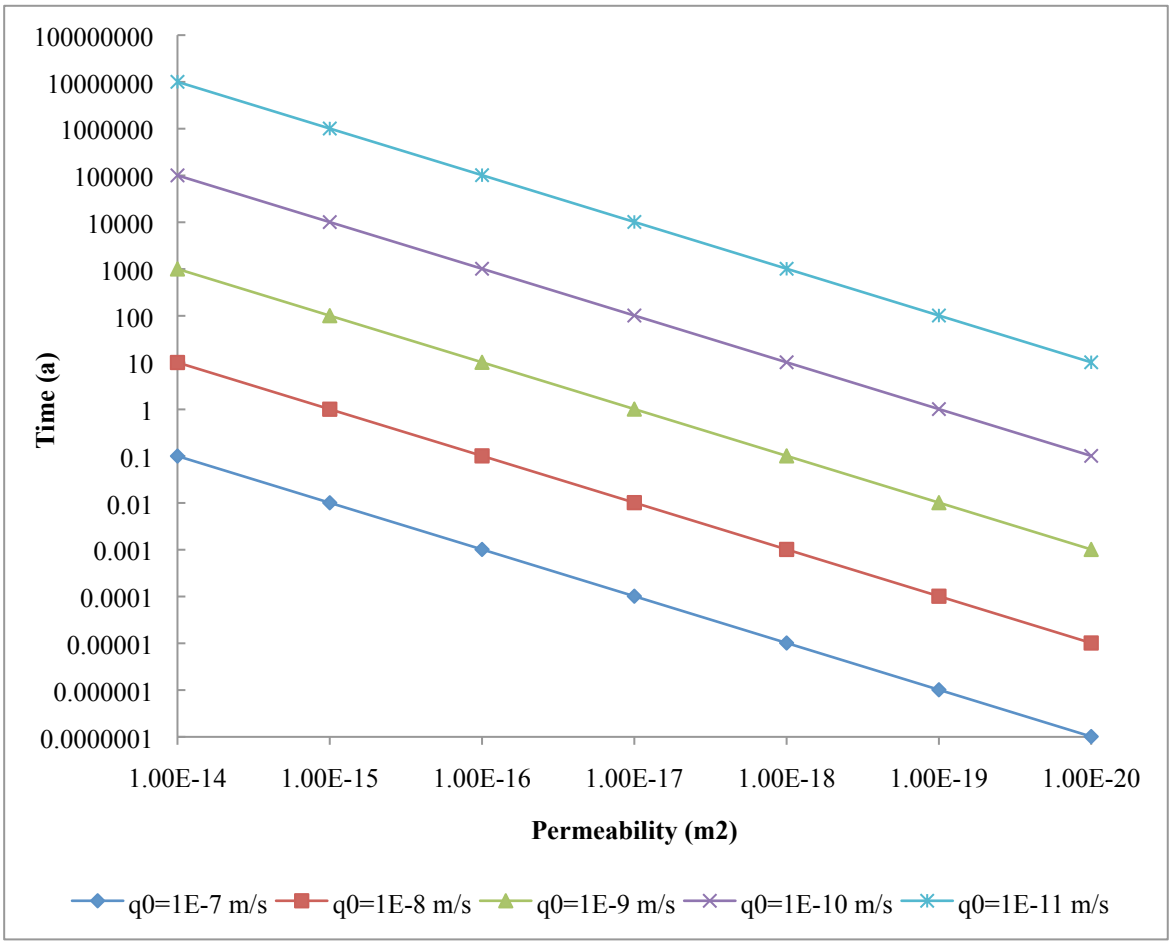


**Figure 17 Log-log plot of permeability of domain, versus time to reach 90% of overpressure required to induce fracturing for various flow rates. Using a specific storage of $10^{-7}$ $m^{-1}$.**

### 5.1.3 Comparing both models

Two models are proposed for the generation of overpressures, one with an internal source of fluids within the layer, and another with an external source of fluids. The internal forcing model of Neuzil (1995) has been utilised to describe general permeability and overpressure generation in geothermal and metamorphic systems (Manning and Ingebritsen, 1999), including for geothermal systems in the TVZ (Sibson and Rowland, 2003; Rowland and Sibson, 2004; Rowland and Simmons, 2012). It is

more elegant, in a sense, than the alternative presented here, as it provides a drive for flow, and also the flow is a function of the permeability of the system. In the alternative external forcing model, the flow rate is imposed on the system and does not explicitly take into account the permeability of the system, although it is clear that the flow rate entering the model will be a function of permeability. This makes it difficult to assess the flow rates through the system, if the bulk permeability conditions were to change (Figure 15) through processes such as fracture mineralisation (bulk permeability decrease) or fracture creation or reactivation (bulk permeability increase).

However, the geological forcing model (internal forcing) proposed by Neuzil (1995) requires large domains with low permeabilities to generate the overpressures required for failure to occur, since the domain size has a low sensitivity to the rate of geological forcing. The constant flux model (external forcing) on the other hand has a domain size that is more sensitive to the flux of fluids (Figure 18).

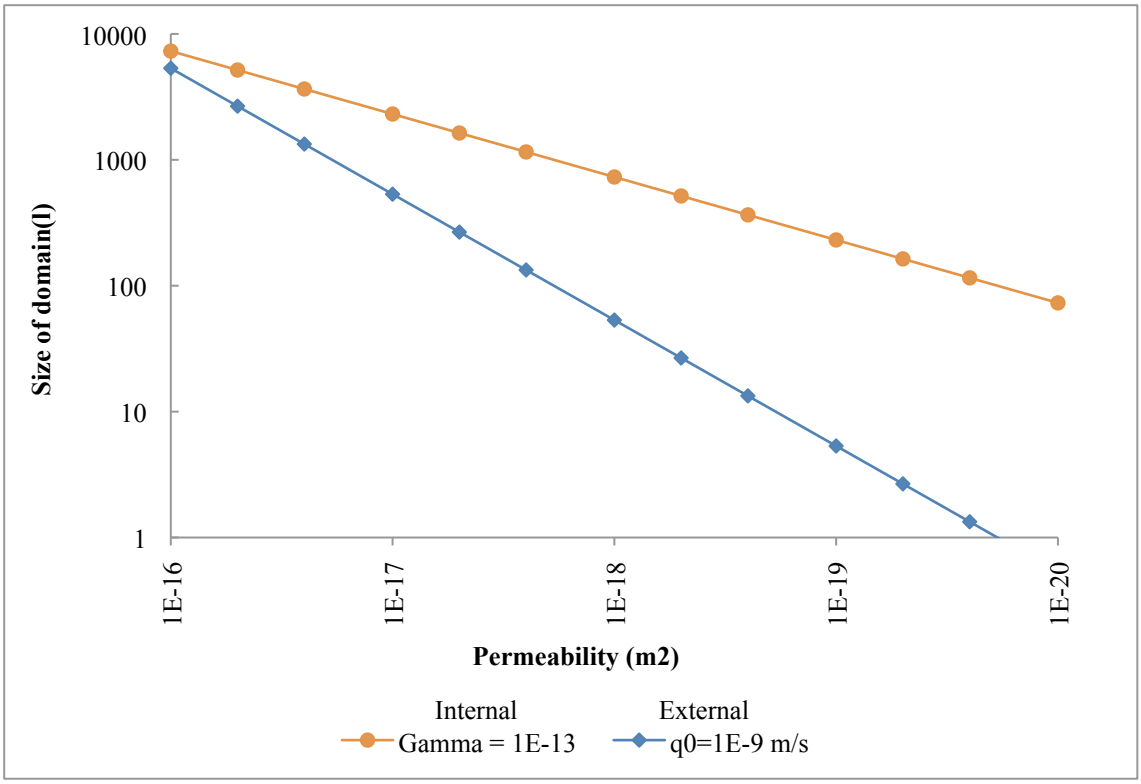


**Figure 18 Log-log plot comparing both internal and external forcing models.**

If the rates of geological forcing published in the literature apply here, then either unrealistically large domains are required for overpressure induced failure, or extreme, undocumented circumstances are required for overpressures to lead to failure of the Rotokawa Andesite. However, if flow rates through the Rotokawa geothermal system are focussed through a smaller area of flow, overpressures at much smaller scales could lead to failure, even at permeabilities consistent with current rock bulk permeabilities.

The one-dimensional analytical models described here are overly simplified and give a general understanding of actual processes leading to fluid overpressure at best. However, the use of multiple datasets retrieved from the Rotokawa Geothermal Field, coupled with the simple models, provide enough leverage to suggest that in order to induce tensile or shear failure through fluid overpressure, internal forcing of fluids

(such as permeability/porosity reduction or mineral devolatilisation) is not a realistic model. An external source of fluid forcing (such as convection of fluids or magmatic gas flux) is more likely to generate overpressure-induced failure in the Rotokawa Andesite. Admittedly, numerical models that demonstrate the process would give more weight to this statement.

## 5.2 Mode of failure of the Rotokawa Andesite

Rock mass properties are used here to predict the primary mode of failure for the Rotokawa Andesite in its current state. It is possible to make an assessment of the rock mass behaviour of the Rotokawa Andesite, using the available core and rock strength data collected (Figure 10). In the case the processes that lead to large-scale failure in a jointed rock mass are discussed, that it is appropriate to use the Hoek-Brown criterion, even if just to demonstrate the effect of rock mass failure. In this case it is clarified that rock mass failure is defined as the occurrence of irreversible strain, caused by the slip, creation and/or amalgamation of new/pre-existing fractures. Given that fractures are important contributors to the Rotokawa Andesite permeability, understanding the process that created the fracture sets observed could be crucial to mapping out permeability within the reservoir.

In the absence of stress-relieving faults, failure of the average Rotokawa Andesite rock mass could occur in two ways; 1) increasing differential stress (strain induced) but maintaining the maximum principal stress constant, and 2) decreasing the average stress, but maintaining the differential stress constant (fluid induced). In order to show the effect of depth on the rock mass failure, two scenarios are presented for the

Rotokawa reservoir; one with stresses consistent for -800 mrL (Figure 19 and Figure 21), and second for stresses at -1200 mRL (Figure 20 and Figure 22). In every case, the Mohr circle representing the initial stress condition is illustrated along with the Mohr circle where failure is induce in the average rock mass.

One possible scenario leading to rock failure is the case where a cohesive Rotokawa Andesite is subject to a fixed strain associated with horizontal tectonic extension. The magnitude of the minimum principal stress will diminish until failure is achieved. The results show that for an average and weakest rock mass, failure occurs in the positive normal stress domain with a shear mode (Figure 19 & Figure 20). By contrast, the strongest rock mass would fail under tensile conditions, whereby tensile fracture propagation would dominate, however the strongest rock mass is rare (e.g. Figure 9).

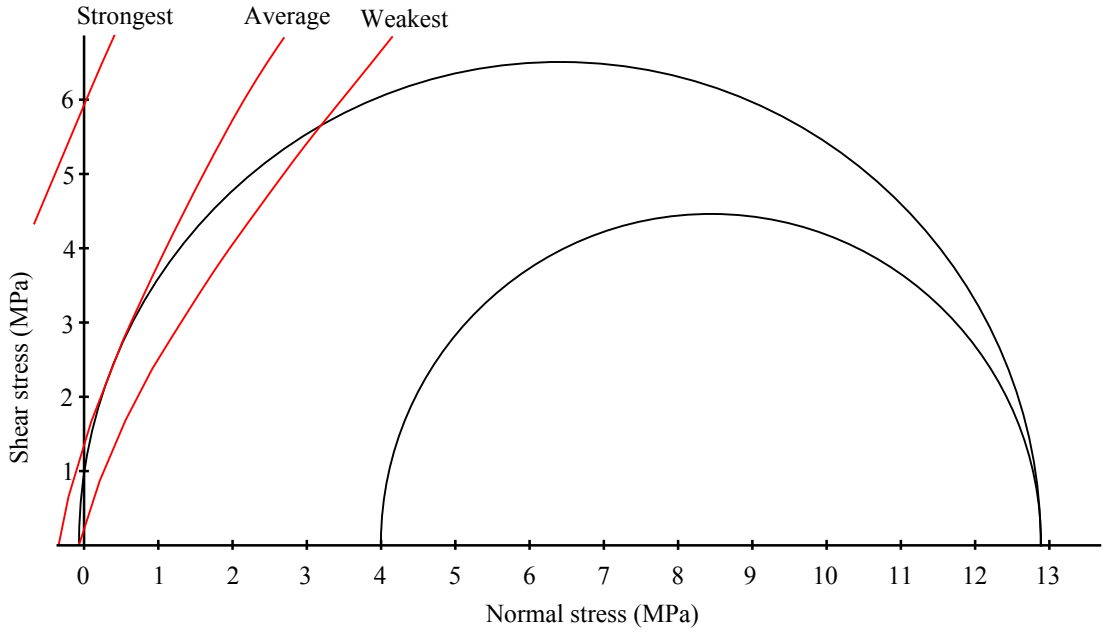


**Figure 19 Mohr diagram showing the increase in differential stress leading to failure. Stress equivalent to -800 mRL (see Figure 8 in Chapter 3).**

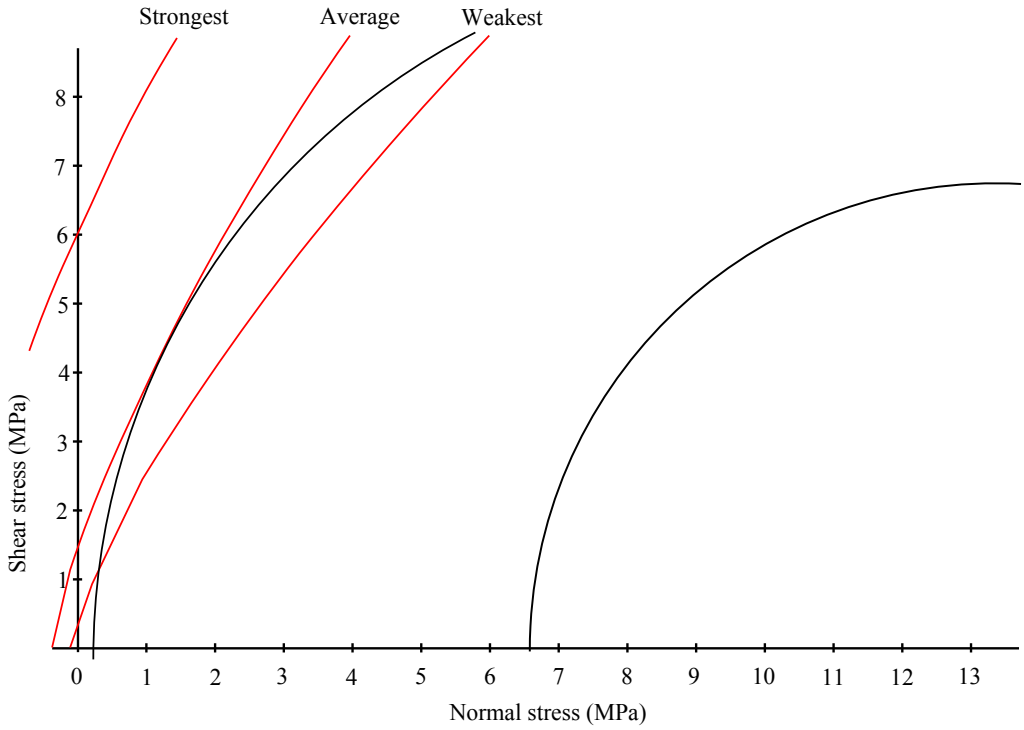


**Figure 20 Mohr diagram showing the increase in differential stress leading to failure. Stress equivalent to -1200 mRL (see Figure 8 in Chapter 3).**

Increasing pore pressure could also lead to rock failure. In such a scenario, the differential stress remains equal, only the magnitudes of the effective principal stresses are affected. In both examples given here, (Figure 21 & Figure 22) failure occurs in shear mode for the average rock mass, although at shallower depths, failure is nearly tensional. A minimal improvement in the condition of the rock mass could lead to failure occurring in tensile conditions, instead of compression. In both examples (Figure 21 & Figure 22), tensile fracture would propagate for the strongest rock mass.

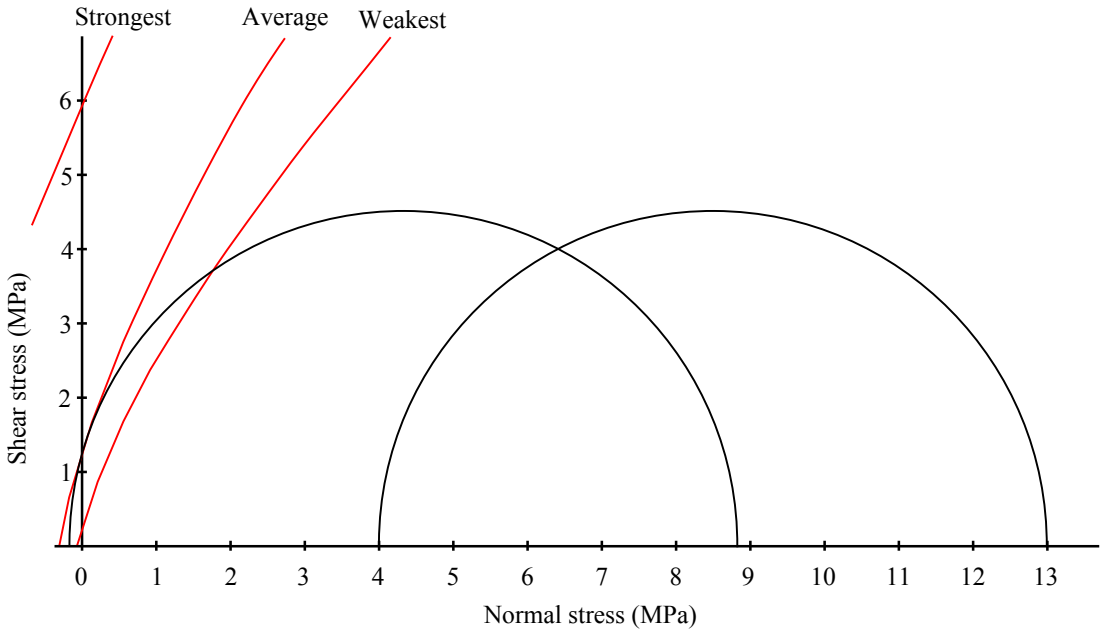


**Figure 21 Mohr diagram showing the increase in pore pressure leading to failure. Stress equivalent to -800 mRL (see Figure 8 in Chapter 3).**

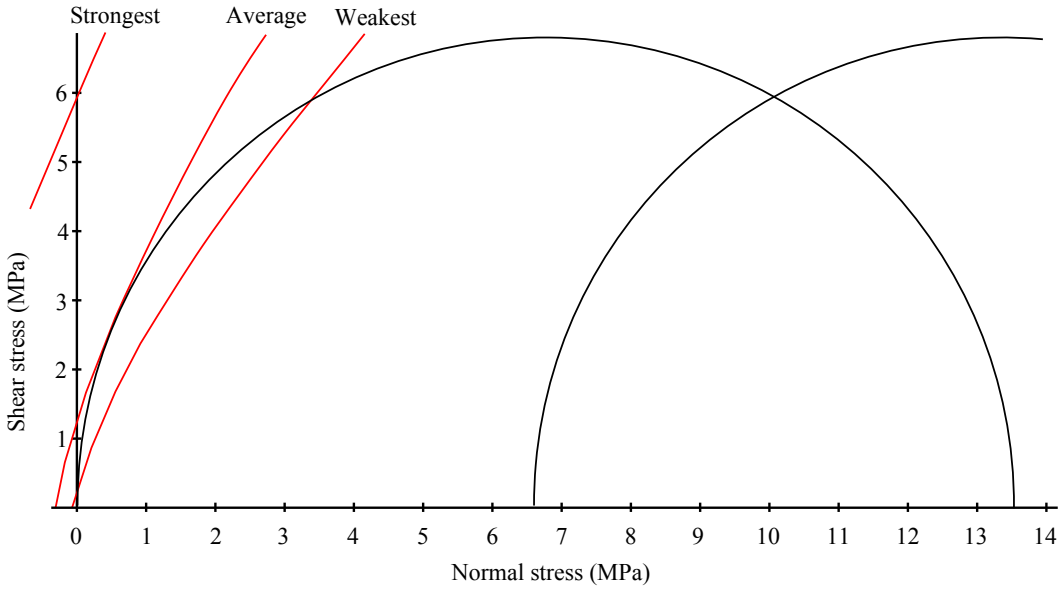


**Figure 22 Mohr diagram showing the increase in pore pressure leading to failure. Stress equivalent to -1200 mRL (see Figure 8 in Chapter 3).**

The rock mass failure conditions were presented, coupled with the estimated state of stress in the Rotokawa reservoir. This lead to the conclusion that with current average rock conditions, shear failure is the most likely mode of failure. However, a minimal

increase in the average rock mass conditions, such as larger spaced discontinuities, a reduced fracture pervasiveness, or increased irregularity on fractures, would cause the rock mass to favour the propagation of tensile fractures. Although the occurrence of the strongest rock mass recorded in the Rotokawa Andesite is rare, it is important to note that it favours tensile fractures in all examples given here.

A recurring theme when considering failure is the importance of scale. The first example was the effect of permeability- the scale at which measurements are performed is crucial. The consequence of this observation was that relatively large domains are required when considering fluid overpressures, unless conditioning of the rock, reducing bulk permeability, has occurred. Strain-induced stress changes occur as a result of tectonic process, which also occur on large scales. In the case of rock mass behaviour, it is assumed that the changes in stress leading to failure are occurring on a relatively large scale, to be precise, at least an order of magnitude larger than the spacing of discontinuities. This assumption is reasonable given the constraints above. However, if stress changes were occurring on a smaller scale (i.e. a high external flux of fluids), the rock would not act as 'Hoek material', and it would be more appropriate to use the 'intact' rock scenario in Figure 10 to describe failure of the Rotokawa Andesite, which, at a glance, will overwhelmingly favour tensile failure.

### 5.3 Observed orientation of fractures in the Rotokawa Andesite

The high densities of fractures are usually oriented within 26º of $\sigma_3$ (Figure 11 - Figure 13). This is consistent with shear fractures forming through 'Healy' faulting. Many of

these fractures plot close to the angle expected for tensile fractures, however the current main failure mechanism is expected to be shear failure (Section 5.2).

In one case, the fracture orientations depart from the norm. In the RK18L2 well, a large population of fractures have near-vertical dips and strike N-S. One third of this population of near-vertical fractures were sampled from the interval 2220-2250 mRF, where the well may have penetrated a fault or fracture zone oriented N-S. These N-S structures may have formed by reactivation of similarly oriented basement fabric (Seebeck et al., 2010; Seebeck, 2012)

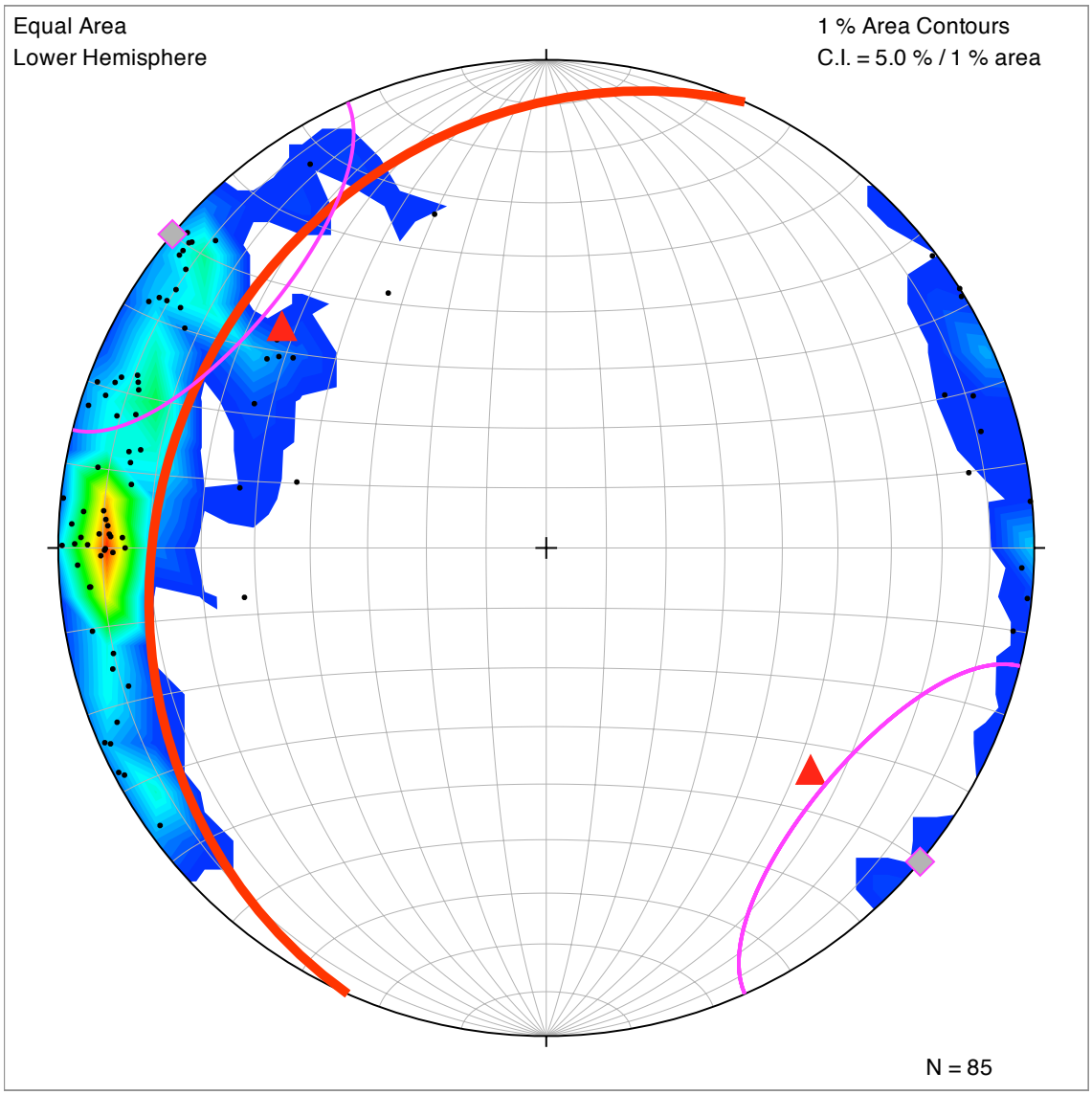


**Figure 23 Lower hemisphere equal-area stereonet (Allmendinger et al., 2012) showing poles to fractures imaged by AFIT in well RK18L2 in the interval 2220-2250 mRF. Contouring is corrected to take sampling bias into account.**

## 5.4 Mechanical behaviour over time.

The Rotokawa Andesite rock mass characterisation is based on fractures observed in core. It is difficult to ascertain whether the origin of these fractures is related to the emplacement of the lavas and breccias, or whether they are later stage fractures formed by tectonic, volcano-tectonic or geothermal processes. In a number of cases, striations

have been observed on fracture surfaces (Rae et al., 2010; Ramirez et al., 2010), suggesting that they have accommodated shear displacement and are most likely to have formed in association with tectonic processes. Supporting this observation, the majority of fractures observed in the acoustic images of wells strike NE-SW (parallel to the Taupo rift), which may indicate a tectonic origin (Figure 11 - 13). Primary fractures such as cooling joints are restricted to individual flow units. Assuming that these fracture types are less continuous than tectonic fractures, then the rock mass of pristine andesite lavas and breccias could have been stronger compared to the present day rock mass. As shown in Figure 19 - 22, even a slight increase in rock mass strength could result in a change in failure mode and favour tensile failure.

Assuming that the Rotokawa Andesite rock mass was stronger before the advent of tectonic fractures and faults, the initial mode of failure is expected to be dominated by tensile fractures. However, continued brittle failure induced by the extension of the TVZ will create large-scale fractures, reducing the rock mass strength, and the rock mass will eventually favour shear failure. Once larger scale tectonic fracture and faults are created, it would be difficult to return to shear failure conditions, unless fracture were sealed, and rock strength was altered over a large interval.

## 6 CONCLUSIONS

Failure of the Rotokawa Andesite can either be caused by the constant tectonic strain imposed on the system, or by an increase in fluid pressure. However, it is unlikely that the overpressures required to induce rock mass failure would be solely generated by porosity/permeability reduction in the Rotokawa geothermal reservoir. It is likely that a

constant external flux of fluids is required to generate the overpressures. Focussing the same volume of flow through a smaller area (increasing the flux) will generate overpressure over small distances even at high permeabilities.

The large-scale failure of the Rotokawa Andesite can be modelled as a rock mass using the Hoek-Brown failure criterion. The examples given here show that shear failure is the current dominant mode of failure for the Rotokawa Andesite at depths below -800 mRL. However, small scale changes in stress, or an increase in rock mass strength would favour tensile failure.

High densities of fractures in the three wells imaged in the Rotokawa Andesite are predominantly oriented within 26º of the minimum principal stress. These orientations are consistent with fractures formed in shear mode during pure triaxial deformation of rock, confirming the results from the Hoek-Brown failure criterion. There is also a high density of N-S oriented structures in the deeper part of one well, an orientation consistent with basement fabrics observed elsewhere in the TVZ. It is proposed that 'Healy' faulting is the main mode of fracture formation in the Rotokawa Andesite, promoting fluid flow within the rock.

## 7 REFERENCES

Allmendinger, R.W., Cardozo, N.C., Fisher, D., 2012. Structural Geology Algorithms: Vectors & Tensors, First. ed. Cambridge University Press, Cambridge, England.

Anderson, E.M., 1951. Dynamics of Faulting and Dyke Formation with Applications to Britain.

Arehart, G., Christenson, B.W., Wood, C., Foland, K., Browne, P.R.L., 2002. Timing of volcanic, plutonic and geothermal activity at Ngatamariki. New Zealand. J Volcan Geotherm. Res 116, 201–214.

Ashby, M., Sammis, C., 1990. The Damage Mechanics of Britte Solids in Compression. Pure Appl. Geophys. 133, 489–521.

Barton, C.A., Zoback, M.D., Moos, D., 1995. Fluid flow along potentially active faults in crystalline rock. Geology 23, 683–686.

Bégué, F., Gravley, D.M., Chambefort, I., Deering, C., Kennedy, B., 2014. Magmatic volatile distribution as recorded by rhyolitic melt inclusions in the Taupo Volcanic Zone, New Zealand. Geol. Soc. London, Spec. Publ. in press.

Bertrand, E.A., Caldwell, T.G., Hill, G.J., Wallin, E.L., Bennie, S.L., Cozens, N., Onacha, S. a., Ryan, G. a., Walter, C., Zaino, A., Wameyo, P., 2012. Magnetotelluric imaging of upper-crustal convection plumes beneath the Taupo Volcanic Zone, New Zealand. Geophys. Res. Lett. 39, 1–6.

Bibby, H.M., Caldwell, T.G., Davey, F., Webb, T.H., 1995. Geophysical evidence on the structure of the Taupo Volcanic Zone and its hydrothermal circulation. J. Volcanol. Geotherm. Res. 68, 29–58.

Blenkinsop, T.G., 2008. Relationships between faults, extension fractures and veins, and stress. J. Struct. Geol. 30, 622–632.

Boseley, C., Cumming, W., Urzúa-monsalve, L., Powell, T., Grant, M.A., 2010. A Resource Conceptual Model for the Ngatamariki Geothermal Field Based on Recent Exploration Well Drilling and 3D MT Resistivity Imaging, in: Proceedings World Geothermal Congress 2010. Bali, Indonesia, p. 8.

Brace, W.F., 1960. An extension of the Griffith theory of fracture to rocks. J. Geophys. Res. 65, 3477.

Brace, W.F., 1980. Permeability of crystalline and argillaceous rocks. Int. J. Rock Mech. Min. Sci. Geomech. Abstr. 17, 241–251.

Brace, W.F., 1984. Permeability of crystalline rocks: New in situ measurements. J. Geophys. Res. 89, 4327.

Brace, W.F., Paulding, B.W.J., Scholz, C.H., 1966. Dilatancy in the fracture of crystalline rocks. J. Geophys. Reserach 71, 3939–3953.

Bredehoeft, J.D., 1997. Fault permeability near Yucca Mountain. Water Resour. Res. 33, 2459–2463.

Browne, P.R.L., 1978. Hydrothermal alteration in active geothermal fields. Annu. Rev. Earth Planet. Sci. 6, 229–250.

Browne, P.R.L., 1979. Minimum age of the Kawerau Geothermal Field, North Island, New Zealand. J. Volcanol. Geotherm. Res. 6, 213–215.

Browne, P.R.L., Lawless, J. V, 2001. Characteristics of hydrothermal eruptions, with examples from New Zealand and elsewhere. Earth-Science Rev. 52, 299–331.

Carslaw, H., Jaeger, J.C., 1959. Conduction of heat in solids, second edi. ed. Clarendon Press, Oxford.

Cathles, L., Erendi, A., Barrie, T., 1997. How Long Can a Hydrothermal System Be Sustained by a Single Intrusive Event. Econ. Geol. 92, 766–771.

Chen, Q., Nur, A., 1992. Pore fluid pressure effects in anisotropic rocks: Mechanisms of induced seismicity and weak faults. Pure Appl. Geophys. PAGEOPH 139, 463–479.

Coulomb, C.A., 1773. Essai sur une application des règles de maximis & minimis à quelques problèmes de statique, relatifs a l'architecture. Mémoires Mathématique Phys. présentés à l'Académie R. des Sci. par Divers Savans, lûs dans ses Assem. 7, 343–382.

Cox, S., 2005. Coupling between deformation, fluid pressures, and fluid flow in ore-producing hydrothermal systems at depth in the crust. Econ. Geol. 100th Anniv. Vol. 39–75.

Dempsey, D., Ellis, S., Archer, R., Rowland, J. V, 2012. Energetics of normal earthquakes on dip-slip faults. Geology 40, 279–282.

Dempsey, D., Rowland, J. V, Zyvoloski, G.A., Archer, R.A., 2012. Modeling the effects of silica deposition and fault rupture on natural geothermal systems. J. Geophys. Res. 117, B05207.

Fairhurst, C., 1964. On the validity of the "Brazilian" test for brittle materials. Int. J. Rock Mech. Min. Sci. Geomech. Abstr. 1, 535–546.

Friedman, M., Handin, J., Alani, G., 1972. Fracture-surface energy of rocks. Int. J. Rock Mech. Min. Sci. Geomech. Abstr. 9, 757–766.

Gaarenstroom, L., Tromp, R.A.J., de Jong, M.C., Brandenburg, A.M., 1993. Overpressures in the Central North Sea: implications for trap integrity and drilling safety, in: Petroloeum Geology of Northwest Europe: Proceedings of the 4th Conference. pp. 1305–1313.

Giggenbach, W., 1995. Variations in the chemical and isotopic composition of fluids discharged from the Taupo Volcanic Zone, New Zealand. J. Volcanol. Geotherm. Res. 68, 89–116.

Grant, M.A., Bixley, P.F., 2011. Geothermal Reservoir Engineering. Academic Press.

Grant, M.A., Wilson, D., 2007. Intereference Testing at Kawerau 2006-2007, in: New Zealand Geothermal Workshop 2007 Proceedings.

Griffith, A., 1921. The Phenomena of Rupture and F low in Solids. Phil. Trans. Roy. Soc.(Lon.) A 221, 163–198.

Hanshaw, B.B., Bredehoeft, J.D., 1968. On the Maintenance of Anomalous Fluid Pressures: II. Source Layer at Depth. Geol. Soc. Am. Bull. 79, 1107–1122.

Hanshaw, B.B., Hill, G.A., 1969. Geochemistry and hydrodynamics of the Paradox Basin region, Utah, Colorado and New Mexico. Chem. Geol. 4, 263–294.

Hatherton, T., Macdonald, W., Thompson, G., 1966. Geophysical methods in geothermal prospecting in New Zealand. Bull. Volcanol. 29, 485–497.

Healy, D., 2009. Anisotropy, pore fluid pressure and low angle normal faults. J. Struct. Geol. 31, 561–574.

Healy, D., Jones, R.R., Holdsworth, R.E., 2006. Three-dimensional brittle shear fracturing by tensile crack interaction. Nature 439, 64–7.

Hoek, E., 2006. Practical Rock Engineering.

Hoek, E., Bieniawski, Z., 1965. Brittle fracture propagation in rock under compression. Int. J. Fract. Mech. 1, 137–155.

Hoek, E., Brown, E., 1980. Empirical Strength Criterion for Rock Masses. J. Geotech. Eng. Div. 106, 1013–1035.

Hubbert, M.K., Rubey, W.W., 1959. Role of Fluid pressure in Mechanics of overthrust faulting. Geol. Soc. Am. Bull. 70, 115.

Klimczak, C., Schultz, R.A., Parashar, R., Reeves, D.M., 2010. Cubic law with aperture-length correlation: implications for network scale fluid flow. Hydrogeol. J. 18, 851–862.

Leaver, J.D., 1986. A Technical Review of Interference Testing with Application in the Ohaaki Geothermal Field.

Leonard, G.S., Begg, J.G., Wilson, C.J.N., 2010. Geology of the Rotorua Area: scale 1:250,000. Low. Hutt Inst. Geol. Nucl. Sci. Ltd. 102.

Lockner, D.A., 1993. The role of acoustic emission in the study of rock fracture. Int. J. Rock Mech. Min. Sci. Geomech. Abstr. 30, 883–899.

Manning, C.E., Ingebritsen, S.E., 1999. Permeability of the continental crust: Implications of geothermal data and metamorphic systems. Rev. Geophys. 37, 127.

Manville, V., Wilson, C.J.N., 2004. The 26 . 5 ka Oruanui eruption , New Zealand : a review of the roles of volcanism and climate in the post-eruptive sedimentary response. New Zeal. J. Geol. Geophys. 47, 525–547.

Marinos, V., Marinos, P., Hoek, E., 2005. The geological strength index: applications and limitations. Bull. Eng. Geol. Environ. 64, 55–65.

Massiot, C., McNamara, D., Lewis, B., n.d. Processing and analysis of high temperature geothermal acoustic borehole image logs, New Zealand. submitted.

McNamara, D., Massiot, C., Lewis, B., Wallis, I., n.d. Heterogeneity of structure and stress in the Rotokawa Geothermal Field, New Zealand. prep.

Mielke, P., 2009. Properties of the Reservoir Rocks in the Geothermal Field of Wairakei/New Zealand.

Montazer, P., Wilson, W., 1984. Conceptual Hydrologic Model of Flow in the Unsaturated Zone, Yucca Mountain, Nevada. USGS Water-Resources Invrestigations Rep. 84-4345 55.

Nara, Y., Meredith, P.G., Yoneda, T., Kaneko, K., 2010. Influence of macro-fractures and micro-fractures on permeability and elastic wave velocities in basalt at elevated pressure. Tectonophysics 503, 52–59.

Neuzil, C.E., 1995. Abnormal Pressures as Hydrodynamic Phenomena. Am. J. Sci. 295, 742–786.

O'Brien, J., Mroczek, E., Boseley, C., 2011. Chemical Structure of the Ngatamariki Geothermal Field, Taupo Volcanic Zone, N.Z., in: New Zealand Geothermal Workshop 2011 Proceedings.

Pochee, A., 2010. Mass transfer and hydrothermal alteration in the Rotokawa Andesite , Rotokawa geothermal field , New Zealand, M.Sc. Thesis, Auckland University.

Pollyea, R.M., Fairley, J.P., 2012. Implications of spatial reservoir uncertainty for CO2 sequestration in the east Snake River Plain, Idaho (USA). Hydrogeol. J. 20, 689–699.

Pritchett, J., Rice, L.F., Garg, S.K., 1979. Summary of Reservoir Engineering data: Wairakei Geothermal Field, New Zealand: Geothermal Reservoir Engineering Management Program. Lawrence Berkeley Lab. LBL-8669, GREMP-2 25.

Quinao, J.J., Sirad-Azwar, L., 2012. Correlation of Reservoir Monitoring and Continuous Production Data to Interpret Unexpected Well Behavior in Rotokawa, in: New Zealand Geothermal Workshop 2012 Proceedings. pp. 1–5.

Quinao, J.J., Sirad-azwar, L., Clearwater, J., Hoepfinger, V., Le Brun, M., Bardsley, C., 2013. Analyses and Modelling of Reservoir Pressure Changes to Interpret the Rotokawa Geothermal Field Response to Nga Awa Purua Power Station Operation, in: Thirty-Eight Workshop on Geothermal Reservoir Engineering.

Rae, A.J., 2007. Rotokawa Geology and Geophysics. GNS Sci. Consult. Rep. 2007/83, 11.

Rae, A.J., McCoy-West, A.J., Ramirez, L.E., McNamara, D., 2010. Geology of Production Wells RK30L1 and RK30L2 Rotokawa Geothermal Field. GNS Sci. Consult. Rep. 2010/02, 40.

Ramirez, L.E., McCoy-West, A.J., Rae, A.J., McNamara, D., 2010. Geology of Production Well RK18L2, Rotokawa Geothermal Field. GNS Sci. Consult. Rep. 2010/31, 37.

Ramsey, J.M., Chester, F.M., 2004. Hybrid fracture and the transition from extension fracture to shear fracture. Nature 428, 63–6.

Reches, Z., 1978. Analysis of faulting in three-dimensional strain field. Tectonophysics 47, 109–129.

Reches, Z., Lockner, D.A., 1994. Nucleation and growth of faults in brittle rocks. J. Geophys. Res. 99, 18159.

Rissmann, C., Nicol, A., Cole, J.W., Kennedy, B., Fairley, J.P., Christenson, B., Leybourne, M., Milicich, S., Ring, U., Gravley, D., 2011. Fluid flow associated with silicic lava domes and faults, Ohaaki hydrothermal field, New Zealand. J. Volcanol. Geotherm. Res. 204, 12–26.

Rosenberg, M.D., Bignall, G., Rae, A.J., 2009. The geological framework of the Wairakei–Tauhara Geothermal System, New Zealand. Geothermics 38, 72–84.

Rowland, J. V, Sibson, R.H., 2001. Extensional fault kinematics within the Taupo Volcanic Zone, New Zealand: soft-linked segmentation of a continental rift system. New Zeal. J. Geol. Geophys. 44, 271–284.

Rowland, J. V, Sibson, R.H., 2004. Structural controls on hydrothermal flow in a segmented rift system, Taupo Volcanic Zone, New Zealand. Geofluids 4, 259–283.

Rowland, J. V, Simmons, S.F., 2012. Hydrologic, Magmatic, and Tectonic Controls on Hydrothermal Flow, Taupo Volcanic Zone, New Zealand: Implications for the Formation of Epithermal Vein Deposits. Econ. Geol. 107, 427–457.

Santhanam, A., Gupta, Y., 1968. Cleavage surface energy of calcite. Int. J. Rock Mech. Min. Sci. 5, 253–259.

Screaton, E.J., Wuthrich, D.R., Dreiss, S.J., 1990. Permeabilities, fluid pressures, and flow rates in the Barbados Ridge Complex. J. Geophys. Res. 95, 8997.

Seebeck, H.C., 2012. Normal Faulting, Volcanism and Fluid Flow, Hikurangi subduction Plate Boundary, New Zealand.

Seebeck, H.C., Nicol, A., Stern, T., Bibby, H.M., Stagpoole, V., 2010. Fault controls on the geometry and location of the Okataina Caldera, Taupo Volcanic Zone, New Zealand. J. Volcanol. Geotherm. Res. 190, 136–151.

Seebeck, H.C., Nicol, A., Walsh, J.J., Childs, C., Beetham, R.D., Pettinga, J., 2014. Fluid flow in fault zones from an active rift. J. Struct. Geol. 62, 52–64.

Sewell, S.M., Cumming, W.B., Azwar, L., Bardsley, C., 2012. Integrated MT and Natural State Temperature Interpretation for a Conceptual Model Supporting Reservoir Numerical Modelling and Well Targeting at the Rotokawa Geothermal Field, New Zealand, in: Proceedings: Thirty-Seventh Workshop on Geothermal Reservoir Engineering. Stanford University, Stanford California.

Sewell, S.M., Cumming, W.B., Bardsley, C.J., Winick, J.A., Quinao, J.J., Wallis, I.C., Sherburn, S., Bourguignon, S., Bannister, S., 2013. Interpretation of Microearthquakes at the Rotokawa Geothermal Field, 2008 to 2012, in: New Zealand Geothermal Workshop 2013 Proceedings.

Sibson, R.H., 1987. Earthquake rupturing as a mineralizing agent in hydrothermal systems. Geology 1985–1988.

Sibson, R.H., 1992. Implications of fault-valve behaviour for rupture nucleation and recurrence. Tectonophysics 211, 283–293.

Sibson, R.H., 1996. Structural permeability of fluid-driven fault-fracture meshes. J. Struct. Geol. 18, 1031–1042.

Sibson, R.H., 1998. Brittle failure mode plots for compressional and extensional tectonic regimes. J. Struct. Geol. 20, 655–660.

Sibson, R.H., 2000. Fluid involvement in normal faulting. J. Geodyn. 29, 469–499.

Sibson, R.H., Rowland, J. V, 2003. Stress, fluid pressure and structural permeability in seismogenic crust, North Island, New Zealand. Geophys. J. Int. 154, 584–594.

Siratovich, P.A., Heap, M.J., Villenueve, M.C., Cole, J.W., Reuschle, T., 2014. Physical properties and relationships between microstructure, strength and permeability for the Rotokawa Andesite, the host rock of a significant geothermal reservoir in the Taupo Volcanic Zone, New Zealand. Geotherm. Energy submitted.

Terzaghi, K. von, 1925. Erdbaumechanik auf bodenphysikalischer grundlage.

Terzaghi, R., 1965. Sources of error in joint surveys. Geotechnique 15, 287–304.

Titley, S.R., 1990. Evolution and style of fracture permeability in intrusion-centered hydrothermal systems, in: Comittee, G.S. (Ed.), The Role of Fluids in Crustal Processes. pp. 50–63.

Townend, J., Zoback, M.D., 2000. How faulting keeps the crust strong. Geology 28, 399–402.

Walder, J., Nur, A., 1984. Porosity reduction and crustal pore pressure development. J. Geophys. Res. 89, 11539–11548.

Wallis, I.C., Bardsley, C.J., Powell, T., Rowland, J. V, Brien, J.M.O., 2013. A Structural Model for the Rotokawa Geothermal Field, New Zealand, in: New Zealand Geothermal Workshop 2013 Proceedings.

Wilson, C.J.N., Houghton, B.F., McWilliams, M.O., Lanphere, M. a., Weaver, S.D., Briggs, R.M., 1995. Volcanic and structural evolution of Taupo Volcanic Zone, New Zealand: a review. J. Volcanol. Geotherm. Res. 68, 1–28.

Winick, J.A., Powell, T., Mroczek, E., 2009. The Natural-State Geochemistry of the Rotokawa Reservoir, in: New Zealand Geothermal Workshop 2009 Proceedings.

Wiprut, D., Zoback, M.D., 2000. Fault reactivation and fluid flow along a previously dormant normal fault in the northern North Sea. Geology 28, 595–598.

Wright, I.C., 1992. Shallow structure and active tectonism of an offshore continental back-arc spreading system: the Taupo Volcanic Zone, New Zealand. Mar. Geol. 103, 287–309.

# CHAPTER 6:

## Conclusions & Future work

# 1 CONCLUSIONS

Several different methods were used to assess the effect of discontinuities such as faults and fractures on the bulk permeability of rocks, and the conditions required to generate faults and fracturing in rock. Here, the main conclusions of the thesis are summarised and suggestions made for future research.

- The results of radon gas surveys are consistent with the hypothesis that radon anomalies around faults are mainly due to an increase in the emanation potential of soils.
- There is some evidence indicating advective flow of $^{222}Rn$, however this is at specific locations along the Paeroa Fault, most of which are associated with advectively flowing features such as hot springs and fumaroles, confirming the channelized flow of fluids along faults.
- Other researchers have used the lack of a correlation between $^{222}Rn$ and its parent $^{226}Ra$ as evidence for advective flow of $^{222}Rn$ gas. This research proves that this is not always true, as $^{222}Rn$ is affected by small-scale diffusion.
- It is possible to show which Leak-off tests were conducted in permeable formations, and did not open fractures. These tests cannot be used for stress estimations.
- A degree of uncertainty is associated with estimating the weight of the overburden model in a volcanic and volcaniclastic terrain. However, the density variation between stratigraphic units is greater than within.

- Standard methods of modeling the maximum horizontal stress have not constrained this principal stress due to the thermal effects at the wellbore wall not being sufficiently quantified, and the range of mechanical properties of the rocks being too great.
- The estimations of stress from Leak-off Tests are consistent with a crust in frictional equilibrium, where the differential stress in the crust is defined by the frictional properties of the rock. The dependence of stress magnitude on alteration and clay content highlights the fact that slip processes are important in the shallow parts of hydrothermal systems.
- For all possible values of the intermediate stress, a significant population of fractures are oriented prone to slip, even though the intermediate stress must be constrained to precisely quantify the fracture population that will be orientated for slip at Rotokawa.
- The permeability structure in the Rotokawa Andesite is complex, where in some cases slip promotes permeability, and in others slip has a negative effect on permeability.
- Estimating the shear and normal stress ratio of fractures is not an effective method for independently determining zone of high fluid flow on its own; however, it might be an effective tool to combine with other datasets, in order to draw conclusions on the nature of bulk permeability in geothermal wells.
- Failure of the Rotokawa Andesite can either be caused by the constant tectonic strain imposed on the system, or by an increase in fluid pressure. If failure occurs by overpressures, it is likely that a constant external flux of fluids is required to generate the overpressures.

- The large-scale failure of the Rotokawa Andesite can be modelled as a rock mass using the Hoek-Brown failure criterion. Shear failure is the current dominant mode of failure for the Rotokawa Andesite, however, small scale changes in stress, or an increase in rock mass strength would favour tensile failure. The orientations of imaged fractures (within 26º of the minimum principal stress) are consistent with fractures formed in shear mode.

## 2 FUTURE WORK

Future research using radon soil gas surveys could target the sites that could not be explained by diffusion, and assess the cause for these outliers. Other methods, such as deep temperature measurements and $CO_2$ flux measurements could help confirm the advection of gases. Soil samples could verify if the emanation is on the same trend as the main population, or if the anomaly is due to an increase in $^{222}Rn$ emanation. Another promising avenue for the radon sampling is the sampling of geothermal fluids themselves. The presence of $^{220}Rn$ in the steam at Waikite means that it is a useful tool to assess the flow rate and/or the depth to the water table, as the source of $^{220}Rn$ has to be in the liquid. This could potentially be useful when conducting baseline environmental assessments, such as quantifying the variation of geothermal activity at the surface

Future research in stress estimation could include gathering of Leak-off Tests time data from various sources appropriate sources (most deep drilling conduct LOT) to bolster the New Zealand stress data. This could reveal interesting relationships between the state of stress in the crust and various other criteria, as was shown in this study. The

complicated relationship between slip on fractures and permeability has great economic implications, and it would be useful to have a separate line of evidence confirming these conclusions. The method used by Pochee (2010) could be applied to core retrieved from the wells that have been imaged by borehole televiewer, as these wells were drilled after his thesis was completed. This could demonstrate if a high porosity exists in wells where slip has a negative effect on permeability, as suggested in Chapter 4.

The external forcing of fluids is considered important in this thesis using one-dimensional analytical formulae. However, the process could be demonstrated using numerical models, especially since a numerical model of the Rotokawa Geothermal Field exists and is calibrated to the well behaviour. This could be a first step in proving or disproving whether a constant flux of fluids could cause overpressure required to induce failure. Another avenue, which might be promising, is the detailed interpretation of seismic signals. Work done in volcanological forecasting suggests that it is possible to distinguish between tensile and shear failure of rock when interpreting seismic signal (S.Karl, pers.comms. 2013). The constant monitoring of microseismicity at Rotokawa would be a great dataset to try and apply the theory put forth by others.

## 3 REFERENCES

Pochee, A., 2010. Mass transfer and hydrothermal alteration in the Rotokawa Andesite , Rotokawa geothermal field , New Zealand, M.Sc. Thesis, Auckland University

# APPENDICES

**Appendix A – Diffusion model**

The governing equation that is used to model the diffusion of a radioactive gas is:

$$\frac{d^2\theta}{d\xi^2} = \alpha\theta - \beta \tag{1}$$

with:

- $\xi$ is the dimensionless distance, a function of the distance from the base of the considered area (x, in m) and L, the distance from base to the surface, defined as:

  $$\xi = x/L \tag{2}$$

- $\theta$, the dimensionless concentration, a function of concentration at x (C, in mg/kg) and the initial concentration at $x = 0$($C_0$, in mg/kg), defined as :

  $$\theta = C/C_0 \tag{3}$$

- $\alpha$ is the dimensionless decay constant, a function of the decay constant of L, and of the radon isotope $\lambda$(in $s^{-1}$) and the diffusivity of the species in air D ($m^2\ s^{-1}$):

  $$\alpha = \lambda L^2/D$$

- and β is the dimensionless production rate, which is a function of R the species production rate (in kg $s^{-1}$ $m^{-3}$), ρ, the density of air, and L, D and $C_{0:}$

  $\beta = RL^2/D\rho C_0$

By imposing the following boundary conditions:

$$\theta(\xi = 0) = 1;$$
$$\theta(\xi = 1) + \varepsilon \frac{d\theta}{d\xi}(\xi = 1) = 0$$

Here, ε is a function of the mass transfer Biot number, which controls the rate at which the gas is escaping from the soil profile at ξ=1.

We get the following solution:

$$\theta = \frac{(1+\varepsilon\sqrt{\alpha})(\beta-\alpha)e^{\sqrt{\alpha}} + \beta}{\alpha\left[\sinh(\sqrt{\alpha}) + \varepsilon\sqrt{\alpha}\cosh(\sqrt{\alpha})\right]}\sinh(\sqrt{\alpha}\xi) + (1-\frac{\beta}{\alpha})e^{\sqrt{\alpha}\xi} + \frac{\beta}{\alpha}$$

In order to model the highest possible concentration (θ) that could be achieved by diffusion, we consider the distance from 1.2 m depth (i.e. just below our measurement depth) to the surface. At 1.2 m we consider $C_0$ to be the highest possible concentration achievable through production in soil, which we estimate by multiplying the highest $^{220}$Rn concentration measured in the field (i.e. the highest soil radon emanation, 65200

$Bq/m^3$) by the dominant parent ratio from the linear model at Waikite (0.337), which gives us a $C_0$ of 21972 $Bq/m^3$ (or $9.35x10^{-9}$ mg/kg, if $\rho$=1.225 $kg/m^3$).

**Table 1 Parameter values chosen for diffusion model and their respective sensitivity**

| Parameter | Value | Sensitivity |
|---|---|---|
| $C_0$ | $9.35x10^{-8}$ | High |
| L | 1.2 | Medium |
| $\lambda$ | $2.09x10^{-6}$ | High |
| D | 1.2 | Low |
| $\rho$ | 1.225 | Low |
| h | $2.04x10^{-4}$ | Low |
| R | Variable, depending on $^{220}Rn$ | Low-High |

The recharge rate was assumed to be a function of the $^{220}Rn$ emanation rate, and hence the radon soil emanation rate. In this situation, it is practical that radon concentration is measured in $Bq/m^3$, as this measures the number of radon nuclides decaying/$m^3$. We assume that the $^{220}Rn$ concentration that we measure is in secular equilibrium with the production rate, and that therefore the number of radon decay/s is equivalent to the number of radon being produced. In the case of the $^{222}Rn$ production rate, we use the dominant parent ratio in order to estimate the recharge from the $^{220}Rn$ decay rate. The Diffusion model is very sensitive if the Recharge rate is increased (by orders of magnitude), however it is not sensitive at all if decreased. This makes sense, as the

recharge rates we consider would produce more radon than the original concentration, it is increased even slightly.

**Appendix B: Estimating radon emanation from soil samples.**

In order to estimate the radon emanation of a soil sample, we inserted the sample in closed loop with the RAD7 and measured the concentration of $^{222}$Rn and $^{220}$Rn every hour for 24 hours. Since both radon isotopes have much shorter half-life than their parent isotopes, the amount of time required for the daughter to reach secular equilibrium (i.e.: where the daughter production rate matches the daughter decay rate) is only dependent on the daughter half-life. It is generally accepted that 4 half-lives are required for secular equilibrium in such a case. $^{220}$Rn comes into secular equilibrium very quickly (5 min) with its parent, so we used the concentration measured as an estimate of the $^{220}$Rn emanation potential.

However, $^{222}$Rn requires much longer to come into secular equilibrium (16 days), it was more practical to use the build-up of $^{220}$Rn over 1 day to estimate the production rate of $^{220}$Rn. Figure 1 shows the measurements of $^{220}$Rn from a soil sample in blue, with the build-up of radon using our estimated production rate represented by the line in red. This procedure was repeated for all soil samples we measured.

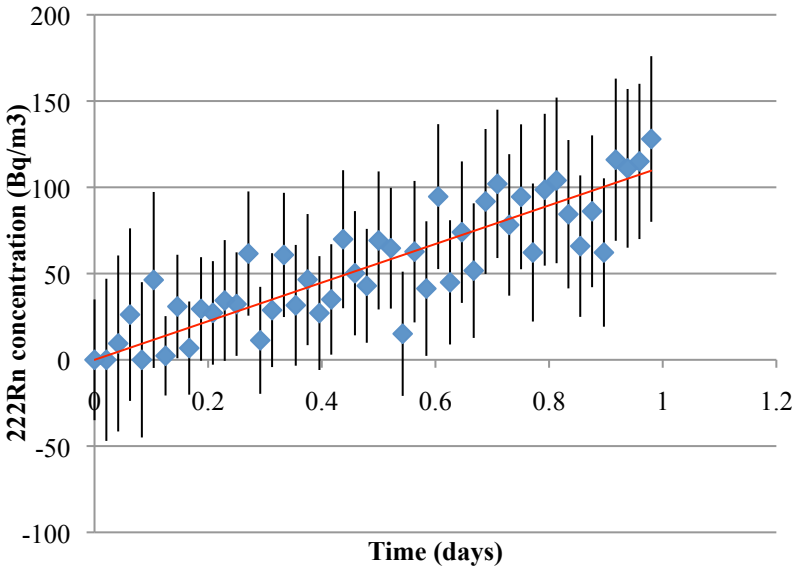


**Figure 1 222Rn measurements from soil sample GK 164.**

**Appendix C , Leak off Test Data.**

The following pages include the pressure vs time graphs, and the dP/dt vs pressure graphs for all the LOT that were interepreted as belonging to either of the three groups mentioned in Chapter 3

**Permeable formation Category**

RK33, -656.95mRL

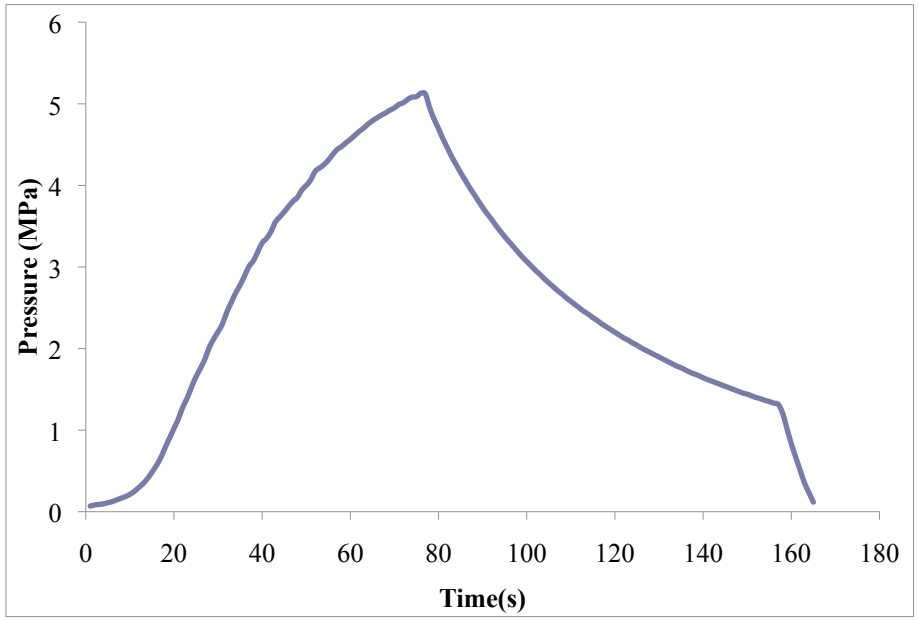


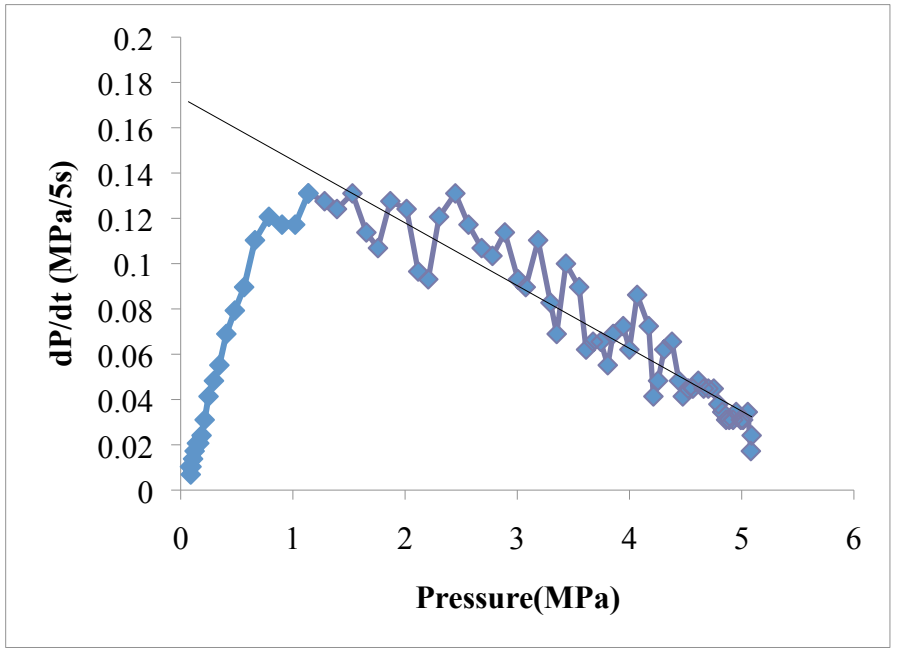

RK 14 -930mRL

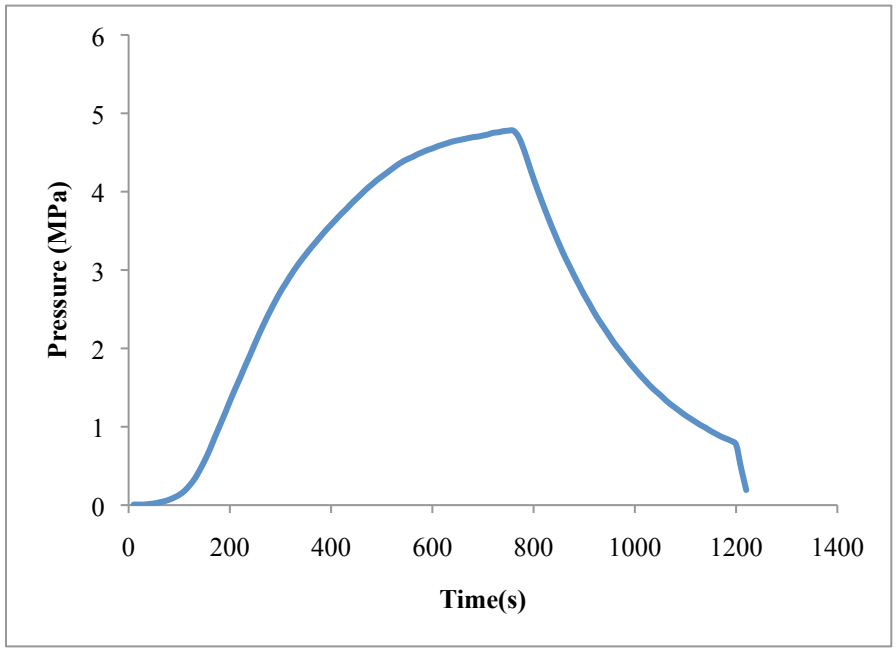
Pressure (MPa)
Time(s)
0
1
2
3
4
5
6
0
200
400
600
800
1000
1200
1400

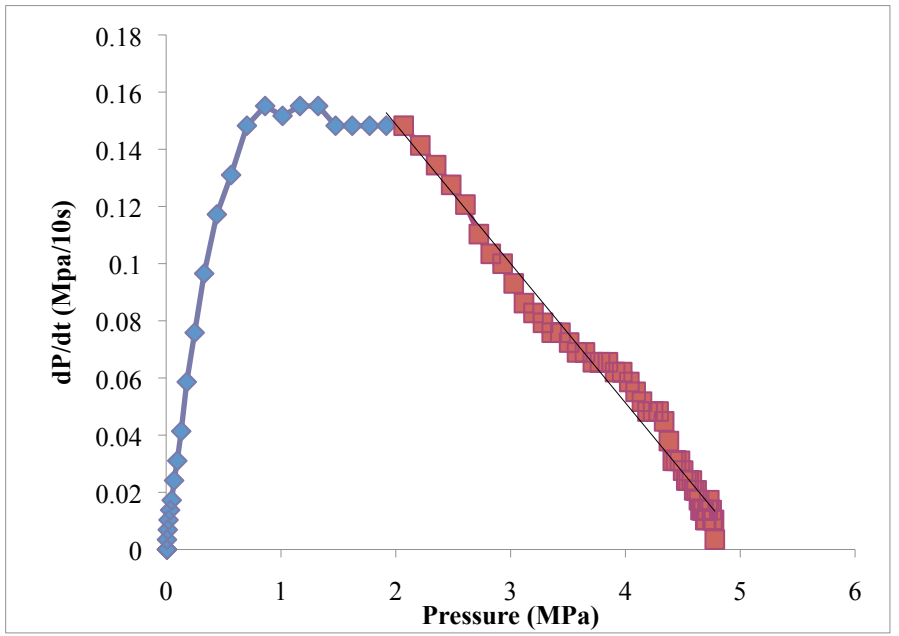
dP/dt (Mpa/10s)
Pressure (MPa)
0
0.02
0.04
0.06
0.08
0.1
0.12
0.14
0.16
0.18
0
1
2
3
4
5
6

RK32, -907.95mRL

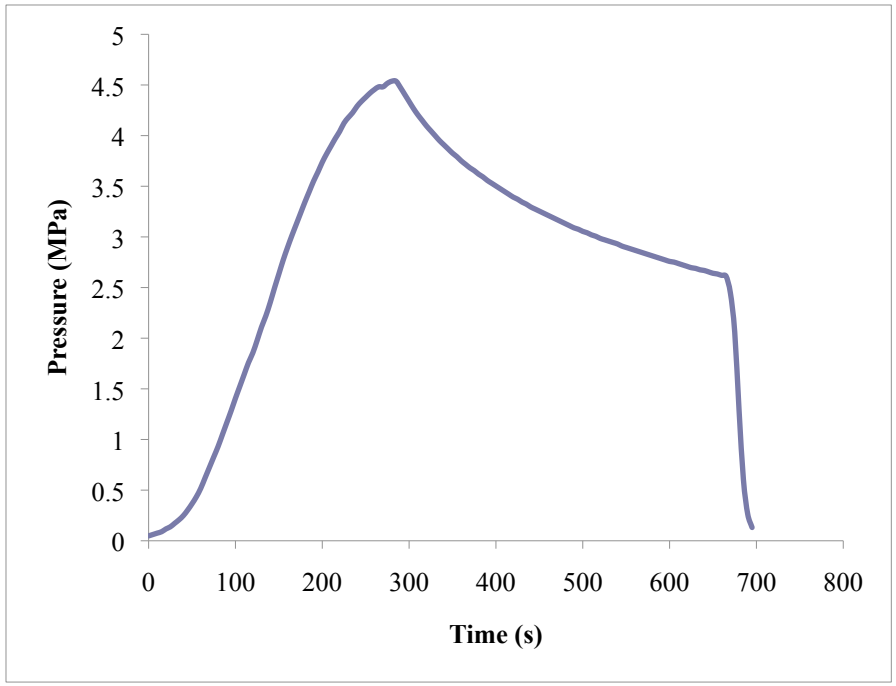


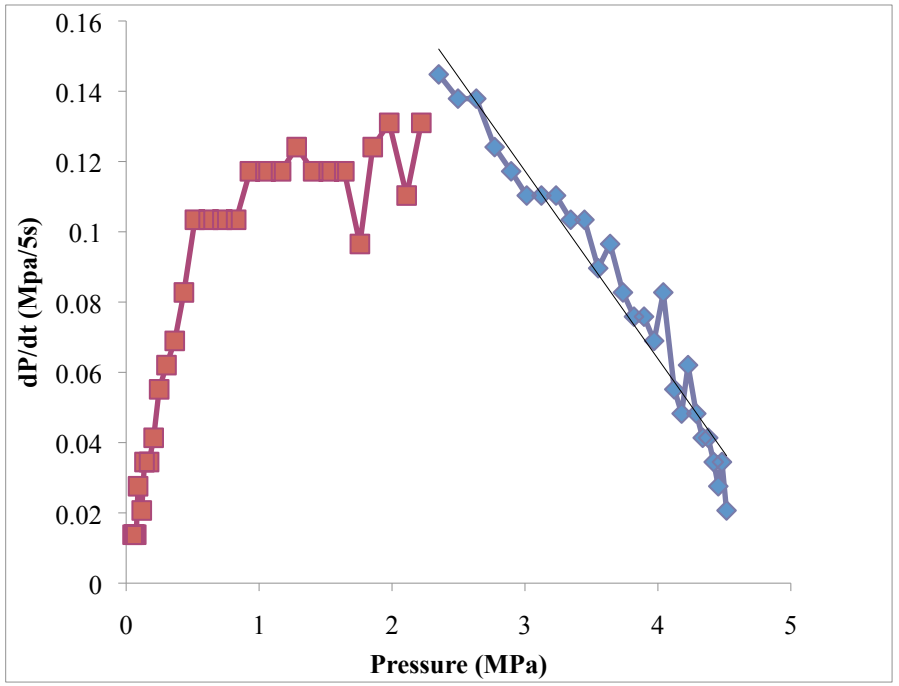

Rk21, -880mRL

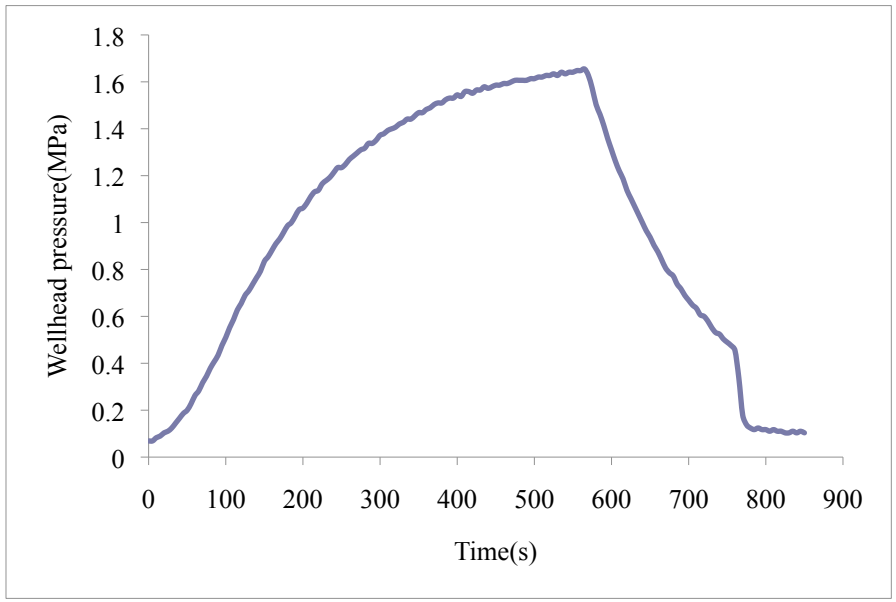
Wellhead pressure(MPa)
1.8
1.6
1.4
1.2
1
0.8
0.6
0.4
0.2
0
0
100
200
300
400
500
600
700
800
900
Time(s)

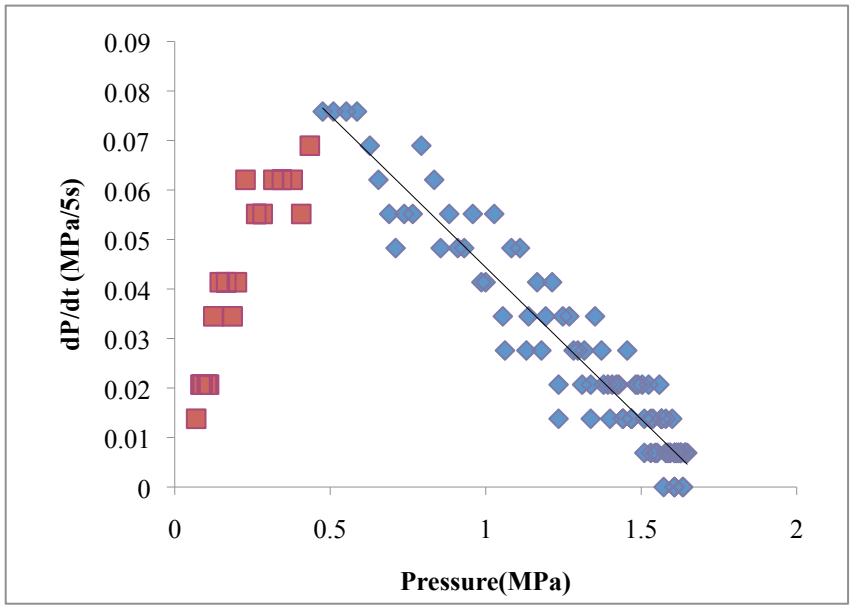
dP/dt (MPa/5s)
0.09
0.08
0.07
0.06
0.05
0.04
0.03
0.02
0.01
0
0
0.5
1
1.5
2
Pressure(MPa)

RK30, -770mRL

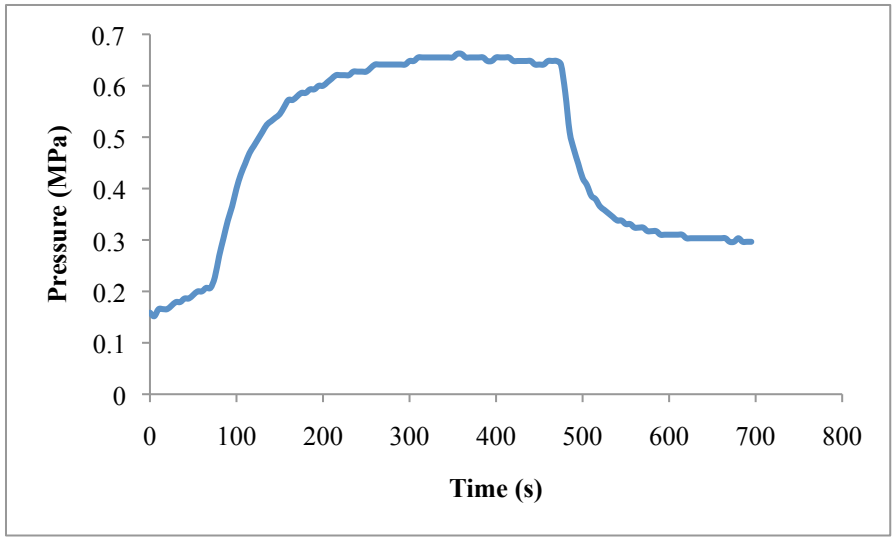
Pressure (MPa)
0.7
0.6
0.5
0.4
0.3
0.2
0.1
0
0
100
200
300
400
500
600
700
800
Time (s)

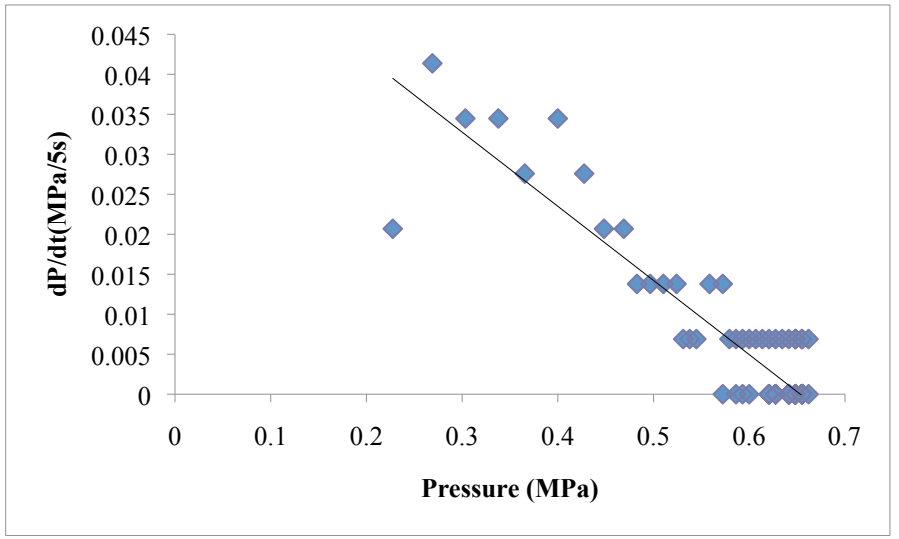
dP/dt(MPa/5s)
0.045
0.04
0.035
0.03
0.025
0.02
0.015
0.01
0.005
0
0
0.1
0.2
0.3
0.4
0.5
0.6
0.7
Pressure (MPa)

RK14, -335mRL

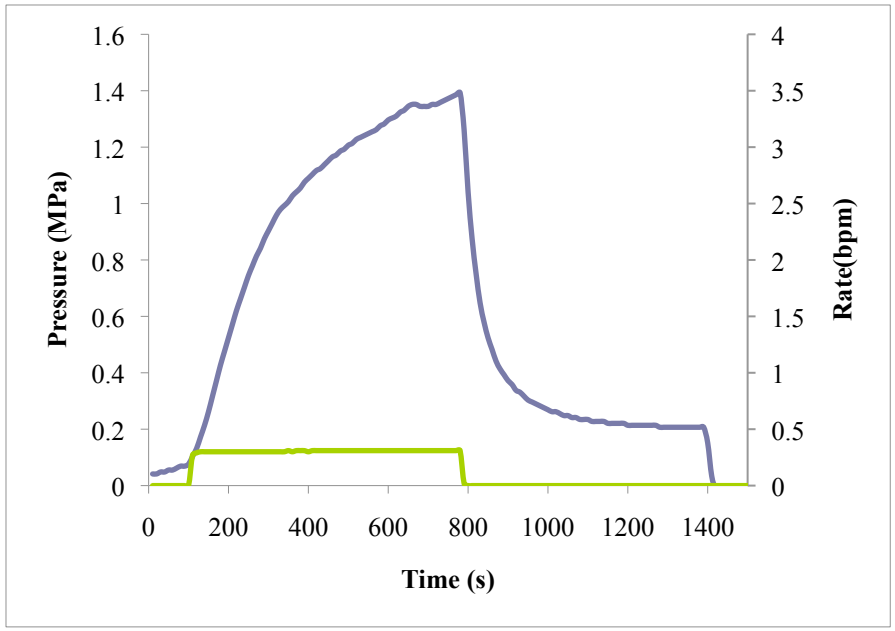
Pressure (MPa)
Rate(bpm)
Time (s)
0
0.2
0.4
0.6
0.8
1
1.2
1.4
1.6
0.5
1.5
2
2.5
3
3.5
4
200
400
600
800
1000
1200
1400

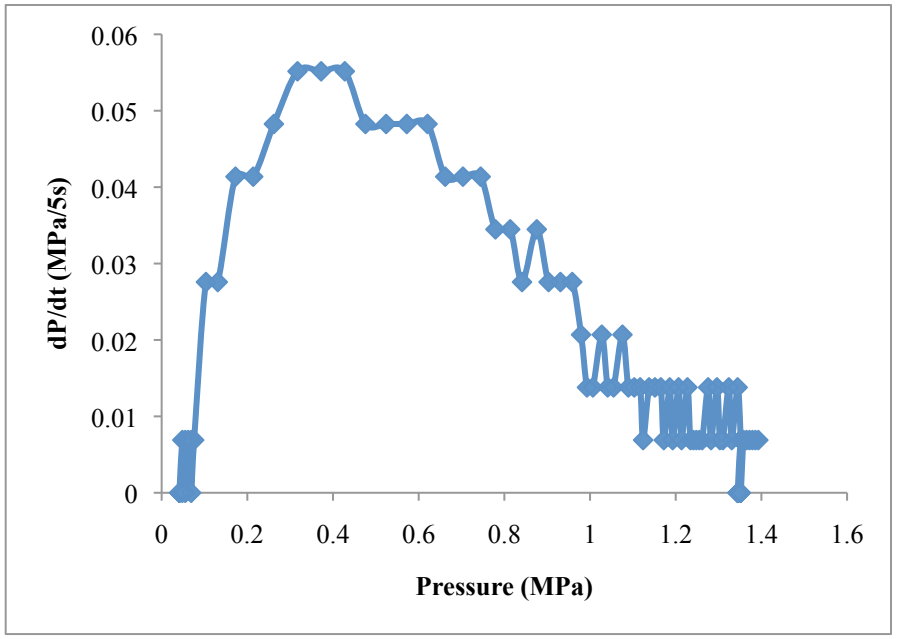
dP/dt (MPa/5s)
Pressure (MPa)
0
0.01
0.02
0.03
0.04
0.05
0.06
0.2
0.4
0.6
0.8
1
1.2
1.4
1.6

RK18, -79mRL

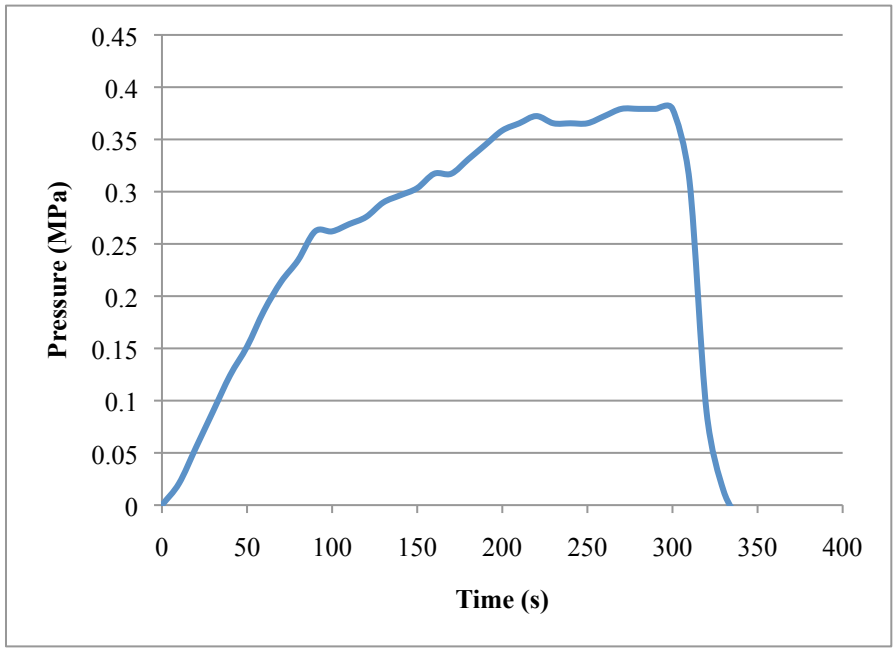
Pressure (MPa)
0.45
0.4
0.35
0.3
0.25
0.2
0.15
0.1
0.05
0
0
50
100
150
200
250
300
350
400
Time (s)

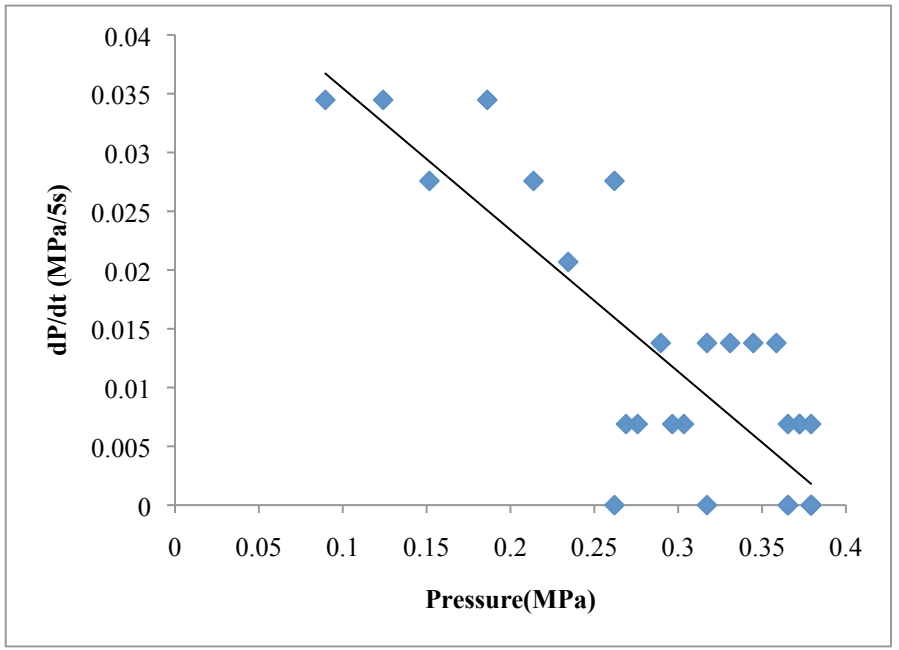
dP/dt (MPa/5s)
0.04
0.035
0.03
0.025
0.02
0.015
0.01
0.005
0
0
0.05
0.1
0.15
0.2
0.25
0.3
0.35
0.4
Pressure(MPa)

RK21, -9mRL

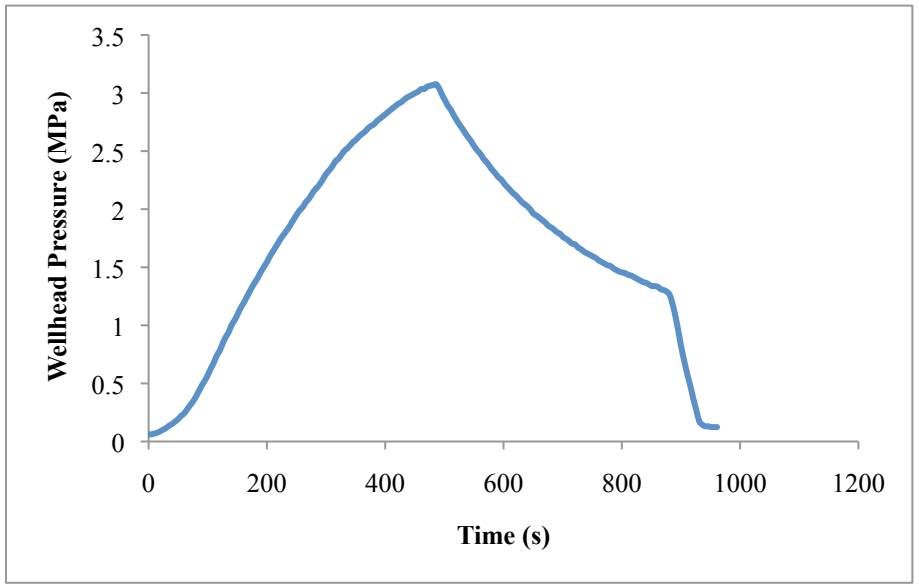
Wellhead Pressure (MPa)
3.5
3
2.5
2
1.5
1
0.5
0
0
200
400
600
800
1000
1200
Time (s)

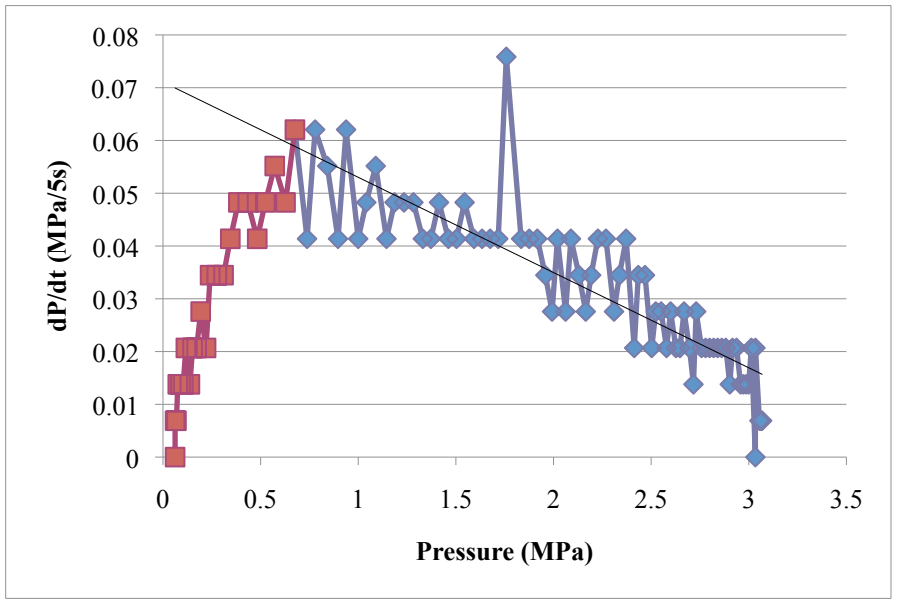
dP/dt (MPa/5s)
0.08
0.07
0.06
0.05
0.04
0.03
0.02
0.01
0
0
0.5
1
1.5
2
2.5
3
3.5
Pressure (MPa)

RK21, 299mRL

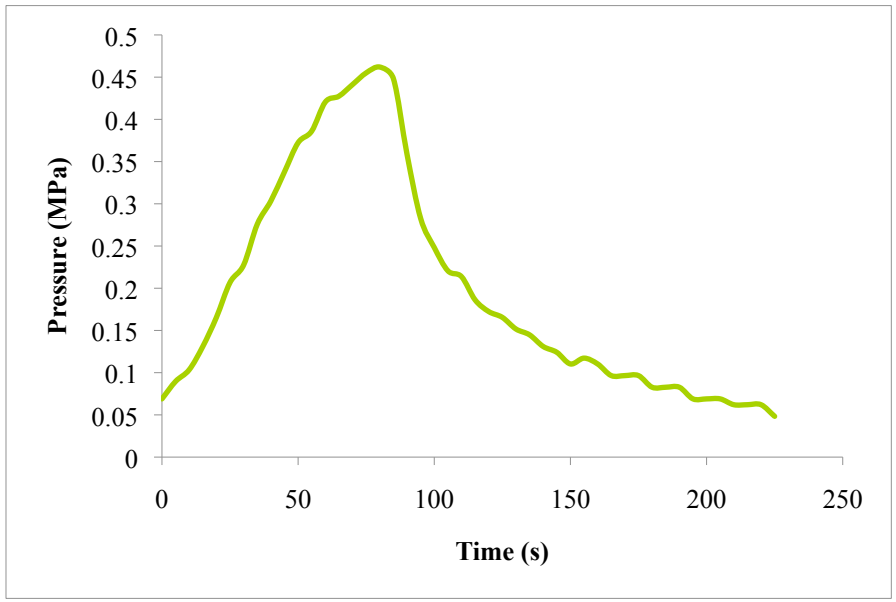
Pressure (MPa)
0.5
0.45
0.4
0.35
0.3
0.25
0.2
0.15
0.1
0.05
0
0
50
100
150
200
250
Time (s)

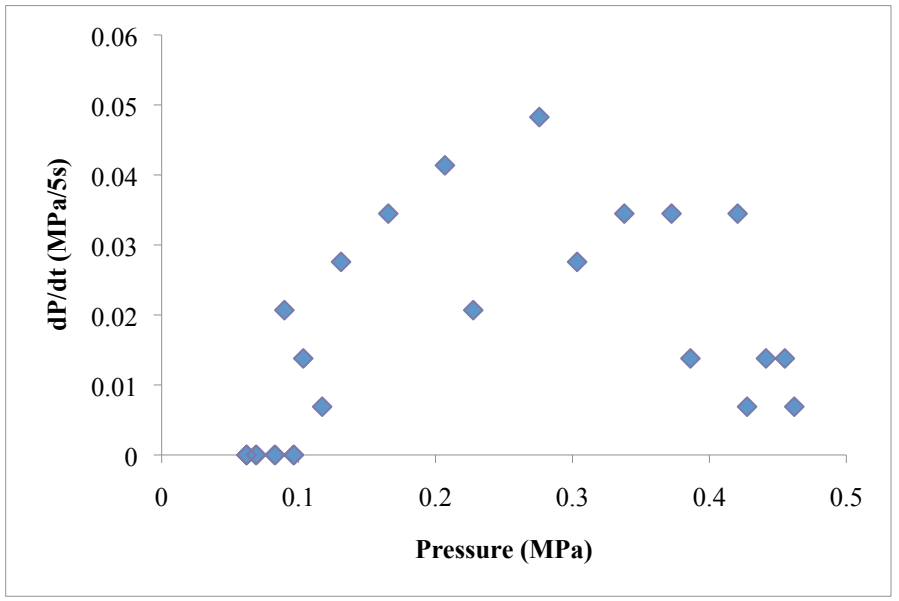
dP/dt (MPa/5s)
0.06
0.05
0.04
0.03
0.02
0.01
0
0
0.1
0.2
0.3
0.4
0.5
Pressure (MPa)

**Fracture Reactivation Category**

RK17, -633mRL

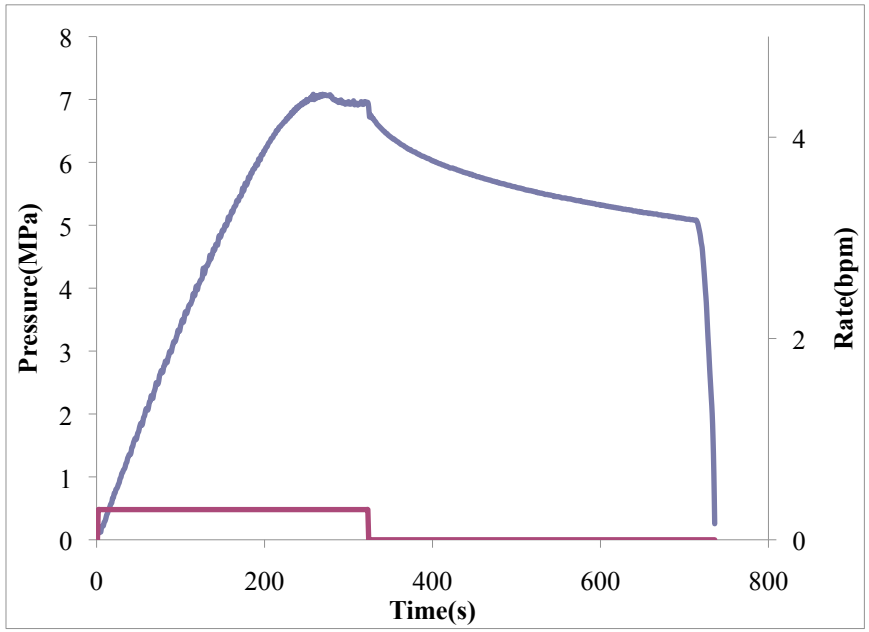


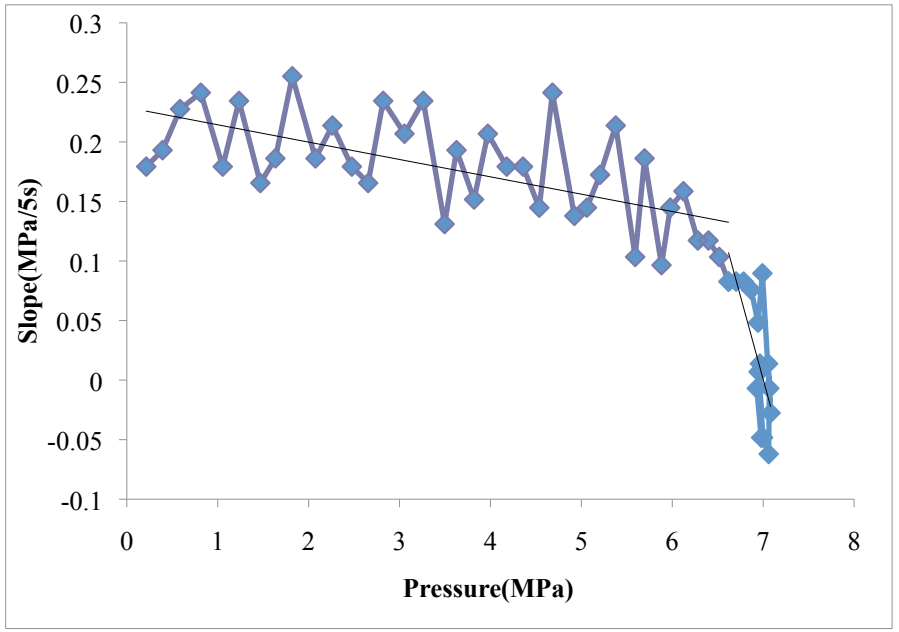

RK14, -120mRL

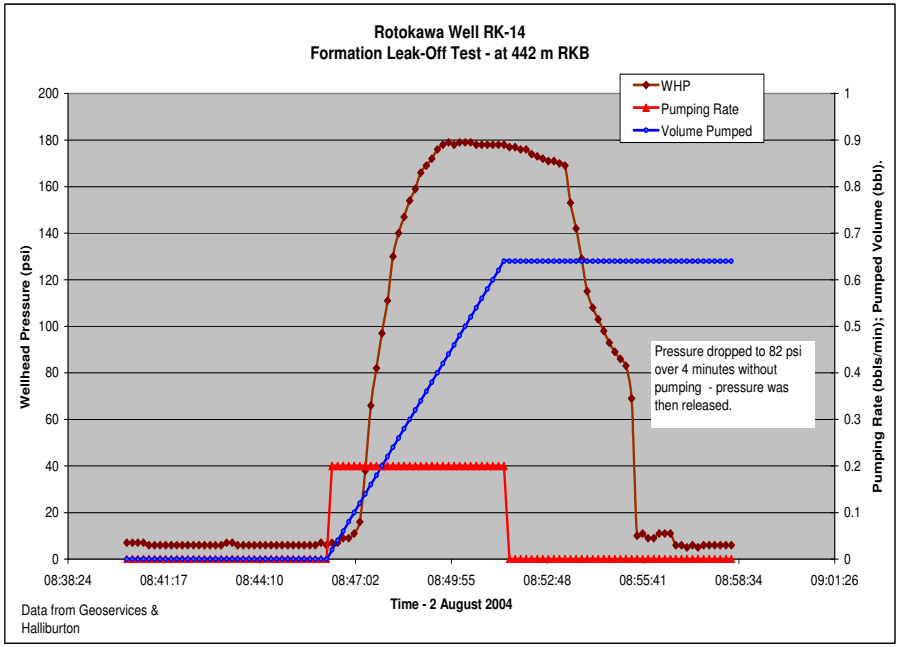
Rotokawa Well RK-14
Formation Leak-Off Test - at 442 m RKB
WHP
Pumping Rate
Volume Pumped
Wellhead Pressure (psi)
Pumping Rate (bbls/min); Pumped Volume (bbl).
Pressure dropped to 82 psi over 4 minutes without pumping - pressure was then released.
Time - 2 August 2004
Data from Geoservices & Halliburton

RK32, 262mRL

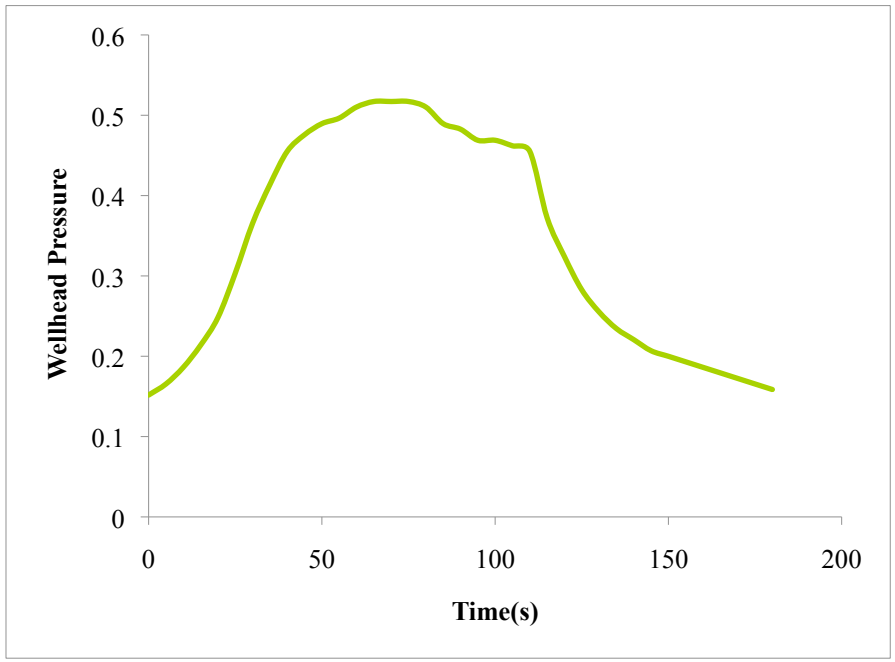
Wellhead Pressure
0.6
0.5
0.4
0.3
0.2
0.1
0
0
50
100
150
200
Time(s)

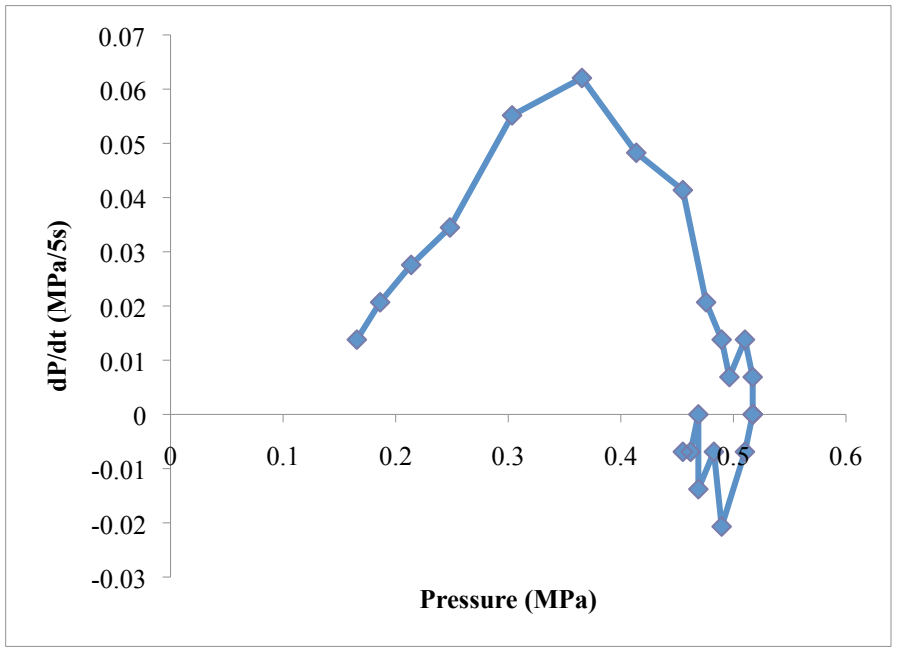
dP/dt (MPa/5s)
0.07
0.06
0.05
0.04
0.03
0.02
0.01
0
-0.01
-0.02
-0.03
0
0.1
0.2
0.3
0.4
0.5
0.6
Pressure (MPa)

Rk33, -56mRL

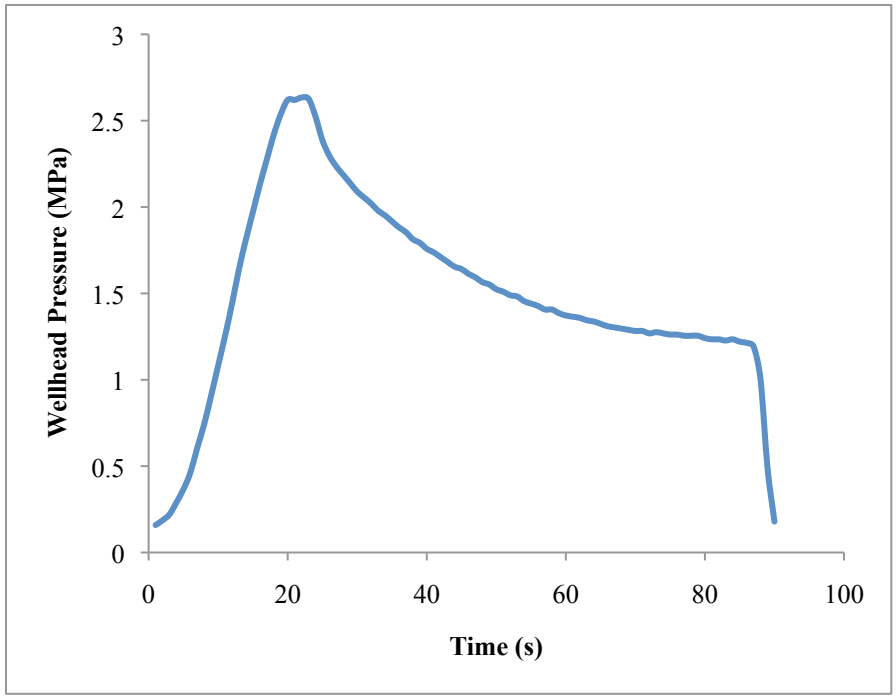
Wellhead Pressure (MPa)
3
2.5
2
1.5
1
0.5
0
0
20
40
60
80
100
Time (s)

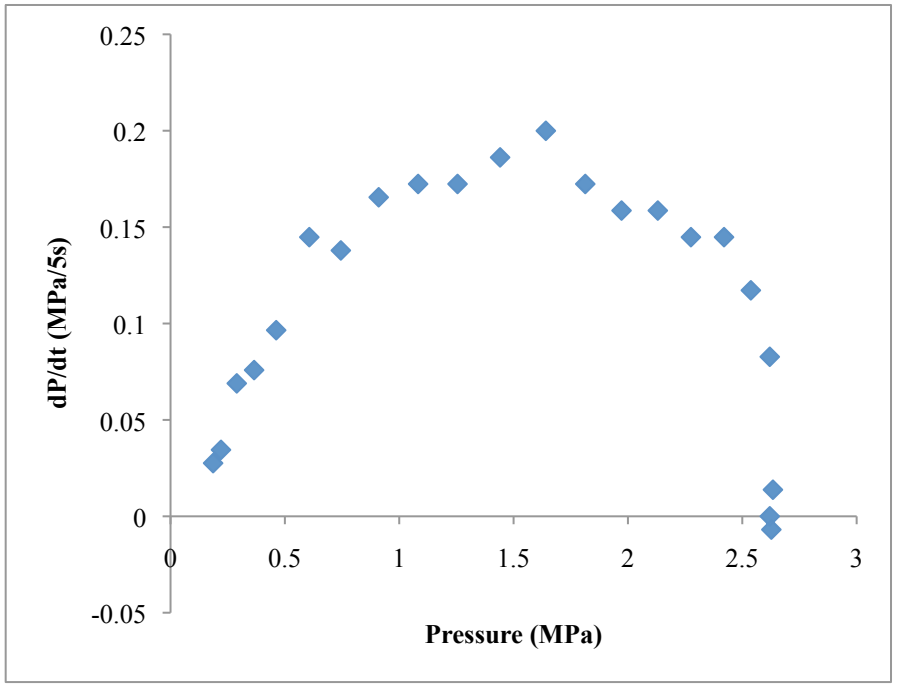
dP/dt (MPa/5s)
0.25
0.2
0.15
0.1
0.05
0
-0.05
0
0.5
1
1.5
2
2.5
3
Pressure (MPa)

**Fracture forming Category**

RK16, -1176mRL

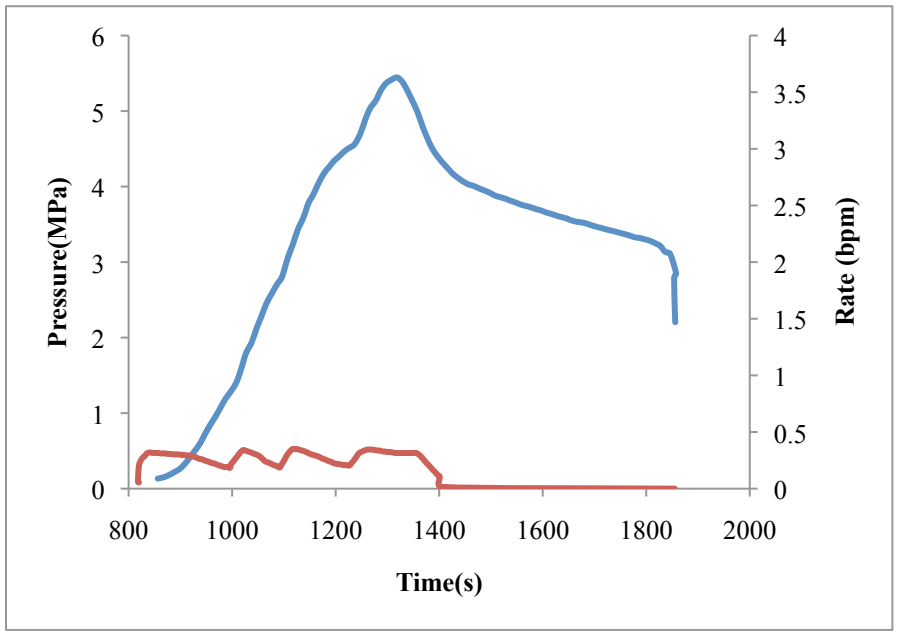


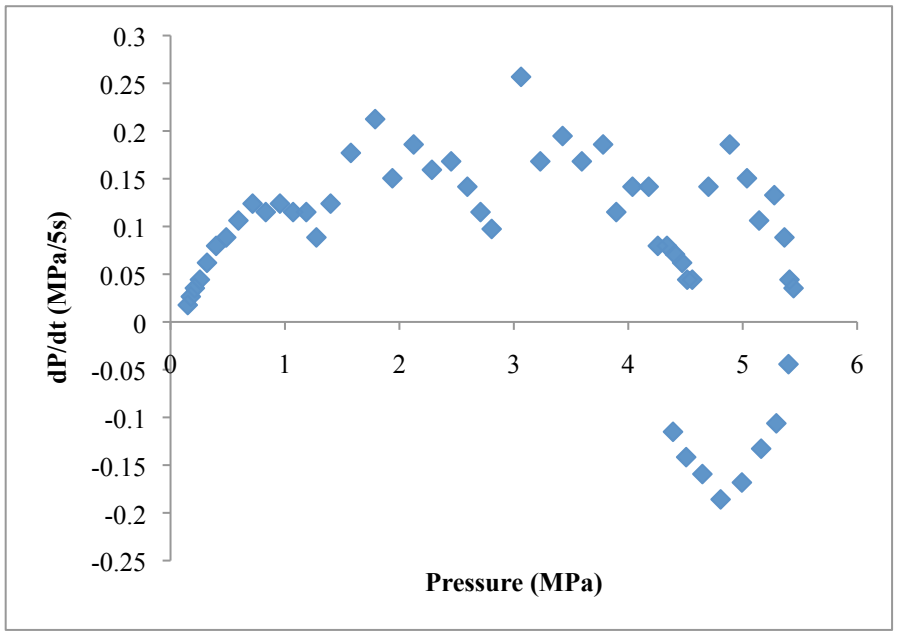

RK32, - 51.76mRL

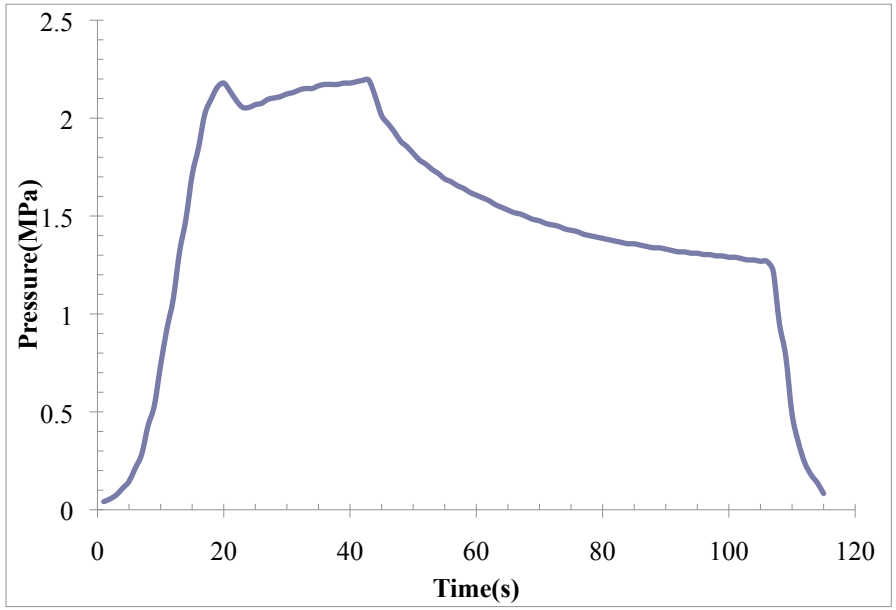


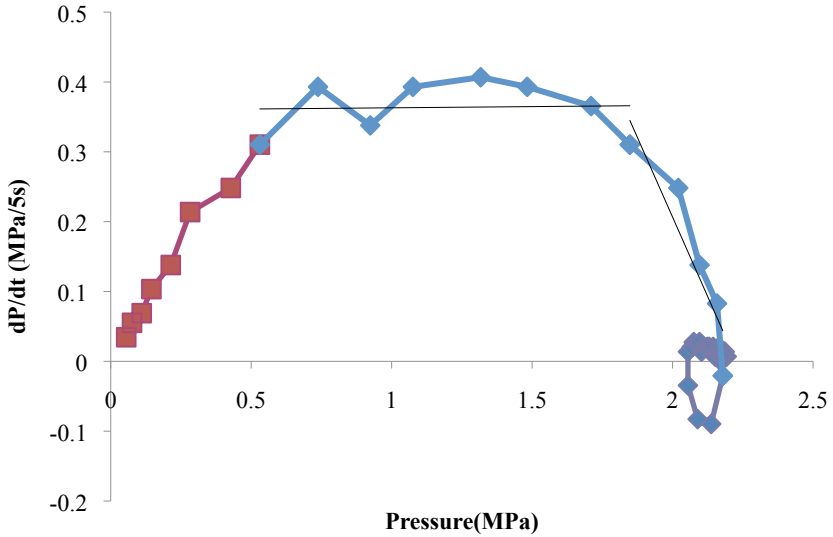

RK32, 186mRL

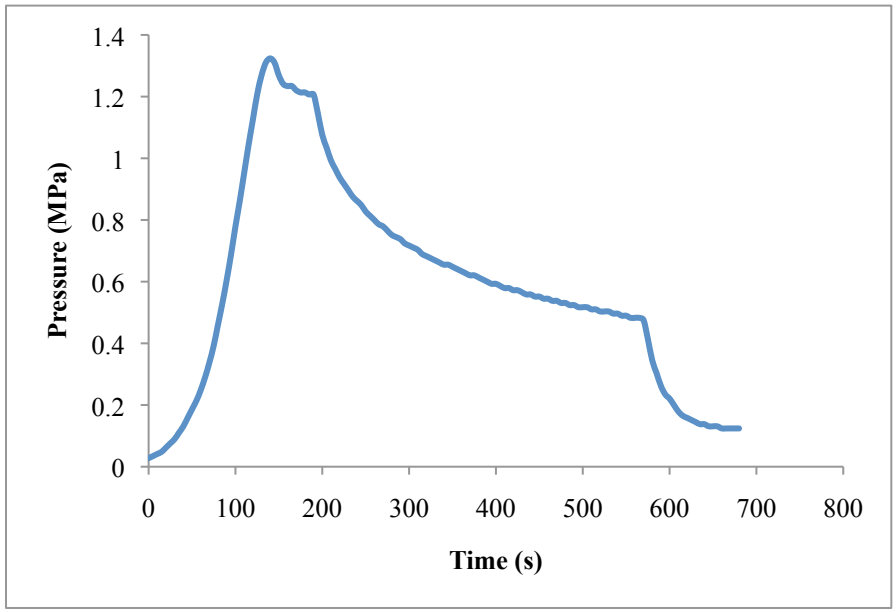
Pressure (MPa)
1.4
1.2
1
0.8
0.6
0.4
0.2
0
0
100
200
300
400
500
600
700
800
Time (s)

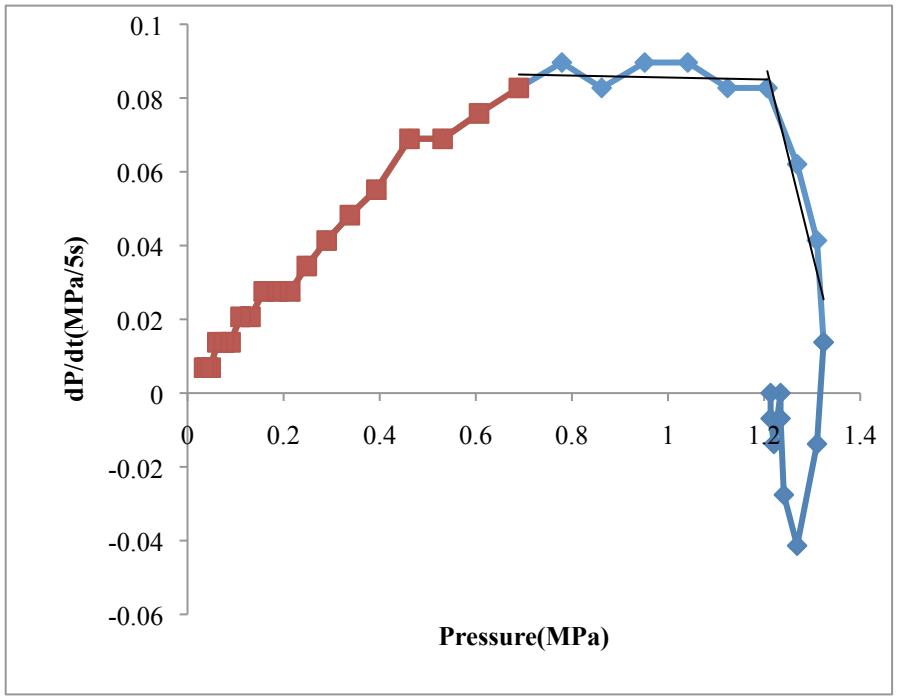
dP/dt(MPa/5s)
0.1
0.08
0.06
0.04
0.02
0
-0.02
-0.04
-0.06
0
0.2
0.4
0.6
0.8
1
1.2
1.4
Pressure(MPa)

RK27, 212mRL

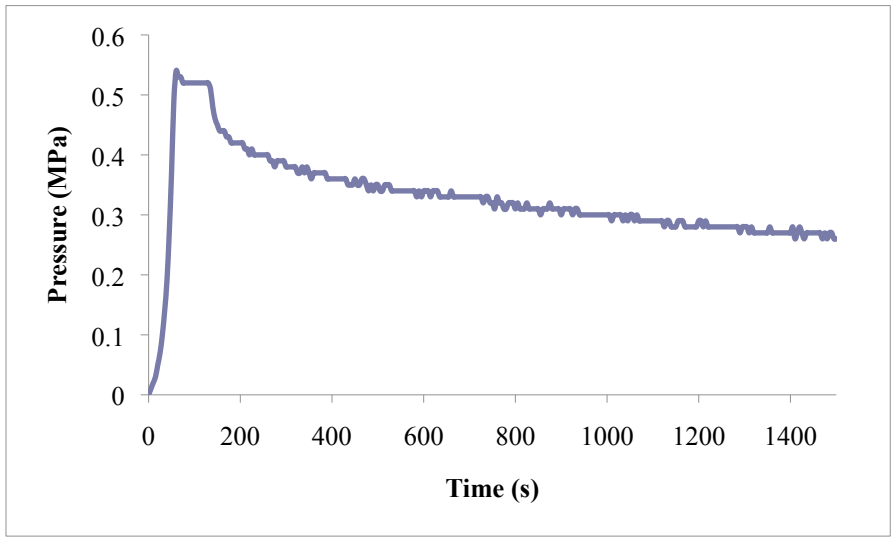
Pressure (MPa)
0.6
0.5
0.4
0.3
0.2
0.1
0
0
200
400
600
800
1000
1200
1400
Time (s)

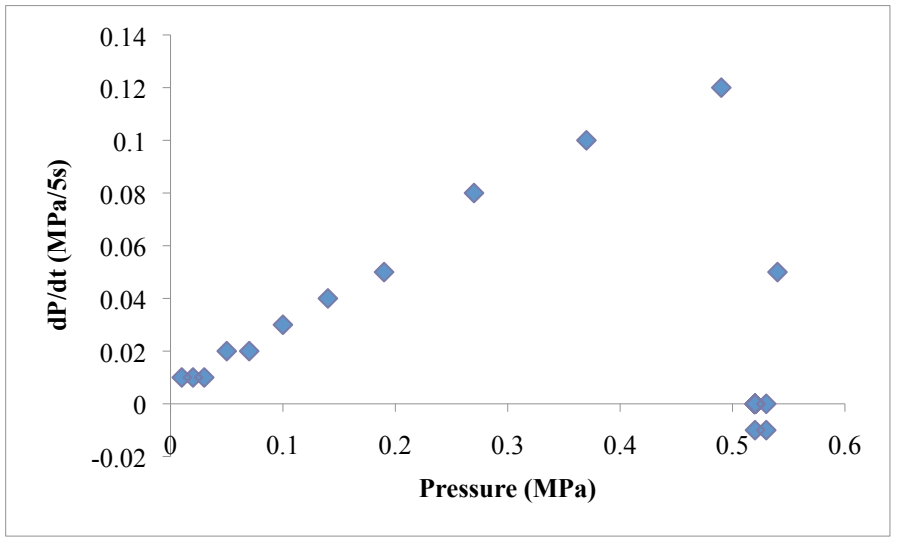
dP/dt (MPa/5s)
0.14
0.12
0.1
0.08
0.06
0.04
0.02
0
-0.02
0
0.1
0.2
0.3
0.4
0.5
0.6
Pressure (MPa)

**Appendix D , Peska & Zoback 1995 method.**

In this appendix, the method used for Figure 8 in Chapter 4 is described. This information is all available in Appendix A of Peska & Zoback (1995).

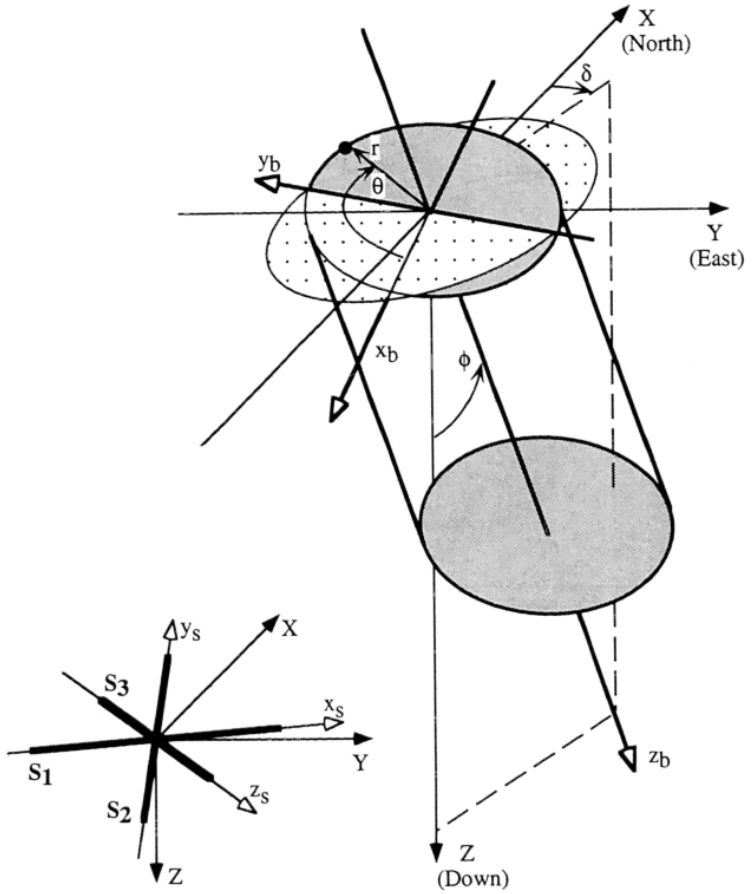


**Figure A1.** Borehole coordinate systems $(x_b,y_b,z_b)$ and $(r,\theta,z_b)$ and a stress coordinate system $(x_s,y_s,z_s)$ with respect to the geographic coordinates $(X,Y,Z)$. The system $(x_s,y_s,z_s)$ coincides with the far-field principal stresses $S_1$, $S_2$, $S_3$. The borehole orientation relative to the geographic coordinates is described by the azimuth $\delta$ and inclination $\phi$..

**Figure 2 Angular relationships between wellbore orientation, stress field and geographical North used in Peska & Zoback.**

In order to assess the stress at the borehole wall using far field stresses, a number of transformations are required. The first transformation is transforming the stress tensor to a generalised stress tensor in the current geographic coordinates. The second

transformation then transforms the tensor to that is aligned with the borehole azimuth and inclination. This tensor can be used to compute the modifications of stresses due to the void, using a version of the Kirsch equations.

Once the stress at the borehole wall have been computed, we used the formula of the minimum tangential stress, coupled with the Stephens & Voight (1982) temperature induce tangential stress to assess the effect of rock properties and temperature on the stresses required to induce tensile failure. A loop formula was run in Matlab for every intermediate stress magnitude ($S_2$) between the estimated $S_3$ and $S_1$, and every instance negative tangential stress was flagged, which allowed for the construction of the curves in Figure 8.